

Cover Page



Universiteit Leiden



The handle <http://hdl.handle.net/1887/62922> holds various files of this Leiden University dissertation.

**Author:** Doney, K.D.

**Title:** Infrared spectroscopy of astrophysically relevant hydrocarbons

**Issue Date:** 2018-06-20

# **Infrared Spectroscopy of Astrophysically Relevant Hydrocarbons**

Kirstin Danielle Doney

© Kirstin Danielle Doney 2018

Nothing in this publication may be reproduced, stored in an automated database or made public in any form or in any manner without the prior written permission of the author.

Niets uit deze uitgave mag worden verveelvoudigd, opgeslagen in een geautomatiseerd gegevensbestand of openbaar gemaakt worden in enige vorm of op enige wijze zonder voorafgaande schriftelijke toestemming van de auteur.

Infrared Spectroscopy of Astrophysically Relevant Hydrocarbons, Thesis, Leiden University

140 pages; illustrated, with bibliographic references and summary in Dutch and English

Printed by Ipskamp Drukkers

ISBN: 978-94-028-1044-8

Cover design by Kirstin Danielle Doney, Image (Cassini in the Enceladus plume in 2015) Credit: NASA/JPL-Caltech

*This work has been financially supported by the Nederlandse Organisatie voor Wetenschappelijk Onderzoek (NWO), Nederlandse Onderzoekschool voor Astronomie (NOVA) and by the European Research Council (ERC).*

# Infrared Spectroscopy of Astrophysically Relevant Hydrocarbons

## **Proefschrift**

ter verkrijging van  
de graad van doctor aan de Universiteit Leiden  
op gezag van de Rector Magnificus prof. mr. C. J. J. M. Stolker  
volgens besluit van het College voor Promoties  
te verdedigen op woensdag 20 Juni 2018  
klokke 11:15 uur

door

Kirstin Danielle Doney  
geboren te Dallas, Texas, USA  
in 1988

Promotiecommissie

Promotor Prof. dr. H. V. J. Linnartz

Co-promotor Dr. D. Zhao at University of Science and Technology of China

Overige leden Prof. dr. H. J. A. Röttgering

Prof. dr. A. G. G. M. Tielens

Prof. dr. W. J. Buma at Universiteit van Amsterdam

Dr. H. S. P. Müller at Universität zu Köln

Dr. T. J. Lee at NASA Ames

“Since every piece of matter in the Universe is in some way affected by every other piece of matter in the Universe, it is in theory possible to extrapolate the whole of creation - every sun, every planet, their orbits, their composition and their economic and social history - from, say, one small piece of fairy cake” – Douglas Adams



## CONTENTS

---

List of Figures

List of Tables

1	INTRODUCTION	1
1.1	Introduction	2
1.1.1	Astronomical formation of hydrocarbons	2
1.2	Theory of ro-vibrational spectroscopy	4
1.3	<i>Ab initio</i> methods to predict spectroscopic parameters	7
1.4	Experimental measurements of ro-vibrational spectra	10
1.5	This Thesis	13
1.6	Bibliography	14
2	THE <i>ab initio</i> CALCULATION OF SMALL POLYYNES	17
2.1	Introduction	18
2.2	Computational Methods	19
2.3	Results and Discussion	20
2.3.1	Equilibrium structure	20
2.3.2	Spectroscopic properties of acetylene and diacetylene	21
2.3.3	Spectroscopic properties of triacetylene	24
2.3.4	Spectroscopic properties of tetraacetylene	25
2.4	Conclusions	26
2.5	Acknowledgements	27
2.6	Bibliography	27
3	HIGH-RESOLUTION INFRARED SPECTRUM OF THE $\nu_4$ FUNDAMENTAL AND NEARBY HOT BANDS OF DIACETYLENE	31
3.1	Introduction	32
3.2	Experiment	33
3.3	Results and discussion	34
3.3.1	Experimental spectra	34
3.3.2	Spectral analysis	36
3.3.3	Vibrational excitation temperatures	42
3.4	Conclusions	44
3.5	Acknowledgements	44
3.6	Bibliography	44

4	HIGH-RESOLUTION INFRARED SPECTRUM OF THE $\nu_5$ FUNDAMENTAL AND NEARBY HOT BANDS OF TRIACETYLENE	47
4.1	Introduction	48
4.2	Experimental methods	49
4.3	Results and discussion	50
4.3.1	The $5_0^1$ fundamental	52
4.3.2	The $5_0^1 10_1^1$ and $5_0^1 13_1^1$ bands	55
4.3.3	The $5_0^1 11_1^1$ and $1_0^1 8_0^1 11_1^0$ bands	56
4.4	Conclusions	56
4.5	Acknowledgements	57
4.6	Bibliography	57
5	HIGH-RESOLUTION INFRARED SPECTRUM OF THE $\nu_3+\nu_5$ COMBINATION BAND OF PROPYNE	59
5.1	Introduction	60
5.2	Methods	60
5.2.1	Experimental	60
5.2.2	Theoretical	61
5.3	Results and discussion	61
5.4	Conclusion	66
5.5	Acknowledgements	66
5.6	Bibliography	66
6	HIGH-RESOLUTION INFRARED SPECTRA OF THE $\nu_1$ FUNDAMENTAL BANDS OF MONO-SUBSTITUTED $^{13}\text{C}$ PROPYNE ISOTOPOLOGUES	69
6.1	Introduction	70
6.2	Methods	71
6.3	Results and discussion	71
6.3.1	Calculation results	71
6.3.2	Experimental results	73
6.3.3	Perturbation Analysis	77
6.4	Conclusions	78
6.5	Acknowledgement	79
6.6	Bibliography	79
7	HIGH-RESOLUTION INFRARED SPECTRUM OF THE $\nu_4$ FUNDAMENTAL BAND OF CYCLOPROPENYL CATION	81
7.1	Introduction	82
7.2	Experimental method	83
7.3	Results and analysis	84
7.4	Astrophysical implications	85
7.5	Conclusions	86

7.6	Acknowledgements	86
7.7	Bibliography	86
8	ASTRONOMICAL INFRARED SPECTRUM OF DEUTERATED POLYCYCLIC AROMATIC HYDROCARBONS	89
8.1	Introduction	90
8.2	Observations and data reduction	91
8.3	Results and analysis	92
8.4	Discussion	99
8.5	Acknowledgements	101
8.6	Bibliography	101
A	SUPPLEMENTARY MATERIAL	105
A.1	Chapter 2	106
A.2	Chapter 3	108
A.3	Chapter 4	114
A.4	Chapter 5	119
A.5	Chapter 6	121
A.6	Chapter 7	123
	SAMENVATTING	127
	SUMMARY	131
	LIST OF PUBLICATIONS	135
	CURRICULUM VITAE	137
	ACKNOWLEDGEMENTS	139



## LIST OF FIGURES

---

Figure 1.1	Carbon chain reaction network	3
Figure 1.2	IR vibrational frequency chart	5
Figure 1.3	Examples of ro-vibrational bands	7
Figure 1.4	Image of the SPIRAS set up	9
Figure 1.5	Box diagram of the SPIRAS set up	9
Figure 1.6	Schematic of the SPIRAS slit discharge nozzle	10
Figure 1.7	Image of the SPIRAS plasma	11
Figure 1.8	The triggering scheme of SPIRAS	12
Figure 2.1	AE-CCSD(T)/cc-pCVQZ equilibrium geometries of $\text{HC}_{2n}\text{H}$ ( $n = 1 - 4$ )	20
Figure 3.1	Experimental and simulated spectrum of the $\nu_4$ band and associated hot bands of $\text{HC}_4\text{H}$	35
Figure 3.2	Experimental spectra of the $\text{HC}_4\text{H}$ Q-branches	36
Figure 3.3	Excitation temperature plot of $\text{HC}_4\text{H}$	43
Figure 4.1	Experimental and simulated spectrum of the $\nu_5$ band and associated hot bands of $\text{HC}_6\text{H}$	50
Figure 4.2	Observed perturbations in the o-c values of the $\nu_5$ band of $\text{HC}_6\text{H}$	53
Figure 4.3	Best fit simulated spectra of the $\nu_5$ band and the perturbing state of $\text{HC}_6\text{H}$	54
Figure 5.1	Experimental and simulated spectrum of the $\nu_3 + \nu_5$ combination band of $\text{C}_3\text{H}_4$	62
Figure 5.2	The Q-branch of the $\nu_3 + \nu_5$ combination band of $\text{C}_3\text{H}_4$	62
Figure 6.1	Experimental and simulated spectra of $\nu_1$ fundamental bands of $\text{C}_3\text{H}_4$	75
Figure 6.2	Experimental and simulated spectra of the $K$ -subband structure	76
Figure 7.1	Equilibrium geometry of $\text{c-C}_3\text{H}_3^+$	82
Figure 7.2	Experimental and simulated spectrum of the $\nu_4$ band of $\text{c-C}_3\text{H}_3^+$	83
Figure 8.1	Line fitting results of the observed astronomical spectra from 2 - 5 $\mu\text{m}$	95
Figure 8.2	Line fitting results of the observed astronomical spectra in the 4 $\mu\text{m}$ region	96

LIST OF TABLES

Table 2.1	Rotational constants of $\text{HC}_{2n}\text{H}$ ( $n = 1 - 4$ )	21
Table 2.2	Harmonic and anharmonic (VPT2) frequencies of $\text{HC}_2\text{H}$	21
Table 2.3	Harmonic and anharmonic (VPT2) frequencies of $\text{HC}_4\text{H}$	22
Table 2.4	Vibration-rotation interaction constants of $\text{HC}_{2n}\text{H}$ ( $n = 1 - 4$ )	23
Table 2.5	Harmonic and anharmonic (VPT2) frequencies of $\text{HC}_6\text{H}$	24
Table 2.6	Harmonic and anharmonic (VPT2) frequencies of $\text{HC}_8\text{H}$	26
Table 3.1	Vibrational normal modes of $\text{HC}_4\text{H}$	34
Table 3.2	Lower state rotational parameters for the bands of $\text{HC}_4\text{H}$	37
Table 3.3	Upper state rotational parameters for the bands of $\text{HC}_4\text{H}$	38
Table 4.1	Vibrational normal modes of $\text{HC}_6\text{H}$	49
Table 4.2	Lower and upper state spectroscopic parameters for the $\nu_5$ fundamental band and perturber band of $\text{HC}_6\text{H}$	52
Table 4.3	Lower and upper state spectroscopic parameters for the hot bands of $\text{HC}_6\text{H}$	55
Table 5.1	Spectroscopic parameters of the vibrational levels of the $\nu_3+\nu_5$ combination band of $\text{C}_3\text{H}_4$	63
Table 5.2	Effective spectroscopic parameters of the perturbing states of the $\nu_3+\nu_5$ state of $\text{C}_3\text{H}_4$	64
Table 5.3	Harmonic and anharmonic (VPT2) frequencies of $\text{C}_3\text{H}_4$	64
Table 5.4	CCSD(T)/ANO1 vibration-rotation interaction constants of $\text{C}_3\text{H}_4$	65
Table 6.1	Harmonic and anharmonic (VPT2) frequencies of $\text{C}_3\text{H}_4$ isotopologues	72
Table 6.2	CCSD(T)/ANO1 vibration-rotation interaction constants of $\text{C}_3\text{H}_4$ $^{13}\text{C}$ -isotopologues	74
Table 6.3	K-subband spectroscopic parameters of $\text{C}_3\text{H}_4$ isotopologues	75
Table 6.4	Upper state spectroscopic parameters of $\text{C}_3\text{H}_4$ isotopologues	76
Table 7.1	Spectroscopic parameters of $\text{c-C}_3\text{H}_3^+$	86
Table 8.1	AKARI observation log and target parameters	93
Table 8.2	Gaussian profile parameters for ice absorption features and emission lines fitted in the spectra	94
Table 8.3	PAH/ $\text{H}_n$ -PAH fluxes for sources with detectable deuterated features	97
Table 8.4	PAD/ $\text{D}_n$ -PAH fluxes for sources with detectable deuterated features	97
Table A.1	CCSD(T)/ANO1 vibrational anharmonicity constants for $\text{HC}_2\text{H}$	106
Table A.2	CCSD(T)/ANO1 vibrational anharmonicity constants for $\text{HC}_4\text{H}$	106
Table A.3	CCSD(T)/ANO1 vibrational anharmonicity constants for $\text{HC}_6\text{H}$	106
Table A.4	CCSD(T)/ANO1 vibrational anharmonicity constants for $\text{HC}_8\text{H}$	107
Table A.5	Line list of (A1) band of $\text{HC}_4\text{H}$	108
Table A.6	Line list of (A2) band of $\text{HC}_4\text{H}$	108
Table A.7	Line list of $4_0^1 6_1^1$ band of $\text{HC}_4\text{H}$	108
Table A.8	Line list of $\nu_4$ fundamental band of $\text{HC}_4\text{H}$	109

Table A.9	Line list of $4_0^1 9_1^1$ band of $\text{HC}_4\text{H}$	109
Table A.10	Line list of $4_0^1 7_1^1$ band of $\text{HC}_4\text{H}$	110
Table A.11	Line list of (F) band of $\text{HC}_4\text{H}$	110
Table A.12	Line list of (G) band of $\text{HC}_4\text{H}$	110
Table A.13	Line list of $4_0^1 8_1^1$ band of $\text{HC}_4\text{H}$	111
Table A.14	Line list of $4_0^1 7_2^2$ band of $\text{HC}_4\text{H}$	111
Table A.15	Line list of $1_0^1 8_0^1 6_1^0$ band of $\text{HC}_4\text{H}$	111
Table A.16	Line list of $1_0^1 8_0^1 6_2^1$ ( $\Delta$ ) band of $\text{HC}_4\text{H}$	112
Table A.17	Line list of $1_0^1 8_0^1 6_1^1$ ( $\Sigma$ ) band of $\text{HC}_4\text{H}$	112
Table A.18	Line list of $1_0^1 8_0^1 6_1^0 7_1^1$ band of $\text{HC}_4\text{H}$	112
Table A.19	Line list of $1_0^1 8_0^1 6_2^1 7_1^1$ band of $\text{HC}_4\text{H}$	113
Table A.20	Line list of $1_0^1 6_0^1 8_1^0$ band of $\text{HC}_4\text{H}$	113
Table A.21	Line list of $1_0^1 6_0^1 8_1^0 7_1^1$ band of $\text{HC}_4\text{H}$	113
Table A.22	Line list of $\nu_5$ fundamental band of $\text{HC}_6\text{H}$ - Coriolis	114
Table A.23	Line list of $\nu_5$ perturber band of $\text{HC}_6\text{H}$ - Coriolis	114
Table A.24	Line list of $\nu_5$ fundamental band of $\text{HC}_6\text{H}$ - Fermi	115
Table A.25	Line list of $\nu_5$ perturber band of $\text{HC}_6\text{H}$ - Fermi	115
Table A.26	Line list of $5_0^1 13_1^1$ band of $\text{HC}_6\text{H}$	116
Table A.27	Line list of $5_0^1 10_1^1$ band of $\text{HC}_6\text{H}$	117
Table A.28	Line list of $5_0^1 11_1^1$ band of $\text{HC}_6\text{H}$	118
Table A.29	Line list of $1_0^1 8_0^1 11_1^0$ band of $\text{HC}_6\text{H}$	118
Table A.30	Line list of $\nu_3 + \nu_5$ combination band of $\text{C}_3\text{H}_4$	119
Table A.31	Line list of $\nu_3 + \nu_5$ perturber transitions of $\text{C}_3\text{H}_4$	120
Table A.32	CCSD(T)/ANO1 frequencies of $^{12}\text{CH}_3^{13}\text{C}^{13}\text{CH}$	121
Table A.33	Line list of $\nu_1$ fundamental band of (I1) of $^{13}\text{C} - \text{C}_3\text{H}_4$	121
Table A.34	Line list of $\nu_1$ fundamental band of (I2) of $^{13}\text{C} - \text{C}_3\text{H}_4$	121
Table A.35	Line list of $\nu_1$ fundamental band of (I3) of $^{13}\text{C} - \text{C}_3\text{H}_4$	122
Table A.36	CCSD(T)/ANO1 Fermi resonance of $\text{C}_3\text{H}_4$	122
Table A.37	Line list of $\nu_4$ fundamental band of $c\text{-C}_3\text{H}_3^+$	123
Table A.38	continued table	124



Hydrocarbons play an important role in the chemistry of a variety of astronomical environments from the diffuse interstellar medium to dense hydrocarbon atmospheres of solar system bodies (*e.g.*, Titan or Jupiter) and exoplanets. For most astronomical objects, the determination of chemical abundances, and consequently an understanding of the chemical evolution relies upon the observation of molecular spectra. However, to date astronomical models need to make assumptions, because not all of the molecules expected to participate in the reaction pathways have been observed. This is due, in part, to a lack of accurate line position data, which is needed for unambiguous identification. This thesis focuses on the study of the infrared spectroscopy of hydrocarbons, from *ab initio* calculations to high-resolution laboratory measurements to astronomical observations, in order to fill in some of these gaps.

---

## 1.1 INTRODUCTION

Hydrocarbons (with the general formula  $C_nH_m$ ) are a particularly important class of molecules. Carbon's ability to form  $sp$ ,  $sp^2$ , and  $sp^3$  hybridized orbitals, and to undergo catenation ( $\sigma$  bonding between carbon atoms) allows hydrocarbons to form complex and geometrically diverse molecules. In pure carbon molecules, this leads to the physical differences observed between graphene and diamonds. On Earth hydrocarbons are primarily found in their saturated form, as natural gas or petroleum. As such, their predominant use is as a combustible fuel source - directly for heating, or to create electrical energy in power plants. Hydrocarbons in either their saturated or unsaturated forms are also the base molecules in organic synthesis, and are the structural basis of most biological molecules, *e.g.*, fatty acids [ $C_mH_nCOOH$ ] and sugar [ $C_6H_{12}O_6$ ] molecules.

In most astronomical environments, such as the interstellar medium (ISM) or circumstellar shells, the conditions are much harsher than on Earth, and as a result the chemistry and the stability of molecules is vastly different than that seen on Earth. For example, in the diffuse interstellar medium the low temperature ( $\sim 10 - 100$  K) and the low density ( $\sim 10 - 100$  particles/cm<sup>3</sup>) allow unstable molecules, such as  $CH^+$ , to live for hundreds of years; while in the laboratory it may only last for fractions of a second. As such, the typical chemical formation mechanisms used to synthesize hydrocarbon molecules in "bench-top chemistry" do not work in astronomical environments. Instead, simplified reaction schemes are invoked to explain the observed presence of such molecules. The mechanisms are limited to: radiative association, dissociative recombination, ion-neutral and radical-neutral reactions, photodissociation, photoionization, and grain mediated reactions (Wakeham et al., 2012). Even with the simplified chemistry, around 200 molecules have been detected in astronomical objects, and a vast majority of them are unsaturated hydrocarbons or their O-, N-, S-bearing derivatives (Müller et al., 2005).

1.1.1 *Astronomical formation of hydrocarbons*

Based on the wide range of environments where hydrocarbons have been observed: planetary atmospheres (Kim et al., 1985; Waite et al., 2007), ejecta of evolved stars (Winnewisser & Walmsley, 1978; Cernicharo & Guélin, 1996), protoplanetary nebulae (Cernicharo et al., 2001; Malek et al., 2012), molecular clouds (Bell et al., 1999; Araki et al., 2017), HII regions (Allamandola et al., 1989), and protoplanetary disks (Gibb et al., 2007), one prevailing condition for high abundances of hydrocarbon formation is high density. Current astronomical models and theories assume simple hydrocarbons, *e.g.*, acetylene [ $H_2C_2$ ] and methane [ $CH_4$ ] (through sequential H-addition reactions), along with polycyclic aromatic hydrocarbons (PAHs) are formed in the atmospheres of dying red giant (or asymptotic giant branch, A.G.B.) stars under combustion-like conditions. In such cases, the HACA (hydrogen abstraction, carbon addition) model is the principle formation mechanism (Cherchneff, 2011; Agúndez, M. et al., 2017). These molecules are then ejected into the ISM where they become part of molecular clouds.

Gas-phase reactions are unlikely to form complex molecules unless in high density environments. In most cases molecules subsequently freeze out onto dust grains, such as in protoplanetary disks, where they undergo various photoprocessing and radical-radical reactions to form complex organic molecules (COMs). Such reaction schemes are thought to be the source of molecules like ethanol [ $C_2H_5OH$ ] or glycolaldehyde [ $HC(O)CH_2OH$ ] (Chuang et al., 2016). In dense environments with a nearby radiation source, such as warm core molecular clouds or the atmospheres of planets, long hydrocarbon chains like diacetylene [ $HC_4H$ ] or benzene [ $C_6H_6$ ] can be formed through gas-phase ion-neutral reactions (Figure 1.1; Smith (1992); McEwan et al. (1999); Sakai & Yamamoto (2013)).

Comparison of observed molecular abundances with those predicted from models gives insight into the reaction pathways, and thus the chemistry taking place in the different astronomical environments. Since molecular formation mechanisms are typically branched, with the branching

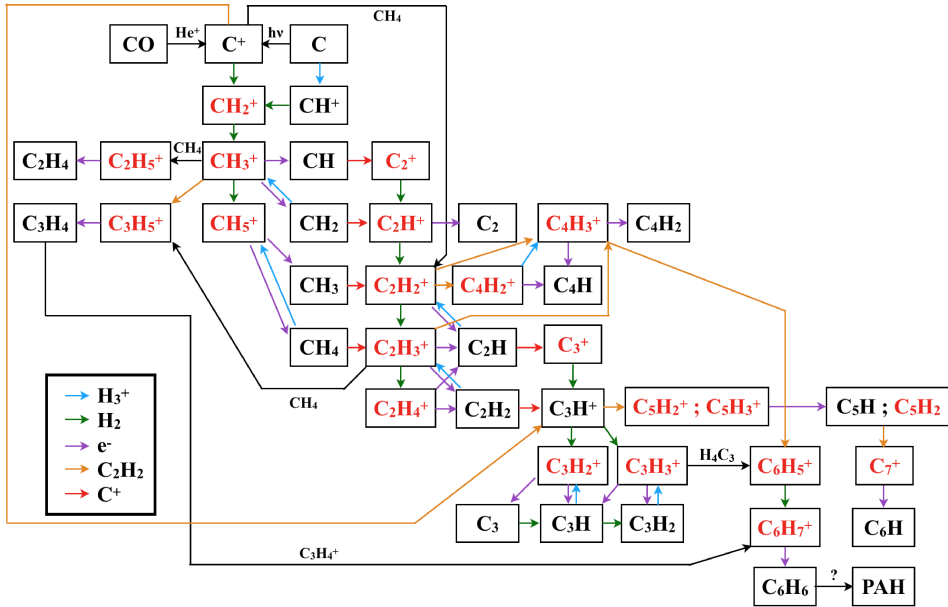


Figure 1.1: Part of the ISM gas-phase hydrocarbon reaction network based on Smith (1992); McEwan et al. (1999); Sakai & Yamamoto (2013). Molecules labeled in black have been detected spectroscopically in space, while molecules labeled in red have yet to be detected.

ratios temperature and pressure dependent, knowing the abundance of different molecules in the network can infer the how, when, and where these molecules were produced. Studying the abundance and spatial distribution of chemicals can also give direct diagnostics of the physical conditions of the astronomical environment. For example, the relative intensities of  $K'$ -subbands in a symmetric top molecule such as propyne [ $C_3H_4$ ] or methyl cyanide [ $CH_3CN$ ] probes the kinetic temperature (Churchwell & Hollis, 1983), or the gas density can be probed based on the presence of particular molecules in the gas-phase, like hydrogen cyanide [ $HCN$ ] or the formyl cation [ $HCO^+$ ] (Papadopoulos, 2007; van Kempen et al., 2009).

In nearby objects, *i.e.*, solar system objects where probes can be sent, the chemistry can be inferred from the chemical abundances determined by mass spectrometry of atmospheric or soil samples. In such cases, cationic hydrocarbons have been detected in relatively high abundances compared to their neutral species (Waite et al., 2007), suggesting the cationic-neutral formation mechanism is reasonable under high density and temperature conditions of planetary atmospheres. However, most astronomical objects are light years away, and understanding of their chemistry requires remote detections through emission or absorption spectroscopy. Unambiguous identification of a particular molecule can be accomplished through observation of its unique rotational transitions (typically in the microwave spectral range), or through observation of the ro-vibrational transitions (typically in the infrared (IR) spectral range). To date, few ionic species have been observed spectroscopically in the interstellar or circumstellar medium (Müller et al., 2005), and as such, the gas-phase ion-neutral formation mechanism is difficult to prove in distant environments.

Recent advancements in resolution of astronomical spectra, with instruments such as the Atacama Large Millimeter Array (ALMA) in the submillimeter/THz observations and CRIRES+ in the IR, mean that new forests of “weak” molecular transitions can now be observed. Unfortunately, some of the observed transitions cannot be assigned to any known molecular transition (Cernicharo et al., 2013). The non-detections can be attributed, in part, to a lack of accurate line positions for

the proposed molecules.

Accurate line positions for different molecular transitions can be obtained from high level *ab initio* calculations or from experimental measurements. While current *ab initio* theory can predict ground electronic state vibrational frequencies and rotational constants (A, B, and C) to within a few percent, experimental measurements are still required to determine the true value. In the past few decades, experimental techniques including cavity enhanced and cavity ring-down spectroscopy have improved the detection sensitivity such that transitions can be measured even for species with low molecular concentrations (O’Keefe & Deacon, 1988). There have also been advances in transient specie production with plasma discharge sources making *in situ* observation of unstable hydrocarbons possible (Motylewski & Linnartz, 1999).

In many cases, the infrared transitions of molecules are intrinsically stronger than their pure rotational transitions, and in some cases, *e.g.*, centrosymmetric molecules, pure rotational transitions are forbidden. As such, in order to measure new transitions of astrophysically relevant hydrocarbons, which are typically produced in low concentrations under laboratory conditions, we will focus on their strong C-H ro-vibrational transitions, a region that is accessible with precise laser systems in the laboratory and astronomical telescopes.

## 1.2 THEORY OF RO-VIBRATIONAL SPECTROSCOPY

Molecular spectroscopy is used to understand the nature of nuclear and electronic motions of a molecule by observing the interactions of the molecule with radiation. The absorption or emission of a photon with energy  $h\nu$  by a molecule results in changes in its energy state, which can be observed as spectral lines. From the four postulates of quantum mechanics, there is an operator that corresponds to any physical quantity. In the case of absorption spectroscopy the corresponding operator is the Hamiltonian ( $\hat{H}$ ), which includes the kinetic and potential energies of the molecule of interest. A molecule can undergo three types of transitions: electronic (hereafter denoted by subscript e) vibrational (subscript v), and rotational (subscript r), with  $E_e > E_v > E_r$ . The particular energy required to induce a transition can be given by the Schrödinger equation, which in general takes the form

$$\hat{H}(\mathbf{r}, \mathbf{R})\Psi(\mathbf{r}, \mathbf{R}) = E_{e\mathbf{v}\mathbf{r}}\Psi(\mathbf{r}, \mathbf{R}) \quad (1.1)$$

where  $\Psi$  represents the electronic wavefunction dependent on the electronic coordinate,  $\mathbf{r}$ , and the nuclear coordinate,  $\mathbf{R}$ , and  $E_{e\mathbf{v}\mathbf{r}}$  is the total molecular energy. In addition, transitions are only allowed if they satisfy

$$\int \Psi_f \hat{\mu} \Psi_i d\tau \neq 0 \quad (1.2)$$

where  $\Psi_i$  is the initial state wavefunction of the transition,  $\Psi_f$  the final state wavefunction, and  $\hat{\mu}$  is the electronic dipole moment operator. For infrared spectroscopy, this means to only transitions with an induced dipole moment (*e.g.*, an asymmetric stretch) can be observed.

The Schrödinger equation can only be solved exactly for the hydrogen atom. As such, for all other molecules a series of approximations are made in order to predict the molecular properties, such as the vibrational frequencies. In the simplest case the vibrational motion of molecules can be approximated as a harmonic oscillator; solving the Schrödinger equation for a harmonic oscillator gives the following energy levels:

$$E(\mathbf{v}) = \sum_{i=1}^{3N-5} \left( v_i + \frac{1}{2} \right) \omega_e \quad (1.3)$$

where  $v_i$  is the vibrational level and  $\omega_e$  is the equilibrium harmonic frequency. However, real molecular bonds are anharmonic oscillators, and the vibrational level spacings become closer as

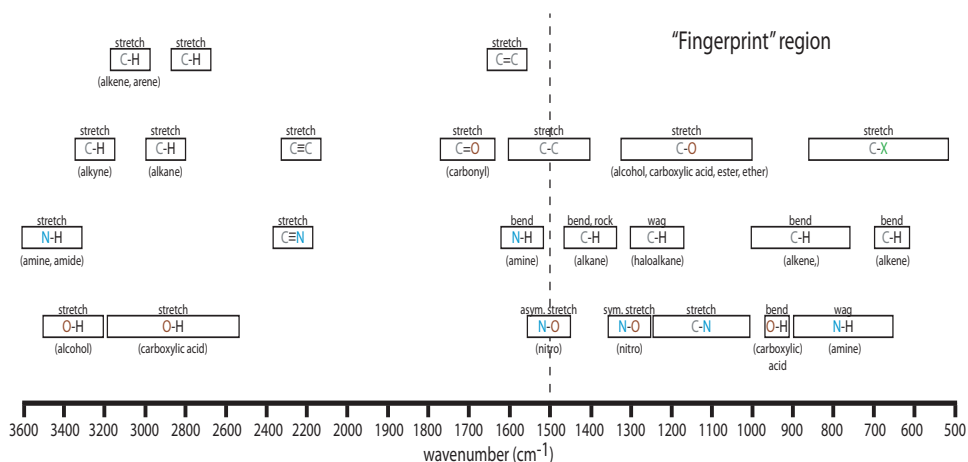


Figure 1.2: A chart of the characteristic frequency ranges for different vibrational motions, adapted from McMurry (2016).

$\nu_i$  increases. To take this into account, the vibrational energy level equation can be described as a series expansion with successively higher order correction terms:

$$E(\nu) = \sum_{i=1}^{3N-5} \left( \nu_i + \frac{1}{2} \right) \omega_e + \sum_i \sum_{j \geq i} x_{ij} \left( \nu_i + \frac{1}{2} \right) \left( \nu_j + \frac{1}{2} \right) + \sum_i \sum_{j \geq i} g_{ij} l_i l_j + \text{h.o.t.} \quad (1.4)$$

where  $x_{ij}$  and  $g_{ij}$  are the anharmonicity constant between two states  $i$  and  $j$ ,  $l$  is the vibrational angular momentum quantum number, and h.o.t. stands for higher order terms.

For a symmetric top molecule, which in the extreme case is a linear molecule, there are two types of vibrations: either the dipole moment remains along the intranuclear axis during the vibration, a parallel band, or the dipole moment becomes orthogonal to the intranuclear axis during the vibration, a perpendicular band. Furthermore, transitions of  $\Delta v = 1$  from the ground state result in fundamental modes, while transitions of  $\Delta v > 1$  result in overtone modes, and transitions involving more than one vibrational state results in a combination state.

Different vibrational motions have characteristic frequencies, based on the atoms and bonds involved (see Figure 1.2). For some vibrational motions, like stretching vibrations, all molecules in the same family have roughly the same vibrational frequency, which can make molecular identification ambiguous. However, some vibrational motions, like bending vibrations, are particular to the size and shape of the molecule making their frequencies more unique to a particular molecule (even between members of the same molecular family). These motions are typically at  $\leq 1500 \text{ cm}^{-1}$ , which is aptly named the “Fingerprint” region.

In the gas-phase, transitions between vibrational levels include rotational transitions. The energy levels corresponding to rotational transitions can be approximated assuming the molecule is a rigid rotor. As such for symmetric top molecule (where linear molecules can be thought of as an extreme case,  $K = 0$ ), the solution to the Schrödinger equation for pure rotation levels gives the following expression:

$$E(J, K, l) = B J(J+1) + (A - B) K^2 + 2A \zeta l K \quad (1.5)$$

where  $J$  is the total angular momentum quantum number,  $K$  is the projection quantum number,  $\zeta$  is the Coriolis coupling constant, and  $A$  and  $B$  are the rotational constants, such that for example

$$B = \frac{h}{8\pi^2 c I_B} = \frac{h}{8\pi^2 c \sum m_i r_i^2} \quad (1.6)$$

Real molecules are not perfectly rigid, and when they rotate, centrifugal stretching changes the spacing between the rotational levels. Taking into account the correction terms, the rotational energy level equation becomes:

$$E(J, K, l) = B_J(J+1) + (A-B)K^2 + 2A\zeta_l K - D_J J^2(J+1)^2 - D_{JK} J(J+1)K^2 - D_K K^4 \quad (1.7)$$

where  $D_J$ ,  $D_{JK}$ , and  $D_K$  are the centrifugal distortion constants, and for a linear molecule  $K = 0$ . Allowed pure rotational transitions are between  $\Delta J = \pm 1$  and  $\Delta K = 0$ .

Combining the vibrational and rotational parts gives the energy level equation for ro-vibrational transitions:

$$E(v, J, K, l) = \sum_{i=1}^{3N-5} \left(v_i + \frac{1}{2}\right) \omega_e + \sum_i \sum_{j \geq i} \left(v_i + \frac{1}{2}\right) \left(v_j + \frac{1}{2}\right) x_{ij} + B_J(J+1) \quad (1.8)$$

$$+ (A-B)K^2 + 2A\zeta_l K - D_J J^2(J+1)^2 - D_{JK} J(J+1)K^2 - D_K K^4$$

For a particular vibrational state the vibrational dependent rotational constants are given by:

$$A_v = A_e - \sum_i \alpha_i^A \left(v_i + \frac{d_i}{2}\right) \sim A_0 - \sum_i (v_i \alpha_i^A) \quad (1.9a)$$

$$B_v = B_e - \sum_i \alpha_i^B \left(v_i + \frac{d_i}{2}\right) \sim B_0 - \sum_i (v_i \alpha_i^B) \quad (1.9b)$$

where  $\alpha$  is the vibration-rotation interaction constant that can be used to identify the molecule and vibrational states involved in an observed ro-vibrational band.

For a parallel band of a symmetric top molecule, selection rules allow ro-vibrational transitions are between states where

$$\Delta K = 0 \text{ and } \Delta J = 0, \pm 1 \text{ if } K \neq 0$$

$$\Delta K = 0 \text{ and } \Delta J = \pm 1 \text{ if } K = 0$$

Conversely, for a perpendicular band of a symmetric top molecule allowed transitions are only allowed for

$$\Delta K = \pm 1 \text{ and } \Delta J = 0, \pm 1$$

The selection rules for linear molecules have no  $K$  dependencies, however, they do depend on  $l$ . Transitions are allowed for  $\Delta l = 0, \pm 1$ . If both the upper and lower states are  $l = 0$  ( $\Sigma$  states) then the selection rules only allow transitions for

$$\Delta J = \pm 1$$

However, if in either the upper or lower state  $l \neq 0$  then transitions are allowed for

$$\Delta J = 0, \pm 1$$

If the molecule has a center of inversion, then transitions are only allowed between states with opposite symmetries (*i.e.*,  $g$  [symmetric]  $\leftrightarrow$   $u$  [asymmetric]).

The general structure of infrared ro-vibrational bands includes a series of transitions that can be broken up into the P-branch ( $\Delta J = -1$ ), the Q-branch ( $\Delta J = 0$ ), and the R-branch ( $\Delta J = +1$ ); see Figure 1.3. The rotational transition intensities are determined by the Hönl-London factors and the level populations ( $N_J$ ), which are governed by Boltzmann distribution

$$N_J = g(2J+1)\exp(-E/k_B T) \quad (1.10)$$

where  $k_B$  is the Boltzmann constant,  $T$  is the rotational temperature of the molecule, and  $g$  is the degeneracy.

The degeneracy is an effect of the nuclear spin on the rotational level population. For molecules

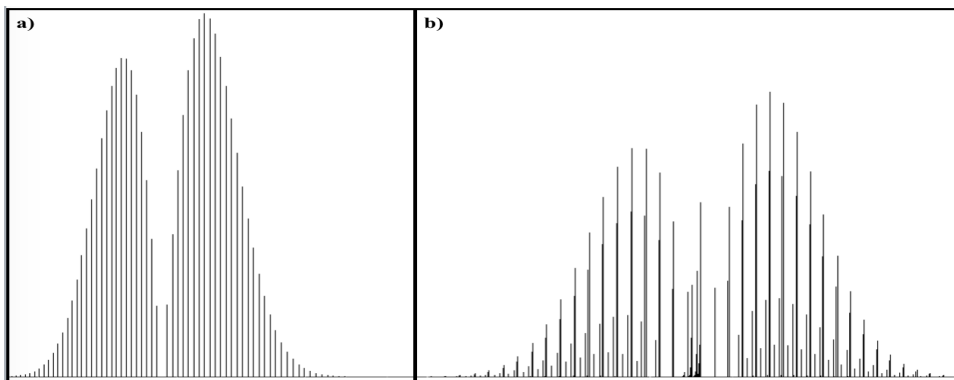


Figure 1.3: An example of a simulated a) linear parallel ( $\Sigma - \Sigma$ ) band with P- and R-branches, and b) symmetric top molecule parallel ( $A_1 - A_1$ ) band with P-, Q-, and R-branches. Both simulated spectra have the same rotational temperature of 20 K.

with a center of inversion (e.g., acetylene,  $\text{HC}_2\text{H}$  or  $\text{C}_3$ ) the degeneracies for the totally symmetric and totally antisymmetric levels differ, and result in observed intensity alternation of the ro-vibrational transitions. The degeneracies are given by:

$$g_{\text{symmetric}} = (2I + 1)(I + 1) \quad (1.11a)$$

$$g_{\text{antisymmetric}} = (2I + 1)I \quad (1.11b)$$

where  $I$  is the spin angular momentum quantum number, which is a whole integer for Bosons (e.g., for C,  $I = 1$ ) and is a half integer for Fermions (e.g., for H,  $I = 1/2$ ). Conversely, for molecules without a center of inversion (e.g., propyne,  $\text{CH}_3\text{C}\equiv\text{CH}$ ) the degeneracies for both symmetric and asymmetric levels are given by:

$$g = (2I_A + 1)(2I_B + 1) \quad (1.12)$$

The intensity of the transitions can also be effected by anharmonic perturbations (e.g., Fermi resonances and Coriolis coupling). A perturbation is the result of the wavefunctions of two modes with similar energy mixing in such a way that the two resulting modes can be described by a linear combination of the two original modes. The two resulting modes are shifted relative to the original modes such that they are pushed apart. In addition, the wavefunction mixing can result in intensity changes, such as intensity borrowing that allows a previously “dark” or forbidden state having observable transitions.

### 1.3 *ab initio* METHODS TO PREDICT SPECTROSCOPIC PARAMETERS

To predict where the ro-vibrational transitions of astrophysically relevant molecules are expected *ab initio* calculations were performed with the development version of the CFOUR (Coupled-Cluster techniques for Computational Chemistry) program (CFOUR, 2017). The calculations in this thesis were performed using the coupled cluster singles and doubles excitation with a perturbative treatment of triples excitation (CCSD(T)) method. In CC theory the wavefunction,  $|\Psi_{\text{CC}}\rangle$ , is given by the exponential ansatz

$$|\Psi_{\text{CC}}\rangle = e^{\hat{T}} |\Phi_0\rangle \quad (1.13)$$

where  $|\Phi_0\rangle$  is the reference wavefunction, a Slater determinant usually constructed from Hartree-Fock molecular orbitals, and  $\hat{T}$  is the cluster operator. It is a post Hartree-Fock method that accounts for electron correlation to approximate the exact energy given in the Schrödinger equation.

With a sufficiently large basis set, CCSD(T) has been shown to accurately reproduce experimental spectroscopic parameters of semi-rigid molecules (Raghavachari et al., 1989; Gauss & Stanton, 1997), and is, in general, called the “gold standard” of computation chemistry.

The correlation consistent polarized X- $\zeta$  basis set (cc-pVXZ; where X = D, T, Q, 5, etc) developed by Dunning and co-workers are built upon a core of Hartree-Fock orbitals, and are designed to converge systematically and smoothly to the complete basis set limit with successively more basis functions. Moreover, the core correlation set (cc-pCVXZ) uses all electrons (AE) and all orbitals (occupied as well as virtual), which is needed for accurate geometry determination. The equilibrium geometries of the molecules studied were determined using the large cc-pCVQZ (quadruple zeta), which features the truncations of [8s7p5d3f1g] (non-hydrogen atoms) and [4s3p2d1f] (hydrogen) of the (15s9p5d3f1g) and (6s3p2d1f) primitive basis set, respectively (Woon & Dunning Jr., 1995; Feller, 1996; Schuchardt et al., 2007). (AE)-CCSD(T)/cc-pCVQZ has been shown to give very accurate equilibrium geometries for unsaturated hydrocarbons (Auer & Gauss, 2001; Bak et al., 2001; Zhang et al., 2007; Simmonett et al., 2009).

The equilibrium geometry calculations, including determination of the equilibrium rotational constants, were done by searching for a minimum on the potential energy surface (PES) using analytic energy derivatives within a Quasi-Newton scheme (Stanton & Gauss, 2000). The calculations start with a unit matrix in the first iteration that is updated using the BFGS scheme. The molecular equilibrium geometry is considered converged when the root-mean-square (rms) gradient fell below  $10^{-10}$  au.

However, it is well known that correlation-consistent basis sets, such as cc-pCVQZ, tend to underestimate the vibrational frequencies of symmetric bending modes ( $\pi_g$ ) of conjugated molecules due to their susceptibility to an intramolecular variant of basis set superposition error (BSSE), *i.e.*, when different parts of the same molecule approach one another their basis functions overlap (Simandiras et al., 1988). It has been shown that one way to avoid this problem is to use basis sets with a large number of Gaussian primitives (particularly f-type), such as the atomic natural orbital (ANO) basis set (which has the primitive basis set (13s8p6d4f2g) for non-hydrogen atoms and (8s6p4dzf) for hydrogen) (Almlöf & Taylor, 1987; Bauschlicher Jr. & Taylor, 1993; Martin et al., 1998). The basis set has a common truncation: [4s3p2d1f] for non-hydrogen atoms and [4s2p1d] for hydrogen (hereafter known as ANO<sub>1</sub>, which is used in this thesis) (Almlöf & Taylor, 1987; Feller, 1996; Schuchardt et al., 2007). Furthermore, the basis set is used such that only the occupied valence orbitals and all virtual orbitals of carbon are considered, *i.e.*, standard frozen-core (fc) calculation. This is because (fc)-CCSD(T)/ANO<sub>1</sub> has been shown to accurately reproduce experimental IR frequencies and intensities for small molecules (Martin et al., 1997, 1998; Vázquez & Stanton, 2007).

At the (fc)-CCSD(T)/ANO<sub>1</sub> optimized geometry, calculations of the harmonic vibrational frequencies and IR intensities were determined using finite difference of analytic gradients in parallel, starting from the harmonic oscillator, rigid-rotor approximation. Subsequently, the anharmonic vibrational frequencies, IR intensities, vibration-rotation interaction constants ( $\alpha$ ), and Fermi resonances were determined from full cubic and the semidiagonal part of the quartic force fields obtained by numerical differentiation of analytic CCSD(T) second derivatives using second-order vibrational perturbation (VPT<sub>2</sub>) theory that also starts from the harmonic oscillator, rigid-rotor approximation (Gauss & Stanton, 1997; Matthews et al., 2007). For most of the calculations carried out in this thesis, the following thresholds for convergence were used: 1) the SCF equations are considered converged when the maximum change in density matrix elements is less than  $10^{-10}$ , 2) the CC amplitudes are considered converged when the maximum of all changes in the amplitudes is less than  $10^{-10}$ , and 3) the linear equations' smallest residual falls below  $10^{-10}$ .

CCSD(T) can be computationally expensive for large molecules, and thus for the theoretical study of PAHs the relatively less accurate, but computationally inexpensive density functional theory (DFT) method was used. DFT uses a functional (the electron density) instead of the wavefunctions to approximate the solution of the Schrödinger equation.



Figure 1.4: The SPIRAS setup at the Sackler Laboratory for Astrophysics at Leiden Observatory.

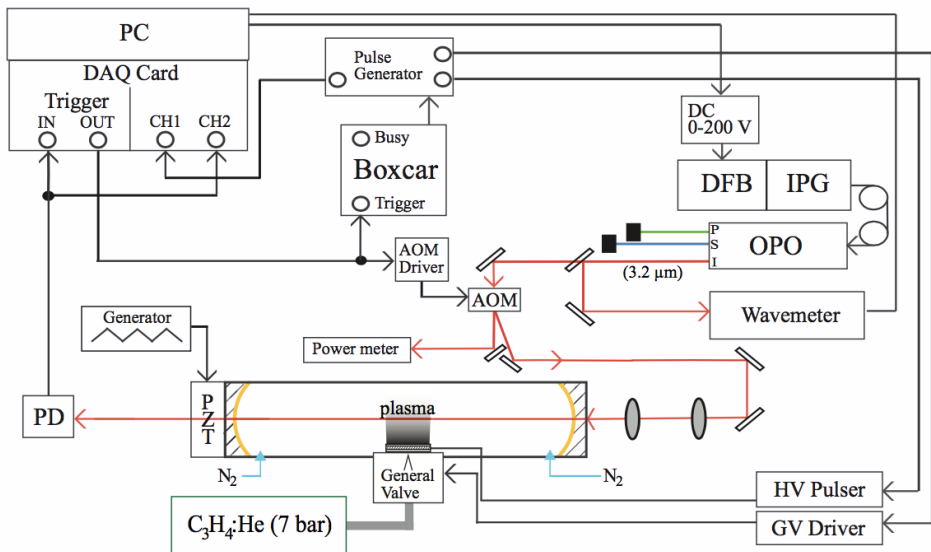


Figure 1.5: Adapted from Zhao et al. (2013), the box diagram of the SPIRAS set up. DFB: distributed feedback fiber laser; IPG: fiber amplifier; OPO: optical parametric oscillator; I: idler beam; S: signal beam; P: pump beam; AOM: acousto-optic modulator; GV: general valve driver; HV: high voltage pulser; PZT: piezoelectric transducer; PD: photovoltaic detector.

## 1.4 EXPERIMENTAL MEASUREMENTS OF RO-VIBRATIONAL SPECTRA

To measure the experimental spectra of astrophysically relevant molecules, the supersonic plasma infrared absorption spectrometer (SPIRAS) at the Sackler Laboratory for Astrophysics was used (Figure 1.5); the experimental setup details are taken from Zhao et al. (2013) and exact experimental settings are given in the relevant chapters.

The main chamber of SPIRAS is formed using a six-way standard ISO160 vacuum chamber mounting the optical cavity and discharge nozzle, and is kept at a stagnation pressure of  $\sim 0.007$  mbar by a vacuum system with a pumping capacity of 4800 m<sup>3</sup>/hour. The analytes, or molecules of study, are introduced into the main chamber through a slit discharge nozzle that is mounted in the center of the main chamber with the slit exit parallel to, and upstream from the axis of the optical cavity. The nozzle is based on the design of Motylewski & Linnartz (1999) (shown in detail in Figure 1.6), and consists of multiple layers starting with a 2 mm pinhole pulsed valve (General Valve, Series 9), followed by a multi-channel body consisting of a series of pin-holes of varying size that regulates the gas distribution towards the exit. The nozzle can be switched to produce either a pulsed and continuous gas flow.

The slit exit is formed by a layered ceramic insulator-anode-ceramic insulator-cathode system.

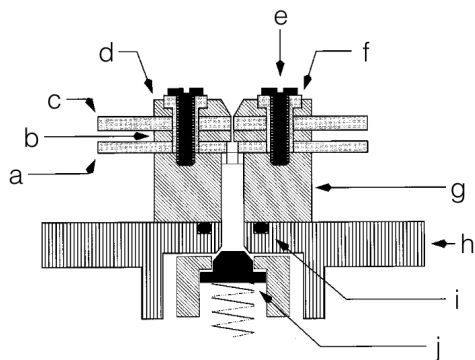


Figure 1.6: Adapted from Motylewski & Linnartz (1999), the schematic of the SPIRAS slit discharge nozzle. a) ceramic insulator plate with  $0.5 \times 20$  mm slit opening, b) anode plate with  $0.5 \times 20$  mm slit opening, c) ceramic insulator plate with  $0.3 \times 30$  mm slit opening, d) one of the metal jaws that make up the cathode, e) screw, f) ceramic screw insulator, g) multi-channel body that consists of a hollow body and six pin-hole openings at the top that have varying diameters that get progressively smaller from outside to inside, h) 2 mm pinhole General Valve, i) O-ring, j) Teflon poppet.

The cathode is composed of two metal plates, or “jaws”, which have a 45 degree edge positioned  $\sim 0.1$  mm away from the edge of the insulator slit edge. The thin slit results in the gas flow being planar instead of conical, and reduces the Doppler broadening of the absorption lines. Furthermore, the precursor gas typically has a backing pressure of a few bars before the nozzle. The large difference between the main chamber stagnation pressure and the backing pressure results in a supersonic expansion of the gas, which results in effective adiabatic cooling and lower Doppler broadening of the molecules in the jet. When necessary, a negative high voltage, typically  $-400$  -  $-700$  V, is applied to the cathode resulting in a plasma discharge.

SPIRAS uses continuous wave cavity ring-down spectroscopy (cw-CRDS) to measure the IR spectrum of the analytes, which are for this work astrophysically relevant hydrocarbon molecules. Cw-CRDS uses a pulse of light from a continuous wave laser as the light source for absorption spectroscopy. This spectroscopic method allows for the high detection sensitivity (absorption,  $A$ ,  $\sim 10^{-6}$  cm<sup>-1</sup>) needed to study the hydrocarbon molecules of astrophysical interest, particularly



Figure 1.7: A typical acetylene plasma expansion produced from the SPIRAS slit discharge nozzle.

compared to direct or multi-pass absorption spectroscopy. This is achieved by using two highly reflective mirrors ( $\sim 99.97\%$  at  $3 \mu\text{m}$ ,  $1 \text{ m}$  radius plano-concave) spaced  $56 \text{ cm}$  apart to form the optical cavity, effectively trapping light inside the cavity, and increasing the absorption path length through the analyte. The signal-to-noise (S/N) is further enhanced by measuring the light that leaks out of the cavity as a function of time, which means the measurements are insensitive to intensity fluctuations in the light source. The  $1/e$  decay time of the light (called the ring-down lifetime) for CRDS can be expressed as:

$$\tau = \frac{L}{c} \frac{1}{(1-R) + \alpha l} \quad (1.14)$$

where  $c$  is the speed of light,  $L$  is the cavity length,  $\alpha$  is the absorptivity constant,  $l$  is the path length, and  $R$  is the reflectivity of the mirrors. In an empty cavity the ring-down time ( $\tau_0$ ) is a measure of the loss of light due to the mirrors, and for most low pressure gases extinction due to scattering is negligible, so the absorbance can be written as

$$A = \alpha l = \frac{L}{c} \left( \frac{1}{\tau} - \frac{1}{\tau_0} \right) \quad (1.15)$$

As such, the greater the value of  $\tau$  the more sensitive the detection. For SPIRAS, operating around  $3 \mu\text{m}$ , typically  $\tau_0$  is  $9 \mu\text{s}$ , but given the wavelength dependent reflectivity of the mirrors it can be up to  $18 \mu\text{s}$ .

The narrowband mid-IR light source used on SPIRAS is produced by a combination pump laser and continuous wave optical parametric oscillator (cw-OPO) system. The output of a DFB fiber laser (NKT photonics, Koheras Basik Y-10) is amplified in a fiber amplifier (IPG Photonics, YAR-10K-1064-LP-SF) to give an output power of  $10 \text{ W}$ . The light is then carried as the pump source through an optic fiber to the single-mode cw-OPO (Aculight Argos 2400SF; module B for  $\lambda = 2.5 - 3.2 \mu\text{m}$  or module C for  $\lambda = 3.2 - 3.9 \mu\text{m}$ ). The cw-OPO unit converts the pump laser into two additional lower energy laser beams, the signal and the idler beams, by a periodically-poled lithium niobate (PPLN) crystal, such that

$$\frac{1}{\lambda_{\text{pump}}} = \frac{1}{\lambda_{\text{signal}}} + \frac{1}{\lambda_{\text{idler}}} \quad (1.16)$$

The output signal and residual pump beam are sent to beam dumps and discarded, while the idler beam is directed towards the optical cavity and used for the experiment. The continuous tunability of the wavelength is accomplished through a number of methods. Course tuning of the wavelength is done using the etalon and crystal inside the optical cavity of the OPO. Rotation of the etalon changes the angle of incidence of the signal laser, and allows for the frequency to be changed in steps of approximately  $1 \text{ cm}^{-1}$ . Varying where the laser crosses the crystal inside the OPO can change the phase-matching conditions, and translating the crystal linearly results in frequency jumps of about  $10 \text{ cm}^{-1}$ . The finest level of tuning is done using a LabVIEW program to change the voltage applied to the piezo-electric transducer (PZT) attached to the seed laser. For

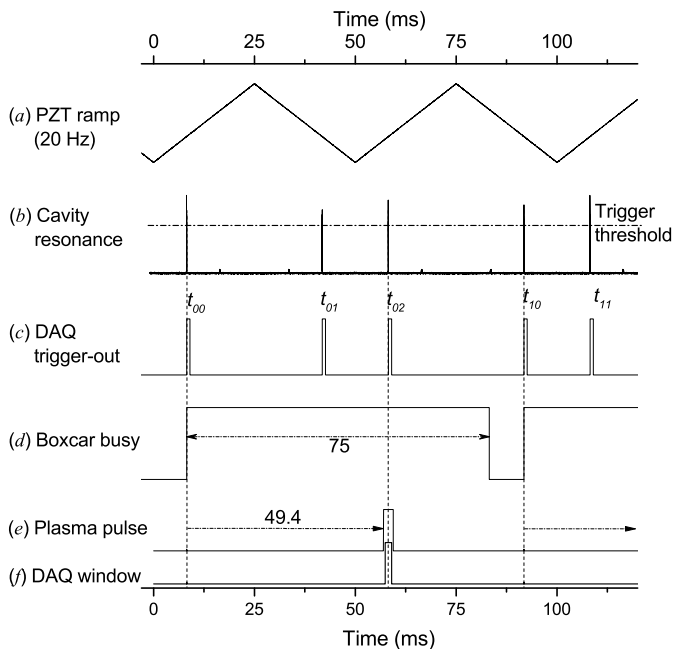


Figure 1.8: The triggering scheme used in the experiment, adapted from (Zhao et al., 2013). a) The triangular function of the applied voltage to the PZT altering the cavity length. b) Traces the cavity modes, where a spike is when the cavity is in resonance. c) Traces the TTL signals generated by the DAQ when the light intensity surpasses the preset threshold level. d) The Boxcar busy window which is generated by the TTL signal sent from DAQ trigger out at  $t_{00}$ . e) Traces the plasma pulse and f) traces the DAQ acquisition window generated by the rising edge of the Boxcar busy signal. Only the cavity resonance at  $t_{02}$  will initiate a measured ring-down event.

one scan the applied voltage is increased from about 90 to 195 V, which changes the idler frequency by up to  $1.4 \text{ cm}^{-1}$ .

The idler beam, in the  $3 \mu\text{m}$  range, has a total output power of about 1.2 W, an effective bandwidth of less than 1 MHz, and a mode structure that is purely  $\text{TEM}_{00}$ . The idler is sent through a beam splitter after it exits the cw-OPO cavity, and roughly 1% of the beam is directed to a continuously self-calibrated wavemeter (Bristol 621-A), to measure the frequency. The remainder of the idler is directed through an acousto-optic modulator (AOM), which when on generates an acoustic wave that diffracts the laser beam into the fundamental and higher orders. The first-order deflection is spatially separated from the fundamental by an angle of  $\sim 15$  degrees, and it is this 10% of the idler that is coupled into the main chamber.

Perfect mode matching the laser to the optical cavity will give the peak light intensity, and limits interference by modes other than the  $\text{TEM}_{00}$ . To mode match the laser's wavelength the cavity length is varied by a PZT mounted on the back of the far mirror, and the cavity length is modulated by an applied triangular function voltage. The period and amplitude of the applied voltage is chosen such that the cavity is transparent to infrared light twice during one period (once on the raising edge and once on the falling edge, Figure 1.8).

The light intensity out of the cavity is detected by an IR-photovoltaic detector (Vigo System S.A., PVI-3TE-5, 50 MHz), and a signal is then sent from the detector to both the signal and trigger input channels of a fast data acquisition (DAQ) card equipped in a computer. In the most general case, when the intensity of the light in the cavity reaches a threshold value, a trigger is sent to the

DAQ card, which generates a transistor-transistor logic (TTL) pulse. The TTL signal is then sent to the AOM driver, switching off the AOM leaving only the fundamental. This gives a “pulse” of light, triggering a ring-down event.

In the past, software-based trigger schemes were used to coincide gas/plasma pulses with ring-down events, but they were relatively complex and inefficient (Birza et al., 2002). SPIRAS instead uses a hardware-based timing and multi-trigger scheme that results in more than 90% of the plasma pulses measured; trigger scheme details are shown in Figure 1.8.

For a given modulation frequency, *e.g.*, 15 kHz, the first time the cavity is in resonance the DAQ card generates a TTL pulse, marked as  $t_{00}$ , which is sent to both the AOM driver and a Boxcar gated integrator (SRS, SR250). The AOM driver switches off the AOM, while the Boxcar gated integrator simultaneously generates a 75 ms wide TTL pulse at its busy output channel (henceforth called the busy gate) and the rising edge of the busy gate is used to trigger a multichannel pulse generator. The width of the busy gate is chosen to be for a duration greater than the period of the PZT ramp, such that it covers at least two cavity resonances: the resonance on the falling PZT ramp,  $t_{01}$ , and a second rising resonance,  $t_{02}$ . The multichannel pulse generator has a built-in delay that is used to trigger the gas valve driver and high voltage pulser at about one period after  $t_{00}$ . The pulse generator also sends a TTL signal synchronized with the HV pulse, but with a narrower width, to the second input channel of the DAQ card. This is the data acquisition time window, if a resonance falls within this window a ring-down event is measured.

The use of a Boxcar integrator avoids the need for an extensive programming code for a software interface with the pulsed plasma generation, and this simplifies data acquisition. Approximately 10 - 14 plasma pulses are effectively generated and measured per second. Non-detections mainly occur in the case that cavity resonances are too close to the turning points of the PZT-sweep, trace a in Figure 1.8. A typical ring-down time ranged from about 5 - 15  $\mu$ s depending on the laser frequency. To further reduce the noise, such as that due to inconsistent gas pulse pressures, fifteen ring-down times are averaged per wavenumber. The final absorption spectrum is recorded by plotting the ring-down time as a function of laser frequency.

## 1.5 THIS THESIS

This thesis is about the study of astrophysically relevant hydrocarbons through infrared spectroscopy. All of the molecules studied are believed to be or have been detected in astronomical environments. The experiments and theoretical calculations detailed here were primarily carried out at the Sackler Laboratory for Astrophysics at Leiden University, with some theoretical work done out at the University of Texas at Austin and some experimental work performed at the University of Science and Technology of China, and the astronomical infrared spectra were taken using the AKARI space telescope. This thesis is organized as follows: The theory of hydrocarbon infrared spectroscopy is given through the computational study of small polyynes [ $\text{HC}_{2n}\text{H}$ ] and propyne [ $\text{CH}_3\text{CCH}$ ]. The theory is then tested through experimental studies of diacetylene [ $\text{HC}_4\text{H}$ ], triacetylene [ $\text{HC}_6\text{H}$ ], propyne [ $\text{CH}_3\text{CCH}$ ], and cyclopropenyl cation [ $\text{c-C}_3\text{H}_3^+$ ]. Finally, experimental spectra and theory are applied to identify deuterated PAHs [ $\text{D}_n\text{-PAHs}$ ] in the interstellar medium (ISM). Through comparison of astronomical spectra and this laboratory or theoretical work adds insight into the physical chemistry of astronomical environments.

### Chapters 2, 3 and 4

Long chain unsaturated hydrocarbons are fairly abundant in carbon-rich environments, *e.g.*, the atmosphere of Titan or the protoplanetary nebulae CRL 618 and SMP LMC 11. In fact, chains have been observed of  $\text{C}_n\text{H}$  (Bell et al., 1999) and  $\text{HC}_n\text{CN}$  (Bell et al., 1992) up to  $n = 8$ . Interestingly though, polyynes [ $\text{HC}_n\text{H}$ ] have only been observed for chain lengths up to  $n = 6$ . We present high resolution experimental spectra of diacetylene [ $\text{HC}_4\text{H}$ ], and triacetylene [ $\text{HC}_6\text{H}$ ] in the 3  $\mu\text{m}$  region, which includes the C-H asymmetric stretch fundamental and a number of sequence bands. In

addition, we present CCSD(T) calculations for acetylene [HC<sub>2</sub>H] and the three smallest polyynes: diacetylene [HC<sub>4</sub>H], triacetylene [HC<sub>6</sub>H], and tetraacetylene [HC<sub>8</sub>H]. The predicted vibrational frequencies and rotational constants agree well with high resolution experimental data for HC<sub>2</sub>H, HC<sub>4</sub>H, and HC<sub>6</sub>H, and suggests similar accuracies for HC<sub>8</sub>H. Based on the calculated parameters, the lack of detection of HC<sub>8</sub>H in astronomical sources is likely a result of spectral overlap of transitions of HC<sub>8</sub>H with transitions of the more abundant HC<sub>4</sub>H and HC<sub>6</sub>H. This work appears in Zhao et al. (2014), Doney et al. (2015) and Doney et al. (2018b).

### Chapter 5 and 6

Another abundant acetylenic hydrocarbon is propyne [H<sub>3</sub>CCCH], which has been seen in for example the atmosphere of Titan, in SMP LMC 11, and in the warm dense gas around the low-mass protostar IRAS 16293-2422. Due to the close spacings of the *K'*-subband transitions, propyne is a good probe of the interstellar kinetic temperature. We present high resolution spectra of the  $\nu_1$  acetylenic C-H stretch fundamental and the  $\nu_3+\nu_5$  combination band of normal isotopologue of propyne, and the  $\nu_1$  acetylenic C-H stretch fundamental of the three mono-substituted <sup>13</sup>C isotopologues. For the <sup>13</sup>C isotopologues this is the first rotationally resolved measurement of the  $\nu_1$  fundamentals, and a full rotational analysis is given to highlight the effect of isotopic position in the carbon chain on anharmonic perturbations. CCSD(T) calculations for all four isotopologues are presented to support the identification and analysis of the new ro-vibrational bands. This work appears in Doney et al. (2017) and Doney et al. (2018a).

### Chapter 7

In most astronomical hydrocarbon chemical networks carbocations are the key intermediates. However, a lack of accurate line positions make their astronomical identification difficult. We present the first high resolution measurement of the cyclopropenyl cation [c-C<sub>3</sub>H<sub>3</sub><sup>+</sup>]; through its  $\nu_4$  C-H stretch fundamental band. The resulting ground state spectroscopic parameters are sufficiently accurate to help astronomical searches for this molecule in both the infrared and sub-millimeter. This work appears in Zhao et al. (2014).

### Chapter 8

In the interstellar medium, the gas-phase D/H ratio is too low to be explained by stellar processing alone. As such, it is believed that some of the missing deuterium is locked up in either dust grains or in molecules. PAHs are good reservoirs for deuterium, due to their relatively stability against photodissociation (meaning they are long-lived, and thus ubiquitous molecule in the interstellar medium) and their large size ( $N_C > 50$ ; meaning that a large number of deuterium can be incorporated into the molecule) Peeters et al. (2004) made the first tentative detection of deuterated PAHs in the Orion Bar and M17 using The Infrared Space Observatory (ISO). Using the AKARI satellite we have confidently observed deuterated PAHs in an addition six Milky Way sources. The comparison between DFT calculations and observations show that the deuterium preferentially add aliphatically to the PAH frame, and that the addition is extremely environmentally dependent. This work appears in Doney et al. (2016).

#### 1.6 BIBLIOGRAPHY

- Agúndez, M., Cernicharo, J., Quintana-Lacaci, G., et al. 2017, *Astronomy & Astrophysics*, 601, A4  
Allamandola, L. J., Tielens, A. G. G. M., & Barker, J. R. 1989, *The Astrophysical Journal Supplements*, 71, 733  
Almlöf, J. & Taylor, P. R. 1987, *The Journal of Chemical Physics*, 86, 4070  
Araki, M., Takano, S., Sakai, N., et al. 2017, *The Astrophysical Journal*, 847, 51  
Auer, A. A. & Gauss, J. 2001, *Physical Chemistry Chemical Physics*, 3, 3001  
Bak, K. L., Gauss, J., Jørgensen, P., et al. 2001, *The Journal of Chemical Physics*, 114, 6548  
Bauschlicher Jr., C. W. & Taylor, P. R. 1993, *Theoretica Chimica Acta*, 86, 13  
Bell, M. B., Avery, L. W., MacLeod, J. M., & Matthews, H. E. 1992, *The Astrophysical Journal*, 400, 551  
Bell, M. B., Feldman, P. A., Watson, J. K. G., et al. 1999, *The Astrophysical Journal*, 518, 740

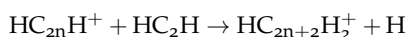
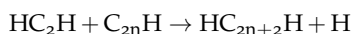
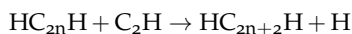
- Birza, P., Motylewski, T., Khoroshev, D., et al. 2002, *Chemical Physics*, 283, 119
- Cernicharo, J., Daniel, F., Castro-Carrizo, A., et al. 2013, *The Astrophysical Journal Letters*, 778, L25
- Cernicharo, J. & Guélin, M. 1996, *Astronomy & Astrophysics*, 309, L27
- Cernicharo, J., Heras, A. M., Tielens, A. G. G. M., et al. 2001, *The Astrophysical Journal Letters*, 546, L123
- CFOUR. 2017, Coupled-Cluster techniques for Computational Chemistry, a quantum-chemical program package by J.F. Stanton, J. Gauss, M.E. Harding, P.G. Szalay with contributions from A.A. Auer, R.J. Bartlett, U. Benedikt, C. Berger, D.E. Bernholdt, Y.J. Bomble, L. Cheng, O. Christiansen, F. Engel, R. Faber, M. Heckert, O. Heun, C. Huber, T.-C. Jagau, D. Jonsson, J. Jusélius, K. Klein, W.J. Lauderdale, F. Lipparini, D.A. Matthews, T. Metzroth, L.A. Mück, D.P. O'Neill, D.R. Price, E. Prochnow, C. Puzzarini, K. Ruud, F. Schiffmann, W. Schwalbach, C. Simmons, S. Stopkowitz, A. Tajti, J. Vázquez, F. Wang, J.D. Watts and the integral packages MOLECULE (J. Almlöf and P.R. Taylor), PROPS (P.R. Taylor), ABACUS (T. Helgaker, H.J. Aa. Jensen, P. Jørgensen, and J. Olsen), and ECP routines by A. V. Mitin and C. van Wüllen. For the current version, see <http://www.cfour.de>.
- Cherchneff, I. 2011, in *EAS Publications Series*, Vol. 46, *EAS Publications Series*, ed. C. Joblin & A. G. G. M. Tielens, 177–189
- Chuang, K.-J., Fedoseev, G., Ioppolo, S., van Dishoeck, E. F., & Linnartz, H. 2016, *Monthly Notices of the Royal Astronomical Society*, 455, 1702
- Churchwell, E. & Hollis, J. M. 1983, *The Astrophysical Journal*, 272, 591
- Doney, K. D., Candian, A., Mori, T., Onaka, T., & Tielens, A. G. G. M. 2016, *Astronomy & Astrophysics*, 586, A65
- Doney, K. D., Zhao, D., Bouwman, J., & Linnartz, H. 2017, *Chemical Physics Letters*, 684, 351
- Doney, K. D., Zhao, D., & Linnartz, H. 2015, *Journal of Molecular Spectroscopy*, 316, 54
- Doney, K. D., Zhao, D., & Linnartz, H. 2018a, *The Journal of Physical Chemistry A*, 122, 582
- Doney, K. D., Zhao, D., Stanton, J. F., & Linnartz, H. 2018b, *Physical Chemistry Chemical Physics*
- Feller, D. 1996, *Journal of Computational Chemistry*, 17, 1571
- Gauss, J. & Stanton, J. F. 1997, *Chemical Physics Letters*, 276, 70
- Gibb, E. L., Van Brunt, K. A., Brittain, S. D., & Rettig, T. W. 2007, *The Astrophysical Journal*, 660, 1572
- Kim, S. J., Caldwell, J., Rivolo, A. R., Wagener, R., & Orton, G. S. 1985, *Icarus*, 64, 233
- Malek, S. E., Cami, J., & Bernard-Salas, J. 2012, *The Astrophysical Journal*, 744, 16
- Martin, J. M. L., Lee, T. J., & Taylor, P. R. 1998, *The Journal of Chemical Physics*, 108, 676
- Martin, J. M. L., Taylor, P. R., & Lee, T. J. 1997, *Chemical Physics Letters*, 275, 414
- Matthews, D. A., Vázquez, J., & Stanton, J. F. 2007, *Molecular Physics*, 105, 2659
- McEwan, M. J., Scott, G. B. I., Adams, N. G., et al. 1999, *The Astrophysical Journal*, 513, 287
- McMurry, J. 2016, *Organic Chemistry*, 9th edn. (Cengage Learning)
- Motylewski, T. & Linnartz, H. 1999, *Review of Scientific Instruments*, 70, 1305
- Müller, H. S., Schlöder, F., Stutzki, J., & Winnewisser, G. 2005, *Journal of Molecular Structure*, 742, 215
- O'Keefe, A. & Deacon, D. A. G. 1988, *Review of Scientific Instruments*, 59, 2544
- Papadopoulos, P. P. 2007, *The Astrophysical Journal*, 656, 792
- Peeters, E., Allamandola, L. J., Bauschlicher Jr., C. W., et al. 2004, *The Astrophysical Journal*, 604, 252
- Raghavachari, K., Trucks, G. W., Pople, J. A., & Head-Gordon, M. 1989, *Chemical Physics Letters*, 157, 479
- Sakai, N. & Yamamoto, S. 2013, *Chemical Reviews*, 113, 8981
- Schuchardt, K. L., Didier, B. T., Elsethagen, T., et al. 2007, *Journal of Chemical Information and Modeling*, 47, 1045
- Simandiras, E. D., Rice, J. E., Lee, T. J., Amos, R. D., & Handy, N. C. 1988, *The Journal of Chemical Physics*, 88, 3187
- Simmonett, A. C., Schaefer III, H. F., & Allen, W. D. 2009, *The Journal of Chemical Physics*, 130, 044301
- Smith, D. 1992, *Chemical Reviews*, 92, 1473
- Stanton, J. F. & Gauss, J. 2000, *International Reviews in Physical Chemistry*, 19, 61
- van Kempen, T. A., van Dishoeck, E. F., Salter, D. M., et al. 2009, *Astronomy & Astrophysics*, 498, 167
- Vázquez, J. & Stanton, J. F. 2007, *Molecular Physics*, 105, 101
- Waite, J. H., Young, D. T., Cravens, T. E., et al. 2007, *Science*, 316, 870
- Wakelam, V., Herbst, E., Loison, J.-C., et al. 2012, *The Astrophysical Journal Supplement Series*, 199, 21
- Winnewisser, G. & Walmsley, C. M. 1978, *Astronomy & Astrophysics*, 70, L37
- Woon, D. E. & Dunning Jr., T. H. 1995, *The Journal of Chemical Physics*, 103, 4572
- Zhang, X., Maccarone, A. T., Nimlos, M. R., et al. 2007, *The Journal of Chemical Physics*, 126, 044312
- Zhao, D., Doney, K. D., & Linnartz, H. 2014, *Journal of Molecular Spectroscopy*, 296, 1
- Zhao, D., Doney, K. D., & Linnartz, H. 2014, *The Astrophysical Journal Letters*, 791, L28
- Zhao, D., Guss, J., Walsh, A. J., & Linnartz, H. 2013, *Chemical Physics Letters*, 565, 132



The full cubic and semidiagonal quartic force field of acetylene ( $C_2H_2$ ), diacetylene ( $C_4H_2$ ), triacetylene ( $C_6H_2$ ), and tetraacetylene ( $C_8H_2$ ) are determined using CCSD(T) (coupled cluster theory with single and double excitations and augmented by a perturbative treatment of triple excitations) in combination with the atomic natural orbital (ANO) basis sets. Application of second-order vibrational perturbation theory (VPT<sub>2</sub>) results in vibrational frequencies that agree well with the known fundamental and combination band experimental frequencies of acetylene, diacetylene, and triacetylene (average discrepancies are less than  $10\text{ cm}^{-1}$ ). Furthermore, the predicted ground state rotational constants ( $B_0$ ) and vibration-rotation interaction constants ( $\alpha_i$ ) are shown to be consistent with known experimental values. New vibrational frequencies and rotational parameters from the presented theoretical predictions are given for triacetylene and tetraacetylene, which can be used to aid laboratory and astronomical spectroscopic searches for characteristic transitions of these molecules.

## 2.1 INTRODUCTION

Due to their reactive nature, unsaturated linear hydrocarbons, such as acetylene and polyynes (general structure  $\text{HC}_{2n}\text{H}$ ;  $\tilde{X}^1\Sigma_g^+$ ), are prevalent in combustion chemistry (Frenklach et al., 1985; Cherchneff et al., 1992; Homann, 1998; Richter & Howard, 2000), plasma processes (Fujii & Kareev, 2001; Thejaswini et al., 2011), chemical synthesis (Shirakawa, 2001; Zhao et al., 2003; Milani et al., 2006; Ma et al., 2008), chemistry of planetary atmospheres (Kunde et al., 1981; de Graauw et al., 1997; Wilson & Atreya, 2003; Kunde et al., 2004; Vuitton et al., 2006; Burgdorf et al., 2006; Meadows et al., 2008; Waite et al., 2007; Gu et al., 2009), and interstellar gas-phase chemistry (Cernicharo et al., 2001a,b; Bernard-Salas et al., 2006; Wakelam et al., 2010; Fonfría et al., 2011; Malek et al., 2012). They are of particular interest for astronomers, because they are believed to act as the ultraviolet (UV) shield in hydrocarbon-rich atmospheres (Bandy et al., 1992, 1993; Frost et al., 1995; Bizzocchi et al., 2011), and in the formation and destruction of polycyclic aromatic hydrocarbons (PAHs) (Frenklach & Feigelson, 1989; Ekern et al., 1998; Krestinin, 2000; Waite et al., 2007; Kress et al., 2010), a major reservoir of carbon in the universe. In astronomical environments, the formation of long chain polyynes from acetylene is believed to occur through polymerization reactions (Woods et al., 2003; Gu et al., 2009; Sakai & Yamamoto, 2013),



Although long carbon chain molecules (e.g.,  $\text{HC}_n$  and  $\text{HC}_n\text{N}$  for  $n \leq 9$ ) (Cernicharo & Guélin, 1996; Bell et al., 1997; Bell et al., 1999; Vuitton et al., 2007) and small polyynes ( $\text{HC}_{2n}\text{H}$  for  $n \leq 3$ ) have been detected in carbon-rich astronomical sources (Cernicharo et al., 2001a,b; Vuitton et al., 2007), tetraacetylene has yet to be observed. One limiting factor is that as centrosymmetric molecules, polyynes lack a permanent dipole moment, and cannot be detected by radioastronomy using pure rotational transitions, unlike, e.g.,  $\text{HC}_n\text{N}$ . Therefore, ro-vibrational spectra in the infrared (IR) region are the most important spectroscopic tools to detect polyynes both in the laboratory and in space. In particular, detection of acetylene, diacetylene, and triacetylene in planetary atmospheres and protoplanetary nebulae has been realized primarily through observation of the strongest perpendicular band ( $\nu_5$ ,  $\nu_8$ , and  $\nu_{11}$ , respectively, at  $\sim 13 - 17 \mu\text{m}$ ) and the second strongest parallel band ( $\nu_4 + \nu_5$ ,  $\nu_6 + \nu_8$ , and  $\nu_8 + \nu_{11}$ , respectively, at  $\sim 8 \mu\text{m}$ ) (Kunde et al., 1981; de Graauw et al., 1997; Cernicharo et al., 2001a,b). However, accurate line positions for tetraacetylene are lacking, from either laboratory or theoretical studies.

Extensive theoretical and experimental studies have been carried out for acetylene and diacetylene in the past few decades, including high-resolution spectroscopic studies of all the fundamental bands and a significant number of the combination bands (Plyler et al., 1963; Palmer et al., 1972; Pliva, 1972a,b; Guelachvili et al., 1984; Owen et al., 1987; McNaughton & Bruget, 1992; Arié & Johns, 1992; Vanderauwera et al., 1993; Gambogi et al., 1995; Bizzocchi et al., 2011; Zhao et al., 2014a), and high level *ab initio* calculations that take into account anharmonic effects (Temsamani & Herman, 1995; Martin et al., 1998; Thorwirth et al., 2008; Simmonett et al., 2009). The combination of these studies shows that current quantum chemical theory, particularly coupled cluster theory with single and double excitations and augmented by a perturbative treatment of triple excitations (CCSD(T)) (Raghavachari et al., 1989), is able to accurately reproduce equilibrium geometries, experimental vibrational frequencies, vibration-rotation interaction constants ( $\alpha_i$ ), and ground state rotational constants ( $B_0$ ).

Triacetylene and tetraacetylene are not as thoroughly studied, notably in terms of rotational information. While all of the fundamental vibrational modes of triacetylene have been measured,

there is only rotational information for the IR active fundamental modes (Bjarnov et al., 1974), and the strongest IR combination band ( $\nu_8+\nu_{11}$ ) (Matsumura et al., 1988b; McNaughton & Bruget, 1991; Haas et al., 1994b,a; Doney et al., 2015). However, theoretical studies of triacetylene do give rotational information for the remaining modes from CCSD(T) calculations of the vibration-rotation interaction constants (Chang et al., 2016) and the equilibrium geometry (Sattelmeyer & Stanton, 2000). In addition, the harmonic frequencies of triacetylene were calculated using partial fourth-order many-body perturbation theory [SDQ-MBPT(4)] (Sattelmeyer & Stanton, 2000). Conversely though, to the authors' knowledge, there is almost no rotational information for tetraacetylene. There has been only one low-resolution spectroscopic study of tetraacetylene, which measured three of the fundamentals ( $\nu_6$ ,  $\nu_8$ ,  $\nu_{14}$  at 3329.4, 2023.3, and 621.5  $\text{cm}^{-1}$ , respectively), one combination band ( $\nu_{10}+\nu_{14}$  at 1229.7  $\text{cm}^{-1}$ ), and gives an estimate for the electronic ground state rotational constant,  $B_0$  (Shindo et al., 2001). Unfortunately, the theoretical knowledge of tetraacetylene is equally limited, with only two studies of the equilibrium geometry (at the Hartree-Fock (Toto et al., 1996) and B3LYP (Kaiser et al., 2010) level of theory), and a calculation of the harmonic vibrational frequencies at the SVWN level of theory (Shindo et al., 2001). While the two modes that are most useful for astronomical identification ( $\nu_{14}$  and  $\nu_{10}+\nu_{14}$ ) were measured, the uncertainty associated with the line positions is too large to allow for an unambiguous assignment. Moreover, some high-resolution IR searches have been attempted (Zhao et al., 2013, 2014a; Doney et al., 2015; Chang et al., 2016), but so far no transitions have been assigned to tetraacetylene.

In this paper, we report the *ab initio* calculations for acetylene, diacetylene, triacetylene, and tetraacetylene. Due to the centrosymmetric nature of these molecules, observations in the laboratory and in space are most easily accomplished through their infrared spectra. As such, the properties computed and presented here are those related to that technique: fundamental vibrational frequencies, ground state rotational constants, and intramolecular interactions. The computational approach is calibrated using the well studied acetylene and diacetylene, and then extended to make predictions for triacetylene and tetraacetylene.

## 2.2 COMPUTATIONAL METHODS

All calculations were carried out at the CCSD(T) level of theory, which with a sufficiently large basis set has been shown to accurately reproduce experimental values of semi-rigid molecules (Raghavachari et al., 1989; Lee & Scuseria, 1995; Bartlett, 1995; Gauss & Stanton, 1997; Gauss, 1998; Martin et al., 1998; Thorwirth et al., 2008; Simmonett et al., 2009; McCaslin & Stanton, 2013). Equilibrium geometries were determined using the large core-valence correlation-consistent quadruple- $\zeta$  basis set (cc-pCVQZ), which features [8s7p5d3f1g] (non-hydrogen atoms) and [4s3p2d1f] (hydrogen) of (15s9p5d3f1g) and (6s3p2d1f) primitive basis sets, respectively (Woon & Dunning Jr., 1995; Feller, 1996; Schuchardt et al., 2007). All electron (AE)-CCSD(T)/cc-pCVQZ has been shown to give very accurate equilibrium geometries for unsaturated hydrocarbons (Auer & Gauss, 2001; Bak et al., 2001; Zhang et al., 2007; Simmonett et al., 2009). Optimizations were done using analytic energy derivatives (Stanton & Gauss, 2000), and were considered converged when the root-mean-square (rms) gradient fell below  $10^{-10}$  au.

However, it is well known that correlation-consistent basis sets, such as cc-pCVQZ, tend to underestimate the vibrational frequencies of symmetric bending modes ( $\pi_g$ ) of conjugated molecules, e.g., polynes, due to their susceptibility to an intramolecular variant of basis set superposition error (BSSE) (Simandiras et al., 1988; Simmonett et al., 2009). It has been shown that one way to avoid this problem is to use basis sets with a large number of Gaussian primitives (particularly f-type), such as the atomic natural orbital (ANO) basis set (with the primitive basis set (13s8p6d4f2g) for non-hydrogen atoms and (8s6p4d2f) for hydrogen) (Almlöf & Taylor, 1987; Bauschlicher Jr. & Taylor, 1993; Martin et al., 1998). The basis set has two common truncations: [4s3p2d1f] for non-hydrogen atoms and [4s2p1d] for hydrogen (hereafter known as ANO1), and [5s4p3d2f1g] (non-hydrogen atoms) and [4s3p2d1f] (hydrogen) (hereafter known as ANO2) (Almlöf & Taylor, 1987; Feller, 1996;

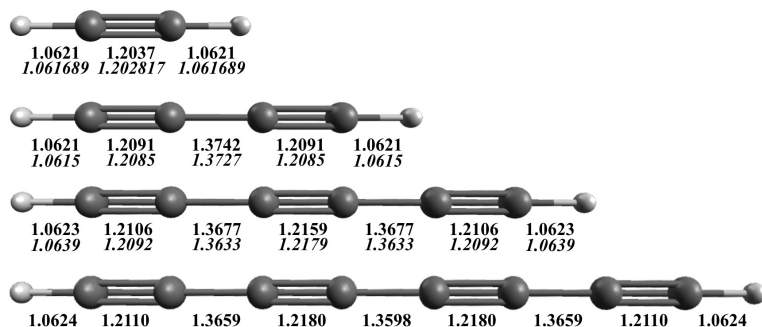


Figure 2.1: AE-CCSD(T)/cc-pCVQZ equilibrium geometries (Å) for HC<sub>2n</sub>H. Experimentally determined equilibrium bond lengths for acetylene (Tamassia et al., 2016), diacetylene (Thorwirth et al., 2008), and triacetylene (Tay et al., 1995) are given in italics below.

Schuchardt et al., 2007). In addition, only the valence electrons of carbon are considered in the correlation treatment, *i.e.*, standard frozen-core (fc) calculations. (fc)-CCSD(T)/ANO1 has been shown to accurately reproduce experimental frequencies and intensities for small molecules (Martin et al., 1997, 1998; Vázquez & Stanton, 2007). Using the (fc)-CCSD(T)/ANO1 optimized geometry, second-order vibrational perturbation (VPT2) theory calculations were determined from full cubic and the semidiagonal part of the quartic force fields obtained by numerical differentiation of analytic CCSD(T) second derivatives (Gauss & Stanton, 1997; Matthews et al., 2007). All calculations were performed with the development version of the CFOUR program (CFOUR, 2017).

## 2.3 RESULTS AND DISCUSSION

### 2.3.1 Equilibrium structure

The AE-CCSD(T)/cc-pCVQZ equilibrium geometries are shown in Figure 2.1, with comparison to experimentally derived values (in italics) when known (Tay et al., 1995; Tamassia et al., 2016; Thorwirth et al., 2008). The theoretical equilibrium bond lengths for acetylene, diacetylene, and triacetylene all agree within 0.5% of the structures determined from experimentally measured rotational constants. As the length of the carbon chain increases, the C-H bond lengths stay essentially the same,  $\sim 1.062$  Å, consistent with a sp-H type C-H bond. However, the C $\equiv$ C bond lengths increase (particularly the internal C $\equiv$ C bonds), while the C-C bond lengths decrease, becoming closer to that typical of CC double bonds. This suggests that the  $\pi$  electrons become more delocalized over the internuclear axis, and the polyynes configuration moves from a strict triple-single bond alternation to more of a consecutive double bond character of the CC bonds, making the overall structure more rigid as C<sub>2</sub> units are added, an effect that also qualitatively acts to increase the biradical character of the molecule as the size grows.

The equilibrium rotational constants,  $B_e$ , obtained from the AE-CCSD(T)/cc-pCVQZ equilibrium geometries are summarized in Table 2.1, and agree well with experimental ground state rotational constants ( $B_0$ ). As such, the equilibrium rotational constants suggest that the calculations predict the correct ground state geometry, because for linear molecules with more than three atoms the summation of vibration-rotation interaction constants ( $\alpha_i$ ) is expected to be close to zero, and from

$$B_0 = B_e - \frac{1}{2} \sum_i \alpha_i \quad (2.1)$$

it becomes that  $B_0 \sim B_e$ .

In addition, as seen for other carbon chains (*e.g.*, HC<sub>n</sub>, HC<sub>2n+1</sub>N, and H<sub>2</sub>C<sub>n</sub>) the centrifugal

Table 2.1: CCSD(T)/ANO1 rotational constants (in  $\text{cm}^{-1}$ ) of  $\text{HC}_{2n}\text{H}$  ( $n = 1 - 4$ )

	$\text{HC}_2\text{H}$	$\text{HC}_4\text{H}$	$\text{HC}_6\text{H}$	$\text{HC}_8\text{H}$
Calc.				
$B_e$	1.181 053	0.146 248	0.044 064	0.018 823
$B_0$	1.175319	0.146 167	0.044 092	0.018 844
$D_e \times 10^8$	160	1.5	0.086	0.012
Expt.				
$B_0$	1.176 646 32(18) (Kabbadj et al., 1991)	0.146 4123(17) (Zhao et al., 2014a)	0.044 1735(12) (Doney et al., 2015)	0.020(3) (Shindo et al., 2001)
$D_0 \times 10^8$	159.8(9) (Kabbadj et al., 1991)	1.568 25(20) (Bizzocchi et al., 2011)	0.107(7) (Doney et al., 2015)	

distortion constant ( $D_e$ ) decreases with increasing molecular size, with a theoretical  $D_e = 1.6 \times 10^{-6} \text{ cm}^{-1}$  for acetylene,  $D_e = 1.5 \times 10^{-8} \text{ cm}^{-1}$  for diacetylene,  $D_e = 8.6 \times 10^{-10} \text{ cm}^{-1}$  for triacetylene, and  $D_e = 1.2 \times 10^{-10} \text{ cm}^{-1}$  for tetraacetylene (Thaddeus et al., 1998). These values are consistent with those found experimentally for the respective vibrational ground states (Table 2.1). As noted by Thaddeus et al. (1998), this behavior of increasing stiffness with chain length is a distinguishing characteristic associated with *bona fide* chains.

### 2.3.2 Spectroscopic properties of acetylene and diacetylene

The quality of the present calculations is checked by comparison to the experimentally well studied acetylene and diacetylene. The harmonic and VPT2 fundamental frequencies of the fundamental and combination bands are given in Tables 2.2 and 2.3, for acetylene and diacetylene respectively,

Table 2.2: Harmonic and anharmonic (VPT2) frequencies (in  $\text{cm}^{-1}$ ) of  $\text{HC}_2\text{H}$  fundamental and selected combination bands

Mode	CCSD(T)/ANO1 <sup>a</sup>		Experimental
	$\omega$	$\nu$	$\nu$
$\nu_1(\sigma_g^+)$	3514.2(0)	3375.2(0)	3372.851 (Palmer et al., 1972)
$\nu_2(\sigma_g^+)$	2001.5(0)	1964.8(0)	1974.317 (Palmer et al., 1972)
$\nu_3(\sigma_u^+)$	3414.6(84.7)	3285.9(74.8)	3288.58075 (Vanderauwera et al., 1993)
$\nu_4(\pi_g)$	600.5(0)	600.6(0)	612.871 (Pliva, 1972a)
$\nu_5(\pi_u)$	752.3(90.5)	734.7(91.7)	730.332 (Pliva, 1972a)
$\nu_4 + \nu_5(\sigma_u^+)$	1352.8	1329.2(10.8)	1328.074 (Pliva, 1972a)
$\nu_2 + \nu_5(\pi_u)$	2753.8	2698.3(0.1)	2701.907 (Pliva, 1972b)
$\nu_3 + \nu_4(\pi_u)$	4015.1	3878.5(0.5)	3882.4060 (Palmer et al., 1972)
$\nu_1 + \nu_5(\tau_u)$	4266.5	4098.9(0.5)	4091.17326 (D'Cunha et al., 1991)
$\nu_1 + \nu_3(\sigma_u^+)$	6928.7	6551.9(2.0)	6556.46 (Plyler et al., 1963)
Anharmonic ZPE = 5760.1			

a. Intensities in  $\text{km/mol}$  are given in parenthesis.

and experimental values are included for comparison. The (fc)-CCSD(T)/ANO1 VPT2 fundamental frequencies show good agreement with experimental values, with most observed-calculated deviations (o-c) being less than  $5 \text{ cm}^{-1}$  and all being less than  $15 \text{ cm}^{-1}$ .

Table 2.3: Harmonic and anharmonic (VPT2) frequencies (in  $\text{cm}^{-1}$ ) of  $\text{HC}_4\text{H}$  fundamental and selected combination bands

Mode	CCSD(T)/ANO1 <sup>a</sup>		Experimental
	$\omega$	$\nu$	$\nu$
$\nu_1(\sigma_g^+)$	3465.8(0)	3332.5(0)	3332.15476 (McNaughton & Bruget, 1992)
$\nu_2(\sigma_g^+)$	2240.2(0)	2193.1(0)	2188.9285 (Guelachvili et al., 1984)
$\nu_3(\sigma_g^+)$	891.1(0)	859.2(0)	871.9582 (Guelachvili et al., 1984)
$\nu_4(\sigma_u^+)$	3465.9(152.7)	3333.1(135.5)	3333.6634 (Zhao et al., 2014a)
$\nu_5(\sigma_u^+)$	2054.1(0.2)	2016.9(0.5)	2022.2415 (Guelachvili et al., 1984)
$\nu_6(\pi_g)$	636.3(0)	624.2(0)	625.643507 (Bizzocchi et al., 2011)
$\nu_7(\pi_g)$	479.8(0)	476.9(0)	482.7078 (Guelachvili et al., 1984)
$\nu_8(\pi_u)$	636.3(78.7)	624.1(78.8)	628.040776 (Bizzocchi et al., 2011)
$\nu_9(\pi_u)$	220.7(7.3)	219.6(7.3)	219.97713 (Arié & Johns, 1992)
$2\nu_9(\sigma_g^+)$	441.4	438.5(0)	438.47757 (Arié & Johns, 1992)
$\nu_7 + \nu_9(\sigma_u^+)$	700.5	696.3(0.8)	701.8939 (Bizzocchi et al., 2011)
$\nu_6 + \nu_9(\sigma_u^+)$	857.0	843.9(0.01)	845.655513 (Bizzocchi et al., 2011)
$\nu_8 + \nu_9(\sigma_g^+)$	857.0	843.9(0)	848.365918 (Bizzocchi et al., 2011)
$\nu_7 + \nu_8(\pi_u)$	1116.1	1103.1(0.6)	1111 (Owen et al., 1987)
$\nu_6 + \nu_8(\sigma_u^+)$	1272.6	1244.7(21.8)	1241.060828 (McNaughton & Bruget, 1992)
$2\nu_6 + \nu_8(\pi_u)$	1909.0	1864.6(0.0)	1863.2512 (Guelachvili et al., 1984)
$\nu_2 + \nu_9(\pi_u)$	2460.9	2410.0(0.04)	2406.4251 (Guelachvili et al., 1984)
$\nu_5 + \nu_7(\pi_u)$	2533.9	2489.0(0.01)	2500.6458 (Guelachvili et al., 1984)
$\nu_5 + \nu_6(\pi_u)$	2690.4	2637.0(0.04)	2643.32323 (McNaughton & Bruget, 1992)
$\nu_2 + \nu_8(\pi_u)$	2876.6	2810.9(0.4)	2805 (Owen et al., 1987)
$\nu_1 + \nu_9(\pi_u)$	3686.5	3551.6(0.1)	3551.56158159 (McNaughton & Bruget, 1992)
$\nu_1 + \nu_8(\pi_u)$	4102.1	3946.9(0.7)	3939 (Owen et al., 1987)
$\nu_4 + \nu_6(\pi_u)$	4102.3	3947.8(0.7)	
$\nu_2 + \nu_5(\sigma_u^+)$	4294.3	4194.0(0.1)	
$\nu_4 + \nu_3(\sigma_u^+)$	4357.0	4192.3(0.1)	
$\nu_1 + \nu_4(\sigma_u^+)$	6931.7	6557.2(3.4)	6565.472 (Gambogi et al., 1995)
Anharmonic ZPE = 7966.9			

a. Intensities in  $\text{km}/\text{mol}$  are given in parenthesis.

Based on previous studies of acetylene (Martin et al., 1998) and diacetylene (Thorwirth et al., 2008), the use of the ANO2 basis set was evaluated compared to the ANO1 basis set. For some of the vibrational modes, such as the  $\nu_4$  mode of acetylene [ $612.88 \text{ cm}^{-1}$  (observed)] (Pliva, 1972a), Martin et al. (1998) showed CCSD(T)/ANO2 can give a slightly better agreement (o-c value of  $\sim 2 \text{ cm}^{-1}$ ) compared to the ANO1 basis set (o-c value of  $\sim 12 \text{ cm}^{-1}$ ). However, the study by Thorwirth et al. (2008) showed that, for diacetylene, the average o-c value with CCSD(T)/ANO2 is comparable to that for the ANO1 basis set ( $\sim 6 \text{ cm}^{-1}$  and  $\sim 4 \text{ cm}^{-1}$ , respectively). Moreover, the time cost of (fc)-CCSD(T)/ANO2 calculations compared to (fc)-CCSD(T)/ANO1 far outweighs the minor frequency differences, and does not justify the higher computational cost of the ANO2 basis set in predicting the fundamental frequencies of longer polyynes.

The (fc)-CCSD(T)/ANO1 anharmonicity constants ( $x_{ij}$ , **supplementary material**) also accurately account for the known combination bands of acetylene and diacetylene (Tables 2.2 and 2.3, respectively). All the combination bands are within  $5 \text{ cm}^{-1}$  of their observed values. For both acetylene and diacetylene, the ANO1 basis set is able to most accurately reproduce the C-H asymmetric stretch mode ( $\nu_3$  and  $\nu_4$ , respectively). Significant is the agreement between the experimental and

Table 2.4: CCSD(T)/ANO1 vibration-rotation interaction constants<sup>a</sup> ( $\alpha_i$ , in  $\text{cm}^{-1}$ ) of  $\text{HC}_{2n}\text{H}$  ( $n = 1 - 4$ )

Mode	$\text{HC}_2\text{H} \times 10^3$	$\text{HC}_4\text{H} \times 10^4$	$\text{HC}_6\text{H} \times 10^5$	$\text{HC}_8\text{H} \times 10^5$
$\alpha_1$	6.85(6.904 <sup>b</sup> ) (Temsamani & Herman, 1995)	2.16(2.153) (Zhao et al., 2014a)	2.97	0.730
$\alpha_2$	6.01(6.181) (Temsamani & Herman, 1995)	6.61	15.2	4.91
$\alpha_3$	5.80(5.882 <sup>b</sup> ) (Temsamani & Herman, 1995)	3.12(3.110 <sup>b</sup> ) (Simmonett et al., 2009)	7.44	2.55
$\alpha_4$	-1.46(-1.354) (Temsamani & Herman, 1995)	2.14(2.183) (Zhao et al., 2014a)	3.82	3.76
$\alpha_5$	-2.13(-2.232) (Temsamani & Herman, 1995)	3.94(3.948) (Guelachvili et al., 1984)	2.99(3.58) (Doney et al., 2015)	0.930
$\alpha_6$	0.73	-0.700(-0.678) (Bizzocchi et al., 2011)	9.91(9.15) (McNaughton & Bruget, 1991)	0.730
$\alpha_7$	4.06	-2.70(-2.711) (McNaughton & Bruget, 1992)	9.91	4.06
$\alpha_8$	2.33	-0.647(-0.636) (Bizzocchi et al., 2011)	-1.17(-1.071) (McNaughton & Bruget, 1991)	2.33
$\alpha_9$	2.05	-4.13(-4.183) (McNaughton & Bruget, 1992)	-5.83	2.05
$\alpha_{10}$			-7.42(-7.88) (McNaughton & Bruget, 1991)	-0.295
$\alpha_{11}$			-1.06(-1.06) (Matsumura et al., 1988b)	-1.95
$\alpha_{12}$			-5.07	-1.69
$\alpha_{13}$			-8.47(-8.7207) (Haas et al., 1994a)	-2.26
$\alpha_{14}$				-0.295
$\alpha_{15}$				-0.163
$\alpha_{16}$				-2.29
$\alpha_{17}$				-2.80

a. Experimental values are in parentheses.

b. Deperturbed.

our predicted frequencies of  $\nu_6 + \nu_8$  [1241.060 828(38)  $\text{cm}^{-1}$  (observed) (McNaughton & Bruget, 1992) and 1244.7  $\text{cm}^{-1}$  (theoretical)], and  $2\nu_6 + \nu_8$  [1863.251 2(5)  $\text{cm}^{-1}$  (observed) (Guelachvili et al., 1984) and 1864.6  $\text{cm}^{-1}$  (theoretical)] of diacetylene; both of which had only previously been calculated with CCSD(T)/cc-pCVQZ, and had o-c values greater than 20  $\text{cm}^{-1}$  (Simmonett et al., 2009). This suggests that the combination band VPT2 frequencies of polyynes determined using (fc)-CCSD(T)/ANO1 are accurate to aid identification of molecules, such as in astronomical surveys.

The vibration-rotation interaction constants (Table 2.4), are also determined in the course of the VPT2 calculation, and are in good agreement with both previous theoretical studies (Martin et al., 1998; Simmonett et al., 2009) and experimentally determined values (Guelachvili et al., 1984; McNaughton & Bruget, 1992; Temsamani & Herman, 1995; Simmonett et al., 2009; Bizzocchi et al., 2011; Zhao et al., 2014a). Based on the vibration-rotation interaction constants, the ground state rotational constants ( $B_0$ ) were determined using the AE-CCSD(T)/cc-pCVQZ determined  $B_e$  values (Table 2.1). For acetylene,  $B_0 = 1.175\,319\,\text{cm}^{-1}$ , which is a 0.1% difference compared to the experi-

mentally determined value of  $B_0 = 1.176\ 646\ 32(18)\ \text{cm}^{-1}$  (Kabbadj et al., 1991). Diacetylene shows a similar 0.2% difference between the theoretical value of  $B_0 = 0.146\ 167\ \text{cm}^{-1}$ , and the experimentally determined value of  $B_0 = 0.146\ 4123(17)\ \text{cm}^{-1}$  (Zhao et al., 2014a). The consistent accuracy of these values suggests that the method presented is clearly good enough to extrapolated to and aid high-resolution infrared spectroscopic searches for the larger polyynes.

### 2.3.3 Spectroscopic properties of triacetylene

The (fc)-CCSD(T)/ANO1 harmonic and VPT2 fundamental frequencies along with the experimental frequencies are given in Table 2.5. Comparison between theoretical VPT2 frequencies and experimental fundamentals measured with high-resolution techniques show average o-c values that are

Table 2.5: Harmonic and anharmonic (VPT2) frequencies (in  $\text{cm}^{-1}$ ) of  $\text{HC}_6\text{H}$  fundamental and selected combination bands

Mode	CCSD(T)/ANO1 <sup>a</sup>		Experimental
	$\omega$	$\nu$	$\nu$
$\nu_1(\sigma_g^+)$	3463.1(0)	3330.4(0)	3313 (Bjarnov et al., 1974)
$\nu_2(\sigma_g^+)$	2284.0(0)	2213.2(0)	2201 (Bjarnov et al., 1974)
$\nu_3(\sigma_g^+)$	2061.0(0)	2023.2(0)	2019 (Bjarnov et al., 1974)
$\nu_4(\sigma_g^+)$	616.1(0)	612.7(0)	625 (Bjarnov et al., 1974)
$\nu_5(\sigma_u^+)$	3463.1(126.4)	3329.5(175.0)	3329.0533 (Doney et al., 2015)
$\nu_6(\sigma_u^+)$	2172.2(0.0)	2130.4(0.1)	2128.91637 (McNaughton & Bruget, 1991)
$\nu_7(\sigma_u^+)$	1169.6(1.7)	1160.9(0.2)	1115.0 (Haas et al., 1994a)
$\nu_8(\pi_g)$	633.0(0)	620.9(0)	622.38 (Matsumura et al., 1988b)
$\nu_9(\pi_g)$	489.5(0)	486.2(0)	491 (Bjarnov et al., 1974)
$\nu_{10}(\pi_g)$	252.0(0)	251.1(0)	258 (Bjarnov et al., 1974)
$\nu_{11}(\pi_u)$	632.0(80.5)	619.9(83.2)	621.34011 (Haas et al., 1994b)
$\nu_{12}(\pi_u)$	444.7(1.0)	441.8(1.0)	443.5 (Haas et al., 1994a)
$\nu_{13}(\pi_u)$	106.4(4.1)	105.9(3.5)	105.038616 (Haas et al., 1994a)
$\nu_9 + \nu_{13}(\sigma_u^+)$	595.9	591.7(0.8)	
$\nu_{10} + \nu_{12}(\sigma_u^+)$	696.7	691.8(1.8)	
$\nu_8 + \nu_{12}(\sigma_u^+)$	1077.7	1063.5(0.3)	
$\nu_9 + \nu_{11}(\sigma_u^+)$	1121.5	1107.1(0.7)	
$\nu_8 + \nu_{11}(\sigma_u^+)$	1265.0	1237.4(31.4)	1232.904295 (McNaughton & Bruget, 1991)
$\nu_3 + \nu_7(\sigma_u^+)$	3230.5	3182.8(0.1)	
$\nu_2 + \nu_7(\sigma_u^+)$	3453.6	3362.2(2.5)	
$3\nu_7(\sigma_u^+)$	3508.7	3498.7(0.01)	
$\nu_1 + \nu_{13}(\pi_u)$	3569.5	3436.1(0.2)	
$\nu_5 + \nu_{10}(\pi_u)$	3715.1	3583.7(0.1)	
$\nu_4 + \nu_5(\sigma_u^+)$	4079.3	3945.8(0.1)	
$\nu_1 + \nu_{11}(\pi_u)$	4095.2	3940.1(0.8)	
$\nu_5 + \nu_8(\pi_u)$	4096.2	3943.9(0.8)	
$\nu_3 + \nu_6(\sigma_u^+)$	4233.1	4141.1(0.1)	
$\nu_2 + \nu_6(\sigma_u^+)$	4456.2	4334.7(0.1)	
$\nu_2 + \nu_5(\sigma_u^+)$	5747.2	5548.4(0.2)	
$\nu_1 + \nu_5(\sigma_u^+)$	6926.3	6555.1(4.6)	
Anharmonic ZPE = 10095.8			

a. Intensities in  $\text{km/mol}$  are given in parenthesis.

smaller than those seen for acetylene or diacetylene ( $\text{o-c} \sim 2 \text{ cm}^{-1}$ ). For the known combination band, the (fc)-CCSD(T)/ANO1 anharmonicity constants ( $x_{ij}$ , **supplementary material**) are able to reproduce the experimental value to within  $5 \text{ cm}^{-1}$ , suggesting other combination band frequencies are of equal accuracy.

For the modes observed in low-resolution studies (e.g.,  $\nu_1$  and  $\nu_{12}$ ), the agreement is still good with  $\text{o-c}$  values less than  $20 \text{ cm}^{-1}$ . The notable exception is the internal  $\text{C}\equiv\text{C}$  asymmetric stretch mode ( $\nu_7$ ), which differs by  $45 \text{ cm}^{-1}$ . Since no rotationally resolved data can be found for this band, it is possible that the band observed at  $1115.0 \text{ cm}^{-1}$  (Haas et al., 1994a) was mis-assigned as the  $\nu_7$  fundamental. A more likely assignment for this band is the  $\nu_9+\nu_{11}$  combination band, which has a predicted VPT2 frequency of  $1107.1 \text{ cm}^{-1}$ , a calculated intensity of  $0.7 \text{ km/mol}$ , and the same symmetry. Furthermore, the combination band is expected to be  $3.5\times$  more intense than the  $\nu_7$  fundamental at  $0.2 \text{ km/mol}$ , suggesting  $\nu_9+\nu_{11}$  is more likely of the two to be observed. However, rotationally resolved measurements of this band are clearly needed to confirm this speculation.

We note that, a resonance between the  $\nu_5$  fundamental and the  $\nu_2+\nu_7$  and  $3\nu_7$  combination bands must be addressed to achieve the very small ( $< 1 \text{ cm}^{-1}$ )  $\text{o-c}$  difference obtained for the C-H asymmetric stretch mode,  $\nu_5$ . The vibrational frequencies as a result of resonant interactions are calculated by a deperturbation-diagonalization technique followed by transformation of the deperturbed transition moments, as discussed in Vázquez & Stanton (2007) and Matthews et al. (2007). This combination of Fermi and Darling-Dennison interactions shifts the  $\nu_5$  predicted frequency from  $3333.1$  to  $3329.5 \text{ cm}^{-1}$ , which is able to reproduce the experimentally observed frequency [ $3329.0533(2) \text{ cm}^{-1}$  (Doney et al., 2015)] with the same accuracy seen for diacetylene ( $\text{o-c} \sim 0.5 \text{ cm}^{-1}$ ). The combination bands involved are similarly shifted:  $\nu_2+\nu_7$  from  $3329.5$  to  $3362.2 \text{ cm}^{-1}$ , and  $3\nu_7$  from  $3526.7$  to  $3498.7 \text{ cm}^{-1}$ . Since the shift is most pronounced for the two combination bands, future experimental work to observe either of these bands is required to confirm this prediction.

The vibration-rotation interaction constants for triacetylene are given in Table 2.4, and are consistent with the previous CCSD(T)/cc-pCVQZ theoretical study (Chang et al., 2016), and experimentally determined values (Matsumura et al., 1988b; McNaughton & Bruget, 1991; Haas et al., 1994a; Doney et al., 2015). Consequently, the calculated ground state rotational constant  $B_0 = 0.044 092 \text{ cm}^{-1}$  is within  $0.2\%$  of the experimentally observed  $B_0 = 0.044 1735(12) \text{ cm}^{-1}$  (Doney et al., 2015).

### 2.3.4 Spectroscopic properties of tetraacetylene

The (fc)-CCSD(T)/ANO1 harmonic and VPT2 frequencies of the fundamental and combination bands for tetraacetylene are given in Table 2.6, and the (fc)-CCSD(T)/ANO1 anharmonicity constants ( $x_{ij}$ ) are given in the **supplementary material**. For the four experimentally observed bands, agreement of the observed and calculated frequencies is good at  $< 7 \text{ cm}^{-1}$ , which is comparable to the uncertainty of the low resolution measurements. Furthermore, the ANO1 VPT2 frequencies are able to reproduce the experimental frequencies far better than the previous harmonic frequency calculations, which had  $\text{o-c}$  values  $\sim 20 - 100 \text{ cm}^{-1}$  (Shindo et al., 2001). Of the predicted fundamental and combination bands, there are a number of bands that are found/predicted to have sufficient intensity and/or relatively unique frequency range that could offer viable target transitions to use to search for tetraacetylene in future laboratory or astronomical spectra. For example, in the IR the  $\nu_1+\nu_6$  at  $6550.8 \text{ cm}^{-1}$  or  $\nu_{12}+\nu_{15}$  at  $871.9 \text{ cm}^{-1}$  combination bands have both comparable predicted intensity to measured bands of di- and triacetylene, and have transitions in relatively clean regions of the spectrum. In terms of astronomical searches, the  $\nu_{17}$  mode at  $60.7 \text{ cm}^{-1}$ , offers a unique target transition, since it's low frequency makes it accessible by far-IR observations, similar to the  $\nu_2$  bending mode of  $\text{C}_3$  (Cernicharo et al., 2000).

Based on the results discussed for the other small polyynes, the theoretical vibration-rotation interaction constants given in Table 2.4 are sufficient to assist in identification of ro-vibrational bands of tetraacetylene. The  $\alpha_i$  results in a theoretical ground state rotational constant of  $B_0 =$

0.018 844  $\text{cm}^{-1}$  that agrees within errors with the experimentally determined value,  $B_0 = 0.020(3)$   $\text{cm}^{-1}$  (Shindo et al., 2001). Overall, for polyynes the difference between the experimental and calculated rotational constants ( $\Delta B_0$ ) decreases from 0.001 to 0.00008  $\text{cm}^{-1}$  as the chain length is increased, which is consistent with the trend seen for other carbon chain molecules (e.g.,  $\text{HC}_n\text{N}$ ,  $\text{HC}_n$ ,  $\text{C}_n\text{O}$ ) (Etim & Arunan, 2017). Therefore, if the trend continues as expected then the  $\Delta B_0$  for tetraacetylene is equal to or smaller than that seen for triacetylene, and the determined ground state rotational constant is a good approximation of the true value.

## 2.4 CONCLUSIONS

Accurate equilibrium geometries have been determined at the AE-CCSD(T)/cc-pCVQZ level of theory, and the full cubic and semidiagonal quartic force field have been determined at the (fc)-

Table 2.6: Harmonic and anharmonic (VPT2) frequencies (in  $\text{cm}^{-1}$ ) of  $\text{HC}_8\text{H}$  fundamental and selected combination bands

Mode	CCSD(T)/ANO1 <sup>a</sup>		Experimental
	$\omega$	$\nu$	$\nu$
$\nu_1(\sigma_g^+)$	3462.0(0)	3330.5(0)	
$\nu_2(\sigma_g^+)$	2263.2(0)	2208.0(0)	
$\nu_3(\sigma_g^+)$	2134.6(0)	2094.2(0)	
$\nu_4(\sigma_g^+)$	1296.4(0)	1285.8(0)	
$\nu_5(\sigma_g^+)$	470.0(0)	455.3(0)	
$\nu_6(\sigma_u^+)$	3461.6(223.1)	3328.8(214.2)	3329.4 (Shindo et al., 2001)
$\nu_7(\sigma_u^+)$	2254.7(1.0)	2227.6(0.5)	
$\nu_8(\sigma_u^+)$	2064.3(0.3)	2026.6(0.6)	2023.3 (Shindo et al., 2001)
$\nu_9(\sigma_u^+)$	911.6(3.2)	922.4(2.0)	
$\nu_{10}(\pi_g)$	632.4(0)	620.0(0)	
$\nu_{11}(\pi_g)$	489.3(0)	486.0(0)	
$\nu_{12}(\pi_g)$	422.3(0)	419.5(0)	
$\nu_{13}(\pi_g)$	158.8(0)	157.9(0)	
$\nu_{14}(\pi_u)$	632.6(79.6)	619.7(79.9)	621.5 (Shindo et al., 2001)
$\nu_{15}(\pi_u)$	474.2(0.1)	470.9(0.2)	
$\nu_{16}(\pi_u)$	267.7(3.2)	266.7(3.1)	
$\nu_{17}(\pi_u)$	61.0(2.3)	60.7(2.2)	
$\nu_{11} + \nu_{17}(\sigma_u^+)$	550.3	546.5(0.6)	
$\nu_{13} + \nu_{15}(\sigma_u^+)$	633.0	628.5(1.7)	
$\nu_{12} + \nu_{16}(\sigma_u^+)$	690.1	684.8(3.1)	
$\nu_{12} + \nu_{15}(\sigma_u^+)$	896.5	871.9(3.5)	
$\nu_{11} + \nu_{15}(\sigma_u^+)$	963.5	970.5(1.3)	
$\nu_{10} + \nu_{15}(\sigma_u^+)$	1106.6	1092.2(0.6)	
$\nu_{10} + \nu_{14}(\sigma_u^+)$	1265.1	1236.7(37.5)	1229.7 (Shindo et al., 2001)
$\nu_2 + \nu_9(\sigma_u^+)$	3174.8	3130.1(0.5)	
$\nu_4 + \nu_8(\sigma_u^+)$	3360.7	3311.4(0.5)	
$\nu_6 + \nu_{10}(\pi_u)$	4094.0	3939.1(0.8)	
$\nu_1 + \nu_{14}(\pi_u)$	4094.6	3940.6(0.8)	
$\nu_1 + \nu_6(\sigma_u^+)$	6923.6	6550.8(5.7)	
Anharmonic ZPE = 12218.2			

a. Intensities in  $\text{km/mol}$  are given in parenthesis.

CCSD(T)/ANO1 level of theory for acetylene and the three smallest polyynes. No scaling or adjustments had to be included to match theoretical values with those determined by experiment. The resulting VPT2 fundamental vibrational frequencies and vibration-rotation interaction constants agree with known experimental values, showing about a  $5\text{ cm}^{-1}$  deviation in frequencies for bands with high-resolution infrared information. For bands with only low-resolution data, the theoretical frequencies are able to confirm mode assignments or suggest a reassignment, as in the case of the observed band at  $1115.0\text{ cm}^{-1}$  of triacetylene to the  $\nu_9+\nu_{11}$  combination band, which has previously been attributed to the  $\nu_7$  fundamental. The provisional *ab initio* method used here is also able to accurately reproduce the observed frequencies of combination bands.

The calculated fundamental frequencies for triacetylene and tetraacetylene give insight as to why tetraacetylene has not yet been observed in space. Observation of centrosymmetric molecules in astronomical environments is mainly through infrared detection of the high intensity bending modes; e.g.,  $\nu_8$  [ $628.040\ 776(36)\text{ cm}^{-1}$  (Bizzocchi et al., 2011)] and  $\nu_6+\nu_8$  [ $1241.060\ 828(38)\text{ cm}^{-1}$  (McNaughton & Bruget, 1992)] of diacetylene, or  $\nu_{11}$  [ $621.340\ 11(42)\text{ cm}^{-1}$  (Haas et al., 1994b)] and  $\nu_8+\nu_{11}$  [ $1232.904\ 295(74)\text{ cm}^{-1}$  (McNaughton & Bruget, 1991)] of triacetylene. However, the analogous modes for tetraacetylene are the  $\nu_{14}$  [ $621.5(5)\text{ cm}^{-1}$  (Shindo et al., 2001)] and  $\nu_{10}+\nu_{14}$  [ $1229.7(5)\text{ cm}^{-1}$  (Shindo et al., 2001)], and are predicted to be significantly weaker in intensity due to lower column densities (Woods et al., 2003; Sakai & Yamamoto, 2013). Consequently, at these frequencies and resolutions of the previous infrared observations where polyynes were detected (Cernicharo et al., 2001a,b; Bernard-Salas et al., 2006; Fonfría et al., 2011; Malek et al., 2012), the transitions of tetraacetylene are blended with those of triacetylene. Other bands of tetraacetylene would be more suitable for identification, such as  $\nu_1+\nu_6$ ,  $\nu_{12}+\nu_{15}$ , or  $\nu_{17}$  that are expected to be equally strong as bands already used to identify di- and triacetylene.

Overall, the resulting computed geometries lead to equilibrium rotational constants ( $B_e$ ), which when corrected for vibrational zero-point effects give ground state equilibrium constants ( $B_0$ ) that agree with experimental values ( $< 0.2\%$ ). Based on the small o-c values for acetylene, diacetylene, and triacetylene, we are confident that the fundamental frequencies and spectroscopic constants determined here offer an accurate guide for spectroscopic searches focused on detection of ro-vibrational bands of triacetylene and tetraacetylene. Such work is underway in our laboratory.

## 2.5 ACKNOWLEDGEMENTS

We thank Dr. D.J. Nesbitt for helpful discussions. We acknowledge the financial support of the Netherlands Organization for Scientific Research (NWO) through a VICI grant, and the Netherlands Research School for Astronomy (NOVA). D.Z. also acknowledges financial support from the National Key R&D Program of China (2017YFA0303502) and the Fundamental Research Funds for the Central Universities of China.

## 2.6 BIBLIOGRAPHY

- Almlöf, J. & Taylor, P. R. 1987, *The Journal of Chemical Physics*, 86, 4070  
Arié, E. & Johns, J. W. C. 1992, *Journal of Molecular Spectroscopy*, 155, 195  
Auer, A. A. & Gauss, J. 2001, *Physical Chemistry Chemical Physics*, 3, 3001  
Bak, K. L., Gauss, J., Jørgensen, P., et al. 2001, *The Journal of Chemical Physics*, 114, 6548  
Bandy, R. E., Lakshminarayan, C., Frost, R. K., & Zwier, T. S. 1992, *Science*, 258, 1630  
Bandy, R. E., Lakshminarayan, C., Frost, R. K., & Zwier, T. S. 1993, *The Journal of Chemical Physics*, 98, 5362  
Bartlett, R. J. 1995, in *Modern Electronic Structure Theory, Part II*, ed. D. R. Yarkony (Singapore: World Scientific)  
Bauschlicher Jr., C. W. & Taylor, P. R. 1993, *Theoretica Chimica Acta*, 86, 13  
Bell, M. B., Feldman, P. A., Travers, M. J., et al. 1997, *The Astrophysical Journal Letters*, 483, L61  
Bell, M. B., Feldman, P. A., Watson, J. K. G., et al. 1999, *The Astrophysical Journal*, 518, 740  
Bernard-Salas, J., Peeters, E., Sloan, G. C., et al. 2006, *The Astrophysical Journal Letters*, 652, L29  
Bizzocchi, L., Tamassia, F., Degli Esposti, C., et al. 2011, *Molecular Physics*, 109, 2181

- Bjarnov, E., Christensen, D., Nielsen, O., et al. 1974, *Spectrochimica Acta Part A: Molecular Spectroscopy*, 30, 1255
- Burgdorf, M., Orton, G., van Cleve, J., Meadows, V., & Houck, J. 2006, *Icarus*, 184, 634
- Cernicharo, J., Goicoechea, J. R., & Caux, E. 2000, *The Astrophysical Journal Letters*, 534, L199
- Cernicharo, J. & Guélin, M. 1996, *Astronomy & Astrophysics*, 309, L27
- Cernicharo, J., Heras, A. M., Pardo, J. R., et al. 2001a, *The Astrophysical Journal Letters*, 546, L127
- Cernicharo, J., Heras, A. M., Tielens, A. G. G. M., et al. 2001b, *The Astrophysical Journal Letters*, 546, L123
- CFOUR. 2017, Coupled-Cluster techniques for Computational Chemistry, a quantum-chemical program package by J.F. Stanton, J. Gauss, M.E. Harding, P.G. Szalay with contributions from A.A. Auer, R.J. Bartlett, U. Benedikt, C. Berger, D.E. Bernholdt, Y.J. Bomble, L. Cheng, O. Christiansen, F. Engel, R. Faber, M. Heckert, O. Heun, C. Huber, T.-C. Jagau, D. Jonsson, J. Jusélius, K. Klein, W.J. Lauderdale, F. Lipparini, D.A. Matthews, T. Metzroth, L.A. Mück, D.P. O'Neill, D.R. Price, E. Prochnow, C. Puzzarini, K. Ruud, F. Schiffmann, W. Schwalbach, C. Simmons, S. Stopkowitz, A. Tajti, J. Vázquez, F. Wang, J.D. Watts and the integral packages MOLECULE (J. Almlöf and P.R. Taylor), PROPS (P.R. Taylor), ABACUS (T. Helgaker, H.J. Aa. Jensen, P. Jørgensen, and J. Olsen), and ECP routines by A. V. Mitin and C. van Wüllen. For the current version, see <http://www.cfour.de>.
- Chang, C.-H., Agarwal, J., Allen, W. D., & Nesbitt, D. J. 2016, *The Journal of Chemical Physics*, 144, 074301
- Cherchneff, I., Barker, J. R., & Tielens, A. G. G. M. 1992, *The Astrophysical Journal*, 401, 269
- D'Cunha, R., Sarma, Y., Guelachvili, G., et al. 1991, *Journal of Molecular Spectroscopy*, 148, 213
- de Graauw, T., Feuchtgruber, H., Bezaud, B., et al. 1997, *Astronomy & Astrophysics*, 321, L13
- Doney, K. D., Zhao, D., & Linnartz, H. 2015, *Journal of Molecular Spectroscopy*, 316, 54
- Ekern, S. P., Marshall, A. G., Szczepanski, J., & Vala, M. 1998, *The Journal of Physical Chemistry A*, 102, 3498
- Etim, E. E. & Arunan, E. 2017, *Astrophysics and Space Science*, 362, 4
- Feller, D. 1996, *Journal of Computational Chemistry*, 17, 1571
- Fonfría, J. P., Cernicharo, J., Richter, M. J., & Lacy, J. H. 2011, *The Astrophysical Journal*, 728, 43
- Frenklach, M., Clary, D. W., Gardiner, W. C., & Stein, S. E. 1985, *Symposium (International) on Combustion*, 20, 887
- Frenklach, M. & Feigelson, E. D. 1989, *The Astrophysical Journal*, 341, 372
- Frost, R. K., Zavarin, G. S., & Zwier, T. S. 1995, *The Journal of Physical Chemistry*, 99, 9408
- Fujii, T. & Kareev, M. 2001, *Journal of Applied Physics*, 89, 2543
- Gambogi, J. E., Pearson, R. Z., Yang, X., Lehmann, K. K., & Scoles, G. 1995, *Chemical Physics*, 190, 191
- Gauss, J. 1998, in *Encyclopedia of Computational Chemistry*, ed. P. v. R. Schleyer (New York: Wiley)
- Gauss, J. & Stanton, J. F. 1997, *Chemical Physics Letters*, 276, 70
- Gu, X., Kim, Y. S., Kaiser, R. I., et al. 2009, *Proceedings of the National Academy of Sciences*, 106, 16078
- Guelachvili, G., Craig, A. M., & Ramsay, D. A. 1984, *Journal of Molecular Spectroscopy*, 105, 156
- Haas, S., Winnewisser, G., Yamada, K. M. T., Matsumura, K., & Kawaguchi, K. 1994b, *Journal of Molecular Spectroscopy*, 167, 176
- Haas, S., Yamada, K. M. T., & Winnewisser, G. 1994a, *Journal of Molecular Spectroscopy*, 164, 445
- Homann, K.-H. 1998, *Angewandte Chemie International Edition*, 37, 2434
- Kabbadj, Y., Herman, M., Di Lonardo, G., Fusina, L., & Johns, J. W. C. 1991, *Journal of Molecular Spectroscopy*, 150, 535
- Kaiser, R. I., Sun, B. J., Lin, H. M., et al. 2010, *The Astrophysical Journal*, 719, 1884
- Kress, M. E., Tielens, A. G. G. M., & Frenklach, M. 2010, *Advances in Space Research*, 46, 44
- Krestinin, A. V. 2000, *Combustion and Flame*, 121, 513
- Kunde, V. G., Aikin, A. C., Hanel, R. A., et al. 1981, *Nature*, 292, 686
- Kunde, V. G., Flasar, F. M., Jennings, D. E., et al. 2004, *Science*, 305, 1582
- Lee, T. J. & Scuseria, G. E. 1995, in *Quantum Mechanical Electronic Structure Calculations with Chemical Accuracy*, ed. S. Langhoff (Dordrecht: Kluwer Academic Publishers)
- Ma, T.-B., Hu, Y.-Z., & Wang, H. 2008, *Journal of Applied Physics*, 104, 064904
- Malek, S. E., Cami, J., & Bernard-Salas, J. 2012, *The Astrophysical Journal*, 744, 16
- Martin, J. M. L., Lee, T. J., & Taylor, P. R. 1998, *The Journal of Chemical Physics*, 108, 676
- Martin, J. M. L., Taylor, P. R., & Lee, T. J. 1997, *Chemical Physics Letters*, 275, 414
- Matsumura, K., Kanamori, H., Kawaguchi, K., Hirota, E., & Tanaka, T. 1988b, *Journal of Molecular Spectroscopy*, 131, 278
- Matthews, D. A., Vázquez, J., & Stanton, J. F. 2007, *Molecular Physics*, 105, 2659
- McCaslin, L. & Stanton, J. F. 2013, *Molecular Physics*, 111, 1492
- McNaughton, D. & Bruget, D. N. 1991, *Journal of Molecular Spectroscopy*, 150, 620
- McNaughton, D. & Bruget, D. N. 1992, *Journal of Molecular Structure*, 273, 11
- Meadows, V. S., Orton, G., Line, M., et al. 2008, *Icarus*, 197, 585
- Milani, A., Tommasini, M., Del Zoppo, M., Castiglioni, C., & Zerbi, G. 2006, *Physical Review B*, 74, 153418

- Owen, N. L., Smith, C. H., & Williams, G. A. 1987, *Journal of Molecular Structure*, 161, 33
- Palmer, K. F., Mickelson, M. E., & Rao, K. N. 1972, *Journal of Molecular Spectroscopy*, 44, 131
- Pliva, J. 1972a, *Journal of Molecular Spectroscopy*, 44, 165
- Pliva, J. 1972b, *Journal of Molecular Spectroscopy*, 44, 145
- Plyler, E. K., Tidwell, E. D., & Wiggins, T. A. 1963, *Journal of the Optical Society of America*, 53, 589
- Raghavachari, K., Trucks, G. W., Pople, J. A., & Head-Gordon, M. 1989, *Chemical Physics Letters*, 157, 479
- Richter, H. & Howard, J. 2000, *Progress in Energy and Combustion Science*, 26, 565
- Sakai, N. & Yamamoto, S. 2013, *Chemical Reviews*, 113, 8981
- Sattelmeyer, K. W. & Stanton, J. F. 2000, *Journal of the American Chemical Society*, 122, 8220
- Schuchardt, K. L., Didier, B. T., Elsethagen, T., et al. 2007, *Journal of Chemical Information and Modeling*, 47, 1045
- Shindo, F., Bénilan, Y., Chaquin, P., et al. 2001, *Journal of Molecular Spectroscopy*, 210, 191
- Shirakawa, H. 2001, *Review of Modern Physics*, 73, 713
- Simandiras, E. D., Rice, J. E., Lee, T. J., Amos, R. D., & Handy, N. C. 1988, *The Journal of Chemical Physics*, 88, 3187
- Simmonett, A. C., Schaefer III, H. F., & Allen, W. D. 2009, *The Journal of Chemical Physics*, 130, 044301
- Stanton, J. F. & Gauss, J. 2000, *International Reviews in Physical Chemistry*, 19, 61
- Tamassia, F., Cane, E., Fusina, L., & Di Lonardo, G. 2016, *Physical Chemistry Chemical Physics*, 18, 1937
- Tay, R., Metha, G. F., Shanks, F., & McNaughton, D. 1995, *Structural Chemistry*, 6, 47
- Temsamani, M. A. & Herman, M. 1995, *The Journal of Chemical Physics*, 102, 6371
- Thaddeus, P., McCarthy, M. C., Travers, M. J., Gottlieb, C. A., & Chen, W. 1998, *Faraday Discussions*, 109, 121
- Thejaswini, H. C., Majumdar, A., Tun, T. M., & Hippler, R. 2011, *Advances in Space Research*, 48, 857
- Thorwirth, S., Harding, M. E., Muders, D., & Gauss, J. 2008, *Journal of Molecular Spectroscopy*, 251, 220
- Toto, J. L., Toto, T. T., de Melo, C. P., Kirtman, B., & Robins, K. 1996, *The Journal of Chemical Physics*, 104, 8586
- Vanderauwera, J., Hurtmans, D., Carleer, M., & Herman, M. 1993, *Journal of Molecular Spectroscopy*, 157, 337
- Vázquez, J. & Stanton, J. F. 2007, *Molecular Physics*, 105, 101
- Vuitton, V., Doussin, J.-F., Bénilan, Y., Raulin, F., & Gazeau, M.-C. 2006, *Icarus*, 185, 287
- Vuitton, V., Yelle, R. V., & McEwan, M. J. 2007, *Icarus*, 191, 722
- Waite, J. H., Young, D. T., Cravens, T. E., et al. 2007, *Science*, 316, 870
- Wakelam, V., Smith, I. W. M., Herbst, E., et al. 2010, *Space Science Reviews*, 156, 13
- Wilson, E. H. & Atreya, S. K. 2003, *Planetary and Space Science*, 51, 1017
- Woods, P. M., Millar, T. J., Herbst, E., & Zijlstra, A. A. 2003, *Astronomy & Astrophysics*, 402, 189
- Woon, D. E. & Dunning Jr., T. H. 1995, *The Journal of Chemical Physics*, 103, 4572
- Zhang, X., Maccarone, A. T., Nimlos, M. R., et al. 2007, *The Journal of Chemical Physics*, 126, 044312
- Zhao, D., Doney, K. D., & Linnartz, H. 2014a, *Journal of Molecular Spectroscopy*, 296, 1
- Zhao, D., Guss, J., Walsh, A. J., & Linnartz, H. 2013, *Chemical Physics Letters*, 565, 132
- Zhao, X., Ando, Y., Liu, Y., Jinno, M., & Suzuki, T. 2003, *Physical Reviews Letters*, 90, 187401



## HIGH-RESOLUTION INFRARED SPECTRUM OF THE $\nu_4$ FUNDAMENTAL AND NEARBY HOT BANDS OF DIACETYLENE

---

High-resolution infrared spectra of diacetylene ( $\text{HC}_4\text{H}$ ) are recorded in the  $3\ \mu\text{m}$  C-H stretch region using continuous wave cavity ring-down spectroscopy (cw-CRDS). The  $\text{HC}_4\text{H}$  molecules are generated in a pulsed and supersonic planar plasma expansion by discharging a  $\text{C}_2\text{H}_2/\text{He}/\text{Ar}$  gas mixture. The jet-cooling realizes a low rotational temperature of  $T_{\text{rot}} \sim 17\ \text{K}$ . Vibrational temperatures are found to be relatively high, allowing the detection of vibrationally excited  $\text{HC}_4\text{H}$  in direct absorption with energies up to  $1800\ \text{cm}^{-1}$ . In total, sixteen ro-vibrational bands are identified, where nine of them were not reported before. Detailed and systematic rotational analyses are presented, yielding spectroscopic parameters for a series of vibrational levels over energy regions of 0 - 1800 and 3300 - 5100  $\text{cm}^{-1}$ . Using the observed infrared band intensities, two vibrational excitation temperatures of  $\text{HC}_4\text{H}$  in the plasma jet,  $\sim 570(50)\ \text{K}$  for the  $\nu_6$ ,  $\nu_7$ , and  $\nu_8$  bending vibrations, and  $\sim 125(10)\ \text{K}$  for the  $\nu_9$  bending vibration, are deduced.

### 3.1 INTRODUCTION

As a substantial reservoir of carbon in the universe, unsaturated hydrocarbons and their derivatives are important constituents in common reaction schemes (Henning & Salama, 1998). Among them, highly unsaturated (poly)acetylenes of the form of  $\text{HC}_{2n}\text{H}$ , are commonly involved in combustion chemistry (Homann, 1998; Richter & Howard, 2000), plasma processing (Fujii & Kareev, 2001; Thejaswini et al., 2011), chemical syntheses and material sciences (Shirakawa, 2001; Zhao et al., 2003; Milani et al., 2006; Ma et al., 2008). Due to their unstable and highly reactive nature, they also play an important role in the chemical evolution of planet atmospheres and in the chemistry of the interstellar medium (ISM) (Kaiser, 2002; Kahanpää et al., 2003; Gu et al., 2006; Wakelam et al., 2010; Kaiser & Mebel, 2012). In astrochemical models, acetylene, diacetylene and derivatives, including the cyano derivatives HCN and  $\text{HC}_3\text{N}$ , are thought to link known gas-phase molecules and complex organics. Since diacetylene is photochemically reactive (Glicker & Okabe, 1987; Israel et al., 1991; Bandy et al., 1992, 1993; Delpech et al., 1994; Frost et al., 1995), photolysis of diacetylene can result in the production of longer carbon-chain species, such as tri- ( $\text{HC}_6\text{H}$ ) and tetra-acetylene ( $\text{HC}_8\text{H}$ ). Although not conclusively proven yet, acetylene and diacetylene are believed to be important intermediates in the reaction scheme leading to the formation of large organic molecules that make up the “haze” of the atmospheres of gas giant planets (Kaiser, 2002; Kaiser & Mebel, 2012; Bandy et al., 1992; Wilson & Atreya, 2004).

Small polyacetylenes, primarily diacetylene ( $\text{HC}_4\text{H}$ ), have been identified in many carbon-rich atmospheres of planets and their moons. In 1981, diacetylene was identified for the first time in space in the atmosphere of Titan, by Voyager’s infrared interferometer spectrometer (IRIS) (Kunde et al., 1981). In 1997, diacetylene was identified again in Infrared Space Observatory (ISO) spectra from Saturn (de Graauw et al., 1997), which led to the suggestion that small polyacetylenes are involved in giant planet atmospheric chemistry (Kahanpää et al., 2003; Jolly et al., 2010). In 2004, following the predictions of photochemical models (Gladstone et al., 1996; Shindo et al., 2003), diacetylene was detected in the atmospheres of Jupiter (Kunde et al., 2004), and the remaining giant planets Uranus (Burgdorf et al., 2006) and Neptune (Meadows et al., 2008). In the interstellar medium (ISM), detection of small polyacetylenes has been accessed in two carbon-rich protoplanetary nebulae, CRL 618 and CRL 2688 (Cernicharo et al., 2001a,b; Fonfría et al., 2011), in Spitzer infrared observations against the dust shell of a nova like star V4334 Sgr (Evans et al., 2006), as well as in the extragalactic Large Magellanic cloud (LMC) (Bernard-Salas et al., 2006).

Due to the lack of a permanent dipole moment, diacetylene cannot be detected by rotational transitions in the microwave region, and therefore ro-vibrational spectra in the infrared and sub-millimeter-wave region are the most important spectroscopic tools to detect  $\text{HC}_4\text{H}$  both in the laboratory and in astronomical observations (Frost et al., 1995; Kunde et al., 1981; de Graauw et al., 1997; Jolly et al., 2010; Cernicharo et al., 2001a,b; Wilson & Atreya, 2004; Evans et al., 2006; Bernard-Salas et al., 2006; Bizzocchi et al., 2010; Fonfría et al., 2011; Bizzocchi et al., 2011). For example, detections of diacetylene in planetary atmospheres are mainly via the strong perpendicular band  $\nu_8$ , at  $627.9\text{ cm}^{-1}$  (de Graauw et al., 1997; Kunde et al., 2004; Burgdorf et al., 2006; Meadows et al., 2008), and in the protoplanetary nebulae of CRL 618 and CRL 2688 via the parallel combination band  $\nu_6+\nu_8$ , at  $1241\text{ cm}^{-1}$  (Cernicharo et al., 2001a,b; Fonfría et al., 2011).

In the past few decades, series of high-resolution laboratory spectroscopic studies on diacetylene have been reported with spectral coverage ranging from submillimeter-wave to infrared (Matsumura et al., 1981; Matsumura & Tanaka, 1982; Guelachvili et al., 1984; Matsumura et al., 1986; Matsumura & Tanaka, 1986a,b; Owen et al., 1987; McNaughton & Bruget, 1992; Arié & Johns, 1992; Khlifi et al., 1995; Tay et al., 1995; Bizzocchi et al., 2010, 2011). These measurements were generally performed at room temperature with pure diacetylene gas samples synthesized in the laboratory, resulting in accurate spectroscopic parameters for a number of low-lying vibrational levels. These room-temperature spectra, particularly the spectrum in the C-H stretch region at  $\sim 3\text{ }\mu\text{m}$  (Guelachvili et al., 1984), suffer heavily from spectral blending, and Doppler broadened line profiles

which prohibit detailed analysis of weak absorption features, such as low- $J''$  transitions and weak vibrational hot bands. Recently, we demonstrated a new laboratory approach that allows to record high-resolution infrared spectra of hydrocarbons in pulsed supersonic planar plasma (Zhao et al., 2013). It was found that the jet-cooling results in a low rotational temperature of  $\text{HC}_4\text{H}$  and simplifies the experimental spectra. A sensitive cavity ring-down detection scheme allows us to detect the low- $J''$  transitions of a series of weak hot bands. In this work, we present a detailed analysis of the ro-vibrational transition band system of  $\text{HC}_4\text{H}$  in the  $3306 - 3342 \text{ cm}^{-1}$  region. Chemical formation and the non-equilibrium relaxation of vibrationally excited  $\text{HC}_4\text{H}$  in a supersonic plasma jet are also discussed based on the experimental findings.

### 3.2 EXPERIMENT

The experimental setup is described in detail recently (Zhao et al., 2013). Diacetylene molecules are produced in a pulsed supersonic planar plasma jet by discharging 0.5%  $\text{C}_2\text{H}_2$  diluted in a He/Ar 1:1 gas mixture. A gas pulse (1 ms), with a typical backing pressure of  $\sim 15$  bar, is supersonically expanded into a vacuum chamber through a pulsed valve (General Valve, Series 9, 2 mm orifice) that is mounted on top of a  $3 \text{ cm} \times 0.3 \text{ mm}$  multi-layer slit discharge nozzle. The vacuum chamber is evacuated by a roots blower pump station ( $4800 \text{ m}^3/\text{h}$ ). Typical discharge V/I values are  $\sim 1200 \text{ V}/50 \text{ mA}$ . The discharge nozzle is aligned with its slit throat in parallel to and  $\sim 5 \text{ mm}$  away from the optical axis of a high finesse cavity which is used for cavity ring-down measurements. The cavity is 56 cm long and comprises two highly reflective plano-concave mirrors (1 m radius of curvature, reflectivity  $\sim 99.97\%$  at  $3 \mu\text{m}$ ) mounted on opposite sides of the main chamber via high-precision alignment tools. The cavity mirrors are protected from plasma contaminations by special  $\text{N}_2$  curtains in front of the reflective surface of each mirror.

The idler output of a commercial single-frequency single-mode continuous wave optical parametric oscillator (cw-OPO, Aculight, Argos 2400-SF-B), operating at  $\sim 3 \mu\text{m}$  with an output power of  $\sim 1.2 \text{ W}$  and a bandwidth of  $< 1 \text{ MHz}$ , is employed as infrared light source. The infrared beam is led through an acousto-optical modulator (AOM), and the first-order deflection (5%), is spatially filtered by a two-lens telescope system configured with a  $150 \mu\text{m}$  pinhole and then coupled to the ring-down cavity. The cavity length is modulated at 20 Hz by applying a periodic triangle voltage to a piezo-electric transducer mounted on one of the mirror holders. The modulation amplitude is selected to ensure that the cavity is in resonance with the infrared laser at least twice in one period. A hardware (Boxcar integrator) based multi-trigger and timing scheme, which has been recently described in detail in Zhao et al. (2013), is used to coincide each plasma pulse to one ring-down event. Typical ring-down times are  $\sim 5 \mu\text{s}$ , corresponding to  $\sim 3000$  effective passes through the planar plasma jet.

An absorption spectrum is recorded by measuring ring-down times as a function of infrared laser frequency. The full experimental spectrum presented in this paper was recorded over 3 weeks. The laser frequency is simultaneously calibrated using a wavelength meter (Bristol Instruments, 621A-IR, self-calibrated by a stabilized He-Ne laser) which provides relative and absolute frequency accuracies better than 6 MHz and 20 MHz, respectively. The frequency calibration is independently checked by recorded absorption features of the precursor  $\text{C}_2\text{H}_2$  and trace  $\text{H}_2\text{O}$  molecules in the vacuum chamber, indicating a precision of the absolute infrared frequency over one month better than 30 MHz. It should be noted that, when extracting the line positions from our experimental spectra, due to the dense spectral features and heavy line blending, the accuracy of line position determinations for weak and/or heavily blended transitions may be slightly worse, but is still believed to be better than 45 MHz.

## 3.3 RESULTS AND DISCUSSION

3.3.1 *Experimental spectra*

Figure 3.1 shows an overview of our experimental spectrum in the 3306 - 3342  $\text{cm}^{-1}$  region. A small part of the experimental spectra at 3330  $\text{cm}^{-1}$  was already shown in Zhao et al. (2013). Previous experimental work (Bizzocchi et al., 2010, 2011; Guelachvili et al., 1984) and theoretical predictions (Zhang et al., 2004; Simmonett et al., 2009) showed that this region is characteristic of the C-H stretch vibrations (both symmetric and asymmetric) of polyacetylenes. As indicated in Figure 3.1, strong and spectrally contaminating absorption features due to the precursor  $\text{C}_2\text{H}_2$  molecules can be easily discriminated based on the line list available in the HITRAN database (Rothman et al., 2013). Two spectral forests are clearly visible in the 3325 - 3340  $\text{cm}^{-1}$  and 3308 - 3320  $\text{cm}^{-1}$  regions. Based on previous room-temperature FTIR work on  $\text{HC}_4\text{H}$  and  $\text{HC}_6\text{H}$  (Guelachvili et al., 1984; Tay et al., 1995; McNaughton & Bruget, 1991; Matsumura et al., 1993), the former corresponds to the region of the C-H asymmetric stretch (e.g.,  $\nu_4$  of  $\text{HC}_4\text{H}$ , and  $\nu_5$  of  $\text{HC}_6\text{H}$ ) fundamental and associated hot bands of polyacetylenes, and the latter corresponds to the region of the C-H symmetric stretch (e.g.,  $\nu_1$  of  $\text{HC}_4\text{H}$ , and likely  $\text{HC}_6\text{H}$ ) associated hot bands. Our preliminary analysis given in Zhao et al. (2013) has shown that, even in a supersonic jet where the rotational temperature is only  $\sim 17$  K, more than 2000 lines are recorded, including a series of strong vibrational hot bands of  $\text{HC}_4\text{H}$  and  $\text{HC}_6\text{H}$ . This paper will focus on the analysis of the observed vibrational bands of  $\text{HC}_4\text{H}$ , specifically the hot band transitions which provide spectroscopic information of vibrationally excited  $\text{HC}_4\text{H}$ . The  $\text{HC}_6\text{H}$  data will be discussed in a separate paper.

To assist the following analysis and discussion, a summary of the nine normal vibrational modes of  $\text{HC}_4\text{H}$  as available from literature is given in Table 3.1.

Table 3.1: Vibrational normal modes (in  $\text{cm}^{-1}$ ) of  $\text{HC}_4\text{H}$ 

Mode	Nuclear motion	Vibrational frequency		Vib-rot constant $\times 10^{-4}$	
		$\omega^a$	$\nu^b$	$\alpha$ ( <i>ab initio</i> )	$\alpha$ (Expt)
$\nu_1(\sigma_g^+)$	C-H sym. stretch	3489	3332.15	2.167	2.153(10) <sup>c</sup>
$\nu_2(\sigma_g^+)$	$\text{C}\equiv\text{C}$ sym. stretch	2222	2188.93	6.552	
$\nu_3(\sigma_g^+)$	C-C sym. stretch	885	871.96	3.134	1.03 (Bizzocchi et al., 2011) 3.110 <sup>d</sup> (Simmonett et al., 2009)
$\nu_4(\sigma_u^+)$	C-H asym. stretch	3490	3333.66	2.170	2.191 (Guelachvili et al., 1984) 2.183(4) <sup>c</sup>
$\nu_5(\sigma_u^+)$	$\text{C}\equiv\text{C}$ asym. stretch	2050	2022.24	3.911	3.948 (Guelachvili et al., 1984)
$\nu_6(\pi_g)$	$\text{C}\equiv\text{C}$ -H sym. bend	638	625.64	-0.825	-0.678 (Bizzocchi et al., 2011)
$\nu_7(\pi_g)$	$\text{C}\equiv\text{C}$ -C sym. bend	490	482.71	-2.786	-2.711 (McNaughton & Bruget, 1992)
$\nu_8(\pi_u)$	$\text{C}\equiv\text{C}$ -H asym. bend	641	628.04	-0.714	-0.636 (Simmonett et al., 2009)
$\nu_9(\pi_u)$	$\text{C}\equiv\text{C}$ -C asym. bend	223	220.12	-4.194	-4.183 (McNaughton & Bruget, 1992)

a. Williams & Macdonald (1994).

b. Guelachvili et al. (1984).

c. This work.

d. Deperturbed.

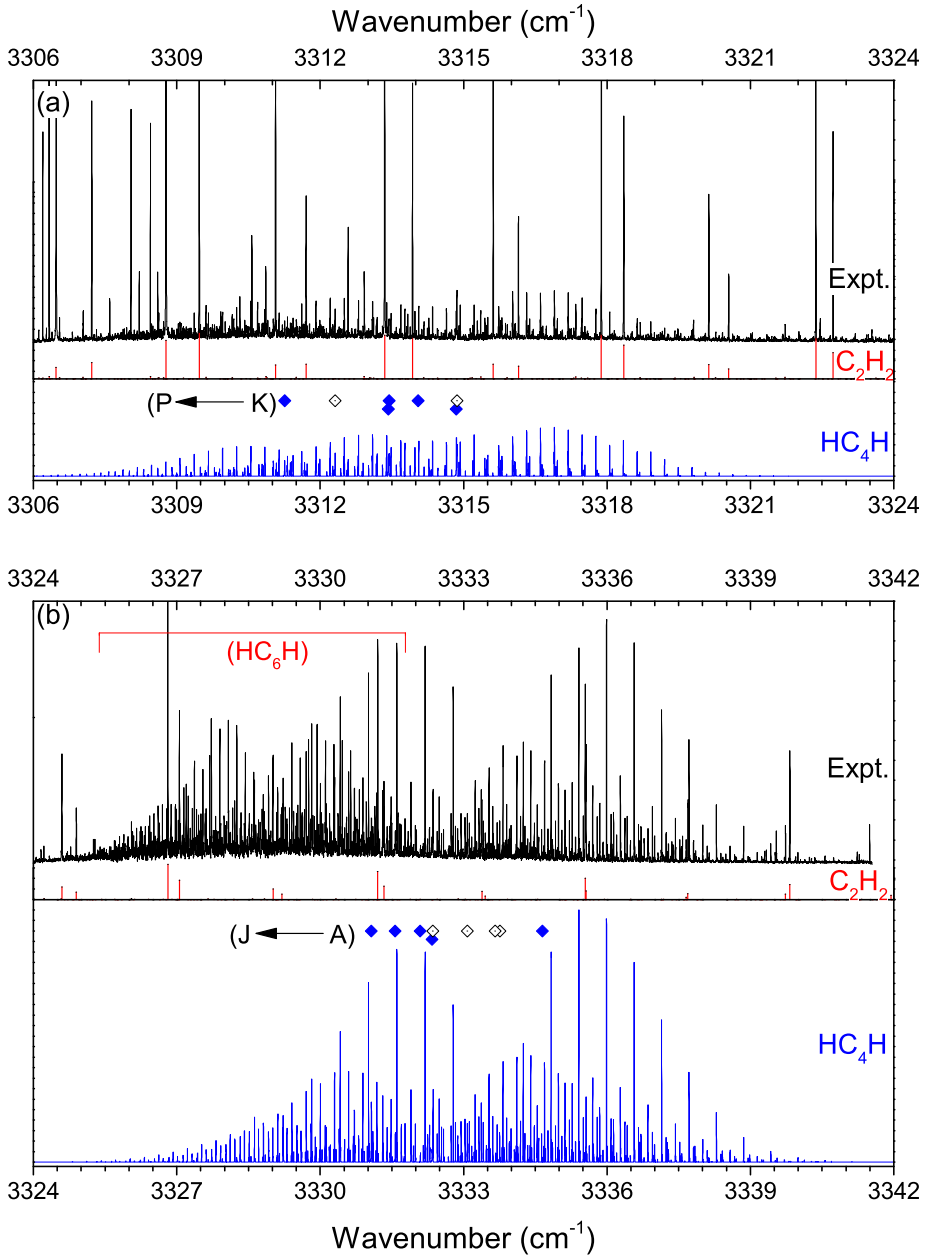


Figure 3.1: In both panels, upper trace: an overview of the experimental spectra recorded through a supersonic hydrocarbon plasma jet; middle trace,  $\text{C}_2\text{H}_2$  lines available from the HITRAN database; lower panel: simulated sum spectrum of the sixteen observed bands of  $\text{HC}_4\text{H}$ , using the spectroscopic parameters and relative level populations as listed in Table 3.2. Band origins are marked by empty and filled diamond symbols for previously reported and newly observed bands, respectively. The spectral region of the strong  $\text{HC}_6\text{H } \nu_5$  fundamental band is marked in panel (b).

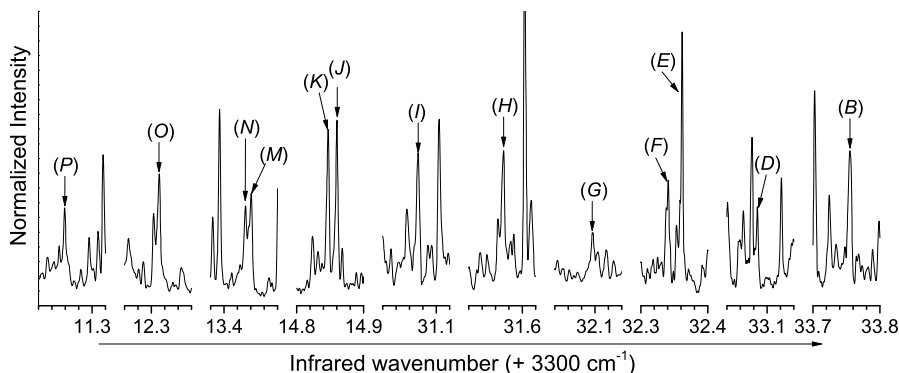


Figure 3.2: The weak Q branches (indicated by arrows, and band labels as in Table 3.3) of the observed degenerated transition bands of  $\text{HC}_4\text{H}$ .

### 3.3.2 Spectral analysis

The preliminary analysis shows that, at least sixteen separate bands of  $\text{HC}_4\text{H}$  can be recognized in our experimental spectrum. Their band origins are marked by diamond symbols in Figure 3.1. Here we label the sixteen bands by capital letters A, B, up to P in a descending order of infrared frequencies of their band origins, as indicated in Figure 3.1 and Tables 3.2 and 3.3. The determined line positions and corresponding rotational assignments from our analysis are given in **supplementary material**. In this spectral region, the  $\nu_4$  fundamental band,  $4_0^1$  (C), and six hot bands,  $4_0^1 6_1^1$  (B),  $4_0^1 9_1^1$  (D),  $4_0^1 9_2^1$ ,  $4_0^1 7_1^1$  (E),  $1_0^1 8_0^1 6_1^0$  (J), and  $1_0^1 6_0^1 8_1^0$  (O), have been previously measured at room temperature, and analyzed by Guelachvili et al. (1984). Among these previously reported bands, only the  $4_0^1 9_2^1$  band is too weak to be unambiguously identified in our spectra. A comparison of line positions measured in the present work to those reported in Guelachvili et al. (1984) shows good agreement, with deviations for most strong and fully resolved lines smaller than  $5 \times 10^{-4} \text{ cm}^{-1}$ . The only exception is the  $4_0^1$  fundamental (*i.e.*, the C-H asymmetric stretch) band, in which some lower- $J$  transition lines ( $10 < J < 25$ ) show a small shift of about  $-8 \times 10^{-4} \text{ cm}^{-1}$  (rms) with respect to the data reported in Guelachvili et al. (1984). The origin of this small, but systematic, offset is unclear as it is not found for other bands (*e.g.*, the  $4_0^1 6_1^1$  hot band) in the same wavenumber range.

All bands observed in the present work are parallel transitions, *i.e.*, the quantum number  $l$ , related to the projection of the total vibrational angular momentum on the symmetry axis, does not change upon vibrational excitation. In total, four types of vibrational transitions are observed:  $\Sigma - \Sigma$ ,  $\Pi - \Pi$ ,  $\Delta - \Delta$ , and  $\Phi - \Phi$ , corresponding to  $l = 0, 1, 2$ , and  $3$ , respectively. The  $\Sigma - \Sigma$  type bands, including the  $\nu_4$  fundamental band, consist of simple P- and R- branches, and exhibit 3:1 line intensity alternations in each branch due to nuclear spin statistics for lower-state rotational levels with different parity facilitated even-/odd- $J$  numbering. The other three band types with  $l \neq 0$  are degenerated due to rotational  $l$ -type doubling, *i.e.*, each rotational line comprises two components with a relative intensity ratio of 3:1:1:3 which are only resolved for some high- $J$  transitions. Moreover, for the  $l \neq 0$  bands, weak and unresolved or partially resolved Q-branches (Figure 3.2) are also observed, with intensities relative to P-/R- branch transitions (in the same band) proportional to  $J^2$ .

The rotational analysis of each band is performed in the PGOPHER software (Western, 2014), starting from a standard ro-vibrational Hamiltonian for linear molecules:

$$H = H_{\text{vib}} + BN^2 - DN^4 \quad (3.1)$$

Table 3.2: Lower state spectroscopic parameters<sup>a</sup> (in cm<sup>-1</sup>) of the observed sixteen infrared bands of HC<sub>4</sub>H

Assignment	G <sub>v</sub>	B <sup>''</sup>	q <sup>''</sup> × 10 <sup>5</sup>	D <sup>''</sup> × 10 <sup>8</sup>	q <sup>''</sup> <sub>D</sub> × 10 <sup>10</sup>	H <sup>''</sup> × 10 <sup>15</sup>
A1		0.146326(11)		1.6 <sup>c</sup>		
A2		0.1461157(89)		1.6 <sup>c</sup>		
B <sup>b</sup>	625.64 <sup>d</sup>	0.146 478 93	-8.289 5	1.574 71	3.96	1.09
C <sup>b</sup>	0	0.146 411 184		1.568 25		
D <sup>b</sup>	219.97 <sup>d</sup>	0.146 829 82	-20.532	1.628 8	4.289	
E	482.71 <sup>d</sup>	0.146 6788(24)	-12.15(23)	1.572(31)	10	
F		0.146 7387(98)	-8(2)	1.6 <sup>c</sup>		
G		0.146 537(12)	-3.3(24)	1.6 <sup>c</sup>		
H	628.04 <sup>d</sup>	0.146 474 73	-8.0374	1.574 8	0.437	1.087
I	962.96 <sup>d</sup>	0.146 9769(53)	-5.3(16) × 10 <sup>-3</sup>	1.6 <sup>c</sup>		
J <sup>b</sup>	625.64 <sup>d</sup>	0.146 478 93	-8.289 5	1.574 71	3.96	1.09
K	1290.4 <sup>e</sup>	0.146 5790(58)		1.6 <sup>c</sup>		
L	1283.2 <sup>e</sup>	0.146 5464(13)		1.539(28)		
M	1144.8 <sup>e</sup>	0.146 7396(46)	-3.0(26) × 10 <sup>-3</sup>	1.6 <sup>c</sup>		
N	1799.6 <sup>e</sup>	0.146 7848(79)		1.6 <sup>c</sup>		
O <sup>b</sup>	628.04 <sup>e</sup>	0.146 474 73	-8.037 4	1.574 8	0.437	1.087
P	1138.1 <sup>e</sup>	0.146 7568(31)	-0.0208(13)	1.6 <sup>c</sup>		

a. Uncertainty corresponding to a standard deviation given in the parentheses.

b. Lower state constants are fixed to Bizzocchi et al. (2011).

c. Fixed in the fit.

d. Vibrational energy fixed to Guelachvili et al. (1984).

e. Vibrational energy calculated using vibrational anharmonicity constants of Simmonett et al. (2009).

which gives the following expression of ro-vibrational energy levels ( $v, l, J$ )

$$E(v, l, J) = G_{v,l} + B_v[J(J+1) - l^2] - D_v[J(J+1) - l^2]^2 \quad (3.2)$$

where  $H_{\text{vib}}$  is the vibrational Hamiltonian,  $\mathbf{N}$  the rotational angular momentum,  $G_{v,l}$  the vibrational energy,  $B_v$  the rotational constant, and  $D_v$  the quartic centrifugal distortion constant, respectively. For the  $\nu_6 = 1$  and  $\nu_8 = 1$  levels, accurate sextic centrifugal distortion constants,  $H_v$ , corresponding to the  $\text{HN}^6$  term in the total Hamiltonian, are available from submillimeter-wave data, and are consequently included in our analysis. For the  $l \neq 0$  degenerated vibrational levels, the rotational  $l$ -type doubling is demonstrated by the off-diagonal term:

$$\frac{q}{2} (\mathbf{N}_+^2 \mathbf{L}_-^2 + \mathbf{N}_-^2 \mathbf{L}_+^2) \quad (3.3)$$

where  $q$  is the rotational  $l$ -type doubling constant, and  $L$  the vibrational orbital angular momentum.

For the  $\Pi - \Pi$  ( $l = 1$ ) type (B), (H), (J), and (O) bands, high- $J$  transition lines have been previously reported in Guelachvili et al. (1984), and the rotational analysis here is performed by combining the low- $J$  transition data in our jet-cooled spectra, and high- $J$  transition data available from Guelachvili et al. (1984), with inclusion of the centrifugal distortion term of the rotational  $l$ -type doubling:

$$\frac{q_D}{2} [\mathbf{N}^2, (\mathbf{N}_+^2 \mathbf{L}_-^2 + \mathbf{N}_-^2 \mathbf{L}_+^2)]_+ \quad (3.4)$$

It should be noted that the parameters  $q$  and  $q_D$  used here correspond to  $-q_t$ , and  $-q_{tj}$  used in Bizzocchi et al. (2010, 2011), respectively, due to a different definition of the signs in our analysis.

Table 3.3: Upper state spectroscopic parameters<sup>a</sup> (in cm<sup>-1</sup>) of the observed sixteen infrared bands of HC<sub>4</sub>H

Assignment	T <sub>v</sub>	B'	q' × 10 <sup>5</sup>	D' × 10 <sup>8</sup>	q' <sub>D</sub> × 10 <sup>10</sup>
A1 (4 <sub>0</sub> <sup>1</sup> ?; Σ <sub>g</sub> <sup>+</sup> - Σ <sub>u</sub> <sup>+</sup> )	3334.6481(2)	0.146 1121(95)		1.6 <sup>b</sup>	
A2 (4 <sub>0</sub> <sup>1</sup> ?; Σ <sub>u</sub> <sup>+</sup> - Σ <sub>g</sub> <sup>+</sup> )	3334.9403(2)	0.145 9024(77)		1.6 <sup>b</sup>	
B (4 <sub>0</sub> <sup>1</sup> 6 <sub>1</sub> <sup>1</sup> ; Π <sub>u</sub> - Π <sub>g</sub> )	3333.7562(1)	0.146 255 4(2)	-8.05(3)	1.570(4)	1.3(7)
C (4 <sub>0</sub> <sup>1</sup> ; Σ <sub>u</sub> <sup>+</sup> - Σ <sub>g</sub> <sup>+</sup> )	3333.6634(1)	0.146 192 9(4)		1.506(24)	
D (4 <sub>0</sub> <sup>1</sup> 9 <sub>1</sub> <sup>1</sup> ; Π <sub>g</sub> - Π <sub>u</sub> )	3333.0862(1)	0.146 614 9(6)	-20.56(6)	1.628(41)	4.29 <sup>b</sup>
E (4 <sub>0</sub> <sup>1</sup> 7 <sub>1</sub> <sup>1</sup> ; Π <sub>u</sub> - Π <sub>g</sub> )	3332.3632(1)	0.146 4595(23)	-12.04(23)	1.572(31)	8.6(5)
F (4 <sub>0</sub> <sup>1</sup> ?; Π <sub>g</sub> - Π <sub>u</sub> )	3332.3429(3)	0.146 6006(98)	-6(2)	1.6 <sup>b</sup>	
G (4 <sub>0</sub> <sup>1</sup> ?; Π <sub>u</sub> - Π <sub>g</sub> )	3332.975(2)	0.146 313(11)	-2.5(22)	1.6 <sup>b</sup>	
H (4 <sub>0</sub> <sup>1</sup> 8 <sub>1</sub> <sup>1</sup> ; Π <sub>g</sub> - Π <sub>u</sub> )	3331.5727(2)	0.146 2642(15)	-7.38(19)	1.6 <sup>b</sup>	
I (4 <sub>0</sub> <sup>1</sup> 7 <sub>2</sub> <sup>1</sup> ; Δ <sub>u</sub> - Δ <sub>g</sub> )	3331.0740(2)	0.146 7864(15)	-2.8(16) × 10 <sup>-3</sup>	5.31(76)	
J (1 <sub>0</sub> <sup>1</sup> 8 <sub>0</sub> <sup>1</sup> 6 <sub>1</sub> <sup>0</sup> ; Π <sub>u</sub> - Π <sub>g</sub> )	3314.8618(2)	0.146 262 2(3)	-8.58(4)	1.584(8)	1.3(14)
K (1 <sub>0</sub> <sup>1</sup> 8 <sub>0</sub> <sup>1</sup> 6 <sub>2</sub> <sup>1</sup> ; Δ <sub>u</sub> - Δ <sub>g</sub> )	3314.8528(3)	0.146 3880(14)	-0.002 <sup>b</sup>	1.6 <sup>b</sup>	
L (1 <sub>0</sub> <sup>1</sup> 8 <sub>0</sub> <sup>1</sup> 6 <sub>2</sub> <sup>1</sup> ; Σ <sub>u</sub> <sup>+</sup> - Σ <sub>g</sub> <sup>+</sup> )	3314.0531(2)	0.146 3374(42)		2.799(386)	
M (1 <sub>0</sub> <sup>1</sup> 8 <sub>0</sub> <sup>1</sup> 6 <sub>0</sub> <sup>0</sup> 7 <sub>1</sub> <sup>1</sup> ; Δ <sub>u</sub> - Δ <sub>g</sub> )	3313.4415(2)	0.146 5373(46)	-4.6(26) × 10 <sup>-3</sup>	1.6 <sup>b</sup>	
N (1 <sub>0</sub> <sup>1</sup> 8 <sub>0</sub> <sup>1</sup> 6 <sub>1</sub> <sup>1</sup> 7 <sub>1</sub> <sup>1</sup> ; Φ <sub>u</sub> - Φ <sub>g</sub> )	3313.4344(2)	0.146 5843(77)		1.6 <sup>b</sup>	
O (1 <sub>0</sub> <sup>1</sup> 6 <sub>0</sub> <sup>1</sup> 8 <sub>0</sub> <sup>0</sup> ; Π <sub>g</sub> - Π <sub>u</sub> )	3312.3136(2)	0.146 260 9(7)	-8.46(2)	1.484(32)	
P (1 <sub>0</sub> <sup>1</sup> 6 <sub>0</sub> <sup>1</sup> 8 <sub>0</sub> <sup>0</sup> 7 <sub>1</sub> <sup>1</sup> ; Δ <sub>g</sub> - Δ <sub>u</sub> )	3311.2618(1)	0.146 5414(92)	-1.64(12) × 10 <sup>-2</sup>	1.6 <sup>b</sup>	

a. Uncertainty corresponding to a standard deviation given in the parentheses.

b. Fixed in the fit.

Vibrational assignments of the nine new bands are made based on the vibration-rotation interaction constants of lower and upper states of each band. The vibration-rotation interaction constant ( $\alpha_i$ ) is given by:

$$B_v = B_e - \sum_i \alpha_i \left( v_i + \frac{d_i}{2} \right) = B_0 - \sum_i (v_i \alpha_i^{B_i}) \quad (3.5)$$

where  $i$  represents the vibrational quantum numbers,  $d_i$  is the degree of the degeneracy of the  $v_i$  mode with vibrational quantum number  $v_i$  (see Table 3.1), and  $B_e$  the equilibrium rotational constant. As higher order terms are neglected, calculations using Equation 3.5 may cause relatively large deviations, particularly for highly excited vibrational combination levels. In practice, the variant of Equation 3.5 that is used in our analysis is given by:

$$B_{(j+i)} = B_j - \alpha_i v_i \quad (3.6)$$

where  $j$  represents a well-established vibrational level,  $(i + j)$  the vibrational combination level of level  $j$  and another vibrational mode  $v_i$ . In Table 3.1, also the available values of  $\alpha_i$  for each vibrational mode of HC<sub>4</sub>H are summarized. It can be seen that the *ab initio* predicted values for  $\alpha_3$ ,  $\alpha_4$ ,  $\alpha_5$ ,  $\alpha_7$ , and  $\alpha_9$  in Simmonett et al. (2009) are in good agreement with previously reported (deperturbed) experimental values, *i.e.*, within 1%, while  $\alpha_6$  and  $\alpha_8$  show larger deviations (> 10%). Therefore, the experimental values for  $\alpha_6$  and  $\alpha_8$ , and the *ab initio* predicted values for other modes are used in the analysis of newly observed vibrational combination levels.

Spectral analyses of the nine new bands are performed as follows. The line positions in each band determined in the present work are interpreted in preliminary fits with inclusion of parameters  $T_v$ ,  $B'$  and  $B''$  only, to derive a set of tentative rotational constants. Two types of fits are employed for each band: by fitting the transition frequencies directly, and by fitting lower- and upper-state combination differences. In general, the two routines give very similar spectroscopic parameters,

except for one case in which the upper-state level is significantly perturbed. It should be noted that the combination difference fit does not result in band origin values ( $T_v$ ). The resulting rotational constants ( $B'$  and  $B''$ ) are consequently used to calculate the corresponding  $\alpha_i$  constants by Equation 3.6, which yields tentative vibrational assignments for most of the new bands. The vibrational assignments of all observed bands are summarized in Table 3.2. With the vibrational assignments done, systematic rotational analyses on all observed bands are carried out in combination with previous submillimeter-wave and infrared data (Bizzocchi et al., 2010, 2011; Guelachvili et al., 1984; McNaughton & Bruget, 1992; Arié & Johns, 1992). The details for the individual bands are discussed below. The resulting spectroscopic parameters are summarized in Tables 3.2 and 3.3.

### 3.3.2.1 The $4_0^1$ fundamental band (C)

The  $4_0^1$  fundamental band (C) at  $\sim 3333.66 \text{ cm}^{-1}$ , is the strongest band of  $\text{HC}_4\text{H}$  in this region. As mentioned above, some transition lines ( $10 < J'' < 25$ ) determined in our experiment show a small systematic shift ( $\sim 8 \times 10^{-4} \text{ cm}^{-1}$ , rms) compared to data in Guelachvili et al. (1984). Since this shift is not found in other hot bands, and is within the uncertainties of the absolute infrared frequency in both studies, no corrections are made when combining our low- $J''$  spectral data with the high- $J''$  spectral data in Guelachvili et al. (1984).

A lower-state combination difference fit of all available data results in ground-state constants of  $B_0 = 0.146\ 4123(17)$  and  $D_0 = 1.563(22) \times 10^{-8} \text{ cm}^{-1}$ . The inclusion of the sextic centrifugal distortion term does not improve this fit. The values are in good agreement with the most accurate values currently available from Bizzocchi et al. (2011), of  $B_0 = 0.146\ 411\ 184(20)$  and  $D_0 = 1.568\ 25(20) \times 10^{-8} \text{ cm}^{-1}$ . This confirms the reliability of our approach to combine our experimental data with those in Guelachvili et al. (1984). As heavy rotational perturbations for  $J' > 45$  upper-state levels have been found in the previous study (Guelachvili et al., 1984), the upper state constants listed in Table 3.3 are obtained by fixing  $B_0$  and  $D_0$  to the values in Bizzocchi et al. (2011) and fitting  $J' \leq 45$  unperturbed transitions only. The derived  $\alpha_4 = 2.183(4) \times 10^{-4} \text{ cm}^{-1}$  is very close to the *ab initio* predicted value, with a deviation (0.5%) similar as for  $\alpha_3$  and  $\alpha_9$  (Bizzocchi et al., 2011; Simmonett et al., 2009).

### 3.3.2.2 The $4_0^1 6_1^1$ (B) and $1_0^1 8_1^1 6_1^0$ (J) bands

Bands (B) and (J) have the same  $\nu_6 = 1$  ( $\Pi_g$ ) lower state, whose spectroscopic parameters have been accurately determined previously by Bizzocchi et al. (2010, 2011), and thus are fixed in the fits. All the ro-vibrational lines of both bands determined in the present work and in Guelachvili et al. (1984) can be well fitted, resulting in effective upper-state spectroscopic parameters as summarized in Table 3.3.

It is noted that the two upper vibrational levels,  $4^1 6^1$  and  $1^1 8^1$ , are of the same  $\Pi_u$  symmetry, with similar vibrational energies. It is principally possible that the two upper levels interact via Fermi resonance. However, the experimentally determined  $\alpha_{(4+6)} = 1.558(2) \times 10^{-4} \text{ cm}^{-1}$ , and  $\alpha_{(1+8)} = 1.510(3) \times 10^{-4} \text{ cm}^{-1}$ , are only 3% different from the predicted values of  $(\alpha_4 + \alpha_6)$  and  $(\alpha_1 + \alpha_8)$  in Table 3.1. This indicates that the Fermi resonance between the  $4^1 6^1$  and  $1^1 8^1$  levels should be very small and can be neglected, if it exists.

### 3.3.2.3 The $4_0^1 8_1^1$ (H) and $1_0^1 6_1^1 8_1^0$ (O) bands

The  $1_0^1 6_1^1 8_1^0$  band has been reported by Guelachvili et al. (1984), but the  $4_0^1 8_1^1$  hot band was not identified in Guelachvili et al. (1984) due to heavy spectral overlapping in the room-temperature spectrum. Among the newly observed bands in our spectrum, a relatively strong band, (H) at  $\sim 3331.57 \text{ cm}^{-1}$ , is found to have a lower state with a tentative rotational constant  $B'' \sim 0.146\ 48 \text{ cm}^{-1}$  and a  $\Pi_u$  level symmetry that both are consistent with the  $\nu_8 = 1$  level. The vibration-rotation interaction constants ( $\alpha_i$ ) calculated from both lower- and upper-state rotational constants with respect to the  $4_0^1$  band are found to be  $\sim 0.8(1) \times 10^{-4} \text{ cm}^{-1}$ , comparable to  $\alpha_8$ . Therefore, the band (H) is

assigned to the  $4_0^1 8_1^1$  hot band transition.

The two bands,  $4_0^1 8_1^1$  (H) and  $1_0^1 6_0^1 8_1^0$  (O), have the same  $\nu_8 = 1$  ( $\Pi_u$ ) lower state. The spectroscopic parameters of the  $\nu_8 = 1$  level have been accurately determined by Bizzocchi et al. (2010), and are fixed in our fit. Similar as discussed in the previous section, no significant Fermi-type rotational perturbations are found for the two upper vibrational states,  $4_1 8_1$  and  $1_1 6_1$ . The room-temperature spectrum of the  $1_0^1 6_0^1 8_1^0$  band in Guelachvili et al. (1984) shows a heavy perturbation for  $24 < J' < 37$  transition lines. Our analysis indicates that this perturbation is not due to an interaction between the  $4_1 8_1$  and  $1_1 6_1$  levels, and must be caused by other dark states lying around this vibrational energy region. Actually, when analyzing the jet-cooled spectrum of the  $4_0^1 8_1^1$  band, perturbations seem to show up for  $J' > 17$  transitions, but these spectral lines are too weak for an unambiguous identification. As such, the rotational assignments and the fit of the  $4_0^1 8_1^1$  (H) band are only made for  $J' > 17$ . For the  $1_0^1 6_0^1 8_1^0$  band, the perturbed lines with  $25 < J' < 37$  are excluded from the fit.

### 3.3.2.4 The $4_0^1 9_1^1$ (D) band

In the previous room-temperature study (Guelachvili et al., 1984), the  $4_0^1 9_1^1$  band is the strongest hot band in this region, but heavy spectral overlapping with the  $4_0^1$  fundamental band only allows for unambiguously assigning some P-branch transitions of the e component. In our jet-cooled spectra, this band is relatively weak. The reduced Doppler width and low rotational temperature, however, allow the assignment of low- $J''$  transitions of both e and f components. To obtain upper-state spectroscopic parameters, the parameters for the lower  $\nu_9 = 1$  level are fixed to values available from Bizzocchi et al. (2011), and the perturbed P( $J'' > 42$ ) lines in the room-temperature spectrum (Guelachvili et al., 1984) are not included in the fit.

### 3.3.2.5 The $4_0^1 7_1^1$ (E) band

The  $4_0^1 7_1^1$  band is the second strongest hot band in our jet-cooled spectra. Rotational analysis of this band is performed in combination with the room-temperature data from Guelachvili et al. (1984). No significant rotational perturbations are found in our analysis. The resulting spectroscopic parameters for the lower  $\nu_7 = 1$  level, both by fitting the combination differences and by fitting the regular transition frequencies, are in good agreement with the values available from McNaughton & Bruget (1992), which are the most accurate values currently so far.

### 3.3.2.6 The $4_0^1 7_2^1$ (I) band

The band (I) at  $3331.07 \text{ cm}^{-1}$ , with a profile intensity comparable to the bands  $4_0^1 6_1^1$  (B) and  $4_0^1 8_1^1$  (H), has not been reported before. Rotational progressions in P- and R-branches of this band starting from P(3) and R(2) are found, as well as a Q-branch that is stronger than in a typical  $\Pi - \Pi$  band. These traits are consistent with a  $\Delta - \Delta$  ( $l = 2$ ) type transition with characteristic rotational energy ladders in both states starting from  $J'' = 2$ , and a Q-branch intensity that is about four times stronger than in a  $\Pi - \Pi$  type band. The signs of the  $l$ -type doubling constants  $q$  obtained from the rotational analysis determine the symmetry properties of  $g$  and  $u$  for lower and upper levels, respectively. The effective values of  $\alpha$  of both lower and upper levels with respect to the  $4_0^1$  fundamental band are  $\sim 5.7(1) \times 10^{-4} \text{ cm}^{-1}$ , about two times  $\alpha_7$ . Therefore, this band is assigned to the  $4_0^1 7_2^1$  ( $\Delta_u - \Delta_g$ ) transition. The resulting lower- and upper-state spectroscopic parameters are summarized in Tables 3.2 and 3.3.

The  $4_0^1 7_2^1$  ( $\Sigma_u^+ - \Sigma_g^+$ ) component is not found in our spectra, although it is expected to be close to band (I). This may be due to the strong Fermi resonance between the  $7_2$  ( $\Sigma_g^+$ ),  $3_1$  ( $\Sigma_g^+$ ) and  $8_1 9_1$  ( $\Sigma_g^+$ ) levels (Bizzocchi et al., 2011). As will be discussed in Section 3.3, the  $8_1 9_1$  ( $\Sigma_g^+$ ) level involving an excitation of the  $\nu_9$  mode, cannot be efficiently populated in our plasma source. Therefore, this

three-state Fermi resonance system may cause the  $4_0^{172}(\Sigma_u^+ - \Sigma_g^+)$  component to be below our detection limit.

### 3.3.2.7 The $1_0^1 8_0^1 6_1^0 7_1^1$ (M) and $1_0^1 6_0^1 8_1^0 7_1^1$ (P) bands

Similar as for band (I) discussed in the previous section, the two new bands, (M) and (P) with band origins at  $\sim 3313.44$  and  $3311.26 \text{ cm}^{-1}$ , respectively, are identified as  $\Delta - \Delta$  type transitions. The rotational constants of the two bands, for both lower and upper states, are found to be about  $2.8 \times 10^{-4} \text{ cm}^{-1}$  larger than the corresponding values of the  $1_0^1 8_0^1 6_1^0$  ( $\Pi_u - \Pi_g$ ) (J) and  $1_0^1 6_0^1 8_1^0$  ( $\Pi_g - \Pi_u$ ) (O) bands. This difference is nearly the same as the vibration-rotation interaction constant  $\alpha_7$ . Therefore, the bands (M) and (P) are assigned to  $1_0^1 8_0^1 6_1^0 7_1^1$  ( $\Delta_u - \Delta_g$ ) and  $1_0^1 6_0^1 8_1^0 7_1^1$   $\Delta_g - \Delta_u$  transitions, respectively. Although the errors of the  $l$ -type doubling constants  $q$  in our fits are slightly larger, the derived signs of  $q$  are consistent with the different lower-state symmetry properties of  $6_1 7_1$  ( $\Delta_g$ ) and  $8_1 7_1$  ( $\Delta_u$ ). As the lower states of both bands have not been reported before, all spectroscopic parameters (lower- and upper-state) of both bands listed in Tables 3.2 and 3.3 are determined directly from our jet-cooled spectrum.

### 3.3.2.8 The $1_0^1 8_0^1 6_2^1$ (K and L), and $1_0^1 8_0^1 6_2^1 7_1^1$ (N) bands

Two weak bands, (K) and (N), are found very close to  $1_0^1 8_0^1 6_1^0$   $\Pi_u - \Pi_g$  (J), and  $1_0^1 8_0^1 6_1^0 7_1^1$   $\Delta_u - \Delta_g$  (M), respectively. The weak Q-branches of (K) and (N) are found to be only  $\sim 0.01 \text{ cm}^{-1}$  lower than (J) and (M), respectively. A preliminary analysis indicates that (K) and (N) are due to  $\Delta - \Delta$  and  $\Phi - \Phi$  transition types, *i.e.*, with the same increase of  $l$  by one with respect to bands (J) and (M), respectively. Most assigned rotational lines in the two bands are relatively weak, and the corresponding rotational  $l$ -type doubling constants could not be determined. The vibrational assignments of  $1_0^1 8_0^1 6_2^1$  ( $\Delta_u - \Delta_g$ ) for band (K) and  $1_0^1 8_0^1 6_2^1 7_1^1$  ( $\Phi_u - \Phi_g$ ) for band (N), are made based on the derived rotational constants and vibration-rotation interaction constants only. It should be noted that, in the  $1_0^1 8_0^1 6_2^1$  ( $\Delta_u - \Delta_g$ ) (K) band, weak local perturbations are found for  $J' < 3$  transitions, which cause a disagreement between the Q-branch peak position and the band origin derived from fitting the P- and R-branches. The lower-state parameters for band (K) in Table 3.2 are thus obtained from a combination difference fit, while the upper-state parameters in Table 3.3 are obtained with exclusion of the  $J' < 5$  perturbed lines in the fit.

In addition, a  $\Sigma - \Sigma$  type band (L) is found at  $3314.05 \text{ cm}^{-1}$ , with a corresponding lower state symmetry/parity property of  $g/+$  or  $u/-$ . The estimated vibration-rotation interaction constants from the fit indicate that an excitation of the  $\nu_7$  or  $\nu_9$  mode is not involved. As the vibration-rotation interaction constants  $\alpha_6$  and  $\alpha_8$  are very close, the present data does not allow us to determine rotational constants accurate enough to identify the corresponding vibrational assignment. The relative population in the lower state of bands (L) and (K), as will be discussed in detail below, is estimated to be  $\sim 1:2$ , which is consistent with degeneracies of  $\Sigma$  and  $\Delta$  vibrational levels. Thus, with this additional information, band (L) is assigned to the  $l = 0$  ( $\Sigma_u^+ - \Sigma_g^+$ ) component of the  $1_0^1 8_0^1 6_2^1$  transition.

### 3.3.2.9 The unassigned bands (A), (F), and (G)

Three weak bands, (A), (F) and (G), are found in the  $\nu_4$  hot band region. The estimated ( $B' - B''$ ) values of all three bands are  $\sim 2.18(4) \times 10^{-4} \text{ cm}^{-1}$ , and are nearly the same as  $\alpha_4$ , indicating that these bands are due to  $4_0^1$  associated hot band transitions. The tentative rotational assignments of the three bands are given in **supplementary material**. Band (A) at  $3334.9 \text{ cm}^{-1}$  is found to be a  $\Sigma - \Sigma$  type transition, since the  $3:1$  line intensity alternations in both P- and R-branches are clearly seen. Spectral overlap prohibits the identification of the weak P(1) and R(0) lines and the determination of lower-state symmetry/parity properties, and consequently no unambiguous rotational assignment can be made. Two different fits are tried by assuming that the lower state is  $\Sigma_g^+$  or

$\Sigma_u^+$ . Effective lower-state vibration-rotation interaction constants  $\alpha \sim 2.9 \times 10^{-4} \text{ cm}^{-1}$  for the  $\Sigma_g^+$  case and  $\sim 0.9 \times 10^{-4} \text{ cm}^{-1}$  for the  $\Sigma_u^+$  case are obtained. The positive value of  $\alpha$  indicates that the excitation of at least one stretch vibration mode is involved in the lower state, likely the  $\nu_3$  ( $\sigma_g^+$ ) mode with the lowest stretch vibrational energy. A possible assignment of the lower state of band (A) is the  $3_2$  ( $\Sigma_g^+$ ) level perturbed by other nearby  $\Sigma_g^+$  levels, or a complex vibrational combination level of  $\nu_3$  and other bending modes.

The bands (F) and (G) at  $\sim 3332.34$  and  $3332.10 \text{ cm}^{-1}$ , respectively, are heavily overlapped with other bands. The estimated rotational constants and vibration-rotation interaction constants seem to be consistent with lower-state assignments of  $7_1 6_1$  ( $\Delta_g$ ) and a  $6_2$  ( $\Delta_g$ ) for bands (F) and (G), respectively. The relative intensities of weak Q-branches and tentatively assigned R(1) and P(2) transitions in our spectrum (see **supplementary material**) indicate that both bands are likely due to  $\Pi - \Pi$  type transitions. In Tables 3.2 and 3.3, spectroscopic parameters are listed based on a tentative  $\Pi - \Pi$  type assignment in the fit.

In the analysis described above, possible perturbations caused by Fermi resonances or Coriolis couplings are not included. Previous work by Bizzocchi et al. (2011) has shown that, even for some low-lying vibrational levels in the  $900 \text{ cm}^{-1}$  region, heavy perturbations in the Fermi resonance system of  $7_2$  ( $\Sigma_g^+$ ),  $3_1$  ( $\Sigma_g^+$ ) and  $8_1 9_1$  ( $\Sigma_g^+$ ) levels are found. The vibrational bands analyzed in this work have lower and upper state vibrational energies in the  $0 - 1800$  and  $3300 - 5100 \text{ cm}^{-1}$  range, respectively, and thus Fermi-resonance or Coriolis-coupling type perturbations between occasionally nearby vibrational levels may occur. The rotational analyses presented here, and in Guelachvili et al. (1984) indicate that some of these bands exhibit significant heterogeneous perturbations by one or more perturbers. The present experimental dataset, although extensive, does not allow performing a full deperturbation analysis of these specific features at this stage. For this, more accurate measurements of these excited vibrational levels in this wavelength region are needed, as well as an extension of the present data to other IR wavelength regions.

### 3.3.3 Vibrational excitation temperatures

In the previous room-temperature spectra (Guelachvili et al., 1984), the relative band intensities of the  $4_0^1$  associated hot bands follow the order of  $4_0^1 9_1^1 > 4_0^1 9_2^2 > 4_0^1 7_1^1 > 4_0^1 6_1^1 \sim 4_0^1 8_1^1$ , which agrees well with the Boltzmann factors estimated from the corresponding lower-state vibrational energies. However, in our plasma jet-cooled spectrum these relative band intensities are rather different, and the order of the intensity of the  $4_0^1$  associated hot bands becomes:  $4_0^1 7_1^1 > 4_0^1 6_1^1 \sim 4_0^1 8_1^1 > 4_0^1 7_2^2 > 4_0^1 9_1^1$ . It should be noted that the rotational temperature of all  $\text{HC}_4\text{H}$  bands in our spectra is found to be only  $\sim 17(1) \text{ K}$ , which is substantially lower than the vibrational excitation temperature in our plasma jet source. To evaluate the non-Boltzmann populations of  $\text{HC}_4\text{H}$  in its low-lying vibrational levels in the plasma jet expansion, the relative molecular populations in the lower states of the sixteen observed bands are estimated as follows:

- (1) We assume that the transition dipole moments of all  $4_0^1$  associated hot bands are the same as for the  $4_0^1$  fundamental transition, *i.e.*, the bands (A - I) have of the same transition strength  $S(4_0^1)$ . Similarly, the bands (J - N) have a transition strength  $S(1_0^1 8_0^1 6_1^0)$ , and the bands (M) and (N) follow  $S(1_0^1 6_0^1 8_1^0)$ .
- (2) The intensities of the bands (B) and (J)  $\Pi_u - \Pi_g$  which have the same lower vibrational level, are used to estimate the  $S(4_0^1)/S(1_0^1 8_0^1 6_1^0)$  ratio as  $\sim 0.45(3)$ . Similarly, the  $S(4_0^1)/S(1_0^1 6_0^1 8_1^0)$  ratio is estimated to be  $\sim 1.27(5)$  from the bands (H) and (O).

The estimated relative lower-state populations from our spectra shown in Figure 3.1 are listed in Table 3.2, where the numbers are normalized to the ground-state population derived from the  $4_0^1$  band. It should be noted that the full spectrum shown in Figure 3.1 was measured over a period of three weeks, and some small daily fluctuations in the exact discharge conditions may affect the

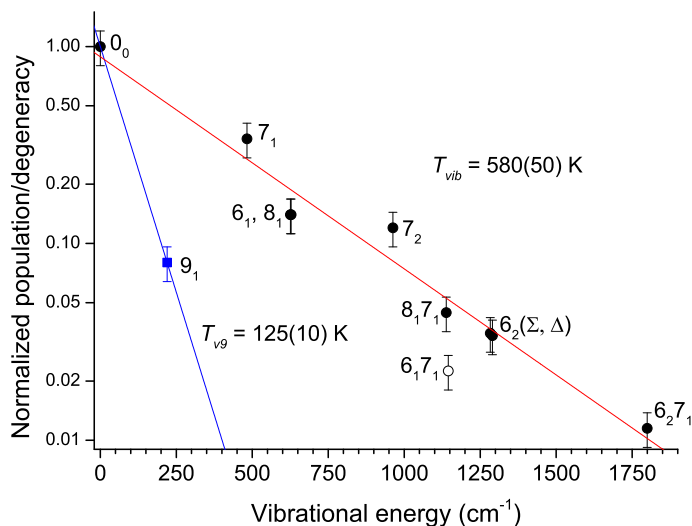


Figure 3.3: A plot of the molecular populations (normalized to the ground state, in natural logarithm scale) vs. lower-state vibrational energy of HC<sub>4</sub>H in our supersonic jet experiment. The data points for 6<sub>1</sub> and 8<sub>1</sub> levels are too close to be distinguished in the plot.

absolute spectral line intensities. Therefore, our estimate relies mainly on the overall pattern of relatively strong P(*J*) and R(*J*) lines ( $2 < J < 12$ ), which cover more than  $7 \text{ cm}^{-1}$  range in each band. The error in the population values listed in Table 3.2 is estimated to be smaller than 20%. A simulated sum spectrum of HC<sub>4</sub>H using the derived spectroscopic parameters and lower-state populations of all sixteen observed bands is shown in Figure 3.1, exhibiting a good agreement in overall spectral pattern with the experimental spectrum.

Figure 3.3 shows a plot of the normalized molecular populations (in a natural logarithm scale) vs. lower-state vibrational excitation energies. Some of the lower-state vibrational energies were not reported before, and are calculated here using the *ab initio* predicted anharmonicity constants in Simmonett et al. (2009). It is found that, in the plasma jet, the population of HC<sub>4</sub>H in the  $\nu_9 = 1$  level follows a relatively low vibrational temperature of  $\sim 125(10) \text{ K}$ , while populations in levels involving excitation of the  $\nu_6$ ,  $\nu_7$  and  $\nu_8$  vibrational modes follow a much higher vibrational temperature of  $\sim 580(50) \text{ K}$ . The population in the 6<sub>1</sub>7<sub>1</sub> level, derived from the  $1_0^1 8_0^1 6_0^0 7_1^1$  (M) band, is slightly smaller than the fitted Boltzmann distribution curve (Figure 3.3). This may be caused by possible Fermi-resonance type (homogeneous) perturbations which can significantly decrease the transition strength of the  $1_0^1 8_0^1 6_0^0 7_1^1$  band. Moreover, the relatively low vibrational temperature for the  $\nu_9$  mode is also consistent with our experimental observation that, except for the  $4_0^1 9_1^1$  band, none of the hot band transitions with lower levels involving an excitation of the  $\nu_9$  mode are observed in the plasma jet, including the  $4_0^1 9_2^2$  band which is the second strongest hot band in the room-temperature spectrum (Guelachvili et al., 1984).

The non-equilibrium vibrational excitation and relaxation of linear polyatomic molecules in a plasma jet has been discussed in Sanz et al. (2005). Although a different discharge nozzle is used in our experiment, the vibrational excitation of HC<sub>4</sub>H shows a similar behavior as that of the linear molecules discussed in Sanz et al. (2005). It is expected that, using our slit discharge nozzle and applying different discharge conditions, other non-polar molecules or radicals in their low-lying vibrational levels up to several hundred  $\text{cm}^{-1}$  can be produced. Although the hot band spectra

complicate the rotational analysis, this also provides an opportunity to derive values for the low-lying vibrational levels of non-polar species, such as polyynes ( $\text{HC}_{2n}\text{H}$ ), bare carbon chains ( $\text{C}_n$ ), and their ions, which are important constituents in the interstellar medium, but are radio-silent and cannot be observed directly via their pure rotational spectrum. These species are spectroscopically accessible via infrared-active ro-vibrational transitions in the mid/far-IR and THz region via low-lying bending modes, as has been demonstrated for astronomical detections of  $\text{HC}_4\text{H}$  and  $\text{C}_3$  (Cernicharo et al., 2001a; Evans et al., 2006; Vanorden et al., 1995; Cernicharo et al., 2000; Giesen et al., 2001).

### 3.4 CONCLUSIONS

In this work, we presented the high-resolution infrared spectra of diacetylene ( $\text{HC}_4\text{H}$ ) in the C-H stretch vibrational region of  $3306 - 3342 \text{ cm}^{-1}$ , recorded in a supersonic planar plasma jet. Detailed and systematic rotational analyses of the observed sixteen bands are performed, resulting in spectroscopic parameters for a series of vibrational levels over wide energy regions of  $0 - 1800$  and  $3300 - 5100 \text{ cm}^{-1}$ .

### 3.5 ACKNOWLEDGEMENTS

This work is financially supported by a NWO-VICI grant, NOVA, SRON and has been performed within the context of the Dutch Astrochemistry Network.

### 3.6 BIBLIOGRAPHY

- Arié, E. & Johns, J. W. C. 1992, *Journal of Molecular Spectroscopy*, 155, 195
- Bandy, R. E., Lakshminarayan, C., Frost, R. K., & Zwier, T. S. 1992, *Science*, 258, 1630
- Bandy, R. E., Lakshminarayan, C., Frost, R. K., & Zwier, T. S. 1993, *The Journal of Chemical Physics*, 98, 5362
- Bernard-Salas, J., Peeters, E., Sloan, G. C., et al. 2006, *The Astrophysical Journal Letters*, 652, L29
- Bizzocchi, L., Degli Esposti, C., & Dore, L. 2010, *Molecular Physics*, 108, 2315
- Bizzocchi, L., Tamassia, F., Degli Esposti, C., et al. 2011, *Molecular Physics*, 109, 2181
- Burgdorf, M., Orton, G., van Cleve, J., Meadows, V., & Houck, J. 2006, *Icarus*, 184, 634
- Cernicharo, J., Goicoechea, J. R., & Caux, E. 2000, *The Astrophysical Journal Letters*, 534, L199
- Cernicharo, J., Heras, A. M., Pardo, J. R., et al. 2001a, *The Astrophysical Journal Letters*, 546, L127
- Cernicharo, J., Heras, A. M., Tielens, A. G. G. M., et al. 2001b, *The Astrophysical Journal Letters*, 546, L123
- de Graauw, T., Feuchtgruber, H., Bezard, B., et al. 1997, *Astronomy & Astrophysics*, 321, L13
- Delpéch, C., Guillemin, J., Paillous, P., et al. 1994, *Spectrochimica Acta Part A: Molecular Spectroscopy*, 50, 1095
- Evans, A., Tyne, V. H., Van Loon, J. T., et al. 2006, *Monthly Notices of the Royal Astronomical Society: Letters*, 373, L75
- Fonfria, J. P., Cernicharo, J., Richter, M. J., & Lacy, J. H. 2011, *The Astrophysical Journal*, 728, 43
- Frost, R. K., Zavarin, G. S., & Zwier, T. S. 1995, *The Journal of Physical Chemistry*, 99, 9408
- Fujii, T. & Kareev, M. 2001, *Journal of Applied Physics*, 89, 2543
- Giesen, T. F., Van Orden, A. O., Cruzan, J. D., et al. 2001, *The Astrophysical Journal Letters*, 551, L181
- Gladstone, G., Allen, M., & Yung, Y. 1996, *Icarus*, 119, 1
- Glicker, S. & Okabe, H. 1987, *The Journal of Physical Chemistry*, 91, 437
- Gu, X., Guo, Y., Zhang, F., Mebel, A. M., & Kaiser, R. I. 2006, *Faraday Discussions*, 133, 245
- Guelachvili, G., Craig, A. M., & Ramsay, D. A. 1984, *Journal of Molecular Spectroscopy*, 105, 156
- Henning, T. & Salama, F. 1998, *Science*, 282, 2204
- Homann, K.-H. 1998, *Angewandte Chemie International Edition*, 37, 2434
- Israel, G., Chassefiere, E., Cabane, M., Raulin, F., & Boon, J. J. 1991, *Annales Geophysicae*, 9, 1
- Jolly, A., Fayt, A., Benilan, Y., et al. 2010, *The Astrophysical Journal*, 714, 852
- Kahanpää, J., Mattila, K., Lehtinen, K., Leinert, C., & Lemke, D. 2003, *Astronomy & Astrophysics*, 405, 999
- Kaiser, R. I. 2002, *Chemical Reviews*, 102, 1309
- Kaiser, R. I. & Mebel, A. M. 2012, *Chemical Society Reviews*, 41, 5490
- Khelifi, M., Paillous, P., Delpéch, C., et al. 1995, *Journal of Molecular Spectroscopy*, 174, 116
- Kunde, V. G., Aikin, A. C., Hanel, R. A., et al. 1981, *Nature*, 292, 686

- Kunde, V. G., Flasar, F. M., Jennings, D. E., et al. 2004, *Science*, 305, 1582
- Ma, T.-B., Hu, Y.-Z., & Wang, H. 2008, *Journal of Applied Physics*, 104, 064904
- Matsumura, K., Etoh, T., & Tanaka, T. 1981, *Journal of Molecular Spectroscopy*, 90, 106
- Matsumura, K., Kawaguchi, K., Hirota, E., & Tanaka, T. 1986, *Journal of Molecular Spectroscopy*, 118, 530
- Matsumura, K., Kawaguchi, K., McNaughton, D., & Bruget, D. N. 1993, *Journal of Molecular Spectroscopy*, 158, 489
- Matsumura, K. & Tanaka, T. 1982, *Journal of Molecular Spectroscopy*, 96, 219
- Matsumura, K. & Tanaka, T. 1986a, *Journal of Molecular Spectroscopy*, 116, 320
- Matsumura, K. & Tanaka, T. 1986b, *Journal of Molecular Spectroscopy*, 116, 334
- McNaughton, D. & Bruget, D. N. 1991, *Journal of Molecular Spectroscopy*, 150, 620
- McNaughton, D. & Bruget, D. N. 1992, *Journal of Molecular Structure*, 273, 11
- Meadows, V. S., Orton, G., Line, M., et al. 2008, *Icarus*, 197, 585
- Milani, A., Tommasini, M., Del Zoppo, M., Castiglioni, C., & Zerbi, G. 2006, *Physical Review B*, 74, 153418
- Owen, N. L., Smith, C. H., & Williams, G. A. 1987, *Journal of Molecular Structure*, 161, 33
- Richter, H. & Howard, J. 2000, *Progress in Energy and Combustion Science*, 26, 565
- Rothman, L. S., Gordon, I. E., Babikov, Y., et al. 2013, *Journal of Quantitative Spectroscopy and Radiative Transfer*, 130, 4
- Sanz, M. E., McCarthy, M. C., & Thaddeus, P. 2005, *The Journal of Chemical Physics*, 122, 194319
- Shindo, F., Benilan, Y., Guillemin, J.-C., et al. 2003, *Planetary and Space Science*, 51, 9
- Shirakawa, H. 2001, *Rev. Mod. Phys.*, 73, 713
- Simmonett, A. C., Schaefer III, H. F., & Allen, W. D. 2009, *The Journal of Chemical Physics*, 130, 044301
- Tay, R., Metha, G. F., Shanks, F., & McNaughton, D. 1995, *Structural Chemistry*, 6, 47
- Thejaswini, H. C., Majumdar, A., Tun, T. M., & Hippler, R. 2011, *Advances in Space Research*, 48, 857
- Vanorden, A., Cruzan, J. D., Provencal, R. A., et al. 1995, in *Astronomical Society of the Pacific Conference Series*, Vol. 73, *From Gas to Stars to Dust*, ed. M. R. Haas, J. A. Davidson, & E. F. Erickson
- Wakelam, V., Smith, I. W. M., Herbst, E., et al. 2010, *Space Science Reviews*, 156, 13
- Western, C. M. 2014, PGOPHER version 8.0, university of Bristol Research Data Repository
- Williams, G. A. & Macdonald, J. N. 1994, *Journal of Molecular Structure*, 320, 217
- Wilson, E. H. & Atreya, S. K. 2004, *Journal of Geophysical Research: Planets*, 109, E06002
- Zhang, C., Cao, Z., Wu, H., & Zhang, Q. 2004, *International Journal of Quantum Chemistry*, 98, 299
- Zhao, D., Guss, J., Walsh, A. J., & Linnartz, H. 2013, *Chemical Physics Letters*, 565, 132
- Zhao, X., Ando, Y., Liu, Y., Jinno, M., & Suzuki, T. 2003, *Physical Reviews Letters*, 90, 187401



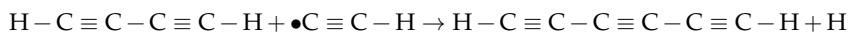
## HIGH-RESOLUTION INFRARED SPECTRUM OF THE $\nu_5$ FUNDAMENTAL AND NEARBY HOT BANDS OF TRIACETYLENE

---

New data are presented that follow from a high-resolution survey, from  $3302$  to  $3352\text{ cm}^{-1}$ , through expanding acetylene plasma, and covering the C-H asymmetric ( $\nu_5$ ) fundamental band of triacetylene ( $\text{HC}_6\text{H}$ ). Absorption signals are recorded using continuous wave cavity ring-down spectroscopy (cw-CRDS). A detailed analysis of the resulting spectra allows revisiting the molecular parameters of the  $\nu_5$  fundamental band in terms of interactions with a perturbing state, which is observed for the first time. Moreover, four fully resolved hot bands ( $5_0^1 10_1^1$ ,  $5_0^1 11_1^1$ ,  $5_0^1 13_1^1$ , and  $1_0^1 8_0^1 11_1^0$ ), with band origins at  $3328.5829(2)$ ,  $3328.9994(2)$ ,  $3328.2137(2)$  and  $3310.8104(2)\text{ cm}^{-1}$ , respectively, are reported for the first time. These involve low lying bending vibrations that have been studied previously, which guarantees unambiguous identifications. Combining available data allows to derive accurate molecular parameters, both for the ground state as well as the excited states involved in the bands.

## 4.1 INTRODUCTION

Polyynes (*i.e.*, polyacetylenes; of the generic form  $\text{HC}_{2n}\text{H}$ ) are believed to play an important role in combustion chemistry, and in a variety of different astrochemical environments (Yung et al., 1984; Homann, 1998; Cernicharo et al., 2001; Vuitton et al., 2003; Wilson & Atreya, 2003; Bernard-Salas et al., 2006; Vuitton et al., 2006; Sakai & Yamamoto, 2013). The linear, unsaturated structure of polyynes results in a class of molecules which are unstable and highly reactive. Through barrierless, polymerization reactions, *e.g.*,



small polyynes can act as intermediates to the formation of larger molecules, such as longer chain (cyano)polyynes, polycyclic aromatic hydrocarbons, and “soot” (Yung et al., 1984; Frenklach et al., 1985; Bandy et al., 1992; Cherchneff et al., 1992; Krestinin, 2000; Stahl et al., 2002; Gu et al., 2009).

Of notable interest is triacetylene ( $\text{HC}_6\text{H}$ ), which has only been observed in the protoplanetary nebulae, CRL 618 and SMP LMC 11 through the  $\nu_8+\nu_{11}$  and  $\nu_{11}$  bands (Cernicharo et al., 2001; Bernard-Salas et al., 2006), but not in the prototypical carbon rich environments of Titan, TMC-1, or the AGB star IRC+10216, where both acetylene and diacetylene, polyyne radicals ( $\text{C}_n\text{H}$ ) up to  $n = 8$ , and the anionic radical  $\text{C}_6\text{H}^-$ , have been observed (Kunde et al., 1981; Ziurys, 2006; McCarthy et al., 2006). Also, the cumulene isomer of  $\text{H}_2\text{C}_6$ , which is less stable compared to triacetylene (Sattelmeyer & Stanton, 2000), has been detected in TMC-1 (Langer et al., 1997). Given that the acetylenic isomer is energetically favored over the cumulene isomer, the low probability of isomerization between the two forms, and observation of the radical form of triacetylene ( $\text{C}_6\text{H}$ ) (Suzuki et al., 1986; Saito et al., 1987), it is expected that triacetylene will be present in other carbon rich environments as well.

One of the particular reasons for the missing detections of polyynes compared to their respective radical or cyano- form is that the polyyne molecules are difficult to observe in the infrared at the typical temperatures found in most astronomical objects, and the lack of a permanent dipole moment associated with centro-symmetric molecules means that for polyynes pure rotational transitions are forbidden, excluding radio astronomical detections. Certain vibrational modes will induce a temporary dipole moment that can be detected as ro-vibrational spectra in the mid- and far-infrared. While, the spectroscopic information of both acetylene and diacetylene has been studied in detail in laboratory studies facilitating their detection (see Zhao et al. (2014a) and Chang et al. (2016) and references therein), the spectroscopic information for triacetylene so far has remained limited. Vibrational frequencies for the fundamental bands of triacetylene, Table 4.1, have been known with a resolution of  $1\text{ cm}^{-1}$  (Bjarnov et al., 1974), but high-resolution rotational information is only known for about half of the modes:  $\nu_5$ ,  $\nu_6$ ,  $\nu_8$ ,  $\nu_{10}$ ,  $\nu_{11}$ , and  $\nu_{13}$  (McNaughton & Bruget, 1991; Matsumura et al., 1993; Haas et al., 1994a,b); it is noted that  $\nu_8$  and  $\nu_{10}$  rotational information is determined from the  $8_0^1 11_0^1$  combination band and the  $8_0^1 11_0^1 10_1^1$  and  $11_0^1 10_1^1$  hot bands, respectively (McNaughton & Bruget, 1991). We adopt here conventional vibronic notation to indicate lower/upper states of each vibrational mode in a transition. Past experiments by Matsumura et al. (1993) noted that the C-H stretch fundamental band is highly perturbed at  $J = 20$  and 50 and 54, and predicted three major hot bands  $5_0^1 13_1^1$ ,  $5_0^1 13_2^1$ , and  $5_0^1 10_1^1$  to be 60, 35, and 28% the intensity of the  $\nu_5$  fundamental at room temperature (Matsumura et al., 1993).

In this work we present an extended high-resolution infrared study of the ro-vibrational transitions of triacetylene in the C-H stretch fundamental region. We have observed the  $\nu_5$  fundamental band of triacetylene and transitions to one of its perturbing levels, three hot bands associated with the  $\nu_5$  mode that are due to doubly degenerate bending vibrational modes ( $\nu_{10}$ ,  $\nu_{11}$ , and  $\nu_{13}$ ), and one hot bands associated with the  $\nu_1$  mode, for which a complete analysis is given here.

Table 4.1: Vibrational normal modes (in  $\text{cm}^{-1}$ ) of  $\text{HC}_6\text{H}$ 

Mode	Nuclear motion	Experimental $\nu$
$\nu_1(\sigma_g^+)$	C-H sym. stretch	3313(1) (Bjarnov et al., 1974)
$\nu_2(\sigma_g^+)$	terminal $\text{C}\equiv\text{C}$ sym. stretch	2201(1) (Bjarnov et al., 1974)
$\nu_3(\sigma_g^+)$	internal $\text{C}\equiv\text{C}$ sym. stretch	2019(1) (Bjarnov et al., 1974)
$\nu_4(\sigma_g^+)$	internal C-C sym. stretch	625(1) (Bjarnov et al., 1974)
$\nu_5(\sigma_u^+)$	C-H asym. stretch	3329.0533(1) <sup>a</sup>
$\nu_6(\sigma_u^+)$	terminal $\text{C}\equiv\text{C}$ asym. stretch	2128.91637(32) (McNaughton & Bruget, 1991)
$\nu_7(\sigma_u^+)$	internal $\text{C}\equiv\text{C}$ asym. stretch	1115.0(5) (Haas et al., 1994a)
$\nu_8(\pi_g)$	$\text{C}\equiv\text{C}$ -H sym. bend	622.38(40) (Matsumura et al., 1988b)
$\nu_9(\pi_g)$	terminal $\text{C}\equiv\text{C}$ -C sym. bend	491(1) (Bjarnov et al., 1974)
$\nu_{10}(\pi_g)$	internal $\text{C}\equiv\text{C}$ -C sym. bend	258(1) (Bjarnov et al., 1974)
$\nu_{11}(\pi_u)$	$\text{C}\equiv\text{C}$ -H asym. bend	621.340111(42) (Haas et al., 1994b)
$\nu_{12}(\pi_u)$	terminal $\text{C}\equiv\text{C}$ -C asym. bend	443.5(5) (Haas et al., 1994a)
$\nu_{13}(\pi_u)$	internal $\text{C}\equiv\text{C}$ -C asym. bend	105.038616(76) (Haas et al., 1994a)

a. This work.

## 4.2 EXPERIMENTAL METHODS

The experimental setup combines pulsed supersonic planar plasma with continuous wave cavity ring-down spectroscopy (cw-CRDS), and is described in detail by Zhao et al. (2013), following Motylewski & Linnartz (1999). Given recent experiments by our group on diacetylene (Zhao et al., 2014a), which also produced triacetylene but in lower concentrations, we have been investigating different sets of experimental settings to discriminate weaker signals. It is found that the optimal conditions to produce triacetylene are by discharging a gas mixture of 0.3%  $\text{C}_2\text{H}_2$  diluted in Ar with an applied negative high voltage of  $\sim -525$  V. Each gas pulse ( $\sim 1$  ms) has a typical backing pressure of  $\sim 15$  bar, and is supersonically expanded through a  $30 \text{ mm} \times 0.3 \text{ mm}$  multi-layer slit discharge nozzle mounted to a pulsed valve (General Valve, Series 9, 2 mm orifice) into a vacuum chamber, which is kept at a few  $10^{-2}$  mbar by a roots blower pump station ( $4800 \text{ m}^3/\text{h}$ ). The discharge nozzle is aligned with the slit throat parallel to and  $\sim 3$  cm, away from the optical axis of a high finesse optical cavity. The optical cavity is formed by two highly reflective plano-concave mirrors (1 m radius of curvature, reflectivity  $\sim 99.97\%$  at  $3 \mu\text{m}$ ) mounted on precision alignment tools 56 cm apart on opposite sides of the main chamber. In order to insure the mirrors retain their high reflectivity throughout the plasma discharge,  $\text{N}_2$  is flowed in front of the reflective surface of each mirror.

The high-resolution infrared spectrum of the plasma products is recorded using cw-CRDS. The idler output of a commercial single-frequency single-mode continuous wave optical parametric oscillator (cw-OPO, Aculight, Argos 2400-SF module B), operating between  $\sim 3000 - 4000 \text{ cm}^{-1}$  with an output power of  $\leq 1.2$  W and a bandwidth of  $< 1$  MHz, is employed as the infrared light source. The infrared beam is subsequently split in order to simultaneously measure the laser frequency and perform ring-down measurements. A fraction of the light is directed to a wavelength meter (Bristol Instruments, 621A-IR, self-calibrated by a stabilized He-Ne laser), which provides relative and absolute frequency accuracies better than 6 MHz and 20 MHz, respectively. Simultaneously, the remainder of the idler is led through an acousto-optical modulator (AOM), and the first order deflection,  $\sim 5\%$  of the power, is coupled into the optical cavity. Given that the idler wavelength is continuously changed during a scan, a piezo-electric transducer with a periodic triangle applied voltage is mounted on one of the mirror holders, behind the mirror, to modulate the cavity length such that the cavity is in resonance with the infrared laser at least twice during one period. Only when the light is effectively coupled into the cavity does the light intensity trigger a

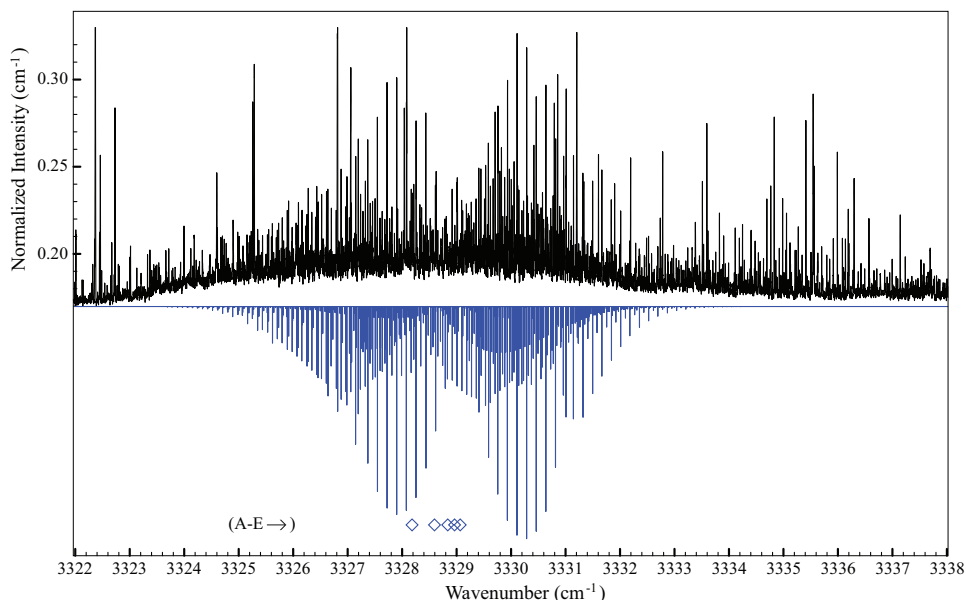


Figure 4.1: A portion of the spectrum highlighting the observed bands related to the C-H asymmetric stretch; the experimental spectrum is plotted on top in black, and the simulated spectrum of the identified triacetylene bands is plotted below in blue. The band origins are marked with empty diamonds in increasing frequency order: A)  $5_1^1 13_1^1$ , B)  $5_0^1 10_1^1$ , C) the perturber state of  $5_1^1$ , D)  $5_0^1 11_1^1$ , and E)  $5_0^1$ . The remaining absorption features are due to other molecules in the plasma, most of which are assigned to acetylene and diacetylene Zhao et al. (2014a).

hardware (Boxcar integrator) based multi-trigger timing scheme, which coincides a plasma pulse to one ring-down event and is described in detail in Zhao et al. (2013). Typical ring-down times are  $\sim 7 \mu\text{s}$ , corresponding to roughly 4000 effective passes of the infrared laser through the plasma jet. An absorption spectrum is recorded by measuring ring-down times as a function of infrared laser frequency. The absolute frequency calibration is determined to be  $\sim 0.001 \text{ cm}^{-1}$  by checking the frequencies of the recorded absorption spectrum of the precursor gas,  $\text{C}_2\text{H}_2$ , against the corresponding HITRAN values (Rothman et al., 2013).

#### 4.3 RESULTS AND DISCUSSION

The high-resolution spectrum is recorded between  $3302\text{--}3352 \text{ cm}^{-1}$  (Figure 4.1). Two particularly dense forests of lines are seen in the experimental spectrum centered at  $3314$  and  $3330 \text{ cm}^{-1}$ . Preliminary analysis based on previous work on  $\text{HC}_4\text{H}$  (Zhao et al., 2014a; Guelachvili et al., 1984), and the vibrational frequencies of  $\text{HC}_6\text{H}$  (Table 4.1), hints for assignment of the first region around  $3314 \text{ cm}^{-1}$  to the C-H symmetric stretch mode region, and the region around  $3330 \text{ cm}^{-1}$  to the C-H asymmetric stretch mode region. The experimental spectrum shows features assigned to the C-H asymmetric stretch fundamental mode of acetylene and diacetylene, and a number of hot bands of diacetylene, which have been described in detail in Zhao et al. (2014a). Additionally, based on a rotational line spacing of  $\sim 0.044 \text{ cm}^{-1}$ , six bands of triacetylene are identified in the experimental spectrum.

Effective band origins, and rotational and centrifugal distortion constants for the lower and up-

per states of each band are determined using PGOPHER software (Western, 2014), starting from a standard ro-vibrational Hamiltonian for linear molecules:

$$H = H_{\text{vib}} + \mathbf{B}\mathbf{N}^2 - \mathbf{D}\mathbf{N}^4 + \mathbf{H}\mathbf{N}^6 + \mathbf{L}\mathbf{N}^8 \quad (4.1)$$

which gives the following expression of ro-vibrational energy levels ( $v, l, J$ )

$$E(v, l, J) = G_{v,l} + B_v[J(J+1) - l^2] - D_v[J(J+1) - l^2]^2 + H_v[J(J+1) - l^2]^3 + L_v[J(J+1) - l^2]^4 \quad (4.2)$$

where  $H_{\text{vib}}$  is the vibrational Hamiltonian,  $\mathbf{N}$  is the rotational angular momentum ( $\mathbf{N} = \mathbf{J} + \mathbf{L}$ ),  $G_{v,l}$  the vibrational energy,  $B_v$  the rotational constant, and  $D_v$ ,  $H_v$  and  $L_v$  are the quartic, sextic, and octic centrifugal distortion constants, respectively, of the corresponding vibrational level. For the degenerate vibrational levels,  $l > 0$ , where  $l$  is the quantum number related to the projection of the total vibrational angular momentum on the symmetry axis, the  $l$ -type doubling constant,  $q$ , is required, and is fit by the operator (Western, 2014)

$$\frac{q}{2} (\mathbf{N}_+^{2l} \mathbf{L}_-^{2l} + \mathbf{N}_-^{2l} \mathbf{L}_+^{2l}) \quad (4.3)$$

Assignment of energy levels is based on the symmetry of the band profiles, *i.e.*  $\sigma - \sigma$ ,  $\pi - \pi$ , etc. corresponding to a linear  $D_{\infty h}$  molecule, and the rotational constant. For previously unreported states, the expected vibrational dependent rotational constant is given by the expression

$$B_v = B_e - \sum_i \alpha_i \left[ v_i + \frac{d_i}{2} \right] \quad (4.4)$$

where  $B_e$  is the equilibrium rotational constant,  $v_i$  represents the vibrational quantum number,  $\alpha_i$  is the vibration-rotation parameter, and  $d_i$  is the degree of the degeneracy of the  $i^{\text{th}}$  vibrational mode. In our analysis, the variant of Equation 4.4 that is used is given by

$$B_v = B_0 - \sum_i (v_i \alpha_i^B) \quad (4.5)$$

For known states the rotational constants and vibration-rotation parameters are taken from previous studies (McNaughton & Bruget, 1991; Matsumura et al., 1993; Haas et al., 1994a,b), while for new or unknown states the rotational constants are determined, to first order approximation, from vibration-rotation parameters estimated based on the known values of the analogous molecule, cyanodiacetylene ( $\text{HC}_5\text{N}$ ) (Degli Esposti et al., 2005). Spectral analysis of new bands is performed by fitting the observed transitions using least-squares analysis to determine tentative lower and upper state rotational constants, as well as the band origin. Based on the preliminary values, the state symmetry, and rotational constants estimated from Equation 4.5, vibrational assignments are made for both the upper and lower states.

In addition to the known  $\nu_5$  fundamental mode of triacetylene, three hot bands built on the  $\nu_5$  mode due to known doubly degenerate bending vibrational modes ( $\nu_{10}$ ,  $\nu_{11}$ , and  $\nu_{13}$ ) are assigned in the  $3330 \text{ cm}^{-1}$  region, and one hot band involving the  $\nu_1$  mode ( $1_0^1 8_0^1 11_0^0$ ) is assigned in the  $3314 \text{ cm}^{-1}$  region. All four of the newly assigned bands show relatively weak Q-branches, and no observable intensity alternation, indicating that they are parallel transitions of  $\pi - \pi$  state symmetries. The assignment and rotational constants for the lower and upper states of each of the bands are summarized in Tables 4.2 and 4.3, and the observed transitions, their rotational assignments, and deviations for each band are given in the **supplementary material**. From the rotational profiles, the rotational temperature of triacetylene is determined to be about 23 K. While from the observed excited modes, the vibrational temperature is estimated to be significantly higher at about 105 K. This difference in temperatures was also noted by both Zhao et al. (2014a) and Chang et al. (2016) for diacetylene, but it is to a much more substantial degree. Systematic rotational analyses on observed bands is then carried out in combination with previous infrared data (McNaughton & Bruget, 1991; Haas et al., 1994a,b).

Table 4.2: Lower and upper state spectroscopic parameters<sup>a</sup> (in  $\text{cm}^{-1}$ ) for the  $\nu_5$  fundamental and perturber band of  $\text{HC}_6\text{H}$ 

	Ground	Coriolis interaction <sup>b</sup>		Fermi resonance <sup>b</sup>	
		$\nu_5$	Perturber	$\nu_5$	Perturber
symmetry	$\sigma_g^+$	$\sigma_u^+$	$\pi_u$	$\sigma_u^+$	$\sigma_u^+$
Band origin		3329.0544(1)	3328.8584(2)	3329.0521(1)	3328.8435(2)
B	0.044 1735(12)	0.044 137 7(2)	0.044 3102(14)	0.044 137 7(2)	0.044 5931(32)
$q \times 10^4$			4.766(7)		
$D \times 10^8$	0.107(7)	0.137(6)	0.308(293)	0.137(7)	1.66(63)
$H \times 10^{12}$		0.020(7)		0.020(7)	
$L \times 10^{18}$		-0.523(233)		-0.505(252)	
		$\zeta = 6.86(5) \times 10^{-4}$		$W = 2.18(2) \times 10^{-2}$	

a. Uncertainty corresponding to one standard deviation given in the parentheses.

b. Simultaneous analysis of jet-cooled data and high- $J$  data from Matsumura et al. (1993) to determine constants.

#### 4.3.1 The $5_0^1$ fundamental

The strongest transitions in the experimental spectrum that are associated with triacetylene belong to the known perturbed  $\nu_5$  C-H asymmetric stretch mode, with a band origin at  $\sim 3329.05 \text{ cm}^{-1}$  (Matsumura et al., 1993), and include newly observed transitions to a perturbing state, which have a band origin at  $\sim 3328.85 \text{ cm}^{-1}$ . The  $5_0^1$  band is a parallel band of symmetry type  $\sigma_u^+ - \sigma_g^+$ , and exhibits the characteristic intensity alternation due to the 3:1 ortho ( $J = \text{even}$ ) and para ( $J = \text{odd}$ ) nuclear spin statistical weights for equivalent H atoms. However, from  $J' = 20$  to 24, the intensity deviates from that expected due to intensity borrowing by the perturber state. The room temperature spectrum of the  $\nu_5$  fundamental has been studied extensively by Matsumura et al. (1993), and is noted to have two strong perturbations, at  $J' = 20$ , and at  $J' = 50$  and 54, as well as two weaker perturbations at  $J' < 10$  and  $J' > 110$ . To date the identity or even the state symmetry of the perturbing levels has remained unclear. Here a perturbation analysis of the  $5_0^1$  band is performed using the combination of low- $J$  ( $J' \leq 39$ ) transitions observed in our jet-cooled spectrum with high- $J$  ( $39 < J' \leq 130$ ) transitions by Matsumura et al. (1993).

The ground state rotational constant is determined by lower state combination differences to be  $B_0 = 0.044 173 5(12) \text{ cm}^{-1}$ , which is in agreement with the values determined by Matsumura et al. (1988b) from the  $11_0^1$  band, and by McNaughton & Bruget (1991) from the cold bands  $5_0^1$ ,  $6_0^1$ ,  $11_0^1$ ,  $8_0^1$ ,  $11_0^1$ . It is also within three times the standard deviation of the values determined by Matsumura et al. (1993) from  $5_0^1$  without taking into account perturbations and by Haas et al. (1994a) from analysis of the  $\nu_{13} \nu = 1, 2, \text{ and } 3$  modes.

The upper state rotational constants for the  $\nu_5 \nu = 1$  state are determined by starting from the previously determined rotational constants by Matsumura et al. (1993), and including either a heterogeneous or homogeneous perturbation coupling constant in the Hamiltonian. It is noted that given the weak perturbation at  $J' < 10$ , those transitions are given half the statistical weight of the other transitions in the fit. By varying the infrared intensity of the transitions to the perturbing state in PGOPHER (Western, 2014), the simulated intensities of the transitions to the  $\nu_5$  state could reasonably reproduce the observed experimental data. For both types of perturbation, the perturbing state was determined to not belong to a dark state, and has an infrared intensity of about 0.1 compared to the  $\nu_5$  state's infrared intensity of 1. As a result of the perturbation analysis of  $\nu_5$ , extra lines which are due to transitions between the ground state and the perturbing level are identified for the first time (see **supplementary material**).

Simultaneous least-squares fitting of the transitions to the  $\nu_5$  states, the transitions to the per-

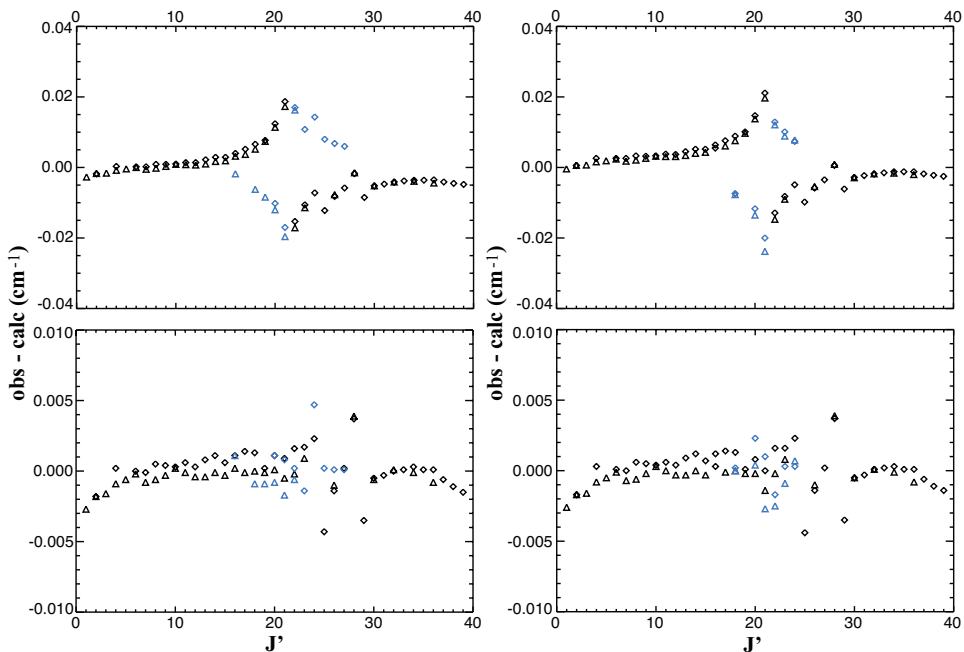


Figure 4.2: Observed perturbation in the  $\nu_5$  state at about  $J'' = 20$ . The unweighted observed-calculated (o-c) values of the  $\nu_5$  fundamental transitions are plotted in black, and the perturber state transitions are plotted in blue. Additionally, R-branch transitions are plotted with diamonds and P-branch transitions are plotted with triangles. The top panels show the o-c deviations of the transitions without Coriolis interaction taken into account (left), and of the transitions without Fermi resonance taken into account (right). The bottom panels show the o-c deviations of the transitions with Coriolis interaction taken into account (left) and of the transitions with Fermi resonance taken into account (right). Note the different scales between the top and bottom panels.

turbing state, and the coupling coefficient results in the best fit parameters, which are given in Table 4.2. The determined  $\nu_5 \nu = 1$  state rotational constants are consistent for the two types of perturbation fits, and gives a rotation-vibration parameter  $\alpha_5 \sim 3.58(6) \times 10^{-5}$ . Furthermore, in both perturbation analyses of the  $5_0^1$  band the higher order rotational terms H and L have to be included to give the best fit, particularly for high- $J''$  transitions; this suggests that the molecule is quite stretchable. From the unweighted observed-calculated (o-c) values without considering the interaction between the two upper levels, *i.e.*, the coupling constant set to zero (upper panels of Figure 4.2), we confirm that the new transitions belong to the same progression, and both bands shows clear evidence of corresponding “avoided crossing” at  $J' = 21$  due to coupling to a perturbing rotational progression. Additionally, identical shifts in both the P- and R-branches in transitions with access to the same upper state, for both bands, unambiguously identify that the interaction takes place in the vibrationally excited state.

As noted earlier, the type of interaction between the  $\nu_5$  state and the perturbing state can be either a heterogeneous, *i.e.*, a Coriolis interaction, or homogeneous perturbation, *i.e.*, a Fermi resonance, which would present spectroscopically differently. The largest perturbation seen in both the jet-cooled spectrum and the room-temperature spectrum of Matsumura et al. (1993) is rotationally “local” around  $J' = 21$ , which suggests a Coriolis interaction, a type of L-uncoupling perturbation, between the  $\nu_5$  state ( $\sigma_u^+$ ) and a  $\pi_u$  vibrational state. The band origin and rotational constant for the  $\nu_5 \nu = 1$  state are determined from least-squares analysis to be  $\nu = 3329.0544(1) \text{ cm}^{-1}$ , and

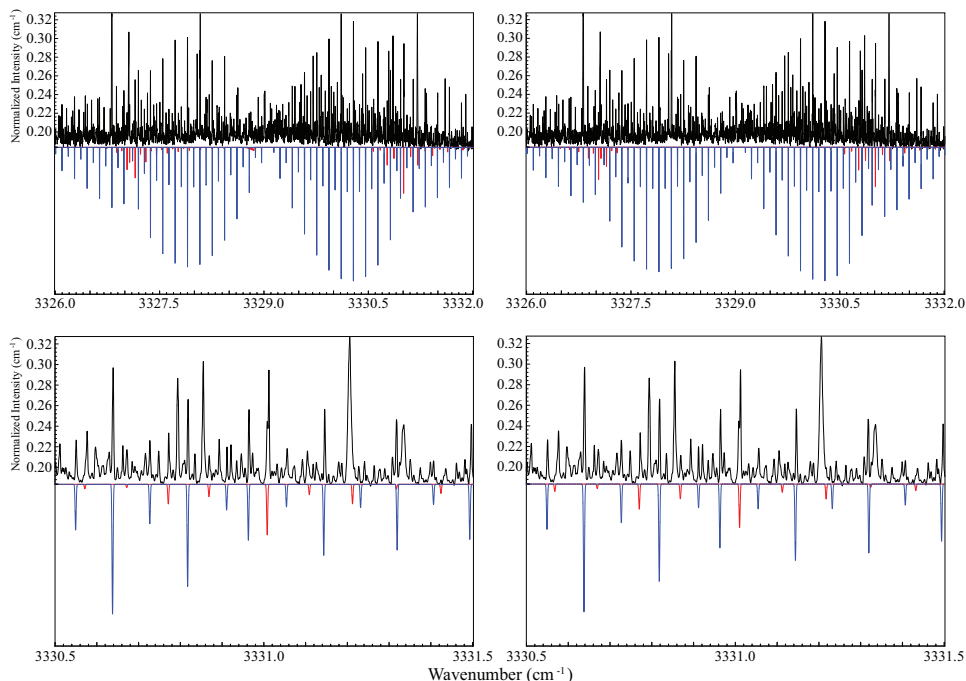


Figure 4.3: Experimental spectrum shown in black with the simulated transitions to the  $\nu_5$  state shown in blue, and the simulated transitions to the perturbing state shown in red. The top panels show the overall fit for the Coriolis interaction (left) and Fermi resonance (right), and bottom panels show a zoom in of the R-branch from R(16) - R(27) of the  $5_0^1$  band and from R(17) - R(25) of the perturber band. It is noted some of the assigned transitions are blended with transitions of other bands, such as those of  $\text{HC}_4\text{H}$ , which accounts for the discrepancies in intensity and line width, *e.g.*, R(19) and R(20) of the perturbing band.

$B' = 0.044\ 137\ 7(2)\ \text{cm}^{-1}$ , while the parameters of the perturbing level are determined to be  $\nu = 3328.8584(2)\ \text{cm}^{-1}$  and  $B' = 0.044\ 310\ 2(14)\ \text{cm}^{-1}$ . The Coriolis coupling coefficient is determined to be  $\zeta = 6.86(5) \times 10^{-4}\ \text{cm}^{-1}$ , which based on the resulting fit (left lower panel of Figure 4.3), and the residuals after the fit (lower left panel of Figure 4.2) well reproduces the intensities and positions of transitions in both bands. The defining feature of the Coriolis interaction is that the transition to the perturbing level is a perpendicular transition ( $\pi - \sigma$ ) with a Q-branch. Unfortunately, as seen in the upper left panel of Figure 4.3, the Q-branch is too weak to be discerned in the experimental spectrum.

An alternative cause of the perturbation is that it is the result of a Fermi resonance between the  $\nu_5$  state and a  $\sigma_u^+$  vibrational state that are very close in energy, and the rotational constants of the two levels are significantly different. In this case, the transition to the perturbing level is a parallel transition ( $\sigma - \sigma$ ), which has no Q-branch, as seen in the upper right panel in Figure 4.3. A Fermi resonance though, unlike the Coriolis interaction, effects the whole band to varying degrees, and could thus account for the small residual shifts seen for  $J' < 10$  and leading up to  $J' = 21$ . From least-squares analysis the  $\nu_5\ v = 1$  state band origin and rotational constant are determined to be  $\nu = 3329.0521(1)\ \text{cm}^{-1}$  and  $B' = 0.044\ 137\ 7(2)\ \text{cm}^{-1}$ , respectively. The corresponding perturbing state band origin and rotational constants are determined from the fit to be  $\nu = 3328.8435(2)\ \text{cm}^{-1}$  and  $B' = 0.044\ 593\ 1(32)\ \text{cm}^{-1}$ , both of which fit the requirements for a Fermi resonance with level crossing. The Fermi coupling coefficient is determined to be  $W = 0.021\ 8(2)\ \text{cm}^{-1}$ , and from the resulting fit (the right panels of Figure 4.3), and the residuals after the fit (the lower right panel of

Table 4.3: Lower and upper state spectroscopic parameters<sup>a</sup> (in  $\text{cm}^{-1}$ ) for the hot bands of  $\text{HC}_6\text{H}$ 

Level	Band origin	$B''$	$q'' \times 10^5$	$D'' \times 10^8$	$B'$	$q' \times 10^5$	$D' \times 10^8$
$1_0^1 8_0^1 11_1^0$ <sup>b</sup> ( $\pi_g - \pi_u$ )	3310.8104(2)	0.044 182 7	0.78	0.097 3	0.044 152 8(9)	0.83(10)	
$5_0^1 10_1^1$ ( $\pi_u - \pi_g$ )	3328.5829(2)	0.044 253 4(7)	1.62(4)	0.16(8)	0.044 221 6(9)	1.60(4)	0.67(8)
$5_0^1 11_1^1$ <sup>b</sup> ( $\pi_g - \pi_u$ )	3328.9994(2)	0.044 182 7	0.78	0.097 3	0.044 146 5(6)	0.73(9)	
$5_0^1 13_1^1$ <sup>c</sup> ( $\pi_g - \pi_u$ )	3328.2137(2)	0.044 258 8	3.82	0.096 83	0.044 226 8(7)	3.72(3)	0.48(5)

a. Uncertainty corresponding to a standard deviation given in the parentheses.

b. Lower state constants are fixed to Haas et al. (1994b).

c. Lower state constants are fixed to Haas et al. (1994a).

Figure 4.2) it is shown that a Fermi resonance offers as good a fit as the Coriolis interaction.

The residuals for the two fits are of the same order of magnitude, which means that the perturbing state is as likely to be  $\sigma$  or  $\pi$  symmetry. The uncertainty in the line positions is on average  $< 0.0015 \text{ cm}^{-1}$ , but ranges from about  $-0.005$  to  $0.005 \text{ cm}^{-1}$ , which is greater than the experimental uncertainty. This error is likely a result of two additional weak perturbing states at  $J' = 1$  and  $J' = 27$  that are not included in the fits. The positive fractional change in  $\Delta B/B$  ( $\sim +0.3\%$  and  $1\%$  for the Coriolis interaction and Fermi resonance fits, respectively) with respect to the unperturbed excited state seen for either perturbation fit suggests that the perturbed state decreases the moment of inertia for end-over-end rotation, which is consistent with a vibrational bending of the CCCCC backbone. Recently, Chang et al. (2016) found a similar type of perturbing state for diacetylene, which, while much weaker than the one seen for triacetylene, is determined to be a Coriolis interaction. As with diacetylene, the large density of states of triacetylene around  $3330 \text{ cm}^{-1}$ , and the number of unknown vibration-rotation constants hinders definitive assignment of the perturbing state (Chang et al., 2016; Matsumura et al., 1993). However, since the state density and excited hot bands are dominated by the lowest frequency modes, it is likely that the perturbing state is a combination vibrational level involving the excitation of  $\nu_{10}$  and/or  $\nu_{13}$ .

#### 4.3.2 The $5_0^1 10_1^1$ and $5_0^1 13_1^1$ bands

A series of three hot bands built on the  $\nu_5$  C-H asymmetric stretch fundamental is observed in the  $3330 \text{ cm}^{-1}$  region, all due to doubly degenerate bending vibrations (Table 4.3). The most intense of the series is assigned to the  $5_0^1 13_1^1$  hot band, which is about 50% the intensity of the  $5_0^1$  band, and has an observed Q-branch at  $3328.2137(2) \text{ cm}^{-1}$ . The upper state rotational constant is determined from least-squares analysis to be  $B' = 0.044 226 8(7) \text{ cm}^{-1}$ , which from Equation 4.5 is in agreement with a the combination state of  $5^1 13^1$ . The lower state is consequently  $\nu_{13} \nu = 1$  ( $\pi_u$ ), and has been accurately determined by Haas et al. (1994a); we fix the lower state parameters to values derived there in order to give the best fit to the line positions.

Given the similar rotational constants and vibration-rotation parameters between the  $\nu_{10}$  C $\equiv$ C-C symmetric bending mode and the  $\nu_{13}$  C $\equiv$ C-C asymmetric bending modes, it is challenging to distinguish between these two options. Fortunately, the presence of a second hot band centered at  $3328.5829(2) \text{ cm}^{-1}$  with a determined upper state  $B' = 0.044 221 6(9) \text{ cm}^{-1}$ , which is consistent with the value estimated for  $5^1 10^1$  from Equation 4.5, clarifies the assignment of the two bands. Additionally, from least-squares fitting the  $\nu_{10} \nu = 1$  ( $\pi_g$ ) lower state is found to have a rotational constant  $B'' = 0.044 253 4(7) \text{ cm}^{-1}$ , which is in agreement with the values found by McNaughton & Bruget (1991), who observed the mode as part of the  $11_0^1 10_1^1$  and  $8_0^1 11_0^1 10_1^1$  hot bands. The  $5_0^1 10_1^1$  band is a factor 2.5 weaker compared to the  $5_0^1 13_1^1$  band, with a relative intensity of about 15% that of the  $5_0^1$  band. It is noted that for both the  $5_0^1 10_1^1$  and the  $5_0^1 13_1^1$  band the o-c deviations are of

the order of or smaller than the experimental accuracy, but show a particular structure, *e.g.*, the P-branch *o-c* values being predominantly positive while the R-branch *o-c* values are negative. This identical trend seen for both bands cannot be accounted for by including higher order terms, and is likely due to an error in the frequency calibration, which is associated with small temperature fluctuations during spectral recording.

#### 4.3.3 The $5_0^1 11_1^1$ and $1_0^1 8_0^1 11_1^0$ bands

The  $5_0^1 11_1^1$  and the  $1_0^1 8_0^1 11_1^0$  bands share the  $\nu_{11} v = 1$  ( $\pi_u$ ) ground state, which has been studied by Haas et al. (1994b), and we have fixed the lower state to values derived there. A series of nine transitions, and another sixteen transitions which are blended by other lines, is tentatively assigned to the  $5_0^1 11_1^1$  band centered at  $3328.9994(2) \text{ cm}^{-1}$ . Additionally, the band is particularly weak with an intensity of about 8% relative to the  $5_0^1$  band. Given the limited number of observed transitions, the upper state rotational constant is determined by least-squares fit to be  $B' = 0.044\ 146\ 5(6) \text{ cm}^{-1}$ , which from Equation 4.5 is assigned to the  $5^1 11^1$  state.

The  $1_0^1 8_0^1 11_1^0$  ( $\pi_u - \pi_g$ ) band, centered at  $3310.8104(2) \text{ cm}^{-1}$ , is the only band not associated with the C-H asymmetric stretch mode, and is instead a combination of the  $\nu_1$  C-H symmetric stretch fundamental mode and two CCC bending modes. The band is the weakest observed band of triacetylene at about 5% the intensity of the  $\nu_5$  fundamental band. As a result of the weak intensity of the band, the line positions are confirmed by comparison of the spectrum in this work and the spectrum recorded by our group which favored diacetylene (Zhao et al., 2014a), and noting consistent changes in line intensities. In this manner, thirty unblended transitions are identified for  $1_0^1 8_0^1 11_1^0$ . Least-squares analysis determined an upper state rotational constant  $B' = 0.044\ 152\ 8(9) \text{ cm}^{-1}$ , which is consistent with the  $B_v$  value determined for the  $1^1 8^1$  state from Equation 4.5.

#### 4.4 CONCLUSIONS

The current high-resolution study of triacetylene using cw-CRDS has yielded accurate measurements of the rotational constants for  $\nu_5 v = 1$  state, taking into account the prominent perturbation, as well as the rotational constants of the perturbing state. While the perturber state of the  $5_0^1$  band still remain inconclusively identified, it has for the first time been observed and rotational constants have been determined, which suggest it is most likely a combination level of the low lying bending modes.

Four newly identified hot bands are also presented, and their rotational constants are reported. It is also found that, even under experimental conditions which favor the production of triacetylene over diacetylene, the number of observed hot bands of triacetylene is significantly less than that observed for diacetylene (Zhao et al., 2014a; Chang et al., 2016). Furthermore, while the vibrational temperature of the produced triacetylene molecules is much greater than their rotational temperature, the difference is not as extreme as that seen for diacetylene (Zhao et al., 2014a; Chang et al., 2016), which suggests that comparatively triacetylene is more efficient at vibrational cooling. The same trend in efficient cooling through intermode vibration-vibration transfer due to an increase in state density is also seen for the cyanopolynes, with cyanodiacetylene having a relatively lower vibrational temperature compared to cyanoacetylene (Sanz et al., 2005).

While the modes seen here are less likely to be observed in astronomical objects compared to the lower excitation bending mode fundamentals, due to either low temperature of the environments or overlap with modes from other polyynes, accurate knowledge of their rotational spectra confirms earlier determinations of the rotational constants. This is of particular importance in the case of  $\nu_{10}$ , which has only been observed through hot or combination bands. Additionally, we have also more conclusively determined the ground state rotational constant for triacetylene, which can be

in turn used to accurately predict the corresponding rotational constants of vibrational levels that, while not observed in the laboratory, could still be present in space, such as the  $\nu_{12}$  fundamental.

#### 4.5 ACKNOWLEDGEMENTS

This work is financially supported by the Netherlands Organization for Scientific Research (NWO) through a VICI grant, the Netherlands Research School for Astronomy (NOVA), and has been performed within the context of the Dutch Astrochemistry Network.

#### 4.6 BIBLIOGRAPHY

- Bandy, R. E., Lakshminarayan, C., Frost, R. K., & Zwier, T. S. 1992, *Science*, 258, 1630
- Bernard-Salas, J., Peeters, E., Sloan, G. C., et al. 2006, *The Astrophysical Journal Letters*, 652, L29
- Bjarnov, E., Christensen, D., Nielsen, O., et al. 1974, *Spectrochimica Acta Part A: Molecular Spectroscopy*, 30, 1255
- Cernicharo, J., Heras, A. M., Tielens, A. G. G. M., et al. 2001, *The Astrophysical Journal Letters*, 546, L123
- Chang, C.-H., Agarwal, J., Allen, W. D., & Nesbitt, D. J. 2016, *The Journal of Chemical Physics*, 144, 074301
- Cherchneff, I., Barker, J. R., & Tielens, A. G. G. M. 1992, *The Astrophysical Journal*, 401, 269
- Degli Esposti, C., Bizzocchi, L., Botschwina, P., et al. 2005, *Journal of Molecular Spectroscopy*, 230, 185
- Frenklach, M., Clary, D. W., Gardiner, W. C., & Stein, S. E. 1985, *Symposium (International) on Combustion*, 20, 887
- Gu, X., Kim, Y. S., Kaiser, R. I., et al. 2009, *Proceedings of the National Academy of Sciences*, 106, 16078
- Guelachvili, G., Craig, A. M., & Ramsay, D. A. 1984, *Journal of Molecular Spectroscopy*, 105, 156
- Haas, S., Winnewisser, G., Yamada, K. M. T., Matsumura, K., & Kawaguchi, K. 1994b, *Journal of Molecular Spectroscopy*, 167, 176
- Haas, S., Yamada, K. M. T., & Winnewisser, G. 1994a, *Journal of Molecular Spectroscopy*, 164, 445
- Homann, K.-H. 1998, *Angewandte Chemie International Edition*, 37, 2434
- Krestinin, A. V. 2000, *Combustion and Flame*, 121, 513
- Kunde, V. G., Aikin, A. C., Hanel, R. A., et al. 1981, *Nature*, 292, 686
- Langer, W. D., Velusamy, T., Kuiper, T. B. H., et al. 1997, *The Astrophysical Journal*, 480, L63
- Matsumura, K., Kanamori, H., Kawaguchi, K., Hirota, E., & Tanaka, T. 1988b, *Journal of Molecular Spectroscopy*, 131, 278
- Matsumura, K., Kawaguchi, K., Mcnaughton, D., & Bruget, D. N. 1993, *Journal of Molecular Spectroscopy*, 158, 489
- McCarthy, M. C., Gottlieb, C. A., Gupta, H., & Thaddeus, P. 2006, *The Astrophysical Journal Letters*, 652, L141
- McNaughton, D. & Bruget, D. N. 1991, *Journal of Molecular Spectroscopy*, 150, 620
- Motylewski, T. & Linnartz, H. 1999, *Review of Scientific Instruments*, 70, 1305
- Rothman, L. S., Gordon, I. E., Babikov, Y., et al. 2013, *Journal of Quantitative Spectroscopy and Radiative Transfer*, 130, 4
- Saito, S., Kawaguchi, K., Suzuki, H., et al. 1987, *Publications of the Astronomical Society of Japan*, 39, 193
- Sakai, N. & Yamamoto, S. 2013, *Chemical Reviews*, 113, 8981
- Sanz, M. E., McCarthy, M. C., & Thaddeus, P. 2005, *The Journal of Chemical Physics*, 122, 194319
- Sattelmeyer, K. W. & Stanton, J. F. 2000, *Journal of the American Chemical Society*, 122, 8220
- Stahl, F., Schleyer, P. v. R., Schaefer III, H. F., & Kaiser, R. I. 2002, *Planetary and Space Science*, 50, 685
- Suzuki, H., Ohishi, M., Kaifu, N., Ishikawa, S. I., & Kasuga, T. 1986, *Publications of the Astronomical Society of Japan*, 38, 911
- Vuitton, V., Doussin, J.-F., Bénilan, Y., Raulin, F., & Gazeau, M.-C. 2006, *Icarus*, 185, 287
- Vuitton, V., Gée, C., Raulin, F., et al. 2003, *Planetary Space Science*, 51, 847
- Western, C. M. 2014, PGOPHER version 8.0, university of Bristol Research Data Repository
- Wilson, E. H. & Atreya, S. K. 2003, *Planetary and Space Science*, 51, 1017
- Yung, Y. L., Allen, M., & Pinto, J. P. 1984, *The Astrophysical Journal Supplement*, 55, 465
- Zhao, D., Doney, K. D., & Linnartz, H. 2014a, *Journal of Molecular Spectroscopy*, 296, 1
- Zhao, D., Guss, J., Walsh, A. J., & Linnartz, H. 2013, *Chemical Physics Letters*, 565, 132
- Ziurys, L. M. 2006, *Proceedings of the National Academy of Sciences*, 103, 12274



## HIGH-RESOLUTION INFRARED SPECTRUM OF THE $\nu_3+\nu_5$ COMBINATION BAND OF PROPYNE

---

We present the first detection of the high-resolution ro-vibrational spectrum of the  $\nu_3+\nu_5$  combination band of propyne around  $3070\text{ cm}^{-1}$ . The fully resolved spectrum is recorded for supersonically jet-cooled propyne using continuous wave cavity ring-down spectroscopy (cw-CRDS). The assignments are supported with the help of accurate *ab initio* vibration-rotation interaction constants ( $\alpha_i$ ) and anharmonic frequencies. A detailed analysis of the rotationally cold spectrum is given.

## 5.1 INTRODUCTION

Propyne, also known as methylacetylene ( $\text{CH}_3\text{C}\equiv\text{CH}$ ), is a small unsaturated hydrocarbon of astro-physical importance. It is believed to play a role in the chemistry of a number of hydrocarbon-rich astronomical objects, including the atmosphere of Titan (Maguire et al., 1981), the dark cloud TMC-1 (Irvine et al., 1981), the circumstellar shell of the AGB star IRC +10216 (Agúndez, M. et al., 2008), and two protoplanetary nebulae CRL 618 (Cernicharo et al., 2001a) and SMP LMC 11 (Malek et al., 2012), where it has been observed in the infrared (IR) through the  $\nu_9$  ( $\text{H-C}\equiv\text{C}$  bending) mode, and by radio astronomy through pure rotational transitions. In addition, the close spacing of the rotational transitions of different  $K'$  subbands, and the relatively low dipole moment ( $\mu = 0.78$  D) (Burrell et al., 1980) make propyne an ideal probe of the interstellar medium's kinetic temperature; since the excitation temperature increases as  $K'$  increases (Solomon et al., 1973; Włodarczak et al., 1988; Müller et al., 2000).

From a pure spectroscopic point of view this molecule is also interesting. As a prolate symmetric top the aliphatic ( $\text{CH}_3$ ) and acetylenic (C-H) stretches are suitably decoupled from each other that the strong acetylenic C-H stretch mode ( $\nu_1$ ) is not strongly perturbed (Kerstel et al., 1994). Studies of spectra that are perturbed through weak near-resonant couplings to background vibrational states, as seen in other transitions of propyne, make it of interest for studying intramolecular vibrational relaxation (IVR) (Go & Perry, 1992; Go et al., 1993; Gambogi et al., 1993; Kerstel et al., 1994; McIlroy et al., 1994; Gambogi et al., 1994; Campargue et al., 1999; Chen et al., 2000). Moreover, comparison between high-resolution measurements as presented here for propyne and *ab initio* methods offers a good test of the accuracy of the Hamiltonians used to describe the involved molecular energy levels.

Propyne has been extensively studied in the electronic ground state ( $\tilde{X}^1A_1$ ) through a number of microwave and IR experimental studies and *ab initio* calculations (El Idrissi et al. (2001), and references therein). In fact, all of the fundamental bands and a substantial number of combination bands involving either  $\nu_3$  ( $\text{C}\equiv\text{C}$  stretch) or  $\nu_5$  (C-C stretch) excitations have been studied at high-resolution (Henfrey & Thrush, 1985, 1987; McIlroy & Nesbitt, 1989; Graner & Wagner, 1990; Pekkala et al., 1991; Kerstel et al., 1994; McIlroy et al., 1994; Campargue et al., 1999, 2000; Müller et al., 2000; El Idrissi et al., 2001; Pracna et al., 2009; Zhao & Linnartz, 2014b). The spectroscopic identification of the  $\nu_3+\nu_5$  combination band has not yet been reported. Based on the published band origins for  $\nu_3$  (Henfrey & Thrush, 1987) and  $\nu_5$  (Pracna et al., 2009), the  $\nu_3+\nu_5$  combination band is expected at  $\sim 3068$   $\text{cm}^{-1}$ . The results of a survey around this wavelength are presented here.

## 5.2 METHODS

### 5.2.1 Experimental

The experimental setup is described in detail in Zhao et al. (2013), and has recently been used to measure the  $\nu_3+\nu_8$  combination band, involving the  $\text{CH}_3$  rocking mode of jet-cooled propyne around  $3175$   $\text{cm}^{-1}$  (Zhao & Linnartz, 2014b). The main difference with the present experiment is that a different single-mode continuous-wave optical parametric oscillator (cw-OPO) had to be used; the Aculight, Argos 2400-SF-C module that covers  $3.2 - 3.9$   $\mu\text{m}$  is used, instead of the B module, which covers  $2.5 - 3.2$   $\mu\text{m}$ .

A gas mixture of 0.05% propyne in 1:1 argon:helium is used as the precursor gas. The gas is then supersonically expanded with a 4 bar backing pressure through a long ( $0.3 \times 30$  mm) slit nozzle connected to a pulsed valve (General valve, serial 9) into a vacuum chamber with a stagnation pressure of  $\sim 1.5 \times 10^{-2}$  mbar, realized by a large roots blower system with a total pumping capacity of  $4800$   $\text{m}^3/\text{hr}$ . The valve runs at 10 Hz, and the typical gas pulse has a duration of about 800  $\mu\text{s}$ . The pulsed gas flow is used to create a high pressure jet expansion, increasing the local number density of propyne molecules at the nozzle slit.

The absorption spectrum is recorded using cw-CRDS, with the IR laser path intersecting the expansion roughly 1 cm downstream from the nozzle body. The optical cavity is comprised of two highly reflective plano-concave mirrors ( $R \sim 99.98\%$ , centered at  $3300 \text{ cm}^{-1}$ ). Typical empty cavity ring-down times ( $\tau_0$ ) are about  $9 \mu\text{s}$ . The hardware (boxcar integrator) based multi-trigger and timing scheme described in detail in Zhao et al. (2013) is used to coincide the laser light and gas pulse. This guarantees that the trigger scheme compensates for the low duty cycle when combining a cw laser with a pulsed gas expansion. For this experiment the optical cavity length is modulated at  $\sim 26 \text{ Hz}$ , using a piezo crystal mounted on the back of one of the cavity mirrors.

The resulting spectrum is recorded in a series of  $\sim 1.2 \text{ cm}^{-1}$  parts that partially overlap to guarantee that spectra can be directly compared. While the spectrum is recorded, the laser frequency is simultaneously measured using a wavelength meter (Bristol Instruments, 621A-IR). The frequency accuracy is independently calibrated by measuring known transitions of ethylene ( $\text{C}_2\text{H}_4$ ) (Rothman et al., 2013). The resulting maximum frequency uncertainty of  $\pm 0.002 \text{ cm}^{-1}$  is dictated by the wavemeter.

### 5.2.2 Theoretical

Equilibrium geometry and second-order vibrational perturbation theory (VPT2) calculations are carried out at the CCSD(T) level of theory. The core-valence correlation-consistent quadruple- $\zeta$  basis set (cc-pCVQZ) (Woon & Dunning Jr., 1995) is used to determine the equilibrium geometry and rotational constants, since it has been shown to give highly accurate geometries for acetylenic molecules (Simmonett et al., 2009; Thorwirth et al., 2008). The atomic natural orbital (ANO) basis set with the truncation  $[4s3p2d1f]$  for non-hydrogen atoms and  $[4s2p1d]$  for hydrogen (hereafter known as ANO1) (Almlöf & Taylor, 1987) is used to determine the anharmonic vibrational frequencies and electronic ground state spectroscopic constants of propyne. It has been shown to reproduce experimental frequencies better than the correlation-consistent basis sets (Martin et al., 1998; Thorwirth et al., 2008). All calculations are performed with the development version of the CFOUR program (CFOUR, 2017).

## 5.3 RESULTS AND DISCUSSION

An overview of the experimental spectrum is shown in the upper trace of Figure 5.1(a). It shows a regular pattern with excellent signal-to-noise spreading over  $15 \text{ cm}^{-1}$ . A parallel band consistent with a  $\text{C}_{3v}$  symmetric top molecule  $A_1 - A_1$  transition is clearly seen with a Q-branch at  $\sim 3070.1 \text{ cm}^{-1}$ , very close to the predicted  $\nu_3 + \nu_5$  frequency of  $3068 \text{ cm}^{-1}$ . The experimental spectrum is analyzed using the PGOPTHER software (Western, 2014), assuming a rotational temperature of 18 K and a Gaussian linewidth of  $0.004 \text{ cm}^{-1}$ . The latter is determined by minimal residual Doppler broadening in the slit nozzle expansion. A first fit of the strongest transitions gives lower state rotational constants in good agreement with those already known for propyne. For a more accurate rotational analysis the lower state constants are fixed to the ground state parameters reported by Pracna et al. (2009). The rotational constants for the upper state are calculated by the standard relation for a prolate symmetric top molecule:

$$E(v_i, l, J, K) = E(v_i) + 2A\zeta lK + (A - B)K^2 + BJ(J + 1) - D_J J^2 (J + 1)^2 - D_{JK} J(J + 1)K^2 - D_K K^4 \quad (5.1)$$

where  $D_J$ ,  $D_{JK}$ , and  $D_K$  are the centrifugal distortion constants,  $\zeta$  is the Coriolis coupling constant (in this case  $\zeta = 0$ ),  $l$  is the quantum number related to the projection of the total vibrational angular momentum on the symmetry axis, and  $A$  and  $B$  are the rotational constants, which can be given as:

$$A_v = A_0 - \sum_i (v_i \alpha_i^A) \quad (5.2)$$

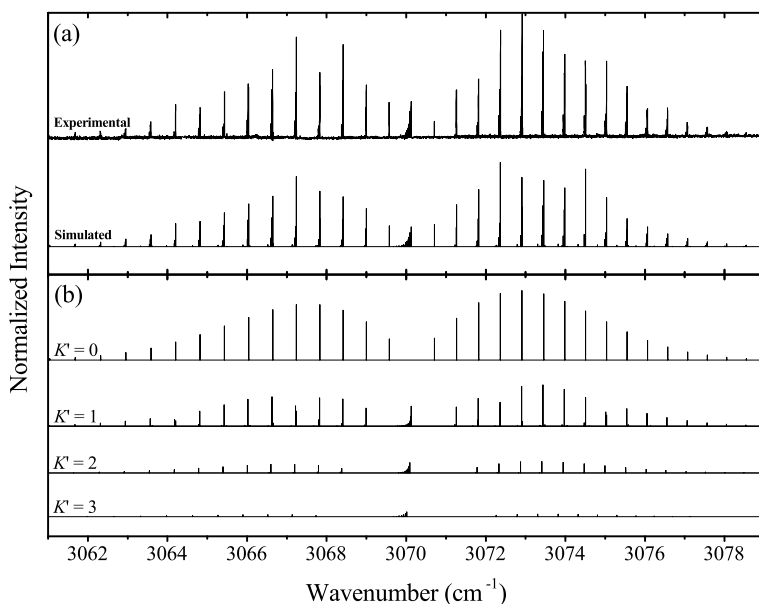


Figure 5.1: (a) The experimental spectrum from 3059.5 - 3080.5 cm<sup>-1</sup> (upper trace), and simulated spectrum (lower trace) of the  $\nu_3+\nu_5$  combination band comprising of different  $K'$  subbands. (b) Simulations of the  $K' = 0, 1, 2,$  and  $3$  subbands (including transitions to perturbing states). A rotational temperature of 18 K is used in the simulated spectra.

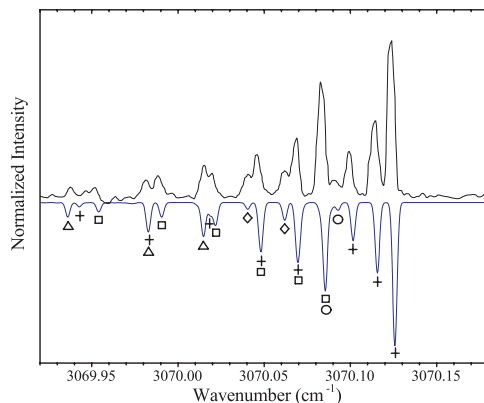


Figure 5.2: A zoom-in of the Q-branch region of the experimental (upper trace) and sum simulated (lower trace) spectrum. Transitions of the  $\nu_3+\nu_5$  subbands are labelled:  $K' = 1$  with crosses,  $K' = 2$  with squares, and  $K' = 3$  with triangles, and the perturber bands (designated P<sub>n</sub>) are labelled:  $K' = 1$  P<sub>1</sub> with circles and  $K' = 2$  P<sub>1</sub> with diamonds; some of the transitions are blended. The transitions are fit using a Gaussian linewidth of 0.004 cm<sup>-1</sup>.

$$B_v = B_0 - \sum_i (v_i \alpha_i^B) \quad (5.3)$$

where  $\alpha_i$  is the vibration-rotation interaction constant.

The rotational analysis starts from a least-squares fit, which gives excited state parameters that reproduce the overall pattern with reasonable accuracy. However, many of the  $K' = 1$  and 2 transitions show large deviations between the observed and calculated frequencies, suggestive of perturbations. As such, the  $K'$  subbands were fit separately, based on the method described by Zhao & Linnartz (2014b); this is shown in Figure 5.1b. The resulting effective spectroscopic parameters, and the parameters of the  $\nu_3$  (Henfrey & Thrush, 1987) and  $\nu_5$  (Pracna et al., 2009) states are summarized in Table 5.1. From a least-squares fit of the  $K' = 0$  subband the band origin is determined to be  $3070.1411(4) \text{ cm}^{-1}$  (which we fix for the  $K' > 0$  subbands), and  $B' = 0.282\ 428(8) \text{ cm}^{-1}$ . In addition to transitions to the main state, transitions to three perturbing states are identified in the experimental spectrum, and the spectroscopic parameters of those bands are summarized in Table 5.2. The observed - calculated deviations of all the assigned transitions are listed in the **supplementary material**. The summed spectrum of all the individual simulated subbands, including transitions to perturbing states, is given in the lower trace of (a) in Figure 5.1, and a zoom-in of the Q-branch is given in Figure 5.2. This shows that the measured and simulated spectra are in excellent agreement. As in the jet-cooled propyne study described previously by Zhao & Linnartz (2014b), only one rotational temperature of  $18 \pm 2 \text{ K}$ , and a 1:1 E:(A<sub>1</sub>,A<sub>2</sub>) statistical weights is needed to reproduce the overall observed intensity pattern.

The  $3000 \text{ cm}^{-1}$  region of the propyne spectrum is expected to have a high density of states,

Table 5.1: Spectroscopic parameters<sup>a</sup> (in  $\text{cm}^{-1}$ ) of the vibrational levels of the  $\nu_3 + \nu_5$  combination band

	Ground state <sup>b</sup>		$\nu_3 + \nu_5$			
	(Pracna et al., 2009)	$K = 0$	$K = 1$	$K = 2$	$K = 3$	
E	0.0	3070.1411(4)	3070.1411 <sup>b</sup>	3070.1411 <sup>b</sup>	3070.1411 <sup>b</sup>	
A	5.308 312 9		5.293 07(40)	5.294 17(12)	5.294 91(10)	
$\alpha_1^A \times 10^3$						
B	0.285 059 768 3	0.282 428(8)	0.282 432(9)	0.282 508(17)	0.282 323(223)	
$\alpha_1^B \times 10^3$						
$D_J \times 10^7$	0.980 422	0.857(350)	0.769(371)	5.99(96)	$3.99(41) \times 10^2$	
$D_{JK} \times 10^5$	0.545 095 8					
$D_K \times 10^5$	9.701 5					
$H_J \times 10^{15}$	-2.227					
$H_{JK} \times 10^{11}$	3.050 3					
$H_{KJ} \times 10^{10}$	1.769 1					
$H_K \times 10^8$	0.0					
$L_{JJK} \times 10^{15}$	-0.210 5					
$L_{JK} \times 10^{15}$	-1.451					
$L_{KKJ} \times 10^{15}$	-13.55					

a. Numbers in parenthesis are one standard deviation in units of the last significant digit.

b. Fixed values.

many of which originate from high-order combination states. As such, the assignment of the experimental data is supported by *ab initio* calculations. The CCSD(T)/ANO1 VPT2 calculations of propyne are able to predict the anharmonic frequencies and intensities of fundamental and combination states; this applies even to states with ten or more quanta of excitation. However, states

Table 5.2: Effective spectroscopic parameters<sup>a</sup> (in  $\text{cm}^{-1}$ ) of the perturbing states

	$K' = 1$		$K' = 2$
	P <sub>1</sub>	P <sub>2</sub>	P <sub>3</sub>
Symmetry	A <sub>1</sub>	A <sub>1</sub>	A <sub>1</sub>
E	3070.0682(7)	3069.9488(6)	3070.1082(8)
A	5.33530(126)	5.33310(592)	5.299 31(42)
B	0.284 210(56)	0.284 160(75)	0.281 290(279)
Perturbation coefficient	0.007(1)	0.011(1)	0.009(1)

a. Numbers in parenthesis are one standard deviation in units of the last significant digit.

Table 5.3: Harmonic and anharmonic (VPT2) frequencies<sup>a</sup> (in  $\text{cm}^{-1}$ ) of  $\text{C}_3\text{H}_4$ 

Mode	Nuclear motion	CCSD(T)/ANO1		Experimental
		Harmonic frequency, $\omega$	VPT2 anharmonic frequency, <sup>a</sup> $\nu$	Fundamental frequency, $\nu$
$\nu_1(A_1)$	C-H stretch	3471.5	3338.0(46.6)	3335.065 90 (Kerstel et al., 1994)
$\nu_2(A_1)$	C-H <sub>3</sub> sym. stretch	3050.3	2938.8(9.5)	2940.999 6 (McIlroy & Nesbitt, 1989)
$\nu_3(A_1)$	C $\equiv$ C stretch	2180.2	2138.0(3.1)	2137.87 (Henfrey & Thrush, 1987)
$\nu_4(A_1)$	C-H <sub>3</sub> umbrella motion	1414.3	1382.7(0.0)	1385.03 (Henfrey & Thrush, 1985)
$\nu_5(A_1)$	C-C stretch	935.3	924.2(0.5)	930.276 530 (Pracna et al., 2009)
$\nu_6(E)$	C-H <sub>3</sub> asym. stretch	3126.4	2976.8(7.3)	2980.860 2 (McIlroy & Nesbitt, 1989)
$\nu_7(E)$	C-H <sub>3</sub> scissoring	1486.6	1449.4(7.7)	1450.271 (Henfrey & Thrush, 1985)
$\nu_8(E)$	C-H <sub>3</sub> rocking	1057.0	1034.3(0.1)	1036.147 539 (Pracna et al., 2009)
$\nu_9(E)$	H-C $\equiv$ C bending	642.8	635.5(45.6)	638.569 14 (Pekkala et al., 1991)
$\nu_{10}(E)$	C-C $\equiv$ C bending	325.3	327.8(7.6)	330.938 56 (Graner & Wagner, 1990)
$\nu_5 + \nu_{10}(E)$		1260.6	1254.9(0.02)	1262.75 (Henfrey & Thrush, 1985)
$\nu_5 + \nu_9(E)$		1578.1	1558.3(0.002)	1566.18 (Henfrey & Thrush, 1985)
$\nu_5 + \nu_8(E)$		1992.4	1956.3(0.002)	1989.7 (Henfrey & Thrush, 1987)
$\nu_5 + \nu_8 + 3\nu_{10}(A_1 + A_2)$		2968.2	2940.0(0.0)	2940.833 (McIlroy & Nesbitt, 1989)
$\nu_3 + \nu_5(A_1)$		3115.6	3060.1(0.14)	3070.1411 <sup>b</sup>
$\nu_3 + \nu_8(E)$		3237.3	3170.5(0.05)	3176.0774 (Zhao & Linnartz, 2014b)
$\nu_3 + \nu_6(E)$		5306.6	5114.3(0.01)	5122.0 (El Idrissi et al., 2001)
$\nu_1 + \nu_3(A_1)$		5651.7	5468.7(0.007)	5465.0 (Campargue et al., 2000)
$\nu_1 + \nu_3 + \nu_5(A_1)$		6587.0	6390.9(0.0)	6398.05 (Campargue et al., 1999)
$2\nu_1(A_1)$		6942.9	6567.2(1.2)	6568.172 (McIlroy et al., 1994)
$2\nu_1 + \nu_5(A_1)$		7878.3	7491.5(0.0)	7500.6 (El Idrissi et al., 2001)
$2\nu_1 + \nu_3(A_1)$		9123.2	8690.6(0.0)	8691.3 (El Idrissi et al., 2001)
ZPE = 12003.1				

a. Intensities in  $\text{km}/\text{mol}$  are given in parenthesis.

b. This work.

involving three or less quanta of excitation are believed to be the most accurate, since many states at that level can be compared to experimentally determined band origins (El Idrissi et al., 2001). As shown in Table 5.3, our VPT2 calculations are able to reproduce the experimental frequencies of both fundamental and combination bands to within  $10 \text{ cm}^{-1}$ . This suggests that the predicted anharmonic frequencies for new transitions are equally accurate. Within  $\sim 100 \text{ cm}^{-1}$  of  $3070 \text{ cm}^{-1}$  the calculations predict only three states with appreciable IR intensity:  $\nu_6$  at  $2976.8 \text{ cm}^{-1}$ , and

$\nu_3+\nu_8$  at  $3170.5\text{ cm}^{-1}$ , which are both E states, and  $\nu_3+\nu_5$  at  $3060.1\text{ cm}^{-1}$ , which is an  $A_1$  state (Table 5.3). The calculated anharmonic frequency for  $\nu_3+\nu_5$  at  $3060.1\text{ cm}^{-1}$  has an o-c difference of  $10.04\text{ cm}^{-1}$  relative to our experimentally determined band origin, which is consistent with that expected for the accuracy of our calculations. In addition, both the calculated and experimental values agree well with the frequency predicted based on the experimental frequencies of the  $\nu_3$  and  $\nu_5$  fundamental bands (Table 5.1), strongly supporting the assignment of the new experimental band as the  $\nu_3+\nu_5$  combination band of propyne.

Furthermore, the CCSD(T)/ANO1 calculations result in vibration-rotation interaction constants (Table 5.4) that are in much better agreement with experimentally derived values compared to

Table 5.4: CCSD(T)/ANO1 vibration-rotation interaction constants<sup>a</sup> (in  $\text{cm}^{-1}$ ) of  $\text{C}_3\text{H}_4$

Mode	$\alpha_1^A \times 10^3$	$\alpha_1^B \times 10^3$
$\nu_1$	0.035(0.41) (Kerstel et al., 1994)	0.646(0.665) (McIlroy & Nesbitt, 1989)
$\nu_2$	55.44(38) (Thomas & Thompson, 1968)	0.077(0.084) (McIlroy & Nesbitt, 1989)
$\nu_3$	2.570(6.6) (Henfrey & Thrush, 1987)	1.476(1.510) (McIlroy & Nesbitt, 1989)
$\nu_4$	-27.42	1.665(0.40) (McIlroy & Nesbitt, 1989)
$\nu_5$	6.012(7.572) (Burrell et al., 1980)	1.285(1.260) (McIlroy & Nesbitt, 1989)
$\nu_6$	35.87(17) (Anttila et al., 1972)	0.064(0.026) (McIlroy & Nesbitt, 1989)
$\nu_7$	39.68(42.89) (Henfrey & Thrush, 1985)	-0.887(-0.26) (McIlroy & Nesbitt, 1989)
$\nu_8$	-29.49(-61.8) (Henfrey & Thrush, 1987)	0.196(0.141) (McIlroy & Nesbitt, 1989)
$\nu_9$	0.652(1.353) (Pekkala, 1990)	-0.187(-0.18) (McIlroy & Nesbitt, 1989)
$\nu_{10}$	1.293(2.170) (Graner & Wagner, 1990)	-0.821(-0.78) (McIlroy & Nesbitt, 1989)

a. Experimental values are given in parenthesis.

previous calculations, particularly  $\alpha_1^A$  (Kerstel et al., 1994). From Equations 5.2 and 5.3, the  $\nu_3+\nu_5$  rotational constants based on our calculated  $\alpha_i$  (Table 5.4) are  $A = 5.2997\text{ cm}^{-1}$  and  $B = 0.28500\text{ cm}^{-1}$ , and based on the experimental  $\alpha_i$  (Table 5.1) we find  $A = 5.2944\text{ cm}^{-1}$  and  $B = 0.28506\text{ cm}^{-1}$ . Both predicted  $B_{(3+5)}$  values differ by less than 1% from our experimental  $B^1$ , providing additional support for the assignment of the  $\nu_3+\nu_5$  combination band to the experimentally observed band shown in Figure 5.1.

For the fit, 31 transitions are assigned to the  $\nu_3+\nu_5$  state  $K' = 0$  subband, while only 3 transitions are assigned to the  $K' = 3$  subband. The fitting of the  $K' = 0$  and 3 subbands (both  $A_1 - A_2$  type transitions) do not show signs of perturbations. However, in the present data set we cannot exclude perturbations in the  $K' = 3$  subband, since only a limited number and only Q-branch transitions are observed. We also cannot exclude any perturbations at high- $J'/K'$  in any of the subbands. Conversely though, 34 transitions are assigned to the  $K' = 1$  subband of the  $\nu_3+\nu_5$  state, and 26 transitions are assigned to the  $K' = 2$  subband. The  $K' = 1$  and 2 subbands (both E - E type transitions) require the inclusion of perturbing states in the fit in order to accurately reproduce the observed line positions.

The perturbing states all have the same  $A_1$  symmetry, and we assume that all of the perturbations are homogeneous perturbations that to our best approximation are independent of any quantum numbers. Two perturbing states are required to accurately reproduce the experimental line positions of the  $\nu_3+\nu_5$  state  $K' = 1$  subband. One ( $P_1$ ) with a perturbation coefficient of  $0.007(1)\text{ cm}^{-1}$  has 8 observed transitions, including a noticeable Q-branch, and it affects the  $J' \leq 5$  transitions. While the second ( $P_2$ ) only has 4 observed transitions, with no observed Q-branch transitions, but it has a larger perturbation coefficient of  $0.011(1)\text{ cm}^{-1}$  and strongly affects  $J' = 9$ . Finally, while only 2 transitions are observed to the  $P_3$  states, the interaction has a perturbation coefficient of  $0.009(1)\text{ cm}^{-1}$ , and significantly influences the  $J' \leq 7$  transitions, particularly the Q-branch, of the  $\nu_3+\nu_5$   $K' = 2$  subband. Unfortunately, at this time we cannot conclusively identify the perturbing

states. However, with the inclusion of the perturbing states the least-square fit analysis gives an effective  $A = 5.293\ 07(40)$ ,  $5.294\ 17(12)$ , and  $5.294\ 91(10)\ \text{cm}^{-1}$ , for the three  $K'$  subbands respectively, which all differ by less than 0.1% from the predicted  $A_{(3+5)}$  values.

The present data set can be compared with the results presented by Zhao & Linnartz (2014b). The VPT2 calculations predict the intensity of the  $\nu_3+\nu_5$  combination band to be about  $3\times$  the intensity of the  $\nu_3+\nu_8$  combination band. A comparison of the  $\nu_3+\nu_5$  data presented here and the  $\nu_3+\nu_8$  data published earlier by Zhao & Linnartz (2014b) - all recorded for similar expansion conditions and corrected for small changes in the ring-down time - results in a factor  $2.8\times$  difference in the intensity. This provides a further argument supporting the assignment made here.

#### 5.4 CONCLUSION

The current high-resolution study of jet-cooled propyne using cw-CRDS has yielded the first fully resolved observation of the  $\nu_3+\nu_5$  state. As also found in the recent work on  $\nu_3+\nu_8$ , our analysis indicates that near-resonant or non-resonant perturbations are involved in the  $\nu_3+\nu_5$  spectrum. The experimental data are fully consistent with high level *ab initio* calculations, presented here, for the anharmonic frequencies. These calculations also give ground state spectroscopic constants accurate enough to aid in the assignment of ro-vibrational spectra of propyne.

#### 5.5 ACKNOWLEDGEMENTS

K.D.D. would like to thank Dr. J.F. Stanton for helpful discussions on performing the *ab initio* calculations. The authors acknowledge financial support by the Netherlands Organization for Scientific Research (NWO) through a VICI grant, and the Netherlands Research School for Astronomy (NOVA). This work has been performed within the context of the Dutch Astrochemistry Network, another NWO initiative. D.Z. acknowledges financial support from the National Key R&D Program of China and the Fundamental Research Funds for the Central Universities of China.

#### 5.6 BIBLIOGRAPHY

- Agúndez, M., Fonfría, J. P., Cernicharo, J., Pardo, J. R., & Guélin, M. 2008, *Astronomy & Astrophysics*, 479, 493
- Almlöf, J. & Taylor, P. R. 1987, *The Journal of Chemical Physics*, 86, 4070
- Anttila, R., Jaakkonen, S., & Sahlstböm, T. 1972, *Spectrochimica Acta Part A: Molecular Spectroscopy*, 28, 1615
- Burrell, P. M., Bjarnov, E., & Schwendeman, R. H. 1980, *Journal of Molecular Spectroscopy*, 82, 193
- Campargue, A., Bertseva, E., Graner, G., & Herman, M. 2000, *Journal of Molecular Spectroscopy*, 201, 156
- Campargue, A., Biennier, L., Garnache, A., et al. 1999, *The Journal of Chemical Physics*, 111, 7888
- Cernicharo, J., Heras, A. M., Pardo, J. R., et al. 2001a, *The Astrophysical Journal Letters*, 546, L127
- CFOUR. 2017, Coupled-Cluster techniques for Computational Chemistry, a quantum-chemical program package by J.F. Stanton, J. Gauss, M.E. Harding, P.G. Szalay with contributions from A.A. Auer, R.J. Bartlett, U. Benedikt, C. Berger, D.E. Bernholdt, Y.J. Bomble, L. Cheng, O. Christiansen, F. Engel, R. Faber, M. Heckert, O. Heun, C. Huber, T.-C. Jagau, D. Jonsson, J. Jusélius, K. Klein, W.J. Lauderdale, F. Lipparini, D.A. Matthews, T. Metzroth, L.A. Mück, D.P. O'Neill, D.R. Price, E. Prochnow, C. Puzzarini, K. Ruud, F. Schiffmann, W. Schwalbach, C. Simmons, S. Stopkowicz, A. Tajti, J. Vázquez, F. Wang, J.D. Watts and the integral packages MOLECULE (J. Almlöf and P.R. Taylor), PROPS (P.R. Taylor), ABACUS (T. Helgaker, H.J. Aa. Jensen, P. Jørgensen, and J. Olsen), and ECP routines by A. V. Mitin and C. van Wüllen. For the current version, see <http://www.cfour.de>.
- Chen, X., Ganot, Y., Bar, I., & Rosenwaks, S. 2000, *The Journal of Chemical Physics*, 113, 5134
- El Idrissi, M. I., Livin, J., Herman, M., Campargue, A., & Graner, G. 2001, *Chemical Physics*, 265, 273
- Gambogi, J. E., Kerstel, E. R. T., Lehmann, K. K., & Scoles, G. 1994, *The Journal of Chemical Physics*, 100, 2612
- Gambogi, J. E., Timmermans, J. H., Lehmann, K. K., & Scoles, G. 1993, *The Journal of Chemical Physics*, 99, 9314
- Go, J., Cronin, T. J., & Perry, D. S. 1993, *Chemical Physics*, 175, 127
- Go, J. & Perry, D. S. 1992, *The Journal of Chemical Physics*, 97, 6994
- Graner, G. & Wagner, G. 1990, *Journal of Molecular Spectroscopy*, 144, 389
- Henfrey, N. F. & Thrush, B. A. 1985, *Journal of Molecular Spectroscopy*, 113, 626
- Henfrey, N. F. & Thrush, B. A. 1987, *Journal of Molecular Spectroscopy*, 121, 150

- Irvine, W. M., Hoglund, B., Friberg, P., Askne, J., & Ellder, J. 1981, *The Astrophysical Journal Letters*, 248, L113
- Kerstel, E. R. T., Lehmann, K. K., Pate, B. H., & Scoles, G. 1994, *The Journal of Chemical Physics*, 100, 2588
- Maguire, W. C., Hanel, R. A., Jennings, D. E., Kunde, V. G., & Samuelson, R. E. 1981, *Nature*, 292, 683
- Malek, S. E., Cami, J., & Bernard-Salas, J. 2012, *The Astrophysical Journal*, 744, 16
- Martin, J. M. L., Lee, T. J., & Taylor, P. R. 1998, *The Journal of Chemical Physics*, 108, 676
- McIlroy, A. & Nesbitt, D. J. 1989, *The Journal of Chemical Physics*, 91, 104
- McIlroy, A., Nesbitt, D. J., Kerstel, E. R. T., et al. 1994, *The Journal of Chemical Physics*, 100, 2596
- Müller, H. S. P., Thorwirth, S., Bizzocchi, L., & Winnewisser, G. 2000, *Zeitschrift Naturforschung Teil A*, 55
- Pekkala, K. 1990, *Journal of Molecular Spectroscopy*, 144, 416
- Pekkala, K., Graner, G., Wlodarczak, G., Demaison, J., & Koput, J. 1991, *Journal of Molecular Spectroscopy*, 149, 214
- Pracna, P., Müller, H. S. P., Urban, S., Horneman, V. M., & Klee, S. 2009, *Journal of Molecular Spectroscopy*, 256, 152
- Rothman, L., Gordon, I., Babikov, Y., et al. 2013, *Journal of Quantitative Spectroscopy and Radiative Transfer*, 130, 4
- Simmonett, A. C., Schaefer III, H. F., & Allen, W. D. 2009, *The Journal of Chemical Physics*, 130, 044301
- Solomon, P. M., Penzias, A. A., Jefferts, K. B., & Wilson, R. W. 1973, *The Astrophysical Journal Letters*, 185, L63
- Thomas, R. & Thompson, H. 1968, *Spectrochimica Acta Part A: Molecular Spectroscopy*, 24, 1337
- Thorwirth, S., Harding, M. E., Muders, D., & Gauss, J. 2008, *Journal of Molecular Spectroscopy*, 251, 220
- Western, C. M. 2014, PGOPHER version 8.0, university of Bristol Research Data Repository
- Wlodarczak, G., Bocquet, R., Bauer, A., & Demaison, J. 1988, *Journal of Molecular Spectroscopy*, 129, 371
- Woon, D. E. & Dunning Jr., T. H. 1995, *The Journal of Chemical Physics*, 103, 4572
- Zhao, D., Guss, J., Walsh, A. J., & Linnartz, H. 2013, *Chemical Physics Letters*, 565, 132
- Zhao, D. & Linnartz, H. 2014b, *Chemical Physics Letters*, 595-596, 256



HIGH-RESOLUTION INFRARED SPECTRA OF THE  $\nu_1$  FUNDAMENTAL BANDS OF MONO-SUBSTITUTED  $^{13}\text{C}$  PROPYNE ISOTOPOLOGUES

---

We present a combined experimental and *ab initio* study on the jet-cooled high-resolution infrared spectra of the  $\nu_1$  (acetylenic stretch) fundamental band for three isotopologues of propyne:  $^{13}\text{CH}_3^{12}\text{C}\equiv^{12}\text{CH}$ ,  $^{12}\text{CH}_3^{13}\text{C}\equiv^{12}\text{CH}$ , and  $^{12}\text{CH}_3^{12}\text{C}\equiv^{13}\text{CH}$ . The experimental spectra are recorded in natural abundance using a continuous supersonic expansion of regular propyne diluted in argon and helium, in combination with continuous wave cavity ring-down spectroscopy (cw-CRDS). The fully rotationally resolved  $K' = 0$  and  $1$  subbands of all three mono-substituted  $^{13}\text{C}$  isotopologues have been measured near  $3330\text{ cm}^{-1}$ , and their spectroscopic analysis is presented here for the first time. The assignment of the bands and perturbation analysis are assisted by high level *ab initio* calculations at the CCSD(T) level of theory, from which vibrational frequencies, rotational constants, and Fermi resonances are predicted for each isotopologue.

## 6.1 INTRODUCTION

Propyne, also known as methylacetylene ( $\text{CH}_3\text{C}\equiv\text{CH}$ ), is a small unsaturated hydrocarbon of importance for studying intramolecular vibrational relaxation (IVR) (Go & Perry, 1992; Go et al., 1993; Gambogi et al., 1993; Kerstel et al., 1994; McIlroy et al., 1994; Gambogi et al., 1994; Campargue et al., 1999; Chen et al., 2000), and chemical evolution in the interstellar medium (ISM), planetary atmospheres, and circumstellar shells of evolved stars (Maguire et al., 1981; Irvine et al., 1981; Cernicharo et al., 2001a; Agúndez, M. et al., 2008; Malek et al., 2012). In particular, propyne is an ideal probe of the interstellar medium's kinetic temperature, since with increasing  $K'$  the subbands have increasing excitation temperatures (Müller et al., 2000). Furthermore, the relatively low dipole moment ( $\mu = 0.78$  D Burrell et al. (1980)) suggests propyne is easily thermalized, relative to more polar molecules, and the narrow spacing between  $K'$  subbands of a given rotational transition, allows for simultaneous observation of multiple  $K$ -transitions (Müller et al., 2000). In addition, the presence of an acetylenic C-H stretch, which with only one quanta of excitation falls into the range of high state density, makes propyne an ideal benchmark molecule to study non- and near-resonant perturbations (Campargue et al., 1999).

The normal isotopologue of propyne ( $^{12}\text{CH}_3^{12}\text{C}^{12}\text{CH}$ ; hereafter referred to as I0) has been extensively studied spectroscopically in its electronic ground state ( $\tilde{X}^1A_1$ ; Doney et al. (2017), and references therein). It is known that many of the vibrational modes of I0 are perturbed (Henfrey & Thrush, 1987; Kerstel et al., 1994; McIlroy et al., 1994; Campargue et al., 1999; Pracna et al., 2009). Furthermore, non- or near-resonant anharmonic interactions play an important role in the IVR that is seen in propyne. The study of such perturbations provides insight into the nature of the IVR process. For example, the acetylenic stretch fundamental of the normal isotopologue does not exhibit any effects due to IVR, while its overtone modes do (Campargue et al., 1999). However, the  $1\nu_1$  acetylenic stretch fundamental is involved in a long range Fermi resonance with the dark state  $\nu_3+2\nu_9$  (Duncan et al., 1976; Kerstel et al., 1994), as well as, a second "double crossing" type anharmonic perturbation (Kerstel et al., 1994). The Fermi resonance affects the observed band origin frequency and overall intensity, while the "double crossing" type perturbation affects the  $K'$ -subband origin order, and consequently can be quantified by the difference of the vibrationally excited and ground state  $A$  rotational constants ( $\Delta A$ ).

The mono-substituted  $^{13}\text{C}$  isotopologues are significantly less spectroscopically studied compared to the normal isotopologue. There exist only two high-resolution studies for all three isotopologues ( $^{13}\text{CH}_3^{12}\text{C}^{12}\text{CH}$ ,  $^{12}\text{CH}_3^{13}\text{C}^{12}\text{CH}$ , and  $^{12}\text{CH}_3^{12}\text{C}^{13}\text{CH}$ , hereafter referred to as I1, I2, and I3, respectively). One is the microwave measurement of the vibrational ground state constants ( $\tilde{X}^1A_1$ ;  $B_0$ ,  $D_0$ , and  $H_0$  (Dubrulle et al., 1978)), and the other a mid-infrared (MIR) study of the  $\nu_2$  fundamental (at  $\sim 2940$   $\text{cm}^{-1}$  (McIlroy & Nesbitt, 1989)). Other vibrational modes of mono-substituted  $^{13}\text{C}$  propyne have been measured at lower resolution; including all ten of the fundamental vibrational modes of I1, the  $\nu_3$  and  $\nu_9$  fundamentals of I2 and I3, two combination bands of I1, and the  $2\nu_9$  overtone band of I1 - I3 (Duncan et al., 1976). In a study by Duncan et al. (1976), the Fermi resonance between  $\nu_1$  and  $\nu_3+2\nu_9$  was reported for I1 and I2, and was inferred to occur for I3. However, observation of the "double crossing" perturbation requires high-resolution spectroscopic measurements to resolve the  $K$ -subband origin spacing.

In this contribution, we present a combined study on the *ab initio* calculations and experimental measurement of the three mono-substituted  $^{13}\text{C}$  propyne isotopologues. The analysis of high-resolution experimental spectra of the  $\nu_1$  fundamental bands of all three isotopologues around  $3330$   $\text{cm}^{-1}$  is supported by anharmonic calculations of the vibrational frequencies and vibration-rotation interaction constants. Anharmonic perturbations are dependent on the energy of the involved transitions, which is affected by the location of the  $^{13}\text{C}$  in the molecule; the present study allows us to investigate the extent to which the three mono-substituted  $^{13}\text{C}$  isotopologues exhibit similar perturbations as I0, such as those for the  $\nu_1$  fundamental.

## 6.2 METHODS

The experimental setup is described in detail in Zhao et al. (2013), and only details relevant to the current experiment are described here. A gas mixture of 0.5% propyne in 1:1 argon:helium is used as the precursor gas, which contains a natural abundance (~1.1%) of the mono-substituted  $^{13}\text{C}$  isotopologues of propyne. Assuming similar intrinsic intensities between the different isotopologues, this comes with an expected reduction in S/N of about a factor 100 with respect to I0. The gas is supersonically expanded with about 0.5 bar backing pressure through a long ( $0.05 \times 32$  mm) slit nozzle into a vacuum chamber with a stagnation pressure of  $0.1 \times 10^{-2}$  mbar. The collimation along a well defined absorption pathway, in combination with an effective adiabatic cooling, increases the detection sensitivity while simplifying the spectral complexity. For these conditions rotational temperatures of the order of 10 - 20 K are typically obtained, and are uniform along the laser beam axis due to the planar jet expansion.

The absorption spectrum is recorded using cw-CRDS, with the IR laser path intersecting the expansion roughly 1 cm downstream from the nozzle slit throat. The optical cavity is comprised of two highly reflective plano-concave mirrors (R~99.98%, centered at  $3300\text{ cm}^{-1}$ ). Typical empty cavity ring-down times ( $\tau_0$ ) are about 7  $\mu\text{s}$ . For this experiment the optical cavity length (about 56 cm) is modulated over at least two free spectral ranges (FSRs) at ~26 Hz, using a piezo crystal stack mounted on the back of one of the cavity mirrors, to achieve resonance with the laser wavelength. The resulting spectrum is recorded in a series of  $\sim 1.2\text{ cm}^{-1}$  parts that partially overlap to guarantee that spectra are merged correctly. The observed noise level is  $\sim 5 \times 10^{-7}\text{ cm}^{-1}$  in the present experimental conditions. While the spectrum is recorded, the laser frequency is simultaneously measured using a wavelength meter (Bristol Instruments, 621A-IR). The frequency accuracy is independently calibrated by measuring known transitions of water ( $\text{H}_2\text{O}$ ) (Rothman et al., 2013). The resulting maximum frequency uncertainty of  $\pm 0.002\text{ cm}^{-1}$  is dictated by the wavemeter.

All *ab initio* calculations are carried out at the CCSD(T) level of theory. The same method has recently been used to study I0, and has been described in detail in Doney et al. (2017); only relevant details will be described here. Equilibrium geometries are determined using the large core-valence correlation-consistent quadruple- $\zeta$  basis set (cc-pCVQZ; (Woon & Dunning Jr., 1995; Feller, 1996; Schuchardt et al., 2007)). While the vibrational frequencies and spectroscopic parameters are determined using the atomic natural orbital (ANO) basis set (with the primitive basis set (13s8p6d4f2g) for non-hydrogen atoms and (8s6p4d2f) for hydrogen) with the truncation [453p2d1f] for non-hydrogen atoms and [4s2p1d] for hydrogen (hereafter known as ANO1; (Almlöf & Taylor, 1987; Feller, 1996; Schuchardt et al., 2007)). Furthermore, only the valence electrons are considered in the correlation treatment, *i.e.*, standard frozen-core (fc) calculations. At the (fc)-CCSD(T)/ANO1 optimized geometry, second-order vibrational perturbation (VPT2) theory calculations are determined from full cubic and the semidiagonal part of the quartic force fields obtained by numerical differentiation of analytic CCSD(T) second derivatives (Gauss & Stanton, 1997; Matthews et al., 2007). All calculations are performed with the development version of the CFOUR program (CFOUR, 2017).

## 6.3 RESULTS AND DISCUSSION

## 6.3.1 Calculation results

Since spectroscopic information for mono-substituted  $^{13}\text{C}$  propyne is limited, accurate theoretical vibrational frequencies and vibration-rotation interactions constants are needed to aid in assignment of new ro-vibrational bands. The CCSD(T)/ANO1 harmonic and anharmonic (VPT2) vibrational frequencies are given in Table 6.1. For modes for which high-resolution data have been reported ( $\nu_1 - \nu_{10}$  of I0 and  $\nu_1 - \nu_2$  of I1 - I3), the predicted frequencies are all within about  $6\text{ cm}^{-1}$  of the experimental values, and for modes with only low-resolution data, the observed - calculated deviations (o-c) is much larger - on average about  $20\text{ cm}^{-1}$ . Based on our previous study of I0, the

Table 6.1: Harmonic and anharmonic (VPT2) frequencies<sup>a</sup> (in  $\text{cm}^{-1}$ ) of propyne with corresponding intensities (in  $\text{km}/\text{mol}$ ) given in parenthesis

Mode	<sup>13</sup> CH <sub>3</sub> <sup>12</sup> C <sup>12</sup> CH (I1)		<sup>12</sup> CH <sub>3</sub> <sup>13</sup> C <sup>12</sup> CH (I2)		<sup>12</sup> CH <sub>3</sub> <sup>12</sup> C <sup>13</sup> CH (I3)	
	$\omega$	$\nu$	$\omega$	$\nu$	$\omega$	$\nu$
$\nu_1(A_1)$	3471.5	3337.2(46.1) 3334.9720 <sup>b</sup>	3470.2	3333.0(34.3) 3325.0133 <sup>b</sup>	3454.3	3321.1(44.3) 3318.6667 <sup>b</sup>
$\nu_2(A_1)$	3047.0	2934.1(9.7) 2936.7668 (McIlroy & Nesbitt, 1989)	3050.3	2938.5(9.6) 2940.7414 (McIlroy & Nesbitt, 1989)	3050.3	2938.7(9.6) 2940.9564 (McIlroy & Nesbitt, 1989)
$\nu_3(A_1)$	2178.9	2136.7(3.1) 2143.37 (Duncan et al., 1976)	2129.3	2092.0(4.2) 2190.72 (Duncan et al., 1976)	2154.8	2113.3(3.1) 2166.74 (Duncan et al., 1976)
$\nu_4(A_1)$	1403.8	1372.8(0.0) 1400.6 (Duncan et al., 1976)	1414.3	1382.2(0.0)	1414.2	1382.6(0.0)
$\nu_5(A_1)$	918.1	907.7(0.6) 946.58 (Duncan et al., 1976)	931.8	920.3(0.6)	925.1	914.6(0.6)
$\nu_6(E)$	3115.2	2967.0(7.2) 2990.5 (Duncan et al., 1976)	3126.4	2976.4(7.2)	3126.4	2976.6(7.2)
$\nu_7(E)$	1485.0	1447.8(7.8) 1452.42 (Duncan et al., 1976)	1486.3	1448.8(7.8)	1486.6	1449.4(7.8)
$\nu_8(E)$	1048.6	1026.1(0.2) 1044.21 (Duncan et al., 1976)	1053.2	1030.6(0.1)	1057.0	1034.3(0.1)
$\nu_9(E)$	642.8	635.4(45.5) 638.65 (Duncan et al., 1976)	642.4	635.2(45.8)	638.4	631.3(45.4)
$\nu_{10}(E)$	324.9	327.5(7.6) 329.5 (Duncan et al., 1976)	317.8	320.5(7.2)	323.4	326.0(7.4)

a. Experimental values are given below in italics.

b. This work.

expected uncertainties for the calculated vibrational frequencies is  $\pm 10 \text{ cm}^{-1}$  (Doney et al., 2017).

For all four isotopologues, the VPT2 calculations predict the  $\nu_1$  state lying at a lower energy relative to the  $\nu_3+2\nu_9$  state. With the exception of I2, this is consistent with the previous assignments by Duncan et al. (1976). We note that, for the CCSD(T)/ANO1 VPT2 calculations of the isotopologue <sup>12</sup>CH<sub>3</sub><sup>13</sup>C<sup>13</sup>CH (hereafter referred to as I4; see **supplementary material**), the  $\nu_3+2\nu_9$  state is predicted at a lower energy relative to the  $\nu_1$  state, with  $\nu_1$  at  $3322.7 \text{ cm}^{-1}$  ( $o-c = -1.6 \text{ cm}^{-1}$ ) and  $\nu_3+2\nu_9$  at  $3305.5 \text{ cm}^{-1}$  ( $o-c = -11.5 \text{ cm}^{-1}$ ) (Duncan et al., 1976).

Fermi resonances between  $\nu_1$ ,  $\nu_3+2\nu_9$ , and  $\nu_7+3\nu_9$  (the latter two of which are dark states) have to be addressed in order to accurately reproduce the observed experimental frequencies (see **supplementary material**). For I0, I1, and I3, the interaction with  $\nu_7+3\nu_9$  is negligible, and only the  $\nu_1$  and  $\nu_3+2\nu_9$  interaction affects the band origins and intensities. In particular, for I0 and I1, the predicted Fermi coupling constant is  $\sim 6.0 \text{ cm}^{-1}$ , which is comparable to that determined by Duncan et al. (1976), and gives the  $\nu_3+2\nu_9$  combination band about 1% the intensity of the  $\nu_1$  fundamental

band. This shifts  $\nu_1$  from the pure anharmonic frequency at  $3338.0 \text{ cm}^{-1}$ , to  $3337.3 \text{ cm}^{-1}$  for I0 and  $3337.2 \text{ cm}^{-1}$  for I1. The band origins accounting for the coupling are about  $-2 \text{ cm}^{-1}$  off from the experimental values (Duncan et al., 1976). Similarly, the Fermi resonance shifts the respective  $\nu_3+2\nu_9$  combination bands from  $3390.5$  to  $3391.2 \text{ cm}^{-1}$  for I0, and from  $3389.1$  to  $3389.9 \text{ cm}^{-1}$  for I1. The combination bands are both observed by Duncan et al. (1976) with Q-branches at  $3381.15$  and  $3379.8 \text{ cm}^{-1}$ , for I0 and I1, respectively, and the resulting o-c of  $-10 \text{ cm}^{-1}$  is within the accuracy of our calculations. For I3, the Fermi resonance is predicted to be only slightly stronger than for I0 or I1. The coupling constant is  $\sim 5.4 \text{ cm}^{-1}$ , which gives the  $\nu_3+2\nu_9$  combination band about 2% the intensity of the  $\nu_1$  fundamental band, and shifts the  $\nu_1$  fundamental from  $3322.0$  to  $3321.1 \text{ cm}^{-1}$  and the  $\nu_3+2\nu_9$  combination band from  $3357.0$  to  $3358.3 \text{ cm}^{-1}$ .

Due to the close band origins, the Fermi resonance between  $\nu_1$  and  $\nu_3+2\nu_9$  in I2 is predicted to be the strongest amongst the three mono-substituted  $^{13}\text{C}$  propyne isotopologues. In addition, unlike for the other three isotopologues, the second Fermi resonance between  $\nu_3+2\nu_9$  and  $\nu_7+3\nu_9$  also influences the  $\nu_3+2\nu_9$  band origin and intensity. The predicted coupling constant is  $\sim 5.9 \text{ cm}^{-1}$  between  $\nu_1$  and  $\nu_3+2\nu_9$ , while the Fermi resonance between  $\nu_3+2\nu_9$  and  $\nu_7+3\nu_9$  is weaker. The predicted coupling constant for the latter is only  $\sim 1.4 \text{ cm}^{-1}$ . These interactions shift the predicted frequencies of  $\nu_1$ ,  $\nu_3+2\nu_9$ , and  $\nu_7+3\nu_9$  from their pure anharmonic values at  $3336.6$ ,  $3346.8$ , and  $3343.5 \text{ cm}^{-1}$  to  $3333.0$ ,  $3345.7$ , and  $3348.3 \text{ cm}^{-1}$ , respectively. Moreover, the anharmonic interactions result in the two dark states borrowing intensity from  $\nu_1$  such that the intensity of  $\nu_3+2\nu_9$  and  $\nu_7+3\nu_9$  is about 30% and 10%, respectively, that of the fundamental. Consequently, the intrinsic intensity of the  $\nu_1$  fundamental of I2 is expected to be about 75% that of the  $\nu_1$  fundamental of either I1 or I3.

In addition to the anharmonic frequencies, we have also computed the VPT2 vibration-rotation interaction constants,  $\alpha_i$ , and the results are given in Table 6.2. For all  $\alpha_i^B$  the predicted value shows a good agreement with the experimental value, as will be discussed in the next section. From previous studies, the calculated  $\alpha^B$  are sufficiently accurate to estimate the rotational constant,  $B_v$ , of a given vibrational state to better than 0.01% (Doney et al., 2017). A similar agreement is seen for  $\alpha_i^A$ , with the exception of  $\alpha_1^A$ . The large o-c value for  $\alpha_1^A$  is a result of perturbations, and is discussed in detail below.

### 6.3.2 Experimental results

The cw-CRDS spectrum from  $3305 - 3355 \text{ cm}^{-1}$  (Figure 6.1a) is dominated by the  $\nu_1$  fundamental of I0, which is the parallel  $A_1 - A_1$  transition with a Q-branch at  $3335.0520 \text{ cm}^{-1}$ . A closer look at the baseline shows that the region is actually a dense forest of weak rotational transitions, in which three additional  $A_1 - A_1$  type transitions are clearly observed with rotational spacings of  $\sim 0.28 \text{ cm}^{-1}$ , consistent with propyne (Figure 6.1b - d).

Effective band origins and rotational constants for the upper states of each band are determined using the PGOPHER software (Western, 2014), and the standard unperturbed ro-vibrational Hamiltonian for a prolate symmetric top molecule, where the subband origins are given by:

$$\nu_{1,\text{subband}} = \nu_1 + (A - B)K^2 + BJ(J + 1) - DJJ^2(J + 1)^2 - DJ_KJ(J + 1)K^2 - D_KK^4 + (\text{h.o.t.}) \quad (6.1)$$

where  $\nu_1$  is the band origin, A and B are the rotational constants, and  $D_J$ ,  $D_{JK}$ ,  $D_K$  are the centrifugal distortion constants. Only transitions of the  $K' = 0, 1$  and occasionally the  $K' = 2$  subbands are observed, which consequently limits the perturbation analysis, as was demonstrated for the  $\nu_1$  fundamental band of I0 (Kerstel et al., 1994). From the rotational profiles, the ro-vibrational transitions can be fit assuming a rotational temperature of 10 K and a Gaussian linewidth of  $0.002 \text{ cm}^{-1}$ .

Table 6.2: CCSD(T)/ANO1 vibration-rotation interaction constants<sup>a</sup> ( $\alpha_i$ , in  $\text{cm}^{-1}$ ) of propyne  $^{13}\text{C}$ -isotopologues

Mode	$^{13}\text{CH}_3^{12}\text{C}^{12}\text{CH}$ (I1)		$^{12}\text{CH}_3^{13}\text{C}^{12}\text{CH}$ (I2)		$^{12}\text{CH}_3^{12}\text{C}^{13}\text{CH}$ (I3)	
	$\alpha_i^A \times 10^3$	$\alpha_i^B \times 10^3$	$\alpha_i^A \times 10^3$	$\alpha_i^B \times 10^3$	$\alpha_i^A \times 10^3$	$\alpha_i^B \times 10^3$
$\nu_1$	0.035	0.622	0.030	0.640	0.027	0.590
	-0.2 <sup>b</sup>	0.630 <sup>b</sup>	101.0 <sup>b</sup>	0.662 <sup>b</sup>	-37.7 <sup>b</sup>	0.625 <sup>b</sup>
$\nu_2$	54.8	0.061	55.4	0.077	55.4	0.073
		-0.113 <sup>c</sup>		-0.080 <sup>c</sup>		-0.148 <sup>c</sup>
$\nu_3$	2.54	1.43	2.42	1.41	2.67	1.46
$\nu_4$	-27.2	1.42	-27.4	1.67	-27.4	1.57
$\nu_5$	6.04	1.25	6.03	1.29	5.90	1.20
$\nu_6$	35.4	0.044	35.9	0.063	35.9	0.060
$\nu_7$	39.6	-0.759	39.7	-0.891	39.7	-0.834
$\nu_8$	-29.2	0.187	-29.3	0.194	-29.5	0.196
$\nu_9$	0.651	-0.180	0.670	-0.186	0.652	-0.156
$\nu_{10}$	1.42	-0.798	1.19	-0.787	1.30	-0.803

a. Experimental values are given below in italics.

b. This work.

c. McLroy & Nesbitt (1989).

Assignment of the energy levels is based on the band origin and rotational constant, B. The expected rotational constants are given by the general vibrational constant equations:

$$A_V = A_0 - \sum_i (\nu_i \alpha_i^A) \quad (6.2)$$

$$B_V = B_0 - \sum_i (\nu_i \alpha_i^B) \quad (6.3)$$

where  $B_0$  is taken from the experimentally known ground state rotational constants (0.277 300, 0.284 942, and 0.276 534  $\text{cm}^{-1}$ , for I1, I2, and I3, respectively Dubrulle et al. (1978)).  $A_0$  is taken from our VPT2 calculations, and  $\alpha$  values are taken from Table 6.2.

Since a long range Fermi resonance and a "double crossing" type perturbation are believed to affect the  $\nu_1$  state of the three isotopologues (I1 - I3), similar to previous findings for I0, the  $K'$  subbands are initially fit separately. We use a least-squares analysis to determine tentative lower and upper state rotational constants, as well as the band origin. Based on these preliminary values, the bands are assigned to the  $\nu_1$  fundamental of I1 with a Q-branch at 3334.9720(4)  $\text{cm}^{-1}$ , the  $\nu_1$  fundamental of I2 with a Q-branch at 3325.0133(4)  $\text{cm}^{-1}$ , and the  $\nu_1$  fundamental of I3 with a Q-branch at 3318.6667(3)  $\text{cm}^{-1}$ .

A more rigorous analysis is performed by fixing the lower state constants to the respective ground state rotational constants known from microwave data for the three isotopologues (Dubrulle et al., 1978), and  $A_0$  from our VPT2 calculations; again fitting the  $K'$  subbands separately. The resulting effective spectroscopic constants are given in Table 6.3, and confirm that the transitions

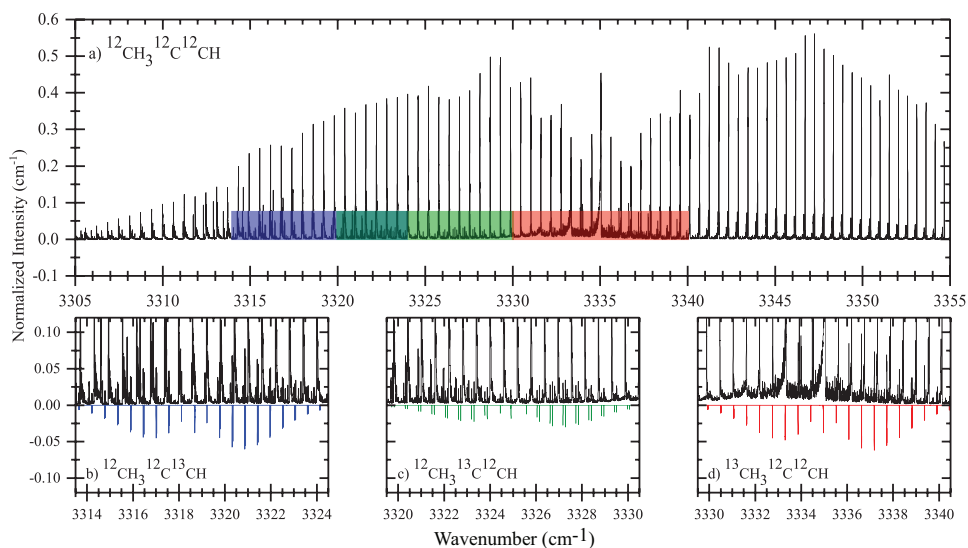


Figure 6.1: The experimental spectrum (in black) of propyne showing a) the  $\nu_1$  band of  $^{12}\text{CH}_3^{12}\text{C}^{12}\text{CH}$  (I<sub>0</sub>), b) the  $\nu_1$  band of  $^{12}\text{CH}_3^{12}\text{C}^{13}\text{CH}$  (I<sub>3</sub>) and its simulated spectrum (in blue), c) the  $\nu_1$  band of  $^{12}\text{CH}_3^{13}\text{C}^{12}\text{CH}$  (I<sub>2</sub>) and its simulated spectrum (in green), and d) the  $\nu_1$  band of  $^{13}\text{CH}_3^{12}\text{C}^{12}\text{CH}$  (I<sub>1</sub>) and its simulated spectrum (in red).

belong to the same band despite the larger than expected  $K'$  spacing. The next step in the fitting routine is combining all  $K'$ -subbands in order to get an approximate value for  $A'$ ; the effective spectroscopic constants resulting from this overall fit are given in Table 6.4. The details of this latter fit are described below.

For I<sub>3</sub>, the Q-branch of the band at  $3318.67\text{ cm}^{-1}$  is predominately obscured, and the band

Table 6.3: The effective spectroscopic parameters (in  $\text{cm}^{-1}$ ) of propyne isotopologues for the separate  $\nu_1$   $K'$ -subbands<sup>a</sup>

$K'$ -subband	Subband origin	$B'$	$D'_J \times 10^6$	$H'_J \times 10^8$
$^{13}\text{CH}_3^{12}\text{C}^{12}\text{CH}$ (I <sub>1</sub> ) <sup>b</sup>				
0	3334.9718(4)	0.276 701(6)	0.5(3)	
1	3334.9731(5)	0.276 702(6)		
$^{12}\text{CH}_3^{13}\text{C}^{12}\text{CH}$ (I <sub>2</sub> ) <sup>b</sup>				
0	3325.0135(4)	0.284 240(6)	4.2(5)	2.4(5)
1	3324.9120(5)	0.284 246(10)	6(1)	6(2)
$^{12}\text{CH}_3^{12}\text{C}^{13}\text{CH}$ (I <sub>3</sub> ) <sup>b</sup>				
0	3318.6672(4)	0.275 894(8)		
1	3318.6951(4)	0.275 905(7)		

a. Numbers in parenthesis are one standard deviation in units of the last significant digit.

b. Ground state values are fixed to those of Dubrulle et al. (1978) and  $A_0$  is taken from our VPT2 calculations.

origin assignment relies on the observed Q<sub>1</sub>(1) and P- and R-branch transitions (Figure 6.1b). This

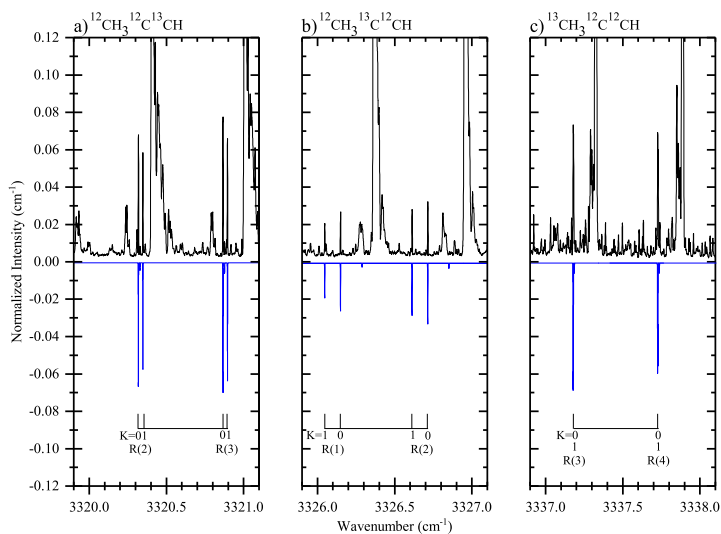


Figure 6.2: The experimental (in black) and simulated (in blue) spectra of a) the R(2) and R(3) transitions of the  $\nu_1$  band of  $^{12}\text{CH}_3^{12}\text{C}^{13}\text{CH}$  (I<sub>3</sub>), b) the R(1) and R(2) transitions of the  $\nu_1$  band of  $^{12}\text{CH}_3^{13}\text{C}^{12}\text{CH}$  (I<sub>2</sub>), and c) the R(3) and R(4) transitions of the  $\nu_1$  band of  $^{13}\text{CH}_3^{12}\text{C}^{12}\text{CH}$  (I<sub>1</sub>). The  $K$  structure in a) and b) is clearly perturbed, and in b) shows a reverse in  $K$ -subband ordering compared to a) and c). The same  $K$ -subband ordering is seen for all measured  $J$  values.

Table 6.4: The effective spectroscopic parameters (in  $\text{cm}^{-1}$ ) of propyne isotopologues for the  $\nu_1$  state<sup>a</sup>

Mode	Band origin	$A'$	$B'$	$D'_J$ $\times 10^7$	$D'_{JK}$ $\times 10^6$	$D'_K$ $\times 10^3$	$H'_J$ $\times 10^8$
$^{13}\text{CH}_3^{12}\text{C}^{12}\text{CH}$ (I <sub>1</sub> )							
$\nu_1$	3334.9720(4)	5.3094(7)	0.276 669(4)	20(6)	-6(1)		
$^{12}\text{CH}_3^{13}\text{C}^{12}\text{CH}$ (I <sub>2</sub> )							
$\nu_1$	3325.0133(4)	5.2078(3)	0.284 270(10)	7.8(9)	0.5 <sup>c</sup>	1.5(5)	8(1)
$^{12}\text{CH}_3^{12}\text{C}^{13}\text{CH}$ (I <sub>3</sub> )							
$\nu_1$	3318.6667(3)	5.3466(1)	0.275 908(5)	1 <sup>c</sup>	1.0(3)	8.89(3)	

a. Uncertainty corresponding to one standard deviation given in the parentheses.

b. Ground state values are fixed to those of Dubrulle et al. (1978) and  $A_0$  is taken from our VPT2 calculations.

c. Fixed value

band origin agrees with the band origin of the  $\nu_1$  fundamental band of I<sub>3</sub> predicted by the VPT2 calculation. The band shows definite  $K$  structure throughout both the P- and R-branch, with the  $K' = 1$  transitions consistently blueshifted by  $\sim 0.03 \text{ cm}^{-1}$  relative to the  $K' = 0$  transitions, and weak  $K' = 2$  transitions redshifted by  $\sim 0.02 \text{ cm}^{-1}$  relative to the  $K' = 1$  transitions (Figure 6.2a). A similar  $K'$ -subband ordering has been reported for the  $\nu_1$  fundamental of I<sub>0</sub> (McIlroy & Nesbitt, 1989; Kerstel et al., 1994). A least-squares fit including all  $K$ -subbands, gives the rotational constants  $B' = 0.275 908(5) \text{ cm}^{-1}$  and  $A' = 5.3466(1) \text{ cm}^{-1}$  (Table 6.4). The upper state B constant agrees with predicted  $B_1 = 0.275 943 \text{ cm}^{-1}$ , confirming the assignment.

For I<sub>2</sub>, the full Q-branch of the band at 3325.01 cm<sup>-1</sup> is clearly seen in the experimental spectrum (Figure 6.1c), and its band origin is consistent with the band origin of the  $\nu_1$  fundamental band of I<sub>2</sub> predicted by the VPT<sub>2</sub> calculation. Moreover, the intensity of the band is about half that of the  $\nu_1$  fundamental of I<sub>3</sub>, which is expected from the calculations. As with the I<sub>3</sub> band, there is a large separation between the  $K' = 0$  and 1 subbands, with the  $K' = 1$  transitions redshifted by 0.1 cm<sup>-1</sup> relative to the  $K' = 0$  transitions (Figure 6.2b). However, no  $K' = 2$  transitions could be observed. A least-squares fit including both  $K$ -subbands, gives the rotational constants  $B' = 0.284\ 270(10)$  cm<sup>-1</sup> and  $A' = 5.2078(3)$  cm<sup>-1</sup> (Table 6.4). The low-resolution study had assigned this band as the  $\nu_3+2\nu_9$  combination band, but while the predicted rotational constants are close ( $B_1 = 0.284\ 292$  cm<sup>-1</sup> and  $B_{(3+2*9)} = 0.283\ 892$  cm<sup>-1</sup>), the o-c value assuming the band is  $\nu_1$  is an order of magnitude smaller compared to that assuming it is  $\nu_3+2\nu_9$ . This suggests that the band is in fact the I<sub>2</sub>  $\nu_1$  fundamental.

For I<sub>1</sub>, the Q-branch of the band at 3334.97 cm<sup>-1</sup> is almost entirely blended with the Q-branch of I<sub>0</sub> (Figure 6.1d), but the Q<sub>1</sub>(1) and a sufficient number of P- and R-branch transitions are visible, allowing for accurate determination of the band origin. Based on the low-resolution study by Duncan et al. (1976) and the VPT<sub>2</sub> calculations, this band can be assigned as the  $\nu_1$  fundamental of I<sub>1</sub>. Unlike with the previous two bands, at low- $J''$  ( $J'' < 4$ ) no  $K$  structure can be observed (Figure 6.2c), but at higher  $J''$  transitions the  $K' = 0$  and  $K' = 1$  transitions begin to separate with the  $K' = 0$  subband origin redshifted relative to the  $K' = 1$  subband origin. A least-squares fit of the two subbands together results in the rotational constants of  $B' = 0.276\ 669(4)$  cm<sup>-1</sup> and  $A' = 5.3094(7)$  cm<sup>-1</sup> (Table 6.4), which agree within their uncertainties with the VPT<sub>2</sub> predicted values of  $B_1 = 0.276\ 677$  cm<sup>-1</sup> and  $A_1 = 5.3092$  cm<sup>-1</sup>, fully in line with the assignment presented here.

While the observed band origins of all three  $\nu_1$  bands are consistent with those predicted by assuming a Fermi resonance with  $\nu_3+2\nu_9$ , no transitions belonging to the combination band for any of the isotopologues could be observed. In the case of I<sub>1</sub> and I<sub>3</sub>, at natural abundances, based on the relative intensities of the  $\nu_1$  bands, the intensity of the  $\nu_3+2\nu_9$  transitions is expected to be comparable to the baseline noise. Conversely, the  $\nu_3+2\nu_9$  band of I<sub>2</sub> could be detectable. However, it falls in a particularly congested portion of our experimental spectrum (around the  $\nu_1$  fundamental band origin of I<sub>0</sub>).

### 6.3.3 Perturbation Analysis

From the VPT<sub>2</sub> calculations it is found that  $A_1 \sim A_0$ , as such at 10 K it is expected that almost no  $K$  structure is discernible, particularly at low- $J''$ . Given the good overall agreement between experimental and calculated  $\alpha_1^B$ , the deviation between experimental and calculated  $\alpha_1^A$ , and the unexpected  $K'$ -subband spacing, is likely a result of perturbations. In the case of I<sub>0</sub>, the inversion of the  $K' = 0$  and 1 subband origins, and the larger than expected  $\alpha_1^A$  (based on the  $K' = 0$  and 1 subband transitions) were determined to be a result of anharmonic coupling of the  $\nu_1$  state with at least two z-axis Coriolis mixed ( $A_1+A_2$ ) states, one of which crosses the  $\nu_1$  state twice, *i.e.*, a “double crossing” type perturbation (Kerstel et al., 1994).

For I<sub>3</sub>, while  $B'$  agrees with that expected from the VPT<sub>2</sub> calculations for  $\nu_1$ ,  $A'$  differs by about three orders of magnitude, similar to that seen for  $\nu_1$  of I<sub>0</sub> (McIlroy & Nesbitt, 1989; Kerstel et al., 1994). The inclusion of a Fermi resonance with  $\nu_3+2\nu_9$  in the fit, does affect the overall position of the  $\nu_1$  band, but it does not resolve the large difference between the calculated and observed  $\alpha^A$ . As determined for I<sub>0</sub>, the perturbations responsible for the observed  $K$ -subband perturbations in I<sub>3</sub> likely result from a “double crossing” type perturbation, where the more prominent component of the “double crossing” intersects between the  $K' = 0$  and 1 subbands, pushing the  $K' = 1$  subband origin to the blue and the  $K' = 0$  to the red.

Similar to I<sub>3</sub>, the experimental  $\alpha^A$  of I<sub>2</sub> differs by four orders of magnitude from the calculated value, and cannot be explained solely with the inclusion of a Fermi resonance with  $\nu_3+2\nu_9$ . This suggests that a similar perturbation as seen in the  $\nu_1$  fundamental of I<sub>0</sub> and I<sub>3</sub> affects the

$K'$ -subband order in the  $\nu_1$  fundamental of I2. However, the observed shift for I2 is significantly larger, and results in a  $K'$ -subband order reversed from that observed for I0 and I3. As such it is likely that the “double crossing” type perturbation intersects between the  $K' = 1$  and 2 subbands, pushing the  $K' = 1$  subband origin further to the red, resulting in a splitting larger than expected.

Interestingly, the  $\nu_1$  fundamental of I1 shows no sign of the “double crossing” type perturbation that is seen in the other isotopologues. However, in order to accurately reproduce the  $K$  splitting at  $J'' \geq 4$ , we had to use  $D_{JK}^1 = -6 \times 10^{-5} \text{ cm}^{-1}$ . The opposite sign of  $D_{JK}$  between the ground and excited state suggests that a perpendicular Coriolis interaction could also be involved, which is not seen in the  $\nu_1$  band of I0 (Kerstel et al., 1994).

For all of the bands, there is no noticeable perturbation in the  $J$  structure, which rules out close Fermi resonances or Coriolis interactions. Furthermore, the observed line shapes are clearly Gaussian, with no detectable Lorentzian character, which is expected for a prominent interaction with background states (Campargue et al., 1999). As such, like the  $\nu_1$  state of I0, the  $\nu_1$  states of the mono-substituted  $^{13}\text{C}$  propyne isotopologues do not seem to exhibit any effects due to IVR.

#### 6.4 CONCLUSIONS

The jet-cooled spectrum of the  $\nu_1$  (acetylenic stretch) fundamental band and high level *ab initio* of all three mono-substituted  $^{13}\text{C}$  propyne isotopologues is presented for the first time. The fundamental frequencies and spectroscopic constants determined here offer an accurate guide for spectroscopic searches of the ro-vibrational bands of mono-substituted  $^{13}\text{C}$  propyne in either the laboratory or astronomical spectra.

The CCSD(T)/ANO1 VPT2 calculations predict small values for  $\alpha^A$  for I1 - I3, which could not be experimentally confirmed for two of the isotopologues (I2 and I3). All three isotopologues presented in this study show similar perturbations in the  $\nu_1$  fundamental, as seen for I0. Moreover, the location of the  $^{13}\text{C}$  in the C-C $\equiv$ C frame greatly influences the effects of these perturbations, with the strongest effects occurring when the  $^{13}\text{C}$  is part of the triple bond. From the *ab initio* calculations, it is clear that the isotopic position heavily influences the impact of the long range Fermi resonance with  $\nu_3+2\nu_9$ . In particular, since  $\nu_1$ ,  $\nu_3$  and  $\nu_9$  are all vibrations of the C $\equiv$ C bond, I0 and I1 are barely affected, but the  $\nu_1$  fundamental of I2, where the  $^{13}\text{C}$  is on the middle C, loses about a third of its intensity to the dark state.

Even more drastic is the affect of the  $^{13}\text{C}$  position on the “double crossing” type perturbation. As shown for the normal  $^{13}\text{C}$  isotopologue, the value for  $\alpha^A$  determined from the jet-cooled spectrum is not the deperturbed value, and a complete perturbation analysis requires room-temperature spectra where higher order  $K'$ -subbands can also be observed (Kerstel et al., 1994). Comparison of the observed  $K' = 0$  and 1 spacing of I2 and I3 with that of I0, for which a complete perturbation analysis has been reported by Kerstel et al. (1994), gives insight into the observed perturbations, and shows that in all except the I1 isotopologue a “double crossing” type perturbation is present, likely the result of an interaction with at least one other ( $A_1+A_2$ ) pair state. Furthermore, from the  $K' = 0$  and 1 band origin order we are able to conclude that while the crossing for I0 and I3 is between the  $K' = 0$  and 1 subbands, for I2 the crossing is likely between the  $K' = 1$  and 2 subbands. This is due to the fact that the  $K' = 0$  and 1 band origin order for I2 is reversed compared to I0 and I3. Despite all the accurate info available from this work, it is not possible to identify the perturbing state. However, it is clear that the inclusion of the  $^{13}\text{C}$  changes the energy spacing between  $\nu_1$  and the main perturbing state such that they are closest when the  $^{13}\text{C}$  is on the middle or acetylenic C (I2 and I3, respectively), but when the  $^{13}\text{C}$  is on the aliphatic C (I1) the two states are sufficiently separated that no noticeable perturbation occurs. If the main perturber state was a vibrational state involving the acetylenic CH bond, then its frequency would shift similar to  $\nu_1$  upon  $^{13}\text{C}$  addition, and there would not be the drastic difference in perturbations observed between the three isotopes. This hints that the  $\nu_1$  and the main perturbing state involve vibrations that occur at opposite ends of the carbon chain.

## 6.5 ACKNOWLEDGEMENT

K.D.D. would like to thank J.F. Stanton for thoughtful discussions on the *ab initio* calculations. The authors thank the financial support of the Netherlands Organization for Scientific Research (NWO) through a VICI grant, and the Netherlands Research School for Astronomy (NOVA). This work has been performed within the context of the Dutch Astrochemistry Network, another NWO initiative. D.Z. acknowledges financial support from the National Key R&D Program of China (2017YFA0303502) and the Fundamental Research Funds for the Central Universities of China.

## 6.6 BIBLIOGRAPHY

- Agúndez, M., Fonfría, J. P., Cernicharo, J., Pardo, J. R., & Guélin, M. 2008, *Astronomy & Astrophysics*, 479, 493
- Almlöf, J. & Taylor, P. R. 1987, *The Journal of Chemical Physics*, 86, 4070
- Burrell, P. M., Bjarnov, E., & Schwendeman, R. H. 1980, *Journal of Molecular Spectroscopy*, 82, 193
- Campargue, A., Biennier, L., Garnache, A., et al. 1999, *The Journal of Chemical Physics*, 111, 7888
- Cernicharo, J., Heras, A. M., Pardo, J. R., et al. 2001a, *The Astrophysical Journal Letters*, 546, L127
- CFOUR. 2017, Coupled-Cluster techniques for Computational Chemistry, a quantum-chemical program package by J.F. Stanton, J. Gauss, M.E. Harding, P.G. Szalay with contributions from A.A. Auer, R.J. Bartlett, U. Benedikt, C. Berger, D.E. Bernholdt, Y.J. Bomble, L. Cheng, O. Christiansen, F. Engel, R. Faber, M. Heckert, O. Heun, C. Huber, T.-C. Jagau, D. Jonsson, J. Jusélius, K. Klein, W.J. Lauderdale, F. Lipparini, D.A. Matthews, T. Metzroth, L.A. Mück, D.P. O'Neill, D.R. Price, E. Prochnow, C. Puzzarini, K. Ruud, F. Schiffmann, W. Schwalbach, C. Simmons, S. Stopkowitz, A. Tajti, J. Vázquez, F. Wang, J.D. Watts and the integral packages MOLECULE (J. Almlöf and P.R. Taylor), PROPS (P.R. Taylor), ABACUS (T. Helgaker, H.J. Aa. Jensen, P. Jørgensen, and J. Olsen), and ECP routines by A. V. Mitin and C. van Wüllen. For the current version, see <http://www.cfour.de>.
- Chen, X., Ganot, Y., Bar, I., & Rosenwaks, S. 2000, *The Journal of Chemical Physics*, 113, 5134
- Doney, K. D., Zhao, D., Bouwman, J., & Linnartz, H. 2017, *Chemical Physics Letters*, 684, 351
- Dubrule, A., Boucher, D., Burie, J., & Demaison, J. 1978, *Journal of Molecular Spectroscopy*, 72, 158
- Duncan, J. L., McKean, D. C., & Nivellini, G. D. 1976, *Journal of Molecular Structure*, 32, 255
- Feller, D. 1996, *Journal of Computational Chemistry*, 17, 1571
- Gambogi, J. E., Kerstel, E. R. T., Lehmann, K. K., & Scoles, G. 1994, *The Journal of Chemical Physics*, 100, 2612
- Gambogi, J. E., Timmermans, J. H., Lehmann, K. K., & Scoles, G. 1993, *The Journal of Chemical Physics*, 99, 9314
- Gauss, J. & Stanton, J. F. 1997, *Chemical Physics Letters*, 276, 70
- Go, J., Cronin, T. J., & Perry, D. S. 1993, *Chemical Physics*, 175, 127
- Go, J. & Perry, D. S. 1992, *The Journal of Chemical Physics*, 97, 6994
- Henfrey, N. F. & Thrush, B. A. 1987, *Journal of Molecular Spectroscopy*, 121, 150
- Irvine, W. M., Hoglund, B., Friberg, P., Askne, J., & Ellder, J. 1981, *The Astrophysical Journal Letters*, 248, L113
- Kerstel, E. R. T., Lehmann, K. K., Pate, B. H., & Scoles, G. 1994, *The Journal of Chemical Physics*, 100, 2588
- Maguire, W. C., Hanel, R. A., Jennings, D. E., Kunde, V. G., & Samuelson, R. E. 1981, *Nature*, 292, 683
- Malek, S. E., Cami, J., & Bernard-Salas, J. 2012, *The Astrophysical Journal*, 744, 16
- Matthews, D. A., Vázquez, J., & Stanton, J. F. 2007, *Molecular Physics*, 105, 2659
- McIlroy, A. & Nesbitt, D. J. 1989, *The Journal of Chemical Physics*, 91, 104
- McIlroy, A., Nesbitt, D. J., Kerstel, E. R. T., et al. 1994, *The Journal of Chemical Physics*, 100, 2596
- Müller, H. S. P., Thorwirth, S., Bizzocchi, L., & Winnewisser, G. 2000, *Zeitschrift Naturforschung Teil A*, 55
- Pracna, P., Müller, H. S. P., Urban, S., Horneman, V. M., & Klee, S. 2009, *Journal of Molecular Spectroscopy*, 256, 152
- Rothman, L., Gordon, I., Babikov, Y., et al. 2013, *Journal of Quantitative Spectroscopy and Radiative Transfer*, 130, 4
- Schuchardt, K. L., Didier, B. T., Elsethagen, T., et al. 2007, *Journal of Chemical Information and Modeling*, 47, 1045
- Western, C. M. 2014, PGOPHER version 8.0, university of Bristol Research Data Repository
- Woon, D. E. & Dunning Jr., T. H. 1995, *The Journal of Chemical Physics*, 103, 4572
- Zhao, D., Guss, J., Walsh, A. J., & Linnartz, H. 2013, *Chemical Physics Letters*, 565, 132



## HIGH-RESOLUTION INFRARED SPECTRUM OF THE $\nu_4$ FUNDAMENTAL BAND OF CYCLOPROPENYL CATION

---

The cyclopropenyl cation ( $c\text{-C}_3\text{H}_3^+$ ) is the smallest aromatic hydrocarbon molecule and considered to be a pivotal intermediate in ion-molecule reactions in space. An astronomical identification has been prohibited so far, because of a lack of gas-phase data. Here we report the first high resolution infrared laboratory gas-phase spectrum of the  $\nu_4$  (C-H asymmetric stretching) fundamental band of  $c\text{-C}_3\text{H}_3^+$ . The  $c\text{-C}_3\text{H}_3^+$  cations are generated in supersonically expanding planar plasma by discharging a propyne/helium gas pulse, yielding a rotational temperature of  $\sim 35$  K. The absorption spectrum is recorded in the  $3.19\ \mu\text{m}$  region using sensitive continuous-wave cavity ring-down spectroscopy. The analysis of about 130 ro-vibrational transitions results in precise spectroscopic parameters. These constants allow for an accurate comparison with high-level theoretical predictions, and provide the relevant information needed to search for this astrochemically relevant carbo-cation in space.

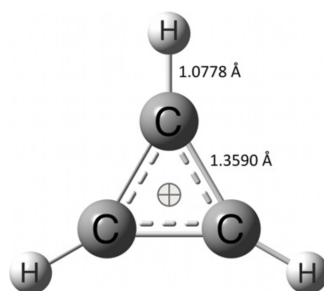
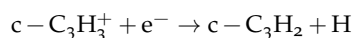


Figure 7.1: Equilibrium geometry of  $c\text{-C}_3\text{H}_3^+$ . The type of CC bond is an intermediate between a typical double bond and single bond. Bond lengths are *ab initio* calculated values by Huang et al. (2011).

## 7.1 INTRODUCTION

The cyclopropenyl cation ( $c\text{-C}_3\text{H}_3^+$ ), a centro-symmetric molecule with  $D_{3h}$  symmetry (Figure 7.1), is the smallest aromatic carbo-cation of high chemical relevance for which accurate spectroscopic data are still incomplete. Astrochemical models consider  $c\text{-C}_3\text{H}_3^+$  as a key intermediate in reaction networks explaining the presence of other hydrocarbons in the interstellar medium (ISM; (Smith, 1992; Agúndez & Wakelam, 2013)). The main formation pathway of cyclopropenyliene ( $c\text{-C}_3\text{H}_2$ ), for example, which is ubiquitous in both diffuse interstellar clouds and dark cloud cores (Cox et al., 1988; Madden et al., 1989), is expected to follow dissociative electron recombination:



The two delocalized  $\pi$  electrons stabilize the aromatic three-member ring structure (Lee et al., 1989), and  $c\text{-C}_3\text{H}_3^+$  is therefore expected to be abundantly present in space. It is also relevant in ion-molecule reactions, driving gas-phase chemistry in the ISM (Smith, 1992) as well as in Titan's atmosphere (Ali et al., 2013), but, contrary to more than 20 cations and anions detected so far in space, an observational identification of  $c\text{-C}_3\text{H}_3^+$  is still pending. The  $c\text{-C}_3\text{H}_3^+$  molecule has no permanent dipole moment, making a radio-astronomical detection through its microwave spectrum impossible. There has been a lack of infrared (IR) gas-phase data of  $c\text{-C}_3\text{H}_3^+$  up to now, prohibiting an astronomical identification through its ro-vibrational spectrum. Instead, in the laboratory, the focus over the past few decades has been on a structural characterization of this cation by IR spectroscopy in the solution of salts and in neon matrices (Craig et al., 1986; Wyss et al., 2001). Vibrational IR predissociation spectra have been reported for weakly bonded complexes of  $c\text{-C}_3\text{H}_3^+$  with various ligands (Dopfer et al., 2002; Roth & Dopfer, 2002). Because of the ligand effect (Botschwina, 2011b) on the molecular geometry of the chromophore, and lower spectral resolution typical for such experiments, these spectra did not allow the deduction of accurate spectroscopic parameters for free, *i.e.*, uncomplexed,  $c\text{-C}_3\text{H}_3^+$ . Such data, however, are available from high-level theory-based *ab initio* calculations of quartic force fields (QFFs), for both  $c\text{-C}_3\text{H}_3^+$  and its  $^{13}\text{C}$ - and D-substituted isotopologues (Huang et al., 2011; Huang & Lee, 2011). These calculated parameters are useful to simulate the expected spectra, as will be demonstrated here, and to guide high resolution laboratory studies, but also hold the potential to guide future astronomical surveys, as will be discussed.

We report the gas-phase identification of free  $c\text{-C}_3\text{H}_3^+$  using high resolution IR absorption spectroscopy. The motivation of this work is a full characterization of the IR spectroscopic properties of  $c\text{-C}_3\text{H}_3^+$  and to make this molecule accessible to astronomers. In parallel, this work allows an independent examination of the applicability of *ab initio* QFF-predictions by Huang et al. (2011) and Huang & Lee (2011) for astronomical use.

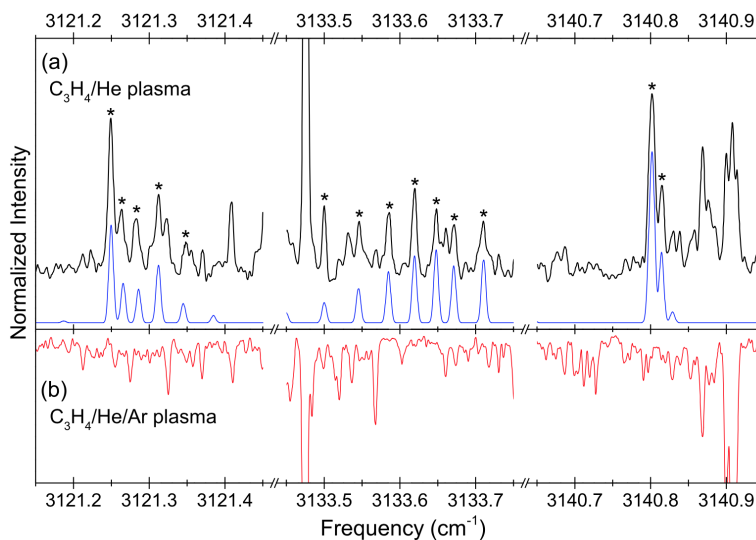


Figure 7.2: Three parts of the experimental spectra recorded in the  $\text{C}_3\text{H}_4/\text{He}$  (a, upper trace) and  $\text{C}_3\text{H}_4/\text{He}/\text{Ar}$  (b) plasma. The latter spectrum is inverted and illustrates absorption features due to other plasma products that also show up in the upper trace of (a). The simulated spectra using the derived spectroscopic parameters (as listed in Table 7.1) are shown in the lower trace of (a). Absorption lines unambiguously identified as ro-vibrational transitions of  $c\text{-C}_3\text{H}_3^+$  are marked by asterisks.

## 7.2 EXPERIMENTAL METHOD

The experimental setup is described in detail by Zhao et al. (2013, 2014a). In brief, the  $c\text{-C}_3\text{H}_3^+$  cations are generated by discharging a propyne ( $\text{C}_3\text{H}_4$ ):He  $\sim 1:200$  gas mixture in a multi-layer slit discharge nozzle (Motylewski & Linnartz, 1999) in combination with a pulsed valve (General Valve, Series 9, 2 mm orifice). The gas mixture is expanded with a backing pressure of  $\sim 7$  bar through a  $300 \mu\text{m} \times 3 \text{ cm}$  slit into a vacuum chamber. A pulsed negative high voltage ( $-600 \text{ V}/300 \text{ mA}$ ) with a  $\sim 600 \mu\text{s}$  duration is found to be optimum for  $c\text{-C}_3\text{H}_3^+$  production, is applied to the expanding gas mixture, and is set to coincide with the expanding gas pulse ( $\sim 800 \mu\text{s}$ ).

Continuous-wave cavity ring-down spectroscopy (cw-CRDS) is used to record spectra in direct absorption. The axis of the optical cavity is aligned parallel to and  $\sim 2 \text{ mm}$  downstream of the slit nozzle throat. A single-mode cw optical parametric oscillator (Aculight), operating at  $\sim 3.15 \mu\text{m}$  with a bandwidth  $< 5 \times 10^{-5} \text{ cm}^{-1}$ , is employed as tunable IR light source. A hardware-based (boxcar integrator) multi-trigger and timing scheme recently reported by Zhao et al. (2013) is used to apply cw-CRDS to the pulsed plasma. In the present experiment, typical ring-down time values are  $\sim 8 - 10 \mu\text{s}$ , corresponding to a detection sensitivity, *i.e.*, noise equivalent absorption, of up to  $\sim 2 \times 10^{-7}$  per centimeter for the 3 cm long plasma jet.

The IR laser frequency is calibrated using a wavelength meter (Bristol Instruments, 621A-IR) and is independently checked by recording  $\text{H}_2\text{O}$  trace gas absorption lines in the vacuum chamber, resulting in a wavelength precision better than  $0.001 \text{ cm}^{-1}$ . The Doppler width in the absorption spectrum of  $\text{C}_3\text{H}_4/\text{He}$  plasma is  $\sim 0.007 \text{ cm}^{-1}$ . The absolute frequency accuracy of the measured positions of absorption lines is better than  $0.003 \text{ cm}^{-1}$ .

## 7.3 RESULTS AND ANALYSIS

The  $c\text{-C}_3\text{H}_3^+$  molecule has four IR-active vibrational modes:  $\nu_4$  (C-H asymmetric stretching),  $\nu_5$  (in-plane wagging),  $\nu_6$  (in-plane scissoring), and  $\nu_7$  (symmetric out-of-plane bending), corresponding to ro-vibrational transition bands centered around  $3135\text{ cm}^{-1}$  ( $3.19\text{ }\mu\text{m}$ ),  $1300\text{ cm}^{-1}$  ( $7.69\text{ }\mu\text{m}$ ),  $925\text{ cm}^{-1}$  ( $10.8\text{ }\mu\text{m}$ ), and  $757\text{ cm}^{-1}$  ( $13.2\text{ }\mu\text{m}$ ), respectively (Lee et al., 1989). In our experiment, the most intense IR band, *i.e.*, the  $\nu_4$  fundamental band, is searched for in the  $3110 - 3160\text{ cm}^{-1}$  range. Parts of the experimental spectrum recorded in the  $\text{C}_3\text{H}_4/\text{He}$  plasma are shown in Figure 7.2a.

The initial step in the assignment of hundreds of observed lines is to simulate the  $c\text{-C}_3\text{H}_3^+$  spectrum using the ab initio results (Huang et al., 2011). This simulated spectrum is compared to the experimental spectrum. Since CRDS lacks mass selectivity, absorption features of other plasma-produced species (neutrals, cat- and anions) are also recorded, resulting in additional transitions, partially overlapping and hindering a straight forward interpretation of the experimental spectrum. Nevertheless, by shifting the calculated spectrum by  $-0.55\text{ cm}^{-1}$ , a remarkably small value, a reasonable first match between theoretical and experimental data is obtained. In addition, contrastive experiments with a different gas mixture ( $\text{C}_3\text{H}_4:\text{He}:\text{Ar} \sim 1:100:100$ ) under similar discharge conditions are performed. An example is shown in Figure 7.2b. It is found that all transitions that can be assigned to  $c\text{-C}_3\text{H}_3^+$  become nearly non-detectable in the  $\text{C}_3\text{H}_4/\text{He}/\text{Ar}$  plasma. This allows us to discriminate between transitions from  $c\text{-C}_3\text{H}_3^+$  and other species that clearly do not share a common chemical history, and makes it possible to assign even weaker absorption lines to  $c\text{-C}_3\text{H}_3^+$ , not directly assignable in the initial step, as these can be labeled just following the plasma settings.

In total, about 130 adjacent lines observed in the experimental spectrum have been assigned to the perpendicular  $\nu_4$  fundamental band of  $c\text{-C}_3\text{H}_3^+$ , with an overall band profile corresponding to a rotational temperature of  $\sim 35\text{ K}$ . The wavenumbers of the observed ro-vibrational transitions are given in the **supplementary material**. Least-squares fits of the observed ro-vibrational transition lines are performed in the PGOPHER software (Western, 2014), using an effective Hamiltonian for symmetric top rotators as discussed by Crofton et al. (1988). In the ground state of  $c\text{-C}_3\text{H}_3^+$ , the rotational level energies can be described by

$$E(J, K) = BJ(J+1) + (C-B)K^2 - D_J J^2(J+1) - D_{JK}J(J+1)K^2 - D_K K^4 \quad (7.1)$$

where B and C are rotational constants, and  $D_J$ ,  $D_{JK}$ , and  $D_K$  are the quartic centrifugal distortion constants. For the degenerate  $\nu_4$  vibrational mode Coriolis coupling takes place, *i.e.*, interaction between the two components ( $l = +1$ , and  $-1$ ) of the degenerated pair of  $\nu_4$ . This results in a splitting of the degenerated vibrational levels which can be described by  $-\zeta_4 lC$ , where  $\zeta_4$  is the first-order Coriolis coupling constant. By analyzing the two vibrational components, it is concluded that the Coriolis coupling effect in  $\nu_4$  must be very small. The QFF- predicted Coriolis coupling constant  $|\zeta_4| = 0.0092$  by Huang et al. (2011) confirms this interpretation. In addition, there is an unusual  $l$ -type doubling effect for the  $K = l = 1$  level (Crofton et al., 1988). In PGOPHER, this  $l$ -type doubling is described by  $\pm (q_4/2)J(J+1)$  for levels with  $A_1(+)$  and  $A_2(-)$  symmetries, where  $q_4$  is the  $l$ -type doubling constant. In the present work, other higher-order terms, such as sextic and octic centrifugal distortion, are not included in the analysis because the rotational temperature is rather low, and nearly no high- $J, K$  ( $> 10$ ) transitions are observed. The ro-vibrational transition selection rules of the perpendicular  $\nu_4$  fundamental band are:  $\Delta J^p = 0, \pm 1$ ;  $\Delta K = \pm 1$ ;  $\Delta l = \pm 1$ , and  $\Delta|K - l| = 0$ . Moreover, the symmetry of the ground-state wave function and the rotational energy diagram is the same as for  $\text{CH}_3^+$  (Crofton et al., 1988), which also has  $D_{3h}$  symmetry. Therefore, due to the nuclear spin statistics of the three symmetric hydrogen atoms, the weight of the ground state populations in ( $A_1', A_1''$ ), ( $A_2', A_2''$ ), and ( $E', E''$ ) rotational levels amounts to 0, 2, and 1, respectively.

A least-squares fit including all parameters may suffer from possible correlations between the constants of ground and excited  $\nu_4$  states. Therefore, the 38 combination differences for ground-

state rotational levels that can be derived from the observed ro-vibrational transitions are fitted as a first step. This yields three independently determined ground-state constants (in  $\text{cm}^{-1}$ ):

$$B_0 = 1.02583(10) \quad D_{J,0} = 3.5(12) \times 10^{-6} \quad D_{JK,0} = -4.5(37) \times 10^{-6}$$

In the second step, a global fit of all observed ro-vibrational transitions is made. It is found that it is not possible to determine the  $C_0$  and  $D_{K,0}$  constants from the  $\nu_4$  spectrum, similar as in the case of the ground state combination difference fit. Therefore,  $C_0$  is fixed to a value of  $0.511\ 65\ \text{cm}^{-1}$  that is derived from the constant  $B_0$  (determined from the ground state combination difference fit) and the QFF-predicted value of  $(1/C_0 - 2/B_0 = 0.004\ 837)$ . This interpretation is based on the assumption that the QFF-predicted inertia defect,

$$\Delta_0 = I_c - I_a - I_b = \left( \frac{h}{8\pi^2 c} \right) \left( \frac{1}{C_0} - \frac{2}{B_0} \right) \quad (7.2)$$

where  $I_c$  and  $I_a = I_b$  are the three rotational moments of inertia, has a comparable error as that for the rotational constant  $B_0$ . For  $D_{K,0}$ , the QFF-predicted value is used and fixed in the fit.

The resulting spectroscopic constants are summarized in Table 7.1. The overall rms of the fit is less than  $0.002\ \text{cm}^{-1}$ , *i.e.*, substantially smaller than the spectral resolution in our experiment. The derived ground state constants  $B_0$ ,  $D_{J,0}$ , and  $D_{JK,0}$  are consistent with the corresponding values derived from the combination difference fit. This is indicative for nearly negligible correlations between the derived ground and  $\nu_4$  excited state constants. The high-level QFF-predicted spectroscopic constants by Huang et al. (2011) are also listed in Table 7.1. A comparison with the experimentally determined values shows excellent agreement; the difference in the calculated rotational constants  $B_0$  and  $B_4$  is only  $\sim 0.03\%$ . The  $\nu_4$  anharmonic vibrational frequency computed by second-order perturbation theory shows a remarkable small offset deviation of  $\sim 0.55\ \text{cm}^{-1}$ , substantially smaller than the typical error (several  $\text{cm}^{-1}$ ) for the used level of theory. The QFF predicted centrifugal distortion constants  $D_J$  and  $D_{JK}$  (for the equilibrium structure) are also very close to the experimentally determined values in the zero-point ground state. These comparisons confirm that the *ab initio* QFF calculations for the tightly bounded  $c\text{-C}_3\text{H}_3^+$  by Huang et al. (2011) are highly accurate and can be used in assisting the assignment of high resolution experimental spectra.

#### 7.4 ASTROPHYSICAL IMPLICATIONS

Since  $c\text{-C}_3\text{H}_3^+$  has no pure rotational transitions, a direct observation of this cation in the ISM is only available via ro-vibrational transitions in the IR. The  $\nu_4$  band is the most intense IR band. Due to the absolute frequency accuracy of our experimental spectrum, the present work provides accurate data that can be directly used for an astronomical search in the  $3.19\ \mu\text{m}$  region. For the other three IR-active fundamental bands ( $\nu_5$  at  $\sim 7.69\ \mu\text{m}$ ,  $\nu_6$  at  $\sim 10.8\ \mu\text{m}$ , and  $\nu_7$  at  $\sim 13.2\ \mu\text{m}$ ), which are not experimentally studied here, spectroscopic constants can be interpreted using the experimentally determined zero-point ground-state constants and the QFF-predicted vibration-rotation interaction constant by Huang et al. (2011). Even without high resolution experimental data for these bands, such interpreted spectroscopic parameters are considered to be of reasonable accuracy to calculate ro-vibrational spectra for astronomical use. It should be noted that due to the level of accuracy of QFF-predicted fundamental vibrational frequencies, a small shift by up to a few  $\text{cm}^{-1}$  might be necessary when applying such calculated spectra to search for  $c\text{-C}_3\text{H}_3^+$  in astronomical IR observations.

The infrared, however, is not the most optimal wavelength domain for high-sensitivity and high resolution studies using ground-based observations. An alternative approach to identify  $c\text{-C}_3\text{H}_3^+$  in space is to search in the radio/millimeter wave-length region for spectral signatures of the (substantially less abundant)  $^{13}\text{C}$  and D mono-substituted isotopologues that have been predicted to possess effective permanent dipole moments (Huang & Lee, 2011). High-level *ab initio* QFF-calculations

Table 7.1: Spectroscopic parameters<sup>a</sup> (in  $\text{cm}^{-1}$ ) of  $c\text{-C}_3\text{H}_3^+$ 

Constants	This work	Huang et al. (2011)
$\nu_4$	3131.1447(5)	3131.7
$B_0$	1.025 84(6)	1.026 10
$C_0^b$	0.511 65	0.511 78
$D_{J,0} (\times 10^6)$	4.3(6)	2.44
$D_{JK,0} (\times 10^6)$	-6.9(6)	-4.07
$D_{K,0}^b (\times 10^6)$	1.8	1.83
$B_4$	1.022 98(7)	1.023 24
$C_4$	0.510 40(2)	0.510 37
$D_{J,4} (\times 10^6)$	3.7(6)	2.44
$D_{JK,4} (\times 10^6)$	-6.3(8)	-4.07
$D_{K,4} (\times 10^6)$	2.2(4)	1.83
$q_4 (\times 10^4)$	1.9(7)	
$\zeta_4 (\times 10^3)$	-7.9(1)	-9.2

a. Numbers in parentheses are one standard deviation in units of the last significant digit.  $\zeta_4$  is dimensionless.

b.  $C_0$  and  $D_{K,0}$  are fixed in the fit (see the text).

on the mono-substituted isotopologues of  $c\text{-C}_3\text{H}_3^+$  have been performed by Huang & Lee (2011). To examine the accuracy, *i.e.*, astronomical applicability of these theoretical predictions, comparisons of the fine rotational structures between the QFF-predicted and simulated experimental spectrum of  $c\text{-C}_3\text{H}_3^+$  are made. It is found that even with an offset of  $-0.55 \text{ cm}^{-1}$  on the QFF-predicted spectrum, discrepancies up to  $\sim 0.03 \text{ cm}^{-1}$  still appear for some strong ro-vibrational transitions, which may be due to small deviations (several MHz) of the QFF predicted rotational constants. This comparison indicates that the QFF predictions by Huang & Lee (2011) for the  $^{13}\text{C}$  and D mono-substituted  $c\text{-C}_3\text{H}_3^+$  isotopologues are useful to guide the data interpretation of a high resolution laboratory-based survey. However, for an astronomical search for  $c\text{-C}_3\text{H}_3^+$  isotopologues in the radio/millimeter wavelength region, these predictions are unfortunately not accurate enough and rest frequencies provided by laboratory experiments will be needed.

## 7.5 CONCLUSIONS

We have presented the first gas-phase detection of  $c\text{-C}_3\text{H}_3^+$  by the high resolution IR spectrum of its  $\nu_4$  band. The accurately determined molecular constants for the ground state and the  $\nu_4$  fundamental vibrational level provide information that is needed to make this molecule accessible to astronomical surveys in the IR.

## 7.6 ACKNOWLEDGEMENTS

This work is financially supported by a NWO-VICI grant, NOVA, SRON, and has been performed within the context of the Dutch Astrochemistry Network. We acknowledge Huang and Lee (NASA Ames) for stimulating discussions and to provide us with the computed Coriolis coupling constant  $\zeta_4$  from their QFF results.

## 7.7 BIBLIOGRAPHY

Agúndez, M. & Wakelam, V. 2013, Chemical Reviews, 113, 8710

- Ali, A., Sittler, E. C., Chornay, D., Rowe, B. R., & Puzzarini, C. 2013, *Planetary Space Science*, 87, 96
- Botschwina, P. 2011b, *Physical Chemistry Chemical Physics*, 13, 14163
- Cox, P., Guesten, R., & Henkel, C. 1988, *Astronomy & Astrophysics*, 206, 108
- Craig, N. C., Pranata, J., Reinganum, S. J., Sprague, J. R., & Stevens, P. S. 1986, *Journal of the American Chemical Society*, 108, 4378
- Crofton, M. W., Jagod, M.-F., Rehfuss, B. D., Kreiner, W. A., & Oka, T. 1988, *The Journal of Chemical Physics*, 88, 666
- Dopfer, O., Roth, D., & Maier, J. 2002, *Journal of the American Chemical Society*, 124, 494
- Huang, X. & Lee, T. J. 2011, *The Astrophysical Journal*, 736, 33
- Huang, X., Taylor, P. R., & Lee, T. J. 2011, *Journal of Physical Chemistry A*, 115, 5005
- Lee, T. J., Willetts, A., Gaw, J. F., & Handy, N. C. 1989, *The Journal of Chemical Physics*, 90, 4330
- Madden, S. C., Irvine, W. M., Swade, D. A., Matthews, H. E., & Friberg, P. 1989, *The Astronomical Journal*, 97, 1403
- Motylewski, T. & Linnartz, H. 1999, *Review of Scientific Instruments*, 70, 1305
- Roth, D. & Dopfer, O. 2002, *Physical Chemistry Chemical Physics (Incorporating Faraday Transactions)*, 4, 4855
- Smith, D. 1992, *Chemical Reviews*, 92, 1473
- Western, C. M. 2014, PGOPHER version 8.0, university of Bristol Research Data Repository
- Wyss, M., Riaplov, E., & Maier, J. P. 2001, *The Journal of Chemical Physics*, 114, 10355
- Zhao, D., Doney, K. D., & Linnartz, H. 2014a, *Journal of Molecular Spectroscopy*, 296, 1
- Zhao, D., Guss, J., Walsh, A. J., & Linnartz, H. 2013, *Chemical Physics Letters*, 565, 132



ASTRONOMICAL INFRARED SPECTRUM OF DEUTERATED POLYCYCLIC AROMATIC HYDROCARBONS

---

The amount of deuterium locked up in polycyclic aromatic hydrocarbons (PAHs) has to date been an uncertain value. We present a near-infrared (NIR) spectroscopic survey of HII regions in the Milky Way, Large Magellanic Cloud (LMC), and Small Magellanic Cloud (SMC) obtained with AKARI, which aims to search for features indicative of deuterated PAHs (PAD or D<sub>n</sub>-PAH) to better constrain the D/H ratio of PAHs. Fifty-three HII regions were observed in the NIR (2.5 - 5 μm), using the Infrared Camera (IRC) on board the AKARI satellite. Through comparison of the observed spectra with a theoretical model of deuterated PAH vibrational modes, the aromatic and (a)symmetric aliphatic C-D stretch modes were identified. We see emission features between 4.4 - 4.8 μm, which could be unambiguously attributed to deuterated PAHs in only six of the observed sources, all of which are located in the Milky Way. In all cases, the aromatic C-D stretching feature is weaker than the aliphatic C-D stretching feature, and, in the case of M17b, this feature is not observed at all. Based on the weak or absent PAD features in most of the observed spectra, it is suggested that the mechanism for PAH deuteration in the ISM is uncommon.

## 8.1 INTRODUCTION

All deuterium (D; heavy hydrogen) was formed during the Big Bang and has subsequently been depleted through the process of astration, *i.e.*, destruction by nuclear reactions in the interior of stars (Epstein et al., 1976; Linsky et al., 2006). As a result, the amount of deuterium in a galaxy, either as a free atom in the gas phase or locked up in molecules or grains, provides a direct measure of cosmic nucleosynthesis and is related to the chemical evolution of the galaxy itself. Of particular interest is the incorporation of deuterium in polycyclic aromatic hydrocarbon (PAH) molecules. These molecules are ubiquitous and abundant in the interstellar medium (ISM); their UV/visible-pumped fluorescence is almost universally believed to give rise to aromatic infrared bands (AIBs). These bands dominate the mid-infrared (MIR) spectra of many interstellar objects, such as HII regions, planetary, and reflection nebulae, the diffuse ISM, and even entire galaxies (Leger & Puget, 1984; Allamandola et al., 1985, 1989; Tielens, 2008; Joblin & Tielens, 2011; Li & Draine, 2012). The large heat capacity associated with aromaticity (Schutte et al., 1993) suggests that once formed in stellar ejecta (Frenklach & Feigelson, 1989; Cherchneff et al., 1992) the PAH molecule is stable against photodissociation, at least compared to other ISM molecules. However, studies of meteorites (Kerridge et al., 1987) and recent laboratory experiments (Sandford et al., 2000; Throver et al., 2012; Klærke et al., 2013) show that PAHs can undergo processing, such as oxidation, reduction, and isotope exchange, which depend on the environments the PAH experience. The large size ( $> 50$  C atoms) and numerous hydrogen atoms of interstellar PAHs allows them to potentially be a large reservoir of deuterium in the ISM (Allamandola et al., 1989; Tielens, 1992; Hudgins et al., 2004). Consequently, deuterium-enriched PAHs have been suggested as a possible explanation for the variation of the gas phase atomic D/H ratio in the intermediate region of the Milky Way galaxy, which has an average value of  $\sim 14$  ppm, but has a range of a factor of 4 - 5 with measurements as low as about 5.0 ppm ( $\theta$  Car) and as high as about 21.8 ppm ( $\gamma^2$  Vel); the 17 ppm depletion in some regions cannot be explained through astration alone (Peeters et al., 2004; Draine, 2004; Linsky et al., 2006; Onaka et al., 2014).

Deuterium atoms can replace hydrogen atom in PAHs and can participate in the same characteristic vibrational modes (Bauschlicher Jr. et al., 1997). The heavier mass of deuterium shifts the C-D vibrational modes to longer wavelengths relative to the corresponding C-H vibrational modes (Bauschlicher Jr. et al., 1997; Allamandola, 1993; Sandford et al., 2000; Hudgins et al., 2004). Hydrogen or deuterium when bonded to the carbon skeleton such that the carbon retains its  $sp^2$  hybridization (denoted PAH or PAD, respectively) results in the aromatic C-H stretch mode at  $3.29 \mu\text{m}$  (Allamandola et al., 1989; Sandford et al., 2013) or the aromatic C-D stretch mode at  $4.40 \mu\text{m}$  (Bauschlicher Jr. et al., 1997; Hudgins et al., 2004). If the hydrogen or deuterium adds to the PAH, resulting in a carbon with  $sp^3$  hybridization (denoted  $H_n$ -PAH or  $D_n$ -PAH, respectively), then the  $CH_2$  or  $CDH$  groups show both asymmetric and symmetric aliphatic stretching modes. These features fall at  $3.40$  and  $3.50 \mu\text{m}$  for the C-H asymmetric and symmetric stretching modes, respectively (Sandford et al., 2013), and  $4.63$  and  $4.75 \mu\text{m}$  for the C-D asymmetric and symmetric stretching modes (Hudgins et al., 2004). Recently, Buragohain et al. (2015) showed that the  $4.75 \mu\text{m}$  feature may also be due to the C-D stretch of deuterated PAH cations ( $D_n$ -PAH $^+$ ). For both C-H and C-D aliphatic stretching modes, the intensity of the asymmetric stretch is intrinsically greater than the symmetric stretch because of the larger dipole moment. Other infrared features indicative of deuterated PAHs can arise in the  $9 - 18 \mu\text{m}$  as a result of bending of the C-D bonds. However, their exact position will vary across that region depending on the number of nonadjacent D atoms (Peeters et al., 2004), in some cases superimposing on the C-H bending modes of standard PAHs.

Detection of PAD/ $D_n$ -PAHs features in the IR spectrum present the astronomer with several challenges. All three of the deuterated C-H features are predicted to be weak (Bauschlicher Jr. et al., 1997; Hudgins et al., 2004). Also, their expected positions coincide with HI emission lines, and the symmetric stretching feature at  $4.75 \mu\text{m}$  is the only feature to lie in a portion of the spectrum clear

of other emission lines. Additionally, ground-based observations of deuterated PAHs are almost impeded by the absorption band of telluric CO<sub>2</sub> between 4.3 - 4.7  $\mu\text{m}$  (Bauschlicher Jr. et al., 1997; Hudgins et al., 2004). The best targets for the search of deuterated PAHs are regions where the PAH emission is strongest, such as the surface layers of photodissociation regions (PDRs) in HII regions.

So far, deuterated PAHs have been detected by ISO-SWS in the Orion Bar and M17 primarily through the C-D asymmetric stretching feature. The estimated number of deuterium atoms relative to hydrogen atoms on PAHs (denoted PAH D/H), based on the ratio of sum of the 4.4 and 4.63  $\mu\text{m}$  intensities to the 3.29 and 3.4 - 3.5  $\mu\text{m}$  intensities, were found to be  $0.17 \pm 0.03$  in the Orion Bar, and  $0.36 \pm 0.08$  in M17 (Peeters et al., 2004) without considering the intrinsic intensities between the C-D and C-H stretching features, a factor of  $\sim 1.75$  (Bauschlicher Jr. et al., 1997). The PAH D/H ratio, based on deuterated PAH features in M17, was indeed consistent with the observed Galactic variation of atomic D/H ratio in the gas phase. Recently, Onaka et al. (2014) reported an upper limit PAH D/H ratio of  $0.029 \pm 0.002$  in the Orion Bar and  $0.023 \pm 0.004$  in M17 with AKARI observations at slightly different pointing positions compared to the ISO-SWS observations, and taking the intrinsic intensities into account. The significant difference in the observed deuterium abundance in PAHs made it desirable to obtain multiple spectra of a large number of sources, at a variety of galactic evolution stages, with high signal-to-noise ratios to better constrain the deuterium abundance in PAHs, and to determine if the deuterium fractionation of PAHs could be not only highly variable between sources, but also within a source. To this end, we present our search for deuterated PAHs in a sample of HII regions observed with AKARI.

## 8.2 OBSERVATIONS AND DATA REDUCTION

The infrared camera (IRC) of the AKARI satellite offers NIR spectroscopy of the 2.5 - 5  $\mu\text{m}$  region with a resolution of  $R \sim 100$  for diffuse sources (Onaka et al., 2007). The observations in this study were taken during the post-helium mission phase (Phase 3) of the AKARI satellite with the N<sub>H</sub> slit ( $1' \times 3''$ ) with grism disperser, providing a dispersion of 0.0097  $\mu\text{m}/\text{px}$  in this range (Onaka et al., 2007). At 5  $\mu\text{m}$  the grism sensitivity decreases compared to 3  $\mu\text{m}$  region, resulting in a larger noise level in the region where the PAD features are expected.

This study is based on the DABUN observational program, which observed seven HII regions in the Large Magellanic Cloud (LMC), five in the Small Magellanic Cloud (SMC), and eight in the Milky Way (MW), chosen based on their corresponding radio data (Paladini et al., 2003; Filipovic et al., 1998). Thirty-three additional Milky Way sources were added from the AKARI Near-Infrared Spectral Atlas of Galactic HII Regions Version 1 public release (Mori et al., 2014). The details of the observation data are given in Table 8.1.

The data reduction was carried out with the official AKARI spectroscopy pipeline for the Phase 3 data (version 20111121; Onaka et al. 2009). Spectra were extracted from the area corresponding to the brightest PAH flux at 3.3  $\mu\text{m}$ . This corresponds to extraction areas of  $10''.22 \times 3''$  for LMC and SMC sources,  $7''.3 \times 3''$  or  $10''.22 \times 3''$  for MW sources that were part of the DABUN program and  $8''.76 \times 3''$  for MW sources retrieved from the AKARI public release catalog of Mori et al. (2014). The resulting spectra were subsequently spatially and spectrally smoothed by 3 pixels to remove shot noise without significantly changing the spatial or spectral resolution. In later observations, the thermal noise was noticeable even after pipeline processing, requiring additional post-pipeline dark current subtraction, which was performed following the procedure outlined by Mori et al. (2014).

For most of the targets, we took two or three observations (Table 8.1). The pointing accuracy of AKARI can vary up to about  $30''$  between the intended and actual target pointing positions; as such we analyzed each observation separately. In the cases with three observations of the same source, the spectrum with significantly different features was removed from analysis based on the assumption that, because of limited pointing accuracy, that spectrum was observing a significantly

different part of the HII region. The selection was further reduced by removing the spectra without sufficient signal-to-noise to quantify extinction or PAH emission features.

### 8.3 RESULTS AND ANALYSIS

All of the analyzed spectra show a number of features, typical of HII regions, such as HI recombination lines, CO<sub>2</sub> ice features, and the PAH bands at 3.29 and 3.4 - 3.6  $\mu\text{m}$  (Figure 8.1). The uncertainty in the relative flux calibration is less than 10%. The MW sources have better signal-to-noise compared to the LMC and SMC sources, which lie on average at distances of  $\sim 50$  kpc (Pietrzyński et al., 2013) and  $\sim 60$  kpc (Hilditch et al., 2005), respectively. As a result, while the PAH aromatic C-H stretching mode at 3.29  $\mu\text{m}$  is seen in all of the spectra, in some of the LMC and SMC spectra the PAH flux is too weak to distinguish the aliphatic C-H features from the noise.

Some of the MW source spectra show ice absorption features of H<sub>2</sub>O and CO<sub>2</sub>, which likely arise from cold interstellar clouds between the source and AKARI. All of the obtained spectra show emission features indicative of ionized gas in HII regions. For example, the prominent HI recombination lines Br $\alpha$  at 4.052  $\mu\text{m}$  and Br $\beta$  at 2.626  $\mu\text{m}$  are seen in all spectra, and a few also show a number of other hydrogen and helium recombination lines, all of which are fit with Gaussian functions; the fit parameters are listed in Table 8.2. There is a shift in the observed central wavelength of the HI lines relative to their literature values, but the discrepancy is within the uncertainty of the wavelength calibration of  $\sim 0.005$   $\mu\text{m}$ .

The continuum is fit with a third order polynomial, taking into account the broad continuum plateau from 3.2 - 3.6  $\mu\text{m}$ , and then subtracted. The H<sub>2</sub>O absorption feature around 3.05  $\mu\text{m}$  is fit via laboratory spectrum of pure H<sub>2</sub>O ice at 10 K taken from the Leiden Ice Database (Gerakines et al., 1996). In contrast, the CO<sub>2</sub> ice feature cannot be completely resolved using the AKARI/IRC slit spectroscopy, and is fit using a negative Gaussian function; details of the fit for the spectra are listed in Table 8.2.

The PAH and D<sub>n</sub>-PAH fluxes at 3.29 and 4.63  $\mu\text{m}$ , respectively, overlap with the HI emission lines Pf $\delta$  at 3.297  $\mu\text{m}$ , Pf $\beta$  at 4.654  $\mu\text{m}$ , and Hue at 4.673  $\mu\text{m}$ . The expected HI emission intensities are determined relative to Br $\alpha$  and Br $\beta$ , assuming case B recombination conditions of  $T_e = 10^4$  K and  $n_e = 10^4$   $\text{cm}^{-3}$  for the Milky Way and  $T_e = 10^4$  K and  $n_e = 10^2$   $\text{cm}^{-3}$  for the LMC and SMC (Storey & Hummer, 1995) and an extinction law of  $A_\lambda = \lambda^{-1.7}$  (Martín-Hernández et al., 2002a). To determine the flux of the underlying features, the overlapping HI lines are modeled as Gaussian functions and subtracted from the spectrum. The extinction-corrected intensity subtraction introduces an uncertainty of  $\sim 10\%$  to the flux of the underlying feature. The observed flux at 4.17 and 4.37  $\mu\text{m}$  can be fit by the HI Hu<sub>13</sub> and Hu<sub>12</sub> expected flux, with some excess flux at 4.4  $\mu\text{m}$ .

The PAH and H<sub>n</sub>-PAH features and their deuterium counterparts are fit with Gaussian functions; the details of the fits are given in Table 8.2. Based on band position coincidence between observed excess flux and laboratory (Sandford et al., 2000) and theoretical data (Hudgins et al., 2004), PAD and/or D<sub>n</sub>-PAH features were detected in six Milky Way sources: IRAS12073-6233, NGC3603, M8, M17b, W51, and G75.783+0.343 (Figures 8.1 and 8.2); the calculated PAH and H<sub>n</sub>-PAH fluxes are summarized in Table 8.3, while the calculated PAD and D<sub>n</sub>-PAH fluxes are summarized in Table 8.4. Of the six sources, IRAS12073-6233 and W51 had two observations that showed PAD and D<sub>n</sub>-PAH features. In addition three sources: IRAS 15384-5348, M17a, and NGC3576, show a less than 3  $\sigma$  detection of the asymmetric C-D stretch, but because of noisy baseline the accompanying symmetric mode was not seen. Aromatic C-H stretch overtone and combination bands, as well as, contributions from aliphatic side groups also fall in the range of 3.4 - 3.6  $\mu\text{m}$  (Allamandola et al., 1989; Sandford et al., 2013; Pilleri et al., 2015), and similarly, contributions from the C-D analogs likely fall between 4.6 - 5.0  $\mu\text{m}$ . For analysis, we assume that aliphatic groups are attached to the main PAH rings, *i.e.*, superhydrogenated PAHs/PADs contribute the majority of the flux in these wavelength ranges, and the determined strength of these bands are consequently upper limits.

The aromatic C-D stretch feature at 4.4  $\mu\text{m}$  and aliphatic C-D (a)symmetric stretch features at

Table 8.1: Observation log and target parameters (in degrees)

Target	Slit center position		Observation ID	Observation date
	RA	Dec		
LMCN4A	73.029	-66.921	4300021.1, 4300021.2, 4301021.1	2008 Dec 4, 2008 Dec 4, 2009 Dec 4
LMCN83B	73.609	-69.184	4300022.1, 4300022.2, 4301022.1	2008 Nov 14, 2008 Nov 14, 2009 Nov 18
LMCN57A	83.104	-67.698	4300023.1, 4300023.2, 4301023.2	2008 Nov 8, 2008 Nov 8, 2009 Nov 8
LMCN105A-IRS1	77.453	-68.879	4300024.1, 4300024.2, 4301024.2	2008 Nov 11, 2008 Nov 11, 2009 Nov 12
LMCN91A	74.313	-68.442	4300025.1, 4300025.2, 4301025.3	2008 Nov 19, 2008 Nov 20, 2009 Nov 24
LMCN77A	72.363	-69.202	4300026.1, 4300026.2, 4301026.3	2008 Nov 16, 2008 Nov 16, 2009 Nov 18
LMCN191A	76.157	-70.908	4300027.1, 4300027.2, 4301027.4	2008 Oct 28, 2008 Oct 28, 2009 Nov 6
SMCN26	12.036	-73.249	4300028.1, 4300028.2	2008 Nov 1, 2008 Nov 2
SMCN10	11.235	-73.170	4300029.1, 4300029.2	2008 Oct 31, 2008 Nov 1
SMCN88A	21.033	-73.151	4300030.1, 4300030.2	2008 Nov 4, 2008 Nov 4
SMCN66	14.772	-72.177	4300031.1, 4300031.2, 4301031.1	2008 Nov 4, 2008 Nov 5, 2009 Nov 6
SMCN81	17.304	-73.194	4300032.1, 4300032.2	2008 Nov 3, 2008 Nov 3
IRAS14567-5846	225.230	-58.981	4300033.1, 4300033.2	2009 Feb 19, 2009, Feb 19
IRAS15384-5348	235.569	-53.976	4300034.1, 4300034.2	2009 Feb 24, 2009 Feb 24
IRAS15502-5302	238.527	-53.194	4300035.1, 4300035.2	2009 Feb 26, 2009 Feb 26
IRAS12073-6233	182.494	-62.832	4300036.1, 4300036.2	2009 Jan 28, 2009 Jan 28
GAL314.2+00.3	216.237	-60.511	4300037.1, 4300037.2	2009 Feb 14, 2009 Aug 19
GAL319.9+00.8	225.905	-57.650	4300038.1, 4300038.2	2009 Feb 19, 2009, Feb 19
GAL336.0+00.1	247.744	-48.164	4300039.1, 4300039.2	2009 Mar 3, 2009 Mar 3
GAL334.7-00.7	247.269	-49.656	4300040.1, 4300040.2	2009 Mar 3, 2009 Mar 4
M8	270.922	-24.377	5200161.1	2008 Sep 23
G8.137+0.228	270.759	-21.800	5200163.1	2008 Sep 22
W31a	272.363	-20.322	5200165.1	2008 Sep 24
W31b	272.255	-20.084	5200167.1	2008 Sep 24
M17b	275.119	-16.204	5200171.1	2008 Sep 28
M17a	275.110	-16.181	5200169.1	2008 Sep 27
W42	279.564	-6.795	5200294.1, 5200294.2	2008 Oct 2, 2008 Oct 2
G29.944-0.042	281.518	-2.653	5200295.1, 5200295.2	2008 Oct 4, 2008 Oct 4
W49A	287.568	9.108	5200299.1, 5200299.2	2008 Oct 12, 2007 Oct 13
G48.596+0.042	290.127	13.930	5200300.1, 5200300.2	2008 Oct 17, 2008 Oct 17
W51	290.561	14.051	5200301.1, 5200301.2	2008 Oct 17, 2008 Oct 18
W58A	300.440	33.548	5201198.1, 5200767.1	2009 May 2, 2009 Nov 6
G70.293+1.600	300.440	33.548	5200337.1	2008 Nov 6
G75.783+0.343	305.422	37.430	5200772.1	2009 May 11
G76.383-0.621	306.863	37.381	5200343.1	2008 Nov 15
G78.438+2.659	304.913	40.943	5200776.1	2009 May 13
DR7	307.037	40.875	5200769.1	2009 May 17
G81.679+0.537	309.752	42.331	5200347.1	2008 Nov 22
G111.282-0.663	349.020	60.038	5200432.1	2009 Jan 16
RCW42	141.106	-51.990	5200452.1	2008 Dec 15
G282.023-1.180	151.653	-57.204	5200436.1	2009 Jan 1
RCW49	156.034	-57.788	5200438.1	2009 Jan 4
NGC3372	160.883	-59.580	5200440.1	2009 Jan 10
G289.066-0.357	164.124	-60.098	5200442.1	2009 Jan 13
NGC3576	167.984	-61.313	5200444.1	2009 Jan 17
NGC3603	168.756	-61.263	5200446.1	2009 Jan 17
G319.158-0.398	225.816	-59.074	5200933.1	2009 Aug 25
G330.868-0.365	242.601	-52.099	5200109.1	2008 Sep 2
G331.386-0.359	243.183	-51.748	5200113.1	2008 Sep 3
G333.122-0.446	245.255	-50.585	5200121.1	2008 Sep 4
G338.398+0.164	250.032	-46.385	5200942.1, 5200942.2	2009 Sep 7, 2009 Sep 7
G338.400-0.201	250.468	-46.582	5200943.2	2009 Sep 7
G345.528-0.051	256.538	-40.962	5200133.1	2008 Sep 11

Table 8.2: Gaussian profile parameters for ice absorption features and emission lines fitted in the spectra

Line	$\lambda_{\text{center}}$ ( $\mu\text{m}$ )	FWHM ( $\mu\text{m}$ )
HI Br $\beta$	2.6259	0.026
HI Pfi3	2.6751	0.026
HI Pfi2	2.7583	0.026
HI Pfi $\eta$	2.8730	0.026
HI Pfi $\epsilon$	3.0392	0.026
PAH	3.29	0.060
HI Pfi $\delta$	3.2970	0.026
H <sub>n</sub> -PAH	3.40	0.058
H <sub>n</sub> -PAH	3.45	0.058
H <sub>n</sub> -PAH	3.50	0.058
H <sub>n</sub> -PAH	3.56	0.058
HI Pfi $\gamma$	3.7406	0.026
H <sub>2</sub> o-o S(13)	3.846	0.026
HI Br $\alpha$	4.0523	0.026
HI Hu13	4.1708	0.026
CO <sub>2</sub>	4.26	0.047
He I ( <sup>3</sup> S <sub>1</sub> - <sup>3</sup> P <sub>0</sub> )	4.2954	0.026
HI Hu12	4.3765	0.026
PAD	4.40	0.047
D <sub>n</sub> -PAH	4.63	0.047
HI Pfi $\beta$	4.6538	0.026
HI Hu $\epsilon$	4.6725	0.026
D <sub>n</sub> -PAH	4.75	0.047
D <sub>n</sub> -PAH	4.80	0.047
D <sub>n</sub> -PAH	4.85	0.047

4.63 - 4.85  $\mu\text{m}$  are present in all eight of the spectra (Figures 8.1 and 8.2), with the exception of M17b. As noted by Peeters et al. (2004) for M17, the nearby source M17b does not show the aromatic C-D stretch band. The aromatic C-D stretch mode is observed to be blended with the HI Hu12 emission line. Nonetheless, two Gaussian profiles are needed to reproduce the observed spectrum, and detections of the same blended feature in multiple sources suggest that the feature is not noise even though they are only  $\sim 1 \sigma$  level detections. The aliphatic C-D asymmetric stretch feature is heavily blended with HI emission lines and, as a result, its intensity is an estimation based on the intrinsic intensity ratio of the C-D symmetric to asymmetric modes and the intensity of the unobscured C-D symmetric feature. Simultaneous fitting of the Pfi $\beta$ , Hu $\epsilon$ , and estimated C-D asymmetric stretch features is able to reproduce the observed spectrum, which suggests that the estimation is good. In the case of IRAS12073-6233 and NGC3603 (Figure 8.1 a), b), c) and Figure 8.2 a), b), c)), the PAD and D<sub>n</sub>-PAH signal to noise was large enough that the minor features seen in the Hudgins et al. (2004) modeled spectra at 4.8 - 4.9  $\mu\text{m}$  are discernible. In NGC3603, however, the minor feature at 4.84  $\mu\text{m}$  has a significantly larger intensity than expected based on the model in Hudgins et al. (2004), which is likely a result of the continuum subtraction.

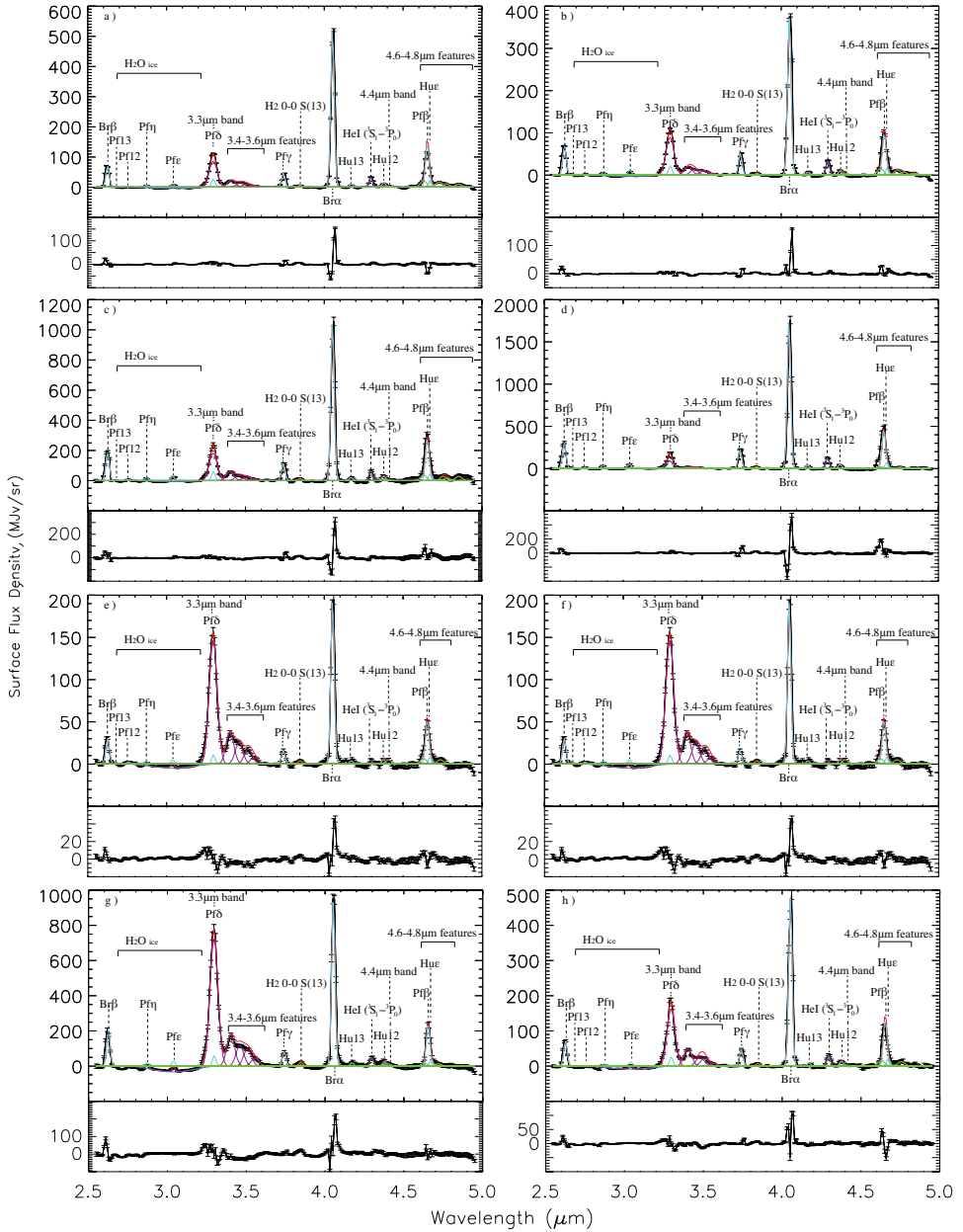


Figure 8.1: Fitting results for the spectra of a) IRAS12073-6233 obs. 1, b) IRAS12073-6233 obs. 2, c) NGC3603, d) M17b, e) W51 obs. 1, f) W51 obs. 2, g) M8, and h) G75.783+0.343 in red. The black line is the observed spectra, the H $\alpha$  emission lines are fit in cyan, the HeI emission line is fit in navy, the H $_2$ O ice absorption line is fit in blue, the H $_2$  rotational line is fit in orange, PAH and H $_n$ -PAH features are fit in purple, and PAD and D $_n$ -PAH features are fit in green. Below each figure is the corresponding residual plot.

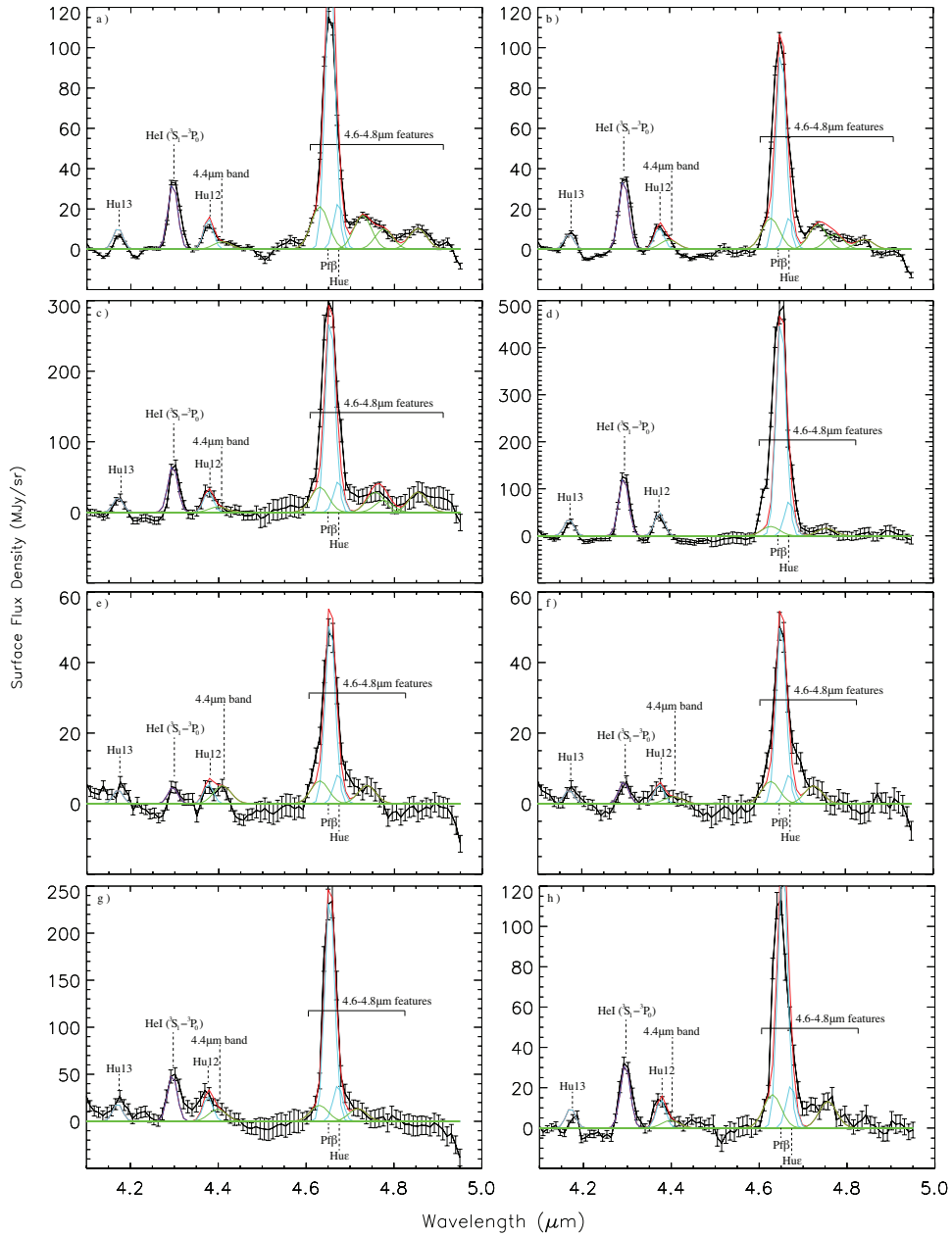


Figure 8.2: Close up of the C-D stretching region of the spectra of a) IRAS12073-6233 obs. 1, b) IRAS12073-6233 obs. 2, c) NGC3603, d) M17b, e) W51 obs. 1, f) W51 obs. 2, g) M8, and h) G75.783+0.343. The fitting results for the spectra is shown in red, the black line is the observed spectra, the H I emission lines are fit in cyan, the He I emission line is fit in navy, and PAD and  $D_n$ -PAH features are fit in green.

Table 8.3: PAH/ $H_n$ -PAH fluxes<sup>a</sup> for sources with detectable deuterated features

Source	$A_v$ (mag)	3.29 $\mu$ m	3.4 $\mu$ m	3.45 $\mu$ m <sup>b</sup>	3.5 $\mu$ m	3.56 $\mu$ m <sup>b</sup>
		Aromatic C-H	Asymmetric Aliphatic C-H	Symmetric Aliphatic C-H		
G75.783+0.343	28	22.2 $\pm$ 2.0 125 $\sigma$	6.2 $\pm$ 0.6 37 $\sigma$	3.3 $\pm$ 0.4 20 $\sigma$	2.9 $\pm$ 0.9 18 $\sigma$	0.9 $\pm$ 0.2 5.5 $\sigma$
NGC3603	22	25.1 $\pm$ 2.4 69 $\sigma$	7.8 $\pm$ 0.8 23 $\sigma$	4.6 $\pm$ 0.6 14 $\sigma$	3.1 $\pm$ 1.2 9.5 $\sigma$	1.2 $\pm$ 0.5 3.7 $\sigma$
W51 obs. 1	26	20.0 $\pm$ 1.8 182 $\sigma$	4.8 $\pm$ 0.5 47 $\sigma$	3.2 $\pm$ 0.3 32 $\sigma$	2.3 $\pm$ 0.5 23 $\sigma$	0.9 $\pm$ 0.2 9.5 $\sigma$
W51 obs. 2	26	20.6 $\pm$ 1.8 232 $\sigma$	4.9 $\pm$ 0.5 59 $\sigma$	3.2 $\pm$ 0.3 39 $\sigma$	2.2 $\pm$ 0.4 27 $\sigma$	1.2 $\pm$ 0.2 15 $\sigma$
M17b	23	12.3 $\pm$ 1.5 20 $\sigma$	2.9 $\pm$ 0.5 5.1 $\sigma$	2.1 $\pm$ 0.4 3.6 $\sigma$	0.8 $\pm$ 0.5 1.5 $\sigma$	0.8 $\pm$ 0.4 1.4 $\sigma$
M8	16	99.1 $\pm$ 8.9 175 $\sigma$	22.9 $\pm$ 2.2 44 $\sigma$	14.7 $\pm$ 1.5 28 $\sigma$	12.1 $\pm$ 2.2 24 $\sigma$	5.5 $\pm$ 0.9 11 $\sigma$
IRAS12073-6233 obs. 1	31	11.7 $\pm$ 1.0 149 $\sigma$	2.9 $\pm$ 0.3 40 $\sigma$	1.9 $\pm$ 0.2 27 $\sigma$	1.3 $\pm$ 0.2 18 $\sigma$	0.6 $\pm$ 0.1 9.0 $\sigma$
IRAS12073-6233 obs. 2	22	12.2 $\pm$ 1.0 69 $\sigma$	2.6 $\pm$ 0.2 16 $\sigma$	1.7 $\pm$ 0.2 11 $\sigma$	1.3 $\pm$ 0.2 8.0 $\sigma$	0.5 $\pm$ 0.1 2.8 $\sigma$

a. In units of  $10^{-17} \text{ Wm}^{-2} \text{ arcsec}^{-2}$ 

b. See text for discussion of the origin of these features.

Table 8.4: PAD/ $D_n$ -PAH fluxes<sup>a</sup> for sources with detectable deuterated features

Source	4.4 $\mu$ m	4.63 $\mu$ m	4.75 $\mu$ m	4.8 $\mu$ m <sup>b</sup>	4.85 $\mu$ m <sup>b</sup>	D/H
	Aromatic C-D	Asymmetric Aliphatic C-D	Symmetric Aliphatic C-D			
G75.783+0.343	0.30 $\pm$ 0.19 1.2 $\sigma$	1.26 $\pm$ 0.53 5.3 $\sigma$	0.99 $\pm$ 0.33 4.2 $\sigma$			0.13 $\pm$ 0.03
NGC3603	0.62 $\pm$ 0.52 1.3 $\sigma$	2.73 $\pm$ 1.57 5.8 $\sigma$	2.13 $\pm$ 0.98 4.7 $\sigma$	1.73 $\pm$ 0.79 3.8 $\sigma$	2.11 $\pm$ 1.07 4.7 $\sigma$	0.37 $\pm$ 0.10
W51 obs. 1	0.41 $\pm$ 0.14 5.4 $\sigma$	0.49 $\pm$ 0.29 6.8 $\sigma$	0.39 $\pm$ 0.18 5.5 $\sigma$			0.07 $\pm$ 0.02
W51 obs. 2	0.16 $\pm$ 0.14 2.1 $\sigma$	0.48 $\pm$ 0.29 6.6 $\sigma$	0.38 $\pm$ 0.18 5.3 $\sigma$			0.06 $\pm$ 0.02
M17b		1.53 $\pm$ 1.19 6.6 $\sigma$	1.19 $\pm$ 0.75 5.3 $\sigma$			0.25 $\pm$ 0.13
M8	1.03 $\pm$ 0.53 4.5 $\sigma$	1.05 $\pm$ 1.00 4.8 $\sigma$	0.82 $\pm$ 0.63 3.8 $\sigma$			0.03 $\pm$ 0.01
IRAS12073-6233 obs. 1	0.30 $\pm$ 0.08 1.2 $\sigma$	1.62 $\pm$ 0.28 6.7 $\sigma$	1.26 $\pm$ 0.17 5.3 $\sigma$	0.76 $\pm$ 0.15 3.2 $\sigma$	0.76 $\pm$ 0.16 3.3 $\sigma$	0.44 $\pm$ 0.05
IRAS12073-6233 obs. 2	0.37 $\pm$ 0.08 3.2 $\sigma$	1.18 $\pm$ 0.23 10.7 $\sigma$	0.92 $\pm$ 0.23 8.5 $\sigma$	0.46 $\pm$ 0.16 4.3 $\sigma$	0.36 $\pm$ 0.14 3.4 $\sigma$	0.31 $\pm$ 0.04

a. In units of  $10^{-17} \text{ Wm}^{-2} \text{ arcsec}^{-2}$ 

b. See text for discussion of the origin of these features.

In the 3.8 - 4.6  $\mu\text{m}$  region, there are a number of features that can be attributed to either HI lines, the 0 - 0  $S(13)$  -  $S(9)$  ro-vibrational transitions of  $\text{H}_2$ , or deuterated PAHs. Notably, the  $S(10)$  transition of  $\text{H}_2$  at 4.4  $\mu\text{m}$  overlaps the expected position of the aromatic C-D stretch mode. The  $S(13)$  transition at 3.85  $\mu\text{m}$  is seen clearly in all eight of the spectra. Based on the intensities of the excess flux at the positions corresponding to the  $S(12)$  -  $S(9)$  transitions of  $\text{H}_2$  and level populations predicted by non-LTE models of  $\text{H}_2$  (Bertoldi et al., 2000), we cannot rule out the  $S(10)$  transition of  $\text{H}_2$  as the carrier of the 4.4  $\mu\text{m}$  excess flux at the present spectral resolution. However, for the analysis we assume the 4.4  $\mu\text{m}$  feature is the aromatic C-D stretch in order to obtain an upper limit on its abundance. In the case of the C-D aliphatic stretch features, the excess fluxes at 4.63  $\mu\text{m}$ , and 4.75  $\mu\text{m}$  do not match the  $S(9)$  transition of  $\text{H}_2$  within the wavelength calibration uncertainties, and thus the  $\text{H}_2$  transition does not influence their assignments.

If we only take the intrinsic intensity ratio of C-D to C-H features into account, which reduces the overall intensities for deuterium features by a factor of  $\sim 1.75$  (Bauschlicher Jr. et al., 1997), the number of deuterium atoms relative to hydrogen atoms on PAHs is then estimated from the ratio of the sum of the corrected deuterated features to the sum of the hydrogenated features. An observed upper limit of the PAH D/H is determined to be between 0.03 and 0.44, which is summarized in Table 8.4.<sup>1</sup> For sources with multiple observations, W51 and IRAS12073-6233, it was found that the PAH D/H ratio is consistent within flux uncertainties in W51, but not in IRAS12073-6233. This may hint that very local conditions are indeed important to the deuterium variations, but more observations at higher spatial resolution are needed to confirm this.

The amount of deuterium at either an aromatic or aliphatic position was also determined through a comparison of observed PAH D/H ratios to those expected if one hydrogen is replaced with a deuterium at either an aromatic or aliphatic position. From the 3.4/3.29  $\mu\text{m}$  ratio, the amount of aliphatic hydrogen relative to aromatic hydrogen,  $N_{\text{aliphatic,H}}/N_{\text{aromatic,H}}$ , of the PAHs in the eight observations was determined to be between 0.2 - 0.3 (Table 8.3), which is significantly larger than the  $N_{\text{aliphatic,H}}/N_{\text{aromatic,H}} \sim 0.02$  typically seen in PAHs in the ISM (Tielens, 2008). Additionally, neutral, small ( $N_{\text{C}} < 50$ ) PAHs molecules are considered to mainly contribute to the 3.3  $\mu\text{m}$  feature, so from the PAH IR Spectral Database (Boersma et al., 2014) six representative PAHs (three extended and three compact) were chosen to determine the expected D/H ratios:  $\text{C}_{40}\text{H}_{22}$ ,  $\text{C}_{40}\text{H}_{16}$ ,  $\text{C}_{32}\text{H}_{18}$ ,  $\text{C}_{32}\text{H}_{14}$ ,  $\text{C}_{24}\text{H}_{14}$ , and  $\text{C}_{24}\text{H}_{12}$ . For example, for  $\text{C}_{40}\text{H}_{22}$  to get an  $N_{\text{aliphatic,H}}/N_{\text{aromatic,H}} \sim 0.22$ , there would be four aliphatic hydrogens and 18 aromatic hydrogens. Replacement of an aromatic hydrogen with an aromatic deuterium would result in an aromatic D/H of 0.06, and replacement of one aliphatic hydrogen for an aliphatic deuterium would result in an aliphatic D/H ratio of 0.33. If this is evaluated for the six representative molecules, on average a monodeuterated  $\text{D}_1$ -PAH would have an expected aliphatic D/H of  $\sim 0.5$ , while a monodeuterated PAD would have an average expected aromatic D/H of  $\sim 0.09$ .

The ratio of the 4.40  $\mu\text{m}$  features to the 3.29  $\mu\text{m}$  features gives a fractional abundance of aromatic deuterium to aromatic hydrogen of  $< 0.05$  for all eight observations. In contrast, based on the sum of the 4.63 and 4.75  $\mu\text{m}$  features relative to the sum of the 3.40 and 3.50  $\mu\text{m}$  features, the fractional abundance of aliphatic deuterium relative to aliphatic hydrogen is much larger, varying from 0.09 to 1. For a representative PAH, for example, the hydrogenated PAH  $\text{C}_{40}\text{H}_{18}$ , these observed deuterium abundances would yield at most 1 aromatic deuterium, 2 aliphatic deuterium, 13 aromatic hydrogen, and 2 aliphatic hydrogen, and a PAH D/H of 0.2, which is roughly representative of the average of the values determined for the eight observations. Based on the expected D/H ratios, it is estimated that in all eight observations less than 10% of the observed PAHs have one aromatic deuterium. Conversely, with the exception of the PAHs in W51 and M8, all of the observed PAHs have at least one aliphatic deuterium. In particular, the aliphatic D/H ratios for IRAS12073-6233

<sup>1</sup> The PAH D/H is calculated as the sum of the deuterium feature fluxes (Table 8.4 columns 2 - 6) divided by a factor of 1.75 to account for intrinsic intensities, divided by the sum of the hydrogen feature fluxes (Table 8.3 columns 3 - 7). The given PAH D/H uncertainties in Table 8.4 do not take errors of various origins into account, including the difference of excitation of PADs/ $\text{D}_n$ -PAHs and PAHs/ $\text{H}_n$ -PAHs, the assignment uncertainties of minor spectral features, or the uncertainties in the intrinsic intensities between different vibrational modes.

and M17b are more in agreement with the PAHs having one aliphatic deuterium for every aliphatic hydrogen. Furthermore, the aliphatic D/H ratios  $\sim 0.4$  and  $\sim 0.30$  for IRAS12073-6233 obs. 1 and obs. 2, respectively, suggest that almost all of the deuterium is in aliphatic positions.

The determined amount of deuterium relative to hydrogen on PAHs are upper limits, and a more complete understanding would include the effects of the emission process on the band intensities; to understand these effects we calculated the emission spectrum of a prototype PAH molecule, neutral ovalene, where one solo hydrogen is substituted with a  $-\text{CH}_2\text{D}$  group ( $N_{\text{C}} = 33$ ). To model the emission process, we follow the procedure described in Candian et al. (2012), where both the infrared spectrum of the molecule in question and its photoabsorption cross-section were evaluated with quantum chemistry techniques. As the effective temperature of the exciting source, we assume  $T_{\text{eff}} = 40000$  K, as in IRAS 12073-6233 (Martín-Hernández et al., 2002b), which is one of the HII regions in our sample.

For this molecule, the intrinsic  $3.3/4.75 \mu\text{m}$  (C-H aromatic/C-D aliphatic) ratio is 1.81 (consistent with earlier calculations of Bauschlicher Jr. et al. (1997)). The emission process brings the band ratio to 0.64, which then will correspond to a D/H range of 0.01 - 0.16 in our sample. These values are clearly sensitive to the parameters assumed in the emission model (e.g., effective temperature, PAH size), for example, M17. Peeters et al. (2004) did not consider the emission process and found a  $\text{D}/\text{H} = 0.36 \pm 0.08$ , while for the same source Onaka et al. (2014) via an emission model that favored larger PAHs found an upper limit  $\text{D}/\text{H} = 0.023 \pm 0.004$ . Similarly, we find a  $\text{D}/\text{H} = 0.09 \pm 0.05$  for the nearby source M17b via our emission model, which favors smaller PAHs. Therefore, the observed band intensity ratio can overestimate the actual relative abundance of deuterium to hydrogen on PAHs and the amount is dependent on the emission process. Stronger constraints on the typical PAH size population and exciting source characteristics in HII regions would improve our estimate of the deuterium abundance.

## 8.4 DISCUSSION

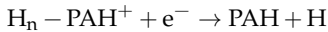
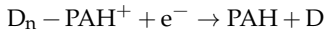
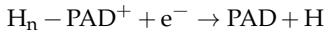
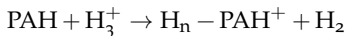
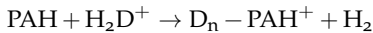
High levels of deuteration have been observed in some species, e.g.,  $\text{CD}_3\text{OH}$ ,  $\text{ND}_3$  (Parise et al., 2004; Lis et al., 2002; van der Tak et al., 2002), which are thought to originate from grain surface chemistry (Roberts et al., 2003). Deuterium fractionation is not as extensive for PAHs. In the best case (IRAS12073-6233 observation 1), the PAH D/H value is 0.44 (Table 8.4), which would translate to a fraction of gas-phase atomic deuterium (relative to hydrogen) locked up in PAHs of roughly 18 ppm; these are determined following the analysis method outlined in Onaka et al. (2014). Of the sources with observed deuterated PAHs, the average PAH D/H fraction is 0.21, which corresponds to a locked up fraction of gas-phase deuterium (relative to hydrogen) of about 10 ppm. Observation of atomic deuterium in the local ISM shows strong variation in the D/H abundance ratio of the gas phase at the 17 ppm level (Linsky et al., 2006). While our observations are not along the same lines of sight, they indicate that PADs and  $\text{D}_n$ -PAHs would be a major reservoir of elemental deuterium. Moreover, our study also reveals strong variation in the deuterated PAH to PAH ratio. Hence, the interaction of atomic deuterium with PAHs could well be at the origin of the observed variation in the gas-phase deuterium abundance.

While deuterated PAHs are not omnipresent, when present, deuteration is efficient; all eight observations have a PAH D/H ratio that is significantly greater than the cosmic gas-phase abundance of  $\sim 10^{-5}$  (Vidal-Madjar et al., 1998). Incorporation of deuterium into PAHs can occur through a number of mechanisms, most of which are driven by the small difference in zero-point energy between hydrogen and deuterium. Deuterium enrichment can take place in the gas phase or through solid state reactions within ice or on grains.

Large deuteration fractionation can occur in PDRs at depths where most of the hydrogen is locked up in  $\text{H}_2$ , but deuterium is still mainly atomic.  $\text{H}_2$  and HD are expected to show different behavior with depth into a cloud, as self-shielding of  $\text{H}_2$  pulls the  $\text{H}/\text{H}_2$  transition to the surface of the PDR. Conversely, self-shielding is of little importance for HD, and photodestruction converts

HD to atomic deuterium (Tielens, 1992). Through gas-phase addition reactions, the free atomic deuterium adds aliphatically to the PAH molecule. Recent theoretical calculations (Ricca et al., 2007; Rauls & Hornekær, 2008; Rasmussen et al., 2011) and experiments (Thrower et al., 2012; Klærke et al., 2013; Demarais et al., 2014) demonstrate that hydrogenation ( $H_n$ -PAH) or deuteration ( $D_n$ -PAH) can be important through reactions in the gas phase in regions of the PDR without intense UV radiation. The addition occurs preferentially on carbons at the edges of PAH molecules and gives the carbon an aliphatic character (Rauls & Hornekær, 2008). Rasmussen et al. (2011) and Rauls & Hornekær (2008) calculated the first hydrogen addition to the periphery has a barrier of 0.06 eV for neutral PAHs, while the second hydrogen addition is barrierless. For cations, hydrogenation is even easier, since the first hydrogen addition is barrierless and the second addition has a negligible barrier (Ricca et al., 2007). Similar mechanisms can be employed to explain the presence of aliphatic deuterium on PAHs. In an evaporating flow, the PAHs move to the surface of the PDR and then into the general ISM, during which the deuterium fractionation is temporarily preserved. In this schematic way, we can understand how PAHs can be highly fractionated, that this fractionation primarily occurs as aliphatic H/D, and that this fractionation behavior is very sensitive to the local conditions and history of the PAHs. Thus, it is expected to vary from one region to the next.

Additionally, ion-molecule and neutral-neutral addition reactions occur at low temperatures, but require that the reaction is exothermic or has no barrier (Dalgarno & Lepp, 1984; Tielens, 1992; Bauschlicher Jr., 1998; Sandford et al., 2001). These reactions, in the gas phase or on grain surfaces, are proposed to lead to both aliphatic and aromatic deuterated or hydrogenated PAHs deep inside dense clouds,



Similar reaction schemes are responsible for the deuteration of small hydrocarbon species, such as  $\text{HCO}^+$  and  $\text{HCN}$ . Deuteration fractionation in these species is observed to reach levels of  $\sim 4 \times 10^{-2}$  (Roberts et al., 2002).

At temperatures less than 50 K, most of the volatile molecules are frozen out onto the dust grains (Boogert et al., 2015). Penetrating UV radiation from nearby O/B stars or photon-induced, cosmic-ray ionization that is deep inside dense cores has enough energy to break the molecular bonds on smaller molecules producing radicals. These highly reactive species, in turn, can go on to form new bonds (Bernstein et al., 2001; Sandford et al., 2001). Laboratory experiments of PAHs in deuterium-enriched water ices demonstrated that under UV irradiations PAHs undergo oxidation, reduction, and deuterium-hydrogen exchange reactions. Deuterium enrichment in ices is independent of the size of the PAH, and seems to favor the aromatic deuterium product (PAD) over aliphatic addition, resulting in enrichment levels of at least  $\text{D}/\text{H} \sim 10^{-4}$  (Sandford et al., 2000).

Independent of the temperature, PAHs can undergo unimolecular photodissociation if they absorb a UV photon with enough energy to break the C-H bond. The aliphatic  $\text{sp}^3$  bonds are more labile compared to the aromatic  $\text{sp}^2$  bonds, favoring the loss of an aliphatic hydrogen or deuterium over an aromatic hydrogen or deuterium atom. The presence of aliphatic bonds also causes the PAH geometry to depart from planarity, adding stress to the molecule and resulting in weaker C-H bonds than in fully aromatic, planar PAH molecules. The lower zero-point energy of deuterium suggests that dehydrogenation is favored over dedeuteration at ISM temperatures,  $T < 70$  K. In addition, since larger PAHs have larger heat capacities relative to small PAHs, unimolecular photodissociation favors PAHs with less than 50 carbon atoms. Theoretical estimates suggest that the expected deuterium fractionation from this method in HII regions is about  $10^{-5}$  (Allamandola

et al., 1989). The low abundance or complete lack of observed deuterated features in a majority of the observed sources suggests that the conditions leading to deuterium addition in the ISM are not common. Further theoretical studies are required to assess the different scenarios in more detail.

The upcoming James Webb Space Telescope (JWST) will offer significantly better spectral resolution in the NIR, from 1 - 5  $\mu\text{m}$ , which will allow for better resolution of the 4.63 and 4.75  $\mu\text{m}$  features, and even better constraint on the abundance of deuterium on PAHs, in the Milky Way, and in the neighboring LMC and SMC. Additionally, JWST will offer similar resolution mid-IR spectroscopy from 5 - 28  $\mu\text{m}$ , which gives access to the intrinsically stronger C-D bending modes in addition to the C-D stretch modes. Since the C-D bending features are hard to unambiguously distinguish from the C-H bending features of PAH cations, the simultaneous detection of the C-D bending and C-D stretching features is needed for a stronger confirmation that deuterated PAHs were detected; this is a unique capability of JWST, which previous telescopes, for example, the Spitzer Space Telescope, were not able to do.

## 8.5 ACKNOWLEDGEMENTS

K.D.D. thanks Dr. E. Peeters for useful and stimulating discussions. This research is based on observations with AKARI, a JAXA project with the participation of ESA. Studies of interstellar PAHs at Leiden Observatory are supported through advanced European Research Council grant 246976 and a Spinoza award.

## 8.6 BIBLIOGRAPHY

- Allamandola, L. J. 1993, in *Astronomical Society of the Pacific Conference Series*, Vol. 41, *Astronomical infrared spectroscopy: Future observational directions*, ed. S. Kwok, 197
- Allamandola, L. J., Tielens, A. G. G. M., & Barker, J. R. 1985, *The Astrophysical Journal*, 290, L25
- Allamandola, L. J., Tielens, A. G. G. M., & Barker, J. R. 1989, *The Astrophysical Journal Supplements*, 71, 733
- Bauschlicher Jr., C. W. 1998, *The Astrophysical Journal*, 509, L125
- Bauschlicher Jr., C. W., Langhoff, S. R., Sandford, S. A., & Hudgins, D. M. 1997, *The Journal of Physical Chemistry A*, 101, 2414
- Bernstein, M. P., Dworkin, J. P., Sandford, S. A., & Allamandola, L. J. 2001, *Meteoritics and Planetary Science*, 36, 351
- Bertoldi, F., Draine, B. T., Rosenthal, D., et al. 2000, in *IAU Symposium*, Vol. 197, *From Molecular Clouds to Planetary*, ed. Y. C. Minh & E. F. van Dishoeck, 191
- Boersma, C., Bauschlicher Jr., C. W., Ricca, A., et al. 2014, *The Astrophysical Journals*, 211, 8
- Boogert, A., Gerakines, P., & Whittet, D. 2015, *ArXiv e-prints*
- Buragohain, M., Pathak, A., Sarre, P., Onaka, T., & Sakon, I. 2015, *Monthly Notices of the Royal Astronomical Society*, 454, 193
- Candian, A., Kerr, T. H., Song, I.-O., McCombie, J., & Sarre, P. J. 2012, *Monthly Notices of the Royal Astronomical Society*, 426, 389
- Cherchneff, I., Barker, J. R., & Tielens, A. G. G. M. 1992, *The Astrophysical Journal*, 401, 269
- Dalgarno, A. & Lepp, S. 1984, *The Astrophysical Journal*, 287, L47
- Demarais, N. J., Yang, Z., Snow, T. P., & Bierbaum, V. M. 2014, *The Astrophysical Journal*, 784, 25
- Draine, B. T. 2004, *ArXiv Astrophysics eprint arXiv:astro-ph/0410310*
- Epstein, R. I., Lattimer, J. M., & Schramm, D. N. 1976, *Nature*, 263, 198
- Filipovic, M. D., Jones, P. A., White, G. L., & Haynes, R. F. 1998, *Astronomy & Astrophysics*, 130, 441
- Frenklach, M. & Feigelson, E. D. 1989, *The Astrophysical Journal*, 341, 372
- Gerakines, P. A., Schutte, W. A., & Ehrenfreund, P. 1996, *Astronomy & Astrophysics*, 312, 289
- Hilditch, R. W., Howarth, I. D., & Harries, T. J. 2005, *Monthly Notices of the Royal Astronomical Society*, 357, 304
- Hudgins, D. M., Bauschlicher Jr., C. W., & Sandford, S. A. 2004, *The Astrophysical Journal*, 614, 770
- Joblin, C. & Tielens, A. G. G. M., eds. 2011, *EAS Publications Series*, Vol. 46, *PAHs and the Universe: A symposium to celebrate the 25th anniversary of the PAH hypothesis*
- Kerridge, J. F., Chang, S., & Shipp, R. 1987, *Geochimica Cosmochimica Acta*, 51, 2527
- Klærke, B., Tokar, Y., Rahbek, D. B., Hornekær, L., & Andersen, L. H. 2013, *Astronomy & Astrophysics*, 549, A84
- Leger, A. & Puget, J. L. 1984, *Astronomy & Astrophysics*, 137, L5

- Li, A. & Draine, B. T. 2012, *The Astrophysical Journal*, 760, L35
- Linsky, J. L., Draine, B. T., Moos, H. W., et al. 2006, *The Astrophysical Journal*, 647, 1106
- Lis, D. C., Roueff, E., Gerin, M., et al. 2002, *The Astrophysical Journal*, 571, L55
- Martín-Hernández, N. L., Peeters, E., Morisset, C., et al. 2002a, *Astronomy & Astrophysics*, 381, 606
- Martín-Hernández, N. L., Vermeij, R., Tielens, A. G. G. M., van der Hulst, J. M., & Peeters, E. 2002b, *Astronomy & Astrophysics*, 389, 286
- Mori, T. I., Onaka, T., Sakon, I., et al. 2014, *The Astrophysical Journal*, 784, 53
- Onaka, T., Lorente, R., & Ita, Y. 2009, IRC data users's manual for Phase 3 ver 1.1
- Onaka, T., Matsuhara, H., Wada, T., et al. 2007, *Publications of the Astronomical Society of Japan*, 59, 401
- Onaka, T., Mori, T. I., Sakon, I., et al. 2014, *The Astrophysical Journal*, 780, 114
- Paladini, R., Burigana, C., Davies, R. D., et al. 2003, *Astronomy & Astrophysics*, 397, 213
- Parise, B., Castets, A., Herbst, E., et al. 2004, *Astronomy & Astrophysics*, 416, 159
- Peeters, E., Allamandola, L. J., Bauschlicher Jr., C. W., et al. 2004, *The Astrophysical Journal*, 604, 252
- Pietrzyński, G., Graczyk, D., Gieren, W., et al. 2013, *Nature*, 495, 76
- Pilleri, P., Joblin, C., Boulanger, F., & Onaka, T. 2015, *Astronomy & Astrophysics*, 577, A16
- Rasmussen, J. A., Henkelman, G., & Hammer, B. 2011, *The Journal of Chemical Physics*, 134, 164703
- Rauls, E. & Hornekær, L. 2008, *The Astrophysical Journal*, 679, 531
- Ricca, A., Bakes, E. L. O., & Bauschlicher Jr., C. W. 2007, *The Astrophysical Journal*, 659, 858
- Roberts, H., Fuller, G. A., Millar, T. J., Hatchell, J., & Buckle, J. V. 2002, *Planetary Space Science*, 50, 1173
- Roberts, H., Herbst, E., & Millar, T. J. 2003, *The Astrophysical Journal*, 591, L41
- Sandford, S. A., Bernstein, M. P., Allamandola, L. J., Gillette, J. S., & Zare, R. N. 2000, *The Astrophysical Journal*, 538, 691
- Sandford, S. A., Bernstein, M. P., & Dworkin, J. P. 2001, *Meteoritics and Planetary Science*, 36, 1117
- Sandford, S. A., Bernstein, M. P., & Materese, C. K. 2013, *The Astrophysical Journal*, 205, 8
- Schutte, W. A., Tielens, A. G. G. M., & Allamandola, L. J. 1993, *The Astrophysical Journal*, 415, 397
- Storey, P. J. & Hummer, D. G. 1995, *Monthly Notices of the Royal Astronomical Society*, 272, 41
- Thrower, J. D., Jørgensen, B., Friis, E. E., et al. 2012, *The Astrophysical Journal*, 752, 3
- Tielens, A. G. G. M. 1992, in *IAU Symposium, Vol. 150, Astrochemistry of Cosmic Phenomena*, ed. P. D. Singh, 91
- Tielens, A. G. G. M. 2008, *Annual Review of Astronomy and Astrophysics*, 46, 289
- van der Tak, F. F. S., Schilke, P., Müller, H. S. P., et al. 2002, *Astronomy & Astrophysics*, 388, L53
- Vidal-Madjar, A., Lemoine, M., Ferlet, R., et al. 1998, *Astronomy & Astrophysics*, 338, 694







## SUPPLEMENTARY MATERIAL

---

### A.1 - Chapter 2

1. CCSD(T)/ANO1 anharmonicity constants for acetylene, diacetylene, triacetylene, and tetraacetylene.

### A.2 - Chapter 3

1. Observed line positions for diacetylene.

### A.3 - Chapter 4

1. Observed line positions for triacetylene.

### A.4 - Chapter 5

1. Observed line positions for the normal isotopologue of propyne.

### A.5 - Chapter 6

1. Harmonic and anharmonic (VPT2) frequencies of  $^{12}\text{CH}_3^{13}\text{C}^{13}\text{CH}$ .
2. Observed line positions for the  $^{13}\text{C}$  isotopologues of propyne.
3. Example of the Fermi analysis for the  $\nu_1$  fundamental band of propyne.

### A.6 - Chapter 7

1. Observed line positions for cyclopropenyl cation.

## A.1 CHAPTER 2

Table A.1: CCSD(T)/ANO1 vibrational anharmonicity constants ( $x_{ij}$ , in  $\text{cm}^{-1}$ ) for  $\text{HC}_2\text{H}$ 

i	j	$x_{ij}$												
1	1	-26.83	2	3	-5.03	4	1	-13.88	4	4	7.01	5	2	-1.21
2	1	-11.49	3	1	-109.27	4	2	-13.48	4	5	-2.69	5	3	-9.08
2	2	-6.85	3	3	-27.22	4	3	-7.99	5	1	-11.01	5	5	-2.63

Table A.2: CCSD(T)/ANO1 vibrational anharmonicity constants ( $x_{ij}$ , in  $\text{cm}^{-1}$ ) for  $\text{HC}_4\text{H}$ 

i	j	$x_{ij}$												
1	1	-27.12	3	5	-1.83	6	4	-9.52	7	7	7.57	9	1	-0.51
1	4	-108.40	4	4	-27.00	6	5	-4.07	7	8	1.14	9	2	-2.59
2	1	-3.27	5	1	-4.24	6	6	-0.33	8	1	-9.80	9	3	3.47
2	2	-6.65	5	2	-15.91	7	1	-1.29	8	2	-6.32	9	4	-0.54
2	4	-3.48	5	4	-3.65	7	2	-8.03	8	3	-0.22	9	5	-1.75
3	1	0.22	5	5	-4.35	7	3	-27.40	8	4	-9.81	9	6	0.12
3	2	-1.35	6	1	-9.53	7	4	-1.27	8	5	-4.99	9	7	-0.11
3	3	-2.81	6	2	-4.95	7	5	-4.86	8	6	-1.06	9	8	0.21
3	4	0.05	6	3	-0.61	7	6	1.67	8	8	0.35	9	9	-0.32

Table A.3: CCSD(T)/ANO1 vibrational anharmonicity constants ( $x_{ij}$ , in  $\text{cm}^{-1}$ ) for  $\text{HC}_6\text{H}$ 

i	j	$x_{ij}$	i	j	$x_{ij}$	i	j	$x_{ij}$	i	j	$x_{ij}$	i	j	$x_{ij}$
1	1	-27.15	5	5	-27.06	9	2	-9.58	10	11	0.26	12	11	0.83
2	1	-0.90	6	1	-2.64	9	3	-3.87	10	12	-0.58	12	12	1.19
2	2	-8.17	6	2	-8.88	9	4	-4.27	11	1	-9.74	13	1	-0.11
2	5	2.06	6	5	-3.43	9	5	-0.61	11	2	-3.27	13	2	-0.72
3	1	-3.25	6	6	-4.19	9	6	-3.81	11	3	-3.73	13	3	-0.33
3	2	-10.81	7	1	0.73	9	7	0.66	11	5	-9.74	13	4	1.64
3	3	-3.29	7	2	-44.61	9	8	0.67	11	6	-4.22	13	5	-0.12
3	5	-2.82	7	3	-1.22	9	9	2.36	11	7	-0.97	13	6	-0.49
3	6	-12.48	7	5	3.15	9	11	0.67	11	8	0.13	13	7	-0.13
4	1	0.00	7	6	-2.43	10	1	-0.36	11	11	-0.31	13	8	-0.02
4	2	-1.92	7	7	7.52	10	2	-2.43	12	1	-0.77	13	9	-0.21
4	3	-0.58	8	1	-9.62	10	3	-1.47	12	2	-2.50	13	10	0.01
4	4	-0.53	8	2	-3.43	10	4	7.44	12	3	-2.54	13	11	0.04
4	5	0.01	8	3	-3.65	10	5	-0.36	12	4	-3.31	13	12	-0.14
4	6	0.38	8	5	-9.61	10	6	-1.66	12	5	-0.77	13	13	-0.12
4	7	-4.65	8	6	-4.08	10	7	0.36	12	6	-4.40			
4	8	-0.25	8	7	-0.97	10	8	0.36	12	7	1.84			
4	11	-0.20	8	8	-0.34	10	9	1.10	12	8	0.72			
5	1	-108.41	9	1	-0.61	10	10	-1.55	12	9	-0.16			

Table A.4: CCSD(T)/ANO1 vibrational anharmonicity constants ( $x_{ij}$ , in  $\text{cm}^{-1}$ ) for  $\text{HC}_8\text{H}$ 

i	j	$x_{ij}$	i	j	$x_{ij}$	i	j	$x_{ij}$	i	j	$x_{ij}$	i	j	$x_{ij}$
1	1	-27.13	7	1	-1.06	11	4	-0.86	13	10	0.33	16	4	-0.18
2	1	-0.43	7	2	-14.38	11	6	-0.24	13	11	0.18	16	5	-9.40
2	2	-7.63	7	6	-1.39	11	7	-5.60	13	12	-0.04	16	6	-0.25
2	6	-0.32	7	7	-3.80	11	8	-3.17	13	13	-0.45	16	7	-1.84
3	1	-1.61	8	1	-2.41	11	9	-11.80	13	14	0.04	16	8	-1.29
3	2	-5.37	8	2	-8.86	11	10	0.34	13	15	-0.28	16	9	1.85
3	3	-3.54	8	3	-10.16	11	11	1.81	13	16	-0.07	16	10	0.08
3	6	-3.33	8	6	-2.04	11	14	0.34	14	1	-9.67	16	11	0.78
3	7	-7.94	8	7	-8.67	12	1	-0.47	14	2	-2.16	16	12	-0.82
4	1	1.61	8	8	-2.61	12	2	-1.98	14	3	-3.91	16	14	0.25
4	2	-7.74	9	1	0.19	12	3	-2.49	14	4	1.13	16	15	0.48
4	3	-3.06	9	2	-0.33	12	4	-0.11	14	6	-9.66	16	16	2.69
4	4	-0.79	9	3	-0.23	12	5	-1.86	14	7	-2.62	17	1	-0.04
4	6	0.01	9	4	-24.05	12	6	-0.47	14	8	-3.02	17	2	-0.30
4	7	18.50	9	6	0.20	12	7	-2.07	14	9	-0.28	17	3	-0.16
4	8	-0.95	9	7	17.63	12	8	-1.58	14	14	-0.83	17	4	-0.10
5	1	0.00	9	8	-0.76	12	9	19.78	15	1	-0.61	17	5	0.97
5	2	-0.96	9	9	-1.28	12	10	0.44	15	2	-4.19	17	6	-0.01
5	3	0.35	10	1	-9.67	12	11	0.43	15	3	-3.02	17	7	-0.34
5	4	-2.72	10	2	-2.17	12	12	0.65	15	4	-0.47	17	8	-0.15
5	5	-0.23	10	3	-3.93	12	14	0.41	15	6	-0.59	17	9	0.09
5	6	0.00	10	4	1.11	12	15	-9.02	15	7	-4.50	17	10	-0.01
5	7	-0.86	10	6	-9.66	13	1	-0.16	15	8	-2.75	17	11	-0.13
5	8	-0.20	10	7	-2.63	13	2	-0.78	15	9	7.18	17	12	-0.07
5	9	-1.14	10	8	-3.03	13	3	-0.55	15	10	0.69	17	13	-0.02
5	10	0.42	10	9	0.00	13	4	-0.29	15	11	7.15	17	14	-0.01
5	11	-2.06	10	10	-0.82	13	5	2.08	15	14	0.72	17	15	-0.02
5	14	-0.08	10	14	0.16	13	6	-0.16	15	15	0.92	17	16	-0.02
5	15	-1.58	11	1	-0.32	13	7	-0.90	16	1	-0.27	17	17	-0.05
6	1	-108.41	11	2	-7.40	13	8	-0.52	16	2	-1.79			
6	6	-27.09	11	3	-2.36	13	9	0.85	16	3	-1.25			

## A.2 CHAPTER 3

Table A.5: Observed line positions (in  $\text{cm}^{-1}$ ) assigned to the  $\Sigma_g - \Sigma_u$  (A1) band of  $\text{HC}_4\text{H}$ 

Transition	Observed	o-c	Transition	Observed	o-c	Transition	Observed	o-c
		$\times 10^4$			$\times 10^4$			$\times 10^4$
R(0)	3334.9407	3	R(8)	3337.2632	6	P(2)	3334.0632*	8
R(1)	3335.232	-1	R(9)	3337.5512	2	P(3)	3333.7675*	-14
R(2)	3335.5235	0	R(10)	3337.8389	0	P(4)	3333.475	1
R(3)	3335.8161*	17	R(11)	3338.1253	-12	P(5)	3333.1808	2
R(4)	3336.1053	3	R(12)	3338.4131	-4	P(6)	3332.8857	-1
R(5)	3336.3946	-4	R(14)	3338.9858	-5	P(8)	3332.2947	-2
R(6)	3336.6846	-1	R(15)	3339.2724	3	P(9)	3331.9986	-3
R(7)	3336.9737	-1	P(1)	3334.3569*	15			

Lines which are blended and given less statistical weight in the fit are indicated by \*.

Table A.6: Observed line positions (in  $\text{cm}^{-1}$ ) assigned to the  $\Sigma_u - \Sigma_g$  (A2) band of  $\text{HC}_4\text{H}$ 

Transition	Observed	o-c	Transition	Observed	o-c	Transition	Observed	o-c
		$\times 10^4$			$\times 10^4$			$\times 10^4$
R(0)	3335.2323	2	R(8)	3337.5518	6	P(3)	3334.0622	-2
R(1)	3335.5240*	5	R(9)	3337.8389	-2	P(4)	3333.7682	-6
R(2)	3335.8156	11	R(10)	3338.126	-6	P(5)	3333.475	1
R(3)	3336.1053	3	R(11)	3338.4131	-7	P(6)	3333.1801	-5
R(4)	3336.3946	-5	R(12)	3338.6981	-23	P(7)	3332.8858	0
R(5)	3336.6846	-2	R(13)	3338.9861	-7	P(8)	3332.5909	3
R(6)	3336.9737	-3	R(14)	3339.2727	1	P(9)	3332.2953	4
R(7)	3337.2632	4	R(15)	3339.5586	6	P(10)	3331.9987	-2

Lines which are blended and given less statistical weight in the fit are indicated by \*.

Table A.7: Observed line positions (in  $\text{cm}^{-1}$ ) assigned to the  $4_0^1 6_1^1$  (B) band of  $\text{HC}_4\text{H}$ 

Transition	Observed	o-c	Transition	Observed	o-c	Transition	Observed	o-c
		$\times 10^4$			$\times 10^4$			$\times 10^4$
Re(1)	3334.3409	2	Rf(16)	3338.6681*	-8	Pe(7)	3331.6956	-12
Rf(2)	3334.6329	2	Re(17)	3338.9509*	-7	Pf(8)	3331.3991	-3
Re(3)	3334.9236	3	Rf(18)	3339.2374	-8	Pe(9)	3331.1042	-2
Rf(4)	3335.2144	-3	Re(19)	3339.5185	-13	Pf(10)	3330.8061	5
Re(5)	3335.5042	1	Rf(20)	3339.805	-7	Pe(11)	3330.5108	6
Rf(6)	3335.7949	0	Re(21)	3340.0864	1	Pf(12)	3330.2104	2
Re(7)	3336.0841	9	Rf(22)	3340.3721	7	Pe(13)	3329.9133	-1
Rf(8)	3336.3738	4	Re(23)	3340.652	10	Pf(14)	3329.6126	-3
Re(9)	3336.6604	-1	Re(25)	3341.2137	-1	Pe(15)	3329.3168	1
Rf(10)	3336.9494	-5	Pf(2)	3333.169	-8	Pf(16)	3329.0138	-1
Re(11)	3337.2368	9	Pe(3)	3332.8756	-7	Pe(17)	3328.7155	-17
Rf(12)	3337.5248	1	Pf(4)	3332.5809	-5	Pf(18)	3328.4141	1
Re(13)	3337.8099	3	Pe(5)	3332.2858	-16	Pe(19)	3328.1165	5
Rf(14)	3338.0972	-5	Pf(6)	3331.9908	-5	Pf(20)	3327.8122	17
Re(15)	3338.3817	2						

Table A.8: Observed line positions (in  $\text{cm}^{-1}$ ) assigned to the  $\nu_4$  fundamental band (C) of  $\text{HC}_4\text{H}$ 

Transition	Observed	o-c	Transition	Observed	o-c	Transition	Observed	o-c
	$\times 10^4$			$\times 10^4$			$\times 10^4$	
R(0)	3333.9565	7	R(16)	3338.5735	-8	P(7)	3331.6036*	-8
R(1)	3334.249	13	R(17)	3338.8584	-8	P(8)	3331.3087	1
R(2)	3334.5398	6	R(18)	3339.1426	-11	P(9)	3331.0125	2
R(3)	3334.8308	5	R(19)	3339.4268	-10	P(10)	3330.716	4
R(4)	3335.1214	5	R(20)	3339.7109	-5	P(11)	3330.4189	5
R(5)	3335.4111	0	R(21)	3339.9939	-6	P(12)	3330.1202	-6
R(6)	3335.701	2	R(22)	3340.2774	2	P(13)	3329.8226	-2
R(7)	3335.9906	4	R(23)	3340.5598*	3	P(14)	3329.5222*	-21
R(8)	3336.2794	3	R(25)	3341.1224	-4	P(15)	3329.2236*	-18
R(9)	3336.5678	3	R(26)	3341.4026	-11	P(16)	3328.9247*	-14
R(10)	3336.8558	3	P(1)	3333.3717	12	P(17)	3328.6244*	-19
R(11)	3337.1438	7	P(2)	3333.0772	-1	P(18)	3328.3251*	-11
R(12)	3337.4303	1	P(3)	3332.7832	-3	P(19)	3328.0239	-16
R(13)	3337.7169	0	P(4)	3332.4886	-9	P(21)	3327.4224	-7
R(14)	3338.0029	-3	P(5)	3332.1944	-4	P(22)	3327.1223*	11
R(15)	3338.2888	-2	P(6)	3331.9004	5	P(25)	3326.2124	-7

Lines which are blended and given less statistical weight in the fit are indicated by \*

Table A.9: Observed line positions (in  $\text{cm}^{-1}$ ) assigned to the  $4_0^1 9_1^1$  (D) band of  $\text{HC}_4\text{H}$ 

Transition	Observed	o-c	Transition	Observed	o-c	Transition	Observed	o-c
	$\times 10^4$			$\times 10^4$			$\times 10^4$	
Rf(1)	3333.6734	7	Rf(13)	3337.1556	5	Pe(2)	3332.4987	-2
Re(2)	3333.9649	9	Re(14)	3337.4362	0	Pf(3)	3332.2027	-7
Rf(3)	3334.2576	2	Rf(15)	3337.7292	-2	Pf(5)	3331.6132	6
Re(4)	3334.5483*	13	Re(16)	3338.0085	-3	Pe(6)	3331.3181	-1
Rf(5)	3334.8398	-6	Rf(17)	3338.3025	6	Pf(7)	3331.0196	-6
Re(6)	3335.1292	9	Re(18)	3338.5793	-4	Pf(9)	3330.4261	0
Rf(7)	3335.4223	6	Rf(19)	3338.8724	-4	Pe(10)	3330.132	-4
Re(8)	3335.7079	0	Re(20)	3339.1481*	-7	Pf(11)	3329.8294	-8
Rf(9)	3336.0018	6	Rf(21)	3339.4418	-1	Pf(13)	3329.2332	6
Re(10)	3336.2852	-5	Re(22)	3339.7161	-1	Pe(14)	3328.9370*	-19
Rf(11)	3336.579	0	Rf(23)	33491	-1	Pf(15)	3328.6331	-3
Re(12)	3336.8623	5	Re(24)	3340.2817	-1	Pe(16)	3328.3403*	7

Lines which are blended and given less statistical weight in the fit are indicated by \*.

Table A.10: Observed line positions (in  $\text{cm}^{-1}$ ) assigned to the  $4_0^1 7_1^1$  (E) band of  $\text{HC}_4\text{H}$ 

Transition	Observed	o-c $\times 10^4$	Transition	Observed	o-c $\times 10^4$	Transition	Observed	o-c $\times 10^4$
Re(1)	3332.9484	-1	Re(19)	3338.1354	-4	Pe(7)	3330.3013	-1
Rf(2)	3333.2423	13	Rf(20)	3338.4238	-2	Pf(8)	33335	3
Re(3)	3333.5322	3	Re(21)	3338.7048	15	Pe(9)	3329.707	-13
Rf(4)	3333.8241	1	Rf(22)	3338.9903	-7	Pf(10)	3329.407	-19
Re(5)	3334.1151	15	Re(23)	3339.2682	-8	Pe(11)	3329.1116	-19
Rf(6)	3334.4061	9	Rf(24)	3339.5577	15	Pf(12)	3328.8115	-12
Re(7)	3334.6943	8	Rf(26)	3340.1202	6	Pe(13)	3328.515	-2
Rf(8)	3334.9849	3	Re(27)	3340.3951	0	Pf(14)	3328.2135	-14
Re(9)	3335.2721	4	Rf(28)	3340.6815	3	Pe(15)	3327.9177	-1
Re(11)	3335.8489	9	Re(29)	3340.9558	4	Pf(16)	3327.6144	-9
Rf(12)	3336.1388	5	Re(43)	3344.8279*	8	Pe(17)	3327.3177	-11
Re(13)	3336.4229	2	Pf(2)	3331.776	1	Pf(18)	3327.0129	-11
Re(15)	3336.9961	6	Pe(3)	3331.4814*	-8	Pe(19)	3326.7164	-6
Rf(16)	3337.2853	6	Pf(4)	3331.1874*	6	Pf(20)	3326.4106*	-3
Re(17)	3337.5665	-1	Pe(5)	3330.8928	1	Pe(21)	3326.1125	-12
Rf(18)	3337.8551	-2	Pf(6)	3330.5969	1	Pf(22)	3325.8048	-13

Lines which are blended and given less statistical weight in the fit are indicated by \*.

Table A.11: Observed line positions (in  $\text{cm}^{-1}$ ) assigned to the (F) band of  $\text{HC}_4\text{H}$ 

Transition	Observed	o-c $\times 10^4$	Transition	Observed	o-c $\times 10^4$	Transition	Observed	o-c $\times 10^4$
Rf(1)	3332.9306*	15	Re(8)	3334.9711	-9	Pf(5)	3330.8711*	-11
Re(2)	3333.2219	3	Rf(9)	3335.2615	-7	Pe(6)	3330.5772*	-16
Rf(3)	3333.5130*	-12	Rf(11)	3335.8427	3	Pe(8)	3329.9885	-1
Re(4)	3333.8073	13	Re(12)	3336.1338	-2	Pf(9)	3329.6903	0
Rf(5)	3334.0984	4	Pe(2)	3331.7534*	-25	Pe(12)	3328.8058	4
Re(6)	3334.3891	-4	Pf(3)	3331.4618	4	Pf(13)	3328.5038	0
Rf(7)	3334.6808	1	Pe(4)	3331.1671	-7			

Lines which are blended and given less statistical weight in the fit are indicated by \*.

Table A.12: Observed line positions (in  $\text{cm}^{-1}$ ) assigned to the (G) band of  $\text{HC}_4\text{H}$ 

Transition	Observed	o-c $\times 10^4$	Transition	Observed	o-c $\times 10^4$	Transition	Observed	o-c $\times 10^4$
Rf(1)	3332.6833	10	Rf(13)	3336.1527	-9	Pe(2)	3331.5109*	0
Re(2)	3332.9747	6	Re(14)	3336.4389	-4	Pf(3)	3331.2179*	8
Rf(3)	3333.2635	-18	Rf(15)	3336.7259	0	Pe(4)	3330.9203*	-21
Re(4)	3333.5545	-18	Re(16)	3337.0116*	13	Pf(5)	3330.6277	-2
Rf(5)	3333.8463	-2	Rf(17)	3337.2953	-12	Pe(6)	3330.3316*	-4
Re(6)	3334.137	4	Re(18)	3337.5788	-8	Pf(7)	3330.0363*	-7
Rf(7)	3334.4265	5	Rf(19)	3337.8661	10	Pe(8)	3329.7407*	7
Re(8)	3334.7157	8	Re(20)	3338.1465	-5	Pf(9)	3329.4436*	-7
Rf(9)	3335.0039	3	Rf(21)	3338.4314	-7	Pe(10)	3329.1465*	5
Re(10)	3335.2919	3	Rf(23)	3338.9984	12	Pf(11)	3328.8512*	13
Rf(11)	3335.5798	3	Re(24)	3339.277	8	Pe(12)	3328.5487*	-16
Re(12)	3335.8656	-7						

Lines which are blended and given less statistical weight in the fit are indicated by \*.

Table A.13: Observed line positions (in  $\text{cm}^{-1}$ ) assigned to the  $4_0^1 8_1^1$  (H) band of  $\text{HC}_4\text{H}$ 

Transition	Observed	o-c	Transition	Observed	o-c	Transition	Observed	o-c
	$\times 10^4$			$\times 10^4$			$\times 10^4$	
Rf(1)	3332.1572	-2	Re(12)	3335.3419	-3	Pf(9)	3328.9197	-3
Re(2)	3332.4492	4	Rf(13)	3335.6305	4	Pe(10)	3328.6246	-8
Rf(3)	3332.7402	-3	Re(14)	3335.9159	1	Pf(11)	3328.3252	-7
Re(4)	3333.0305	-3	Rf(15)	3336.2022	-6	Pe(12)	3328.0297	-13
Rf(5)	3333.3223	4	Re(16)	3336.4892	14	Pf(13)	3327.7298	-2
Re(6)	3333.6121	10	Pe(2)	3330.9865	-1	Pe(14)	3327.4331	-19
Rf(7)	3333.9021	6	Pf(3)	3330.6928	5	Pf(15)	3327.133	4
Re(8)	3334.1904	6	Pe(4)	3330.3991	4	Pe(16)	3326.8363	-11
Rf(9)	3334.4801	7	Pf(5)	3330.104	8	Pf(17)	3326.5325*	-9
Re(10)	3334.7667	-2	Pe(6)	3329.8086	-6	Pe(18)	3326.2393	12
Rf(11)	3335.0558	2	Pf(7)	3329.5125	0			

Lines which are blended and given less statistical weight in the fit are indicated by \*.

Table A.14: Observed line positions (in  $\text{cm}^{-1}$ ) assigned to the  $4_0^1 7_2^2$  (I) band of  $\text{HC}_4\text{H}$ 

Transition	Observed	o-c	Transition	Observed	o-c	Transition	Observed	o-c
	$\times 10^4$			$\times 10^4$			$\times 10^4$	
Rf(2)	3331.9534	-1	Re(15)	3335.7214	-15	Pf(10)	3328.1165	-3
Re(3)	3332.2459	-1	Rf(16)	3336.0088	3	Pe(11)	3327.819	-5
Rf(4)	3332.5366	-14	Re(17)	3336.2977	15	Pf(12)	3327.5204	-1
Re(5)	3332.8289	-7	Rf(18)	3336.579	-9	Pe(13)	3327.2224	-2
Rf(6)	3333.1213	4	Re(19)	3336.8676	3	Pf(14)	3326.9235	13
Re(7)	3333.4128	11	Rf(20)	3337.1495	7	Pe(15)	3326.6245	4
Rf(8)	3333.7026	6	Re(21)	3337.4362	-3	Pf(16)	3326.322	0
Re(9)	3333.9926	5	Pe(3)	3330.1918	9	Pe(17)	3326.023	-9
Rf(10)	3334.2816	1	Pf(4)	3329.897	12	Pf(18)	3325.7217	21
Re(11)	3334.5709	1	Pe(5)	3329.6006	2	Pe(19)	3325.4226	6
Rf(12)	3334.8592	1	Pf(6)	3329.3038	-7	Pf(20)	3325.1133	-17
Re(13)	3335.1467	-11	Pf(8)	3328.7107	-8	Pe(21)	3324.8181	-1
Rf(14)	3335.4343	-5	Pe(9)	3328.4141	-6	Pf(22)	3324.5078	-1

Table A.15: Observed line positions (in  $\text{cm}^{-1}$ ) assigned to the  $1_0^1 8_0^1 6_1^0$  (J) band of  $\text{HC}_4\text{H}$ 

Transition	Observed	o-c	Transition	Observed	o-c	Transition	Observed	o-c
	$\times 10^4$			$\times 10^4$			$\times 10^4$	
Re(1)	3315.4463	0	Rf(16)	3319.777	-4	Pf(8)	3312.5057	3
Rf(2)	3315.7379	-4	Re(17)	3320.0588	2	Pe(9)	3312.2097	-6
Re(3)	3316.0287	-3	Rf(18)	3320.3476	2	Pf(10)	3311.9111	-1
Rf(4)	3316.3204	-2	Re(19)	3320.6268*	-4	Pe(11)	3311.6149	-13
Re(5)	3316.61	1	Rf(20)	3320.916	4	Pf(12)	3311.3165	-5
Rf(6)	3316.9009	-1	Re(21)	3321.1952	12	Pe(13)	3311.0197	-8
Re(7)	3317.1901	10	Re(23)	3321.75968	5	Pf(14)	3310.7203	1
Rf(8)	3317.4791	-7	Pf(2)	3314.2753	0	Pe(15)	3310.423	-1
Re(9)	3317.7677	12	Pe(3)	3313.9818	-1	Pf(16)	3310.1227	1
Rf(10)	3318.0565	-3	Pf(4)	3313.6874	4	Pe(17)	3309.8243	4
Rf(12)	3318.6316	-4	Pe(5)	3313.3933	2	Pf(18)	3309.5215	0
Re(13)	3318.9155	-6	Pf(6)	3313.098	9	Pe(19)	3309.2243	13
Rf(14)	3319.2051	-5	Pe(7)	3312.802	-5	Pf(20)	3308.9186	-11
Re(15)	3319.4877	-5						

Lines which are blended and given less statistical weight in the fit are indicated by \*.

Table A.16: Observed line positions (in  $\text{cm}^{-1}$ ) assigned to the  $1_0^1 8_0^1 6_2^1$  ( $\Delta, K$ ) band of  $\text{HC}_4\text{H}$ 

Transition	Observed	o-c	Transition	Observed	o-c	Transition	Observed	o-c
	$\times 10^4$			$\times 10^4$			$\times 10^4$	
Rf(2)	3315.7262	-38	Re(15)	3319.49	-11	Pf(10)	3311.904	-1
Re(3)	3316.0193	-24	Rf(16)	3319.7772	-6	Pe(11)	3311.6063	-9
Rf(4)	3316.313	1	Re(17)	3320.0652	12	Pf(12)	3311.3091	-7
Re(5)	3316.6041	3	Rf(18)	3320.3517	19	Pe(13)	3311.0116	-5
Rf(6)	3316.8947	5	Re(19)	3320.6412	59	Pf(14)	3310.7136	-4
Re(7)	3317.1844	1	Pe(3)	3313.9732	1	Pe(15)	3310.4152	-4
Rf(8)	3317.4742	1	Pf(4)	3313.6764	-15	Pf(16)	3310.1137	-3
Re(9)	3317.7634	1	Pe(5)	3313.3832	-1	Pe(17)	3309.8171	-4
Rf(10)	3318.0515	-8	Pf(6)	3313.089	9	Pf(18)	3309.5172	-7
Rf(12)	3318.6271	-19	Pe(7)	3312.7937	1	Pe(19)	3309.2175	-4
Re(13)	3318.9155	-13	Pf(8)	3312.4978	9	Pf(20)	3308.9187	1
Rf(14)	3319.2025	-16	Pe(9)	3312.2009	2			

Table A.17: Observed line positions (in  $\text{cm}^{-1}$ ) assigned to the  $1_0^1 8_0^1 6_2^1$  ( $\Sigma, L$ ) band of  $\text{HC}_4\text{H}$ 

Transition	Observed	o-c	Transition	Observed	o-c	Transition	Observed	o-c
	$\times 10^4$			$\times 10^4$			$\times 10^4$	
R(0)	3314.346	2	R(15)	3318.6842	-4	P(7)	3311.9922	-5
R(4)	3315.5122	-1	R(16)	3318.9707	5	P(9)	3311.3997	-5
R(5)	3315.8028	-1	R(17)	3319.2551	-4	P(10)	3311.1026	-7
R(6)	3316.0928	-2	R(19)	3319.8249	4	P(11)	3310.805	-11
R(7)	3316.3828	1	R(20)	3320.108	-2	P(12)	3310.5079	-4
R(8)	3316.6721	1	R(21)	3320.3906	-8	P(13)	3310.2097	-5
R(9)	3316.9611	3	R(22)	3320.6746	2	P(14)	3309.912	4
R(10)	3317.2486	-7	P(1)	3313.7605	5	P(16)	3309.3137	7
R(11)	3317.5379	7	P(2)	3313.4672	7	P(17)	3309.0129	-1
R(12)	3317.8251	3	P(3)	3313.1734	8	P(18)	3308.7135	8
R(13)	3318.1114	-4	P(4)	3312.8783	1	P(19)	3308.4121	3
R(14)	3318.3988	4	P(6)	3312.2879	-4	P(21)	3307.808	-7

Table A.18: Observed line positions (in  $\text{cm}^{-1}$ ) assigned to the  $1_0^1 8_0^1 6_2^1 7_1^1$  ( $M$ ) band of  $\text{HC}_4\text{H}$ 

Transition	Observed	o-c	Transition	Observed	o-c	Transition	Observed	o-c
	$\times 10^4$			$\times 10^4$			$\times 10^4$	
Rf(2)	3314.3196	1	Rf(12)	3317.2196	-6	Pf(8)	3311.0819	-5
Re(3)	3314.6112	-1	Re(13)	3317.5081	11	Pe(9)	3310.7853	-3
Rf(4)	3314.9032	4	Rf(14)	3317.7958	2	Pf(10)	3310.4886	0
Re(5)	3315.1936	-2	Re(15)	3318.0801	-9	Pe(11)	3310.191	0
Rf(6)	3315.4844	-1	Pe(3)	3312.5606	8	Pf(12)	3309.8933	1
Re(7)	3315.7746	0	Pf(4)	3312.2658	7	Pe(13)	3309.595	2
Rf(8)	3316.0644	-2	Pe(5)	3311.9696	-5	Pf(14)	3309.2957	-6
Re(9)	3316.3539	1	Pf(6)	3311.6743	-2	Pe(15)	3308.9972	3
Rf(10)	3316.6432	0	Pe(7)	3311.3779	-8	Pf(16)	3308.6983	5
Re(11)	3316.9314	1						

Table A.19: Observed line positions (in  $\text{cm}^{-1}$ ) assigned to the  $1_0^1 8_0^1 6_2^1 7_1^1$  (N) band of  $\text{HC}_4\text{H}$ 

Transition	Observed	o-c	Transition	Observed	o-c	Transition	Observed	o-c
		$\times 10^4$			$\times 10^4$			$\times 10^4$
Re(3)	3314.605	3	Rf(12)	3317.2147	5	Pe(9)	3310.7776	-3
Rf(4)	3314.8967	5	Re(13)	3317.5018	-3	Pf(10)	3310.4809	2
Re(5)	3315.1882	8	Rf(14)	3317.7898	2	Pe(11)	3310.1835	3
Rf(6)	3315.4788	7	Re(15)	3318.0765	-2	Pf(12)	3309.8846	-6
Re(7)	3315.7685	1	Re(17)	3318.6488	-9	Pe(13)	3309.5851	-17
Rf(8)	3316.0586	1	Pf(4)	3312.2577	0	Pf(14)	3309.2869	-12
Re(9)	3316.3484	4	Pe(5)	3311.9617*	-8	Pe(15)	3308.9883	-6
Rf(10)	3316.6363	-8	Pf(6)	3311.6667	-3	Pf(16)	3308.6913	19
Re(11)	3316.9261	3	Pe(7)	3311.3706	-4	Pe(17)	3308.3939	44

Lines which are blended and given less statistical weight in the fit are indicated by \*.

Table A.20: Observed line positions (in  $\text{cm}^{-1}$ ) assigned to the  $1_0^1 6_0^1 8_1^0$  (O) band of  $\text{HC}_4\text{H}$ 

Transition	Observed	o-c	Transition	Observed	o-c	Transition	Observed	o-c
		$\times 10^4$			$\times 10^4$			$\times 10^4$
Rf(1)	3312.8979	-5	Re(16)	3317.2268	7	Pf(9)	3309.6616	5
Re(2)	3313.1901	4	Rf(17)	3317.5157	2	Pe(10)	3309.3658	2
Rf(3)	3313.4811	-4	Re(18)	3317.7958	0	Pf(11)	3309.0678	7
Re(4)	3313.7713	-2	Rf(19)	3318.0844	-6	Pf(13)	3308.4707	-6
Rf(5)	3314.0623	-6	Rf(21)	3318.6519	-8	Pe(14)	3308.1729	-14
Re(6)	3314.3519	4	Re(22)	3318.9311	12	Pf(15)	3307.8752	12
Rf(7)	3314.6418	-8	Rf(23)	3319.2207*	20	Pe(16)	3307.5767	5
Re(8)	3314.929	-10	Re(24)	3319.4964*	20	Pf(17)	3307.2759	1
Rf(9)	3315.2204	-2	Pe(2)	3311.7261	-13	Pe(18)	3306.9775	11
Re(10)	3315.5063	-3	Pf(3)	3311.4323	-9	Pf(19)	3306.6752	1
Rf(11)	3315.7964	-4	Pe(4)	3311.1388	-7	Pe(20)	3306.3748	0
Re(12)	3316.0817	2	Pf(5)	3310.8441	-1	Pf(21)	3306.0731	13
Rf(13)	3316.3712	-2	Pe(6)	3310.5496	-3	Pe(22)	3305.7709	-7
Re(14)	3316.656	13	Pf(7)	3310.2539	3	Pe(24)	3305.1679	13
Rf(15)	3316.9442	-1	Pe(8)	3309.959	4			

Lines which are blended and given less statistical weight in the fit are indicated by \*.

Table A.21: Observed line positions (in  $\text{cm}^{-1}$ ) assigned to the  $1_0^1 6_0^1 8_1^0 7_1^1$  (P) band of  $\text{HC}_4\text{H}$ 

Transition	Observed	o-c	Transition	Observed	o-c	Transition	Observed	o-c
		$\times 10^4$			$\times 10^4$			$\times 10^4$
Rf(2)	3312.1394	-3	Re(13)	3315.3256	-2	Pf(8)	3308.9	-19
Re(3)	3312.4315	-1	Re(15)	3315.8994	1	Pf(10)	3308.3083	4
Rf(4)	3312.7228	0	Rf(16)	3316.1854	1	Pe(11)	3308.0088	1
Re(5)	3313.0138	0	Re(17)	3316.4711	2	Pf(12)	3307.7122	-1
Rf(6)	3313.3042	0	Rf(18)	3316.7567	1	Pe(13)	3307.4103	-8
Re(7)	3313.5944	-1	Pe(3)	3310.3812	13	Pf(14)	3307.1148	-7
Rf(8)	3313.8843	4	Pf(4)	3310.086	8	Pe(15)	3306.8105	-12
Re(9)	3314.1729	-4	Pe(5)	3309.79	2	Pf(16)	3306.5168	-3
Rf(10)	3314.4614	-4	Pf(6)	3309.4943	0	Pe(17)	3306.2104	2
Re(11)	3314.7502	-3	Pe(7)	3309.1981	1	Pf(18)	3305.9178	4
Rf(12)	3315.0377	-3						

## A.3 CHAPTER 4

Table A.22: Observed line positions (in  $\text{cm}^{-1}$ ) assigned to the  $\nu_5$  fundamental band of  $\text{HC}_6\text{H}$  assuming a Coriolis interaction

Transition	Observed	o-c	Transition	Observed	o-c	Transition	Observed	o-c
		$\times 10^4$			$\times 10^4$			$\times 10^4$
P(37)	3325.7333	-8	P(8)	3328.3451	-8	R(18)	3330.7271	2
P(35)	3325.9156	-1	P(7)	3328.4345	-2	R(19)	3330.8186	11
P(33)	3326.0970	1	P(6)	3328.5228	-6	R(20)	3330.9118	9
P(31)	3326.2771	-6	P(5)	3328.6112	-9	R(21)	3330.9646	16
P(29)	3326.4618*	39	P(4)	3328.6990	-16	R(22)	3331.0559	17
P(27)	3326.6361	-10	P(3)	3328.7874	-18	R(23)	3331.1459	23
P(24)	3326.9030	9	P(2)	3328.8749	-27	R(24)	3331.2275*	-43
P(23)	3326.9873	-2	R(1)	3329.2291	-18	R(25)	3331.3180	-14
P(22)	3327.1116	-5	R(3)	3329.4074	2	R(26)	3331.4067	2
P(21)	3327.1955	1	R(5)	3329.5832	0	R(27)	3331.4971*	37
P(20)	3327.2813	-1	R(6)	3329.6711	-1	R(28)	3331.5766*	-35
P(19)	3327.3688	0	R(7)	3329.7595	5	R(29)	3331.6660	-5
P(18)	3327.4570	-1	R(8)	3329.8472	4	R(30)	3331.7526	-3
P(17)	3327.5460	2	R(9)	3329.9349	3	R(31)	3331.8392	0
P(16)	3327.6342	-3	R(10)	3330.0229	6	R(32)	3331.9254	1
P(15)	3327.7234	-1	R(11)	3330.1104	3	R(33)	3332.0116	3
P(14)	3327.8121	-4	R(12)	3330.1986	8	R(34)	3332.0973	1
P(13)	3327.9010	-4	R(13)	3330.2866	11	R(35)	3332.1831	1
P(12)	3327.9903	-1	R(14)	3330.3739	6	R(36)	3332.2681	-6
P(11)	3328.0796	2	R(15)	3330.4622	11	R(37)	3332.3533	-11
P(10)	3328.1680	-3	R(16)	3330.5506	14	R(38)	3332.4385	-15
P(9)	3328.2565	-6	R(17)	3330.6390	13			

Lines which are blended and given less statistical weight in the fit are indicated by \*

Table A.23: Observed line positions (in  $\text{cm}^{-1}$ ) assigned to the  $\nu_5$  fundamental perturber band of  $\text{HC}_6\text{H}$  assuming a Coriolis interaction

Transition	Observed	o-c	Transition	Observed	o-c	Transition	Observed	o-c
		$\times 10^4$			$\times 10^4$			$\times 10^4$
P(23)	3327.0320	-6	P(17)	3327.4565	11	R(23)	3331.2172*	47
P(22)	3327.0681	-17	R(19)	3330.7722	11	R(24)	3331.3180	2
P(21)	3327.1483	-8	R(20)	3330.8695	8	R(25)	3331.4245	1
P(20)	3327.2253	-9	R(21)	3331.0682	2	R(26)	3331.5321	1
P(19)	3327.3017	-9	R(22)	3331.1076	-14			

Lines which are blended and given less statistical weight in the fit are indicated by \*.

Table A.24: Observed line positions (in  $\text{cm}^{-1}$ ) assigned to the  $\nu_5$  fundamental band of  $\text{HC}_6\text{H}$  assuming a Fermi resonance

Transition	Observed	o-c	Transition	Observed	o-c	Transition	Observed	o-c
		$\times 10^4$			$\times 10^4$			$\times 10^4$
P(37)	3325.7333	-8	P(8)	3328.3451	-7	R(18)	3330.7271	1
P(35)	3325.9156	-1	P(7)	3328.4345	-1	R(19)	3330.8186	8
P(33)	3326.0970	1	P(6)	3328.5228	-5	R(20)	3330.9118	0
P(31)	3326.2771	-5	P(5)	3328.6112	-8	R(21)	3330.9646	16
P(29)	3326.4618*	39	P(4)	3328.6990	-16	R(22)	3331.0559	16
P(27)	3326.6361	-10	P(3)	3328.7874	-17	R(23)	3331.1459	23
P(24)	3326.9030	8	P(2)	3328.8749	-26	R(24)	3331.2275*	-44
P(23)	3326.9873	-2	R(1)	3329.2291	-17	R(25)	3331.3180	-14
P(22)	3327.1116	-14	R(3)	3329.4074	3	R(26)	3331.4067	2
P(21)	3327.1955	-2	R(5)	3329.5832	1	R(27)	3331.4971*	37
P(20)	3327.2813	-2	R(6)	3329.6711	0	R(28)	3331.5766*	-35
P(19)	3327.3688	0	R(7)	3329.7595	6	R(29)	3331.6660	-5
P(18)	3327.4570	-1	R(8)	3329.8472	5	R(30)	3331.7526	-3
P(17)	3327.5459	3	R(9)	3329.9349	4	R(31)	3331.8392	1
P(16)	3327.6342	-3	R(10)	3330.0229	6	R(32)	3331.9254	2
P(15)	3327.7234	0	R(11)	3330.1104	4	R(33)	3332.0116	3
P(14)	3327.8121	-3	R(12)	3330.1986	9	R(34)	3332.0973	1
P(13)	3327.9010	-3	R(13)	3330.2866	12	R(35)	3332.1831	1
P(12)	3327.9903	0	R(14)	3330.3739	7	R(36)	3332.2681	-6
P(11)	3328.0796	3	R(15)	3330.4622	12	R(37)	3332.3533	-11
P(10)	3328.1680	-2	R(16)	3330.5506	14	R(38)	3332.4385	-14
P(9)	3328.2565	-6	R(17)	3330.6390	13			

Lines which are blended and given less statistical weight in the fit are indicated by \*

Table A.25: Observed line positions (in  $\text{cm}^{-1}$ ) assigned to the  $\nu_5$  fundamental perturber band of  $\text{HC}_6\text{H}$  assuming a Fermi resonance

Transition	Observed	o-c	Transition	Observed	o-c	Transition	Observed	o-c
		$\times 10^4$			$\times 10^4$			$\times 10^4$
P(25)	3326.8889	7	P(21)	3327.1483	4	R(20)	3330.8693	10
P(24)	3326.9591	-9	P(19)	3327.2990	0	R(21)	3331.0083	-17
P(23)	3327.0320	-25	R(17)	3330.5680	2	R(22)	3331.1125	3
P(22)	3327.0667	-27	R(19)	3330.7722	23	R(23)	3331.2174	3

Table A.26: Observed line positions (in  $\text{cm}^{-1}$ ) assigned to the  $5_0^1 13_1^1$  band of  $\text{HC}_6\text{H}$ 

Transition	Observed	o-c $\times 10^4$	Transition	Observed	o-c $\times 10^4$	Transition	Observed	o-c $\times 10^4$
Pe(31)	3325.4377	27	Pe(7)	3327.5932	7	Re(17)	3329.7949	-12
Pf(31)	3325.4377	-6	Pf(7)	3327.5932	2	Rf(17)	3329.7949	-2
Pe(30)	3325.5281	22	Pe(6)	3327.6821	7	Re(18)	3329.8817	-16
Pf(30)	3325.5281	-10	Pf(6)	3327.6821	2	Rf(18)	3329.8817	-6
Pe(29)	3325.6181	14	Pe(5)	3327.7708	5	Re(19)	3329.9683	-22
Pf(29)	3325.6181	-17	Pf(5)	3327.7708	1	Rf(19)	3329.9683	-11
Pe(28)	3325.7098	23	Pe(4)	3327.8594	3	Re(20)	3330.0555	-20
Pf(28)	3325.7098	-6	Pf(4)	3327.8594	0	Rf(20)	3330.0555	-9
Pe(27)	3325.8004	23	Pe(3)	3327.9475	-3	Re(21)	3330.1426	-19
Pf(27)	3325.8004	-5	Pf(3)	3327.9475	-6	Rf(21)	3330.1426	-7
Pe(26)	3325.8924	38	Qe(1)	3328.2136	0	Re(22)	3330.2293	-20
Pf(26)	3325.8924	11	Qe(3)	3328.2136	7	Rf(22)	3330.2293	-8
Pe(25)	3325.9815	25	Qf(1)	3328.2136	-1	Re(23)	3330.3161	-20
Pf(25)	3325.9815	0	Qf(2)	3328.2136	-1	Rf(23)	3330.3161	-7
Pe(24)	3326.0729	36	Re(1)	3328.3909	2	Re(24)	3330.4020	-28
Pf(24)	3326.0729	12	Rf(1)	3328.3909	4	Rf(24)	3330.4020	-16
Pe(23)	3326.1626	31	Re(2)	3328.4795	5	Re(25)	3330.4895	-18
Pf(23)	3326.1626	8	Rf(2)	3328.4795	7	Rf(25)	3330.4895	-6
Pe(22)	3326.2521	24	Re(3)	3328.5670	-3	Re(26)	3330.5766*	-12
Pf(22)	3326.2521	3	Rf(3)	3328.5670	0	Rf(26)	3330.5766*	1
Pe(21)	3326.3418	21	Re(4)	3328.6548	-7	Re(27)	3330.6624*	-19
Pf(21)	3326.3418	0	Rf(4)	3328.6548	-4	Rf(27)	3330.6624*	-6
Pe(20)	3326.4326	29	Re(5)	3328.7428	-9	Re(28)	3330.7483	-22
Pf(20)	3326.4326	10	Rf(5)	3328.7428	-5	Rf(28)	3330.7483	-9
Pe(19)	3326.5221	24	Re(6)	3328.8306	-12	Re(29)	3330.8351	-16
Pf(19)	3326.5221	6	Rf(6)	3328.8306	-7	Rf(29)	3330.8351	-3
Pe(18)	3326.6121	27	Re(7)	3328.9183	-15	Re(30)	3330.9214	-14
Pf(18)	3326.6121	10	Rf(7)	3328.9183	-10	Rf(30)	3330.9214	-1
Pe(17)	3326.7017	25	Re(8)	3329.0056	-21	Re(31)	3331.0086*	-1
Pf(17)	3326.7017	9	Rf(8)	3329.0056	-15	Rf(31)	3331.0086*	12
Pe(16)	3326.7908	19	Re(9)	3329.0924*	-32	Re(32)	3331.0925	-21
Pf(16)	3326.7908	5	Rf(9)	3329.0924*	-26	Rf(32)	3331.0925	-8
Pe(15)	3326.8800	16	Re(10)	3329.1804*	-30	Re(33)	3331.1794	-9
Pf(15)	3326.8800	3	Rf(10)	3329.1804*	-23	Rf(33)	3331.1794	5
Pe(14)	3326.9694	15	Re(11)	3329.2694*	-18	Re(34)	3331.2644	-15
Pf(14)	3326.9694	2	Rf(11)	3329.2694*	-11	Rf(34)	3331.2644	-1
Pe(12)	3327.1483*	16	Re(12)	3329.3574	-15	Re(35)	3331.3510*	-4
Pf(12)	3327.1483*	6	Rf(12)	3329.3574	-7	Rf(35)	3331.3510*	10
Pe(11)	3327.2372	12	Re(13)	3329.4455	-10	Re(36)	3331.4358	-9
Pf(11)	3327.2372	3	Rf(13)	3329.4455	-2	Rf(36)	3331.4358	5
Pe(10)	3327.3260	8	Re(14)	3329.5327	-13	Re(37)	3331.5223	3
Pf(10)	3327.3260	-1	Rf(14)	3329.5327	-4	Rf(37)	3331.5223	17
Pe(9)	3327.4150	7	Re(15)	3329.6205	-10	Re(39)	3331.6918	-2
Pf(9)	3327.4150	-1	Rf(15)	3329.6205	0	Rf(39)	3331.6918	11
Pe(8)	3327.5038	4	Re(16)	3329.7073	-15			
Pf(8)	3327.5038	-3	Rf(16)	3329.7073	-5			

Lines which are blended and given less statistical weight in the fit are indicated by \*.

Table A.27: Observed line positions (in  $\text{cm}^{-1}$ ) assigned to the  $5_0^1 10_1^1$  band of  $\text{HC}_6\text{H}$ 

Transition	Observed	o-c $\times 10^4$	Transition	Observed	o-c $\times 10^4$	Transition	Observed	o-c $\times 10^4$
Pe(29)	3325.9877	11	Pe(9)	3327.7843*	5	Re(13)	3329.8151	-2
Pf(29)	3325.9877	0	Pf(9)	3327.7843*	2	Rf(13)	3329.8151	2
Pe(28)	3326.0774	0	Pe(8)	3327.8733	3	Re(14)	3329.9033	5
Pf(28)	3326.0774	-10	Pf(8)	3327.8733	1	Rf(14)	3329.9033	9
Pe(27)	3326.1694	14	Pe(7)	3327.9623	4	Re(15)	3329.9901	-1
Pf(27)	3326.1694	4	Pf(7)	3327.9623	2	Rf(15)	3329.9901	4
Pe(26)	3326.2587	1	Pe(6)	3328.0509	1	Re(16)	3330.0774	-2
Pf(26)	3326.2587	-9	Pf(6)	3328.0509	-1	Rf(16)	3330.0774	3
Pe(25)	3326.3501	11	Pe(5)	3328.1402	6	Re(17)	3330.1644	-4
Pf(25)	3326.3501	2	Pf(5)	3328.1402	4	Rf(17)	3330.1644	1
Pe(24)	3326.4398	6	Pe(4)	3328.2293	9	Re(18)	3330.2523	4
Pf(24)	3326.4398	-3	Pf(4)	3328.2293	7	Rf(18)	3330.2523	9
Pe(23)	3326.5302	7	Pe(3)	3328.3180	9	Re(19)	3330.3383	-7
Pf(23)	3326.5302	-1	Pf(3)	3328.3180	8	Rf(19)	3330.3383	-2
Pe(22)	3326.6189	-7	Pe(2)	3328.4057	-1	Re(20)	3330.4256*	-4
Pf(22)	3326.6189	-16	Pf(2)	3328.4057	-2	Rf(20)	3330.4256*	2
Pe(21)	3326.7104	7	Qe(1)	3328.5829	1	Re(21)	3330.5114*	-15
Pf(21)	3326.7104	-1	Qe(2)	3328.5829	3	Rf(21)	3330.5114*	-9
Pe(20)	3326.7992	-5	Qf(1)	3328.5829	1	Re(23)	3330.6848*	-16
Pf(20)	3326.7992	-12	Qf(3)	3328.5829	2	Rf(23)	3330.6848*	-9
Pe(19)	3326.8897	2	Re(2)	3328.8466	-15	Re(24)	3330.7732*	2
Pf(19)	3326.8897	-5	Rf(2)	3328.8466	-14	Rf(24)	3330.7732*	9
Pe(18)	3326.9785	-8	Re(3)	3328.9359	-4	Re(26)	3330.9462*	3
Pf(18)	3326.9785	-14	Rf(3)	3328.9359	-3	Rf(26)	3330.9462*	11
Pe(17)	3327.0696*	6	Re(4)	3329.0231	-14	Re(27)	3331.0317	-5
Pf(17)	3327.0696*	0	Rf(4)	3329.0231	-13	Rf(27)	3331.0317	3
Pe(16)	3327.1584	-2	Re(5)	3329.1108*	-19	Re(28)	3331.1183	-1
Pf(16)	3327.1584	-7	Rf(5)	3329.1108*	-17	Rf(28)	3331.1183	7
Pe(15)	3327.2482	0	Re(7)	3329.2883	-5	Re(30)	3331.2898	-5
Pf(15)	3327.2482	-5	Rf(7)	3329.2883	-3	Rf(30)	3331.2898	3
Pe(14)	3327.3378	2	Re(8)	3329.3773	6	Re(31)	3331.3749	-12
Pf(14)	3327.3378	-3	Rf(8)	3329.3773	9	Rf(31)	3331.3749	-3
Pe(13)	3327.4273	3	Re(9)	3329.4653	7	Re(32)	3331.4617	-1
Pf(13)	3327.4273	-2	Rf(9)	3329.4653	10	Rf(32)	3331.4617	8
Pe(12)	3327.5164	1	Re(10)	3329.5529	6	Re(33)	3331.5479	6
Pf(12)	3327.5164	-3	Rf(10)	3329.5529	9	Rf(33)	3331.5479	15
Pe(11)	3327.6062	6	Re(11)	3329.6402	2	Re(34)	3331.6313	-14
Pf(11)	3327.6062	2	Rf(11)	3329.6402	5	Rf(34)	3331.6313	-5
Pe(10)	3327.6941*	-6	Re(12)	3329.7279	2			
Pf(10)	3327.6941*	-10	Rf(12)	3329.7279	6			

Lines which are blended and given less statistical weight in the fit are indicated by \*.

Table A.28: Observed line positions (in  $\text{cm}^{-1}$ ) assigned to the  $5_0^1 11_1^1$  band of  $\text{HC}_6\text{H}$ 

Transition	Observed	o-c	Transition	Observed	o-c	Transition	Observed	o-c
		$\times 10^4$			$\times 10^4$			$\times 10^4$
Pe(17)	3327.4874*	2	Re(3)	3329.3535	14	Re(17)	3330.5754*	-24
Pf(17)	3327.4874*	-2	Rf(3)	3329.3535	14	Rf(17)	3330.5754*	-22
Pe(16)	3327.5772*	4	Re(4)	3329.4416	14	Re(19)	3330.7508*	-8
Pf(16)	3327.5772*	1	Rf(4)	3329.4416	15	Rf(19)	3330.7508*	-7
Pe(13)	3327.8455	6	Re(5)	3329.5291	11	Re(21)	3330.9243*	-11
Pf(13)	3327.8455	4	Rf(5)	3329.5291	11	Rf(21)	3330.9243*	-10
Pe(12)	3327.9321*	-20	Re(7)	3329.7026*	-12	Re(25)	3331.2736*	17
Pf(12)	3327.9321*	-22	Rf(7)	3329.7026*	-11	Rf(25)	3331.2736*	17
Pe(11)	3328.0211*	-22	Re(9)	3329.8807*	16	Re(26)	3331.3585	1
Pf(11)	3328.0211*	-24	Rf(9)	3329.8807*	17	Rf(26)	3331.3585	2
Pe(10)	3328.1128*	5	Re(10)	3329.9663*	-4	Re(27)	3331.4432	-16
Pf(10)	3328.1128*	3	Rf(10)	3329.9663*	-3	Rf(27)	3331.4432	-16
Pe(8)	3328.2893*	-11	Re(11)	3330.0557*	15	Re(28)	3331.5322	10
Pf(8)	3328.2893*	-12	Rf(11)	3330.0557*	16	Rf(28)	3331.5322	11
Pe(7)	3328.3797*	5	Re(12)	3330.1408	-8			
Pf(7)	3328.3797*	3	Rf(12)	3330.1408	-7			
Pe(6)	3328.4668	-12	Re(13)	3330.2276*	-13			
Pf(6)	3328.4668	-13	Rf(13)	3330.2276*	-12			

Lines which are blended and given less statistical weight in the fit are indicated by \*.

Table A.29: Observed line positions (in  $\text{cm}^{-1}$ ) assigned to the  $1_0^1 8_0^1 11_1^0$  band of  $\text{HC}_6\text{H}$ 

Transition	Observed	o-c	Transition	Observed	o-c	Transition	Observed	o-c
		$\times 10^4$			$\times 10^4$			$\times 10^4$
Pe(22)	3308.8532	4	Pe(8)	3310.1024	6	Re(11)	3311.8660	-2
Pf(22)	3308.8532	3	Pf(8)	3310.1024	5	Rf(11)	3311.8660	0
Pe(21)	3308.9427	4	Pe(7)	3310.1911	5	Re(12)	3311.9532	-7
Pf(21)	3308.9427	3	Pf(7)	3310.1911	4	Rf(12)	3311.9532	-4
Pe(20)	3309.0327	8	Pe(6)	3310.2802	9	Re(13)	3312.0410	-4
Pf(20)	3309.0327	7	Pf(6)	3310.2802	8	Rf(13)	3312.0410	-1
Pe(19)	3309.1199	-14	Pe(5)	3310.3688	9	Re(14)	3312.1277	-12
Pf(19)	3309.1199	-16	Pf(5)	3310.3688	8	Rf(14)	3312.1277	-9
Pe(18)	3309.2109	2	Re(3)	3311.1634	1	Re(15)	3312.2152	-12
Pf(18)	3309.2109	0	Rf(3)	3311.1634	2	Rf(15)	3312.2152	-8
Pe(17)	3309.3007	6	Re(4)	3311.2511	-3	Re(16)	3312.3037	-1
Pf(17)	3309.3007	5	Rf(4)	3311.2511	-2	Rf(16)	3312.3037	3
Pe(16)	3309.3898	4	Re(5)	3311.3376	-18	Re(17)	3312.3914	3
Pf(16)	3309.3898	2	Rf(5)	3311.3376	-17	Rf(17)	3312.3914	8
Pe(14)	3309.5694	16	Re(6)	3311.4265	-9	Re(18)	3312.4774	-10
Pf(14)	3309.5694	14	Rf(6)	3311.4265	-7	Rf(18)	3312.4774	-5
Pe(12)	3309.7469	8	Re(7)	3311.5146	-7	Re(19)	3312.5649	-6
Pf(12)	3309.7469	7	Rf(7)	3311.5146	-5	Rf(19)	3312.5649	-1
Pe(11)	3309.8361	10	Re(8)	3311.6023	-8	Re(20)	3312.6518	-9
Pf(11)	3309.8361	9	Rf(8)	3311.6023	-6	Rf(20)	3312.6518	-4
Pe(10)	3309.9231*	-9	Re(9)	3311.6903	-6			
Pf(10)	3309.9231*	-10	Rf(9)	3311.6903	-4			
Pe(9)	3310.0136	7	Re(10)	3311.7781	-5			
Pf(9)	3310.0136	6	Rf(10)	3311.7781	-2			

Lines which are blended and given less statistical weight in the fit are indicated by \*.

## A.4 CHAPTER 5

Table A.30: Observed line positions (in  $\text{cm}^{-1}$ ) assigned to the  $\nu_3 + \nu_5$  combination band of  $\text{C}_3\text{H}_4$ 

Subband	Transition	Observed	o-c	Upper State	Subband	Transition	Observed	o-c	Upper State
			$\times 10^4$	- Lower State				$\times 10^4$	- Lower State
$K'=1$	qP1(15)	3061.0276	-3	E - E	$K'=0$	qPo(8)	3065.4341	11	A2 - A1
$K'=0$	qPo(15)	3061.0380	-4	A1 - A2	$K'=2$	qP2(7)	3066.0006	5	E - E
$K'=1$	qP1(14)	3061.6718	10	E - E	$K'=1$	qP1(7)	3066.0270	-9	E - E
$K'=0$	qPo(14)	3061.6840	21	A2 - A1	$K'=0$	qPo(7)	3066.0390	-9	A1 - A2
$K'=1$	qP1(13)	3062.3097	14	E - E	$K'=2$	qP2(6)	3066.6009	-5	E - E
$K'=0$	qPo(13)	3062.3221	20	A1 - A2	$K'=1$	qP1(6)	3066.6270	-10	E - E
$K'=2$	qP2(12)	3062.9138	-1	E - E	$K'=0$	qPo(6)	3066.6406	-9	A2 - A1
$K'=1$	qP1(12)	3062.9409	5	E - E	$K'=2$	qP2(5)	3067.1988	12	E - E
$K'=0$	qPo(12)	3062.9518	-14	A2 - A1	$K'=1$	qP1(5)	3067.2214	13	E - E
$K'=2$	qP2(11)	3063.5428	5	E - E	$K'=0$	qPo(5)	3067.2389	10	A1 - A2
$K'=1$	qP1(11)	3063.5686	20	E - E	$K'=2$	qP2(4)	3067.7899	10	E - E
$K'=0$	qPo(11)	3063.5808	-1	A1 - A2	$K'=1$	qP1(4)	3067.8222	11	E - E
$K'=2$	qP2(10)	3064.1651	2	E - E	$K'=0$	qPo(4)	3067.8298	7	A2 - A1
$K'=1$	qP1(10)	3064.1808	-14	E - E	$K'=2$	qP2(3)	3068.3766	13	E - E
$K'=0$	qPo(10)	3064.2046	11	A2 - A1	$K'=1$	qP1(3)	3068.4070	14	E - E
$K'=2$	qP2(9)	3064.7821	0	E - E	$K'=0$	qPo(3)	3068.4151	2	A1 - A2
$K'=1$	qP1(9)	3064.8121	-0	E - E	$K'=1$	qP1(2)	3068.9866	10	E - E
$K'=0$	qPo(9)	3064.8215	7	A1 - A2	$K'=0$	qPo(2)	3068.9960	4	A2 - A1
$K'=2$	qP2(8)	3065.3955	17	E - E	$K'=0$	qPo(2)	3068.9960	4	A2 - A1
$K'=1$	qP1(8)	3065.4221	-1	E - E	$K'=0$	qPo(1)	3069.5695	-15	A1 - A2
$K'=3$	qQ3(5)	3069.9375	10	A2 - A1	$K'=2$	qQ2(4)	3070.0457	-22	E - E
$K'=2$	qQ2(5)	3069.9375	10	A1 - A2	$K'=1$	qQ1(5)	3070.0467	-19	E - E
$K'=3$	qQ3(4)	3069.9814	-19	A2 - A1	$K'=2$	qQ2(3)	3070.0688	-4	E - E
$K'=3$	qQ3(4)	3069.9814	-19	A1 - A2	$K'=1$	qQ1(4)	3070.0698	-8	E - E
$K'=2$	qQ2(6)	3069.9892	-14	E - E	$K'=2$	qQ2(2)	3070.0838	-17	E - E
$K'=3$	qQ3(3)	3070.0153	4	A2 - A1	$K'=1$	qQ1(3)	3070.0992	-23	E - E
$K'=3$	qQ3(3)	3070.0153	4	A1 - A2	$K'=1$	qQ1(2)	3070.1145	-13	E - E
$K'=2$	qQ2(5)	3070.0198	-20	E - E	$K'=1$	qQ1(1)	3070.1240	-19	E - E
$K'=0$	qRo(0)	3070.7062	3	A2 - A1	$K'=2$	qR2(8)	3074.9949	-8	E - E
$K'=1$	qR1(1)	3071.2567	6	E - E	$K'=1$	qR1(8)	3075.0122	-14	E - E
$K'=0$	qRo(1)	3071.2666	10	A1 - A2	$K'=0$	qRo(8)	3075.0350	-1	A2 - A1
$K'=2$	qR2(2)	3071.7798	4	E - E	$K'=2$	qR2(9)	3075.5126	-3	E - E
$K'=1$	qR1(2)	3071.8123	5	E - E	$K'=1$	qR1(9)	3075.5392	13	E - E
$K'=0$	qRo(2)	3071.8191	-7	A2 - A1	$K'=0$	qRo(9)	3075.5518	-7	A1 - A2
$K'=2$	qR2(3)	3072.3295	13	E - E	$K'=2$	qR2(10)	3076.0252	8	E - E
$K'=1$	qR1(3)	3072.3526	15	E - E	$K'=1$	qR1(10)	3076.0527	9	E - E
$K'=0$	qRo(3)	3072.3692	3	A1 - A2	$K'=0$	qRo(10)	3076.0650	3	A2 - A1
$K'=2$	qR2(4)	3072.8728	7	E - E	$K'=2$	qR2(11)	3076.5283	-18	E - E
$K'=1$	qR1(4)	3072.8993	3	E - E	$K'=1$	qR1(11)	3076.5571	-24	E - E
$K'=0$	qRo(4)	3072.9122	-5	A2 - A1	$K'=0$	qRo(11)	3076.5691	-24	A1 - A2
$K'=2$	qR2(5)	3073.4090	-19	E - E	$K'=2$	qR2(12)	3077.0305	7	E - E
$K'=1$	qR1(5)	3073.4373	-18	E - E	$K'=1$	qR1(12)	3077.0599	-18	E - E
$K'=0$	qRo(5)	3073.4491	-21	A1 - A2	$K'=0$	qRo(12)	3077.0711	-21	A2 - A1
$K'=2$	qR2(6)	3073.9454	8	E - E	$K'=1$	qR1(13)	3077.5589	3	E - E
$K'=1$	qR1(6)	3073.9740	5	E - E	$K'=0$	qRo(13)	3077.5704	8	A1 - A2
$K'=0$	qRo(6)	3073.9854	9	A2 - A1	$K'=1$	qR1(14)	3078.0503	1	E - E
$K'=2$	qR2(7)	3074.4733	5	E - E	$K'=0$	qRo(14)	3078.0612	6	A2 - A1
$K'=1$	qR1(7)	3074.5024	-11	E - E	$K'=1$	qR1(15)	3078.5368	2	E - E
$K'=0$	qRo(7)	3074.5132	8	A1 - A2	$K'=0$	qRo(15)	3078.5460	-4	A1 - A2

Table A.31: Observed line positions (in  $\text{cm}^{-1}$ ) assigned to the perturbing bands of the combination band of  $\text{C}_3\text{H}_4$ 

Subband	Transition	Observed	o-c $\times 10^4$	Upper State - Lower State	Subband	Transition	Observed	o-c $\times 10^4$	Upper State - Lower State
P <sub>2</sub> K'=1	qP <sub>1</sub> (10)	3064.2046	10	E - E	P <sub>3</sub> K'=2	qQ <sub>2</sub> (2)	3070.0618	1	E - E
P <sub>2</sub> K'=1	qP <sub>1</sub> (9)	3064.7774	9	E - E	P <sub>1</sub> K'=1	qQ <sub>1</sub> (1)	3070.0915	-11	E - E
P <sub>1</sub> K'=1	qP <sub>1</sub> (6)	3066.6519	-9	E - E	P <sub>1</sub> K'=1	qR <sub>1</sub> (2)	3071.7932	5	E - E
P <sub>1</sub> K'=1	qP <sub>1</sub> (5)	3067.2354	2	E - E	P <sub>1</sub> K'=1	qR <sub>1</sub> (3)	3072.3665	4	E - E
P <sub>1</sub> K'=1	qP <sub>1</sub> (4)	3067.8030	10	E - E	P <sub>1</sub> K'=1	qR <sub>1</sub> (4)	3072.9237	-1	E - E
P <sub>1</sub> K'=1	qP <sub>1</sub> (3)	3068.3771	-13	E - E	P <sub>2</sub> K'=1	qR <sub>1</sub> (7)	3074.4680	1	E - E
P <sub>3</sub> K'=2	qQ <sub>2</sub> (3)	3070.0405	0	E - E	P <sub>2</sub> K'=1	qR <sub>1</sub> (8)	3075.0350	-0	E - E

## A.5 CHAPTER 6

Table A.32: Harmonic and anharmonic (VPT2) frequencies (in  $\text{cm}^{-1}$ ) of  $^{12}\text{CH}_3^{13}\text{C}^{13}\text{CH}$  (I<sub>4</sub>), with the intensities (in  $\text{km/mol}$ ) given in parenthesis.

mode	$\omega$	$\nu$
$\nu_1$	3453.2(50.6)	3322.7(39.7)
$\nu_2$	3050.3(13.4)	2938.7(9.3)
$\nu_3$	2102.7(3.0)	2063.6(3.0)
$\nu_4$	1414.2(0.1)	1382.1(0.0)
$\nu_5$	922.1(0.8)	911.2(0.6)
$\nu_6$	3126.4(5.9)	2975.5(6.9)
$\nu_7$	1486.3(7.8)	1448.8(7.8)
$\nu_8$	1053.2(0.2)	1030.6(0.1)
$\nu_9$	638.0(45.6)	631.0(45.6)
$\nu_{10}$	315.9(6.7)	318.6(7.0)

Table A.33: Observed line positions (in  $\text{cm}^{-1}$ ) assigned to the  $\nu_1$  fundamental band of  $^{13}\text{CH}_3^{12}\text{C}^{12}\text{CH}$  (I<sub>1</sub>).

Transition	Observed	o-c	Transition	Observed	o-c	Transition	Observed	o-c
		$\times 10^4$			$\times 10^4$			$\times 10^4$
qPo(10)	3329.3689	-5	qPo(1)	3334.4177	3	qRi(5)	3338.2767	1
qPi(10)	3329.3753	-2	qQi(1)	3334.9698	-26	qRo(6)	3338.8162	-31
qPo(9)	3329.9355	-3	qRo(0)	3335.5237	-18	qRi(6)	3338.8208	-22
qPi(9)	3329.9422	17	qRo(1)	3336.0782	6	qRo(7)	3339.362	-15
qPo(8)	3330.4994	-13	qRi(1)	3336.0782	-11	qRi(7)	3339.3688	7
qPi(8)	3330.5063	19	qRo(2)	3336.6298	12	qRo(8)	3339.9055	-6
qPo(7)	3331.0619	-23	qRi(2)	3336.6298	-6	qRi(8)	3339.9127	7
qPi(7)	3331.067	-1	qRo(3)	3337.1802	19	qRo(9)	3340.4473	3
qPo(4)	3332.7476	11	qRi(3)	3337.1802	-1	qRi(9)	3340.455	2
qPi(4)	3332.7476	-7	qRo(4)	3337.7266	0	qRo(10)	3340.9876	15
qPo(2)	3333.8629	13	qRi(4)	3337.7303	12	qRi(10)	3340.9953	-10
qPi(2)	3333.8629	-4	qRo(5)	3338.2714	-23	qRo(11)	3341.5238	4

Table A.34: Observed line positions (in  $\text{cm}^{-1}$ ) assigned to the  $\nu_1$  fundamental band of  $^{12}\text{CH}_3^{13}\text{C}^{12}\text{CH}$  (I<sub>2</sub>).

Transition	Observed	o-c	Transition	Observed	o-c	Transition	Observed	o-c
		$\times 10^4$			$\times 10^4$			$\times 10^4$
qPi(9)	3319.7272	4	qPo(3)	3323.3014	19	qRo(2)	3326.7148	9
qPi(8)	3320.3063	-1	qPi(2)	3323.7715	11	qRi(3)	3327.1762	11
qPi(7)	3320.8896	21	qPo(2)	3323.8739	17	qRo(3)	3327.2773	3
qPo(7)	3320.9887	-5	qPo(1)	3324.4442	-8	qRi(4)	3327.7384	22
qPi(6)	3321.4667	-11	qQi(3)	3324.9	-25	qRo(4)	3327.8376	-4
qPo(6)	3321.5676	-21	qQi(2)	3324.9051	-21	qRi(5)	3328.296	7
qPi(5)	3322.0471	5	qQi(1)	3324.9101	-25	qRo(5)	3328.3963	-9
qPo(5)	3322.148	-3	qRo(0)	3325.5823	5	qRi(6)	3328.8555	18
qPi(4)	3322.6242	11	qRi(1)	3326.0471	2	qRo(6)	3328.9546	-11
qPo(4)	3322.7257	7	qRo(1)	3326.1473	-14	qRi(7)	3329.4136	-2
qPi(3)	3323.1991	14	qRi(2)	3326.6127	7			

Table A.35: Observed line positions (in  $\text{cm}^{-1}$ ) assigned to the  $\nu_1$  fundamental band of  $^{12}\text{CH}_3^{12}\text{C}^{13}\text{CH}$  ( $I_3$ ).

Transition	Observed	o-c	Transition	Observed	o-c	Transition	Observed	o-c
	$\times 10^4$			$\times 10^4$			$\times 10^4$	
qP0(9)	3313.6444	1	qP0(3)	3317.0047	5	qR1(4)	3321.4396	-28
qP1(9)	3313.6748	6	qP1(3)	3317.0337	9	qR0(5)	3321.9585	-3
qP0(8)	3314.2058	-16	qP0(2)	3317.5593	-5	qR1(5)	3321.9872	-8
qP1(8)	3314.2346	-23	qP1(2)	3317.5872	-12	qR0(6)	3322.504	9
qP0(7)	3314.7684	-7	qP0(1)	3318.1126	-16	qR1(6)	3322.5337	13
qP1(7)	3314.798	-5	qQ1(1)	3318.6936	-9	qR0(7)	3323.0471	11
qP0(6)	3315.33	2	qR0(1)	3319.7705	9	qR1(7)	3323.0767	11
qP1(6)	3315.3591	2	qR0(2)	3320.319	3	qR0(8)	3323.5886	9
qP0(5)	3315.8906	15	qR1(2)	3320.3478	4	qR1(8)	3323.6196	19
qP1(5)	3315.9193	12	qR0(3)	3320.8665	-2	qR0(9)	3324.1276	-7
qP0(4)	3316.4484	11	qR1(3)	3320.8956	1	qR1(9)	3324.1586	1
qP1(4)	3316.4765	5	qR0(4)	3321.4117	-17	qR1(10)	3324.697	-12

Table A.36: Vibrational transitions considered in the Fermi resonance analysis:  $^{12}\text{CH}_3^{12}\text{C}^{12}\text{CH}$  given as an example

Lower State	Upper State	Energy ( $\text{cm}^{-1}$ )	Int. (km/mol)
1 2 3 4 5 6 7 8 9 10	→ 1 2 3 4 5 6 7 8 9 10		
0 0 0 0 0 0 0 0 0 0	→ 0 0 0 0 1 0 0 1 1 2	3251.0051	0.0000
0 0 0 0 0 0 0 0 0 0	→ 0 0 0 0 0 0 0 1 3 1	3262.4816	0.0000
0 0 0 0 0 0 0 0 0 0	→ 1 0 0 0 0 0 0 0 0 0	3337.2644	46.1719
0 0 0 0 0 0 0 0 0 0	→ 0 0 0 0 0 0 1 0 3 0	3349.2560	0.0118
0 0 0 0 0 0 0 0 0 0	→ 0 0 1 0 1 0 0 0 0 1	3383.0263	0.0004
0 0 0 0 0 0 0 0 0 0	→ 0 0 1 0 0 0 0 0 2 0	3391.2195	0.4168
0 0 0 0 0 0 0 0 0 0	→ 0 0 1 0 0 0 0 0 1 2	3410.6626	0.0001
0 0 0 0 0 0 0 0 0 0	→ 0 0 1 0 0 0 0 0 0 4	3414.0610	0.0002
0 0 0 0 0 0 0 0 0 0	→ 0 0 0 0 0 0 0 1 4 0	3558.2409	0.0006

Table A.37: Observed line positions (in  $\text{cm}^{-1}$ ) assigned to the  $\nu_4$  fundamental band of  $\text{c-C}_3\text{H}_3^+$ 

Transition	Observed	o-c	Upper State	Transition	Observed	o-c	Upper State
	$\times 10^3$	$\times 10^3$	- Lower State		$\times 10^3$	$\times 10^3$	- Lower State
pP12(12)	3118.071	0	A <sub>2</sub> <sup>''</sup> - A <sub>2</sub> <sup>'</sup>	rQ5(7)	3125.440	2	E <sup>'</sup> - E <sup>'</sup>
pP10(11)	3118.089	1	E <sup>'</sup> - E <sup>'</sup>	pP5(5)	3125.454	4	E <sup>'</sup> - E <sup>'</sup>
pP8(10)	3118.111	2	E <sup>'</sup> - E <sup>'</sup>	pP3(4)	3125.469	4	A <sub>2</sub> <sup>'</sup> - A <sub>2</sub> <sup>''</sup>
pP6(9)	3118.136	1	A <sub>2</sub> <sup>''</sup> - A <sub>2</sub> <sup>'</sup>	pP1(3)	3125.491	4	E <sup>'</sup> - E <sup>'</sup>
pP4(8)	3118.167	1	E <sup>'</sup> - E <sup>'</sup>	rQ4(7)	3126.442	2	E <sup>'</sup> - E <sup>'</sup>
pP2(7)	3118.205	1	E <sup>'</sup> - E <sup>'</sup>	rQ4(6)	3126.481	1	E <sup>'</sup> - E <sup>'</sup>
pP11(11)	3119.134	0	E <sup>'</sup> - E <sup>'</sup>	pP4(4)	3126.494	1	E <sup>'</sup> - E <sup>'</sup>
pP9(10)	3119.149	-1	A <sub>2</sub> <sup>'</sup> - A <sub>2</sub> <sup>''</sup>	pP2(3)	3126.510	1	E <sup>'</sup> - E <sup>'</sup>
pP7(9)	3119.171	1	E <sup>'</sup> - E <sup>'</sup>	rQ3(8)	3127.401	-2	A <sub>2</sub> <sup>'</sup> - A <sub>2</sub> <sup>''</sup>
pP3(7)	3119.228	-1	A <sub>2</sub> <sup>'</sup> - A <sub>2</sub> <sup>''</sup>	rQ3(7)	3127.445	-2	A <sub>2</sub> <sup>'</sup> - A <sub>2</sub> <sup>''</sup>
pP1(6)	3119.268	1	E <sup>'</sup> - E <sup>'</sup>	rQ3(6)	3127.483	-3	A <sub>2</sub> <sup>'</sup> - A <sub>2</sub> <sup>''</sup>
pP10(10)	3120.193	-1	E <sup>'</sup> - E <sup>'</sup>	rQ3(5)	3127.518	-1	A <sub>2</sub> <sup>'</sup> - A <sub>2</sub> <sup>''</sup>
pP8(9)	3120.208	-1	E <sup>'</sup> - E <sup>'</sup>	pP3(3)	3127.532	-2	A <sub>2</sub> <sup>'</sup> - A <sub>2</sub> <sup>''</sup>
pP6(8)	3120.229	-1	A <sub>2</sub> <sup>''</sup> - A <sub>2</sub> <sup>'</sup>	rQ3(4)	3127.547*	0	A <sub>2</sub> <sup>'</sup> - A <sub>2</sub> <sup>''</sup>
pP4(7)	3120.254	-2	E <sup>'</sup> - E <sup>'</sup>	pP1(2)	3127.547*	-3	E <sup>'</sup> - E <sup>'</sup>
pP9(9)	3121.249	-2	A <sub>2</sub> <sup>'</sup> - A <sub>2</sub> <sup>''</sup>	rQ2(6)	3128.493	-1	E <sup>'</sup> - E <sup>'</sup>
pP7(8)	3121.263	-2	E <sup>'</sup> - E <sup>'</sup>	rQ2(5)	3128.526	-2	E <sup>'</sup> - E <sup>'</sup>
pP5(7)	3121.282	-4	E <sup>'</sup> - E <sup>'</sup>	pP2(2)	3128.574	2	E <sup>'</sup> - E <sup>'</sup>
pP3(6)	3121.313	0	A <sub>2</sub> <sup>'</sup> - A <sub>2</sub> <sup>''</sup>	rQ2(3)	3128.581*	2	E <sup>'</sup> - E <sup>'</sup>
pP8(8)	3122.306	2	E <sup>'</sup> - E <sup>'</sup>	rQ1(6)	3129.504	-2	E <sup>'</sup> - E <sup>'</sup>
pP6(7)	3122.321	2	A <sub>2</sub> <sup>''</sup> - A <sub>2</sub> <sup>'</sup>	rQ1(5)	3129.538	-2	E <sup>'</sup> - E <sup>'</sup>
pP4(6)	3122.339	-1	E <sup>'</sup> - E <sup>'</sup>	rQ1(4)	3129.568	0	E <sup>'</sup> - E <sup>'</sup>
pP7(7)	3123.355	-1	E <sup>'</sup> - E <sup>'</sup>	rQ1(3)	3129.590	-1	E <sup>'</sup> - E <sup>'</sup>
pP5(6)	3123.370	0	E <sup>'</sup> - E <sup>'</sup>	rQ1(2)	3129.606	-1	E <sup>'</sup> - E <sup>'</sup>
pP3(5)	3123.391	0	A <sub>2</sub> <sup>'</sup> - A <sub>2</sub> <sup>''</sup>	pP1(1)	3129.606	-1	E <sup>'</sup> - E <sup>'</sup>
pP1(4)	3123.421	2	E <sup>'</sup> - E <sup>'</sup>	rQ0(5)	3130.553*	-5	A <sub>2</sub> <sup>''</sup> - A <sub>2</sub> <sup>'</sup>
rQ6(10)	3124.289	-3	A <sub>2</sub> <sup>''</sup> - A <sub>2</sub> <sup>'</sup>	rQ0(1)	3130.636	2	A <sub>2</sub> <sup>''</sup> - A <sub>2</sub> <sup>'</sup>
rQ6(9)	3124.348	3	A <sub>2</sub> <sup>''</sup> - A <sub>2</sub> <sup>'</sup>	pQ1(8)	3131.457	3	E <sup>'</sup> - E <sup>'</sup>
rQ6(8)	3124.394	0	A <sub>2</sub> <sup>''</sup> - A <sub>2</sub> <sup>'</sup>	pQ1(7)	3131.496*	-3	E <sup>'</sup> - E <sup>'</sup>
pP6(6)	3124.404	0	A <sub>2</sub> <sup>''</sup> - A <sub>2</sub> <sup>'</sup>	pQ1(5)	3131.573	0	E <sup>'</sup> - E <sup>'</sup>
pP4(5)	3124.418	-1	E <sup>'</sup> - E <sup>'</sup>	pQ1(4)	3131.600	-2	E <sup>'</sup> - E <sup>'</sup>
pP2(4)	3124.438	-3	E <sup>'</sup> - E <sup>'</sup>	pQ1(2)	3131.639*	-3	E <sup>'</sup> - E <sup>'</sup>
rQ6(7)	3124.438	0	A <sub>2</sub> <sup>''</sup> - A <sub>2</sub> <sup>'</sup>	pQ1(1)	3131.652*	-2	E <sup>'</sup> - E <sup>'</sup>

Lines which are blended and given less statistical weight in the fit are indicated by \*.

Table A.38: Observed line positions (in  $\text{cm}^{-1}$ ) assigned to the  $\nu_4$  fundamental band of  $c\text{-C}_3\text{H}_3^+$  continued

Transition	Observed	o-c	Upper State	Transition	Observed	o-c	Upper State
		$\times 10^3$	- Lower State			$\times 10^3$	- Lower State
pQ2(10)	3132.368	-1	E'' - E'	rR5(5)	3137.785	0	E' - E''
pQ2(7)	3132.523	2	E'' - E'	rR2(4)	3138.786*	2	E'' - E'
pQ2(6)	3132.563	3	E'' - E'	rRo(3)	3138.788	1	Az'' - Az'
pQ2(5)	3132.596	2	E'' - E'	rR4(5)	3138.788*	1	E'' - E'
pQ2(4)	3132.625	2	E'' - E'	rR6(6)	3138.800	2	Az'' - Az'
pQ2(3)	3132.648	2	E'' - E'	rR1(4)	3139.795*	-1	E' - E''
pQ2(2)	3132.662*	-2	E'' - E'	rR3(5)	3139.795	3	Az'' - Az''
pQ3(9)	3133.451	2	Az' - Az''	rR5(6)	3139.795	-1	E' - E''
pQ3(8)	3133.500	0	Az' - Az''	rR7(7)	3139.809	2	E' - E''
pQ3(6)	3133.585	0	Az' - Az''	rR2(5)	3140.802*	1	E'' - E'
pQ3(5)	3133.619	0	Az' - Az''	rR4(6)	3140.802*	4	E'' - E'
pQ3(4)	3133.648	0	Az' - Az''	rR6(7)	3140.802	-1	Az'' - Az'
pQ3(3)	3133.671	0	Az' - Az''	rR8(8)	3140.815	1	E'' - E'
rR1(1)	3133.710	-1	E' - E''	rR3(6)	3141.801	-3	Az'' - Az''
pQ4(6)	3134.615	2	E'' - E'	rR5(7)	3141.801	-1	E' - E''
pQ4(5)	3134.644	-4	E'' - E'	rR9(9)	3141.816	-3	Az' - Az''
pQ4(4)	3134.673	-3	E'' - E'	rR4(7)	3142.806	3	E'' - E'
rRo(1)	3134.722*	-3	Az'' - Az'	rR6(8)	3142.806	4	Az'' - Az'
rR2(2)	3134.731	-2	E'' - E'	rR2(6)	3142.811*	0	E'' - E'
pQ5(7)	3135.605	1	E' - E''	rR8(9)	3142.811*	3	E'' - E'
pQ5(5)	3135.680	1	E' - E''	rRo(5)	3142.822	-1	Az'' - Az'
rR1(2)	3135.746	1	E' - E''	pR2(4)	3142.853	2	E'' - E'
rR3(3)	3135.755	2	Az' - Az''	rR5(8)	3143.800	-1	E' - E''
pQ6(9)	3136.539	-2	Az'' - Az'	rR7(9)	3143.800	-1	E' - E''
pQ6(8)	3136.589	-3	Az'' - Az'	rR3(7)	3143.807	-1	Az'' - Az''
pQ6(7)	3136.638	1	Az'' - Az'	rR11(11)	3143.819	0	E' - E''
pQ6(6)	3136.678	0	Az'' - Az'	pR1(5)	3143.845	-1	E' - E''
rR2(3)	3136.761	-1	E'' - E'	rR6(9)	3144.797	1	Az'' - Az'
rR4(4)	3136.769	-1	E'' - E'	rR4(8)	3144.801*	-1	E'' - E'
pQ7(7)	3137.675	0	E' - E''	rR2(7)	3144.814	-2	E'' - E'
rR1(3)	3137.775*	1	E' - E''	rR5(9)	3145.793	-1	E' - E''
rR3(4)	3137.775	-1	Az' - Az''	rR3(8)	3145.808	2	Az' - Az''

Lines which are blended and given less statistical weight in the fit are indicated by \*.





## SAMENVATTING

---

### INTRODUCTIE

Dit proefschrift gaat over de studie van koolwaterstoffen via infraroodspectroscopie. Van alle moleculen die in de voorgaande hoofdstukken zijn onderzocht, is bekend dat ze in het heelal bestaan of wordt in ieder geval verwacht dat ze detecteerbaar zullen zijn in het interstellair medium (ISM) of in andere astronomische omgevingen (bijvoorbeeld planetaire atmosferen). Alle experimenten en het merendeel van de theoretische berekeningen werden uitgevoerd in het Sackler Laboratorium voor Astrofysica aan de Universiteit van Leiden, onderbroken door een kort oponthoud aan de Universiteit van Texas en de Universiteit voor Wetenschap en Technologie van China. De astronomische infraroodspectra die in het laatste hoofdstuk worden getoond, zijn opgenomen met de AKARI-ruimtetelescoop.

Koolwaterstoffen vormen de belangrijkste chemische component rondom koolstofrijke sterren (bijv. de AGB-ster IRC +10216 en de protoplanetaire nevel CRL 618) en zijn in overvloed aanwezig in koolwaterstofrijke planetaire atmosferen (bijv. op Jupiter en Saturnus' maan Titan). Gewoonlijk worden moleculen in het heelal geïdentificeerd middels hun rotatie-overgangen in het radio- en submillimeter-domein of door hun rovibratie-overgangen in het infrarood. Recente ontwikkelingen in spectrale resolutie en detectiegevoeligheid, met instrumenten zoals de Atacama Large Millimeter Array (ALMA) in het submillimeter/THz gebied en CRILES+ in het infrarood, geven toegang tot meer precieze spectrale data of spectra die niet eerder konden worden gedetecteerd. Een primair doel van dit proefschrift is het meten van nieuwe moleculaire overgangen van moleculen die bekend zijn, of waarvan verwacht wordt, dat ze in het heelal aanwezig zijn, om zo astronomen te helpen bij de toekenning van observatiespectra en als leidraad voor toekomstige astronomische surveys.

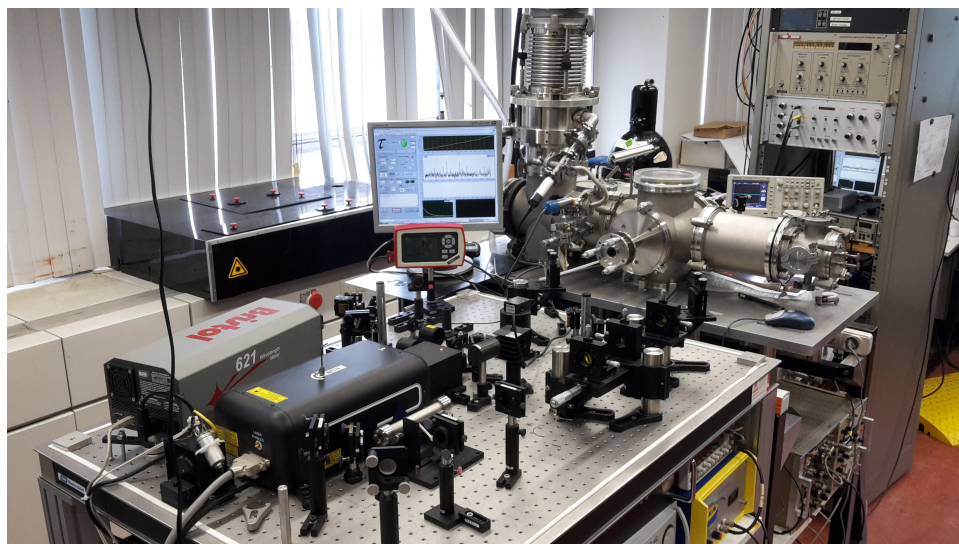
Gezien de verdeling van de elementen in het heelal (H, He, O, C, N, S), is het logisch om aan te nemen dat koolwaterstoffen (met de algemene formule  $C_nH_m$ ) en hun (geladen) derivaten een groot deel vormen van de mogelijke moleculen die verantwoordelijk zijn voor onbekende transitities. Voornamelijk omdat de fysieke omstandigheden in het heelal extremer zijn dan die op aarde - met een zeer lage deeltjesdichtheid, over het algemeen zeer lage temperaturen en grote hoeveelheden ioniserende straling - is de chemie en stabiliteit van moleculen in het heelal enorm verschillend. Dit betekent dat moleculen zoals  $HC_4H$ ,  $C_3$  of  $c-C_3H_3^+$ , die slechts een fractie van een seconde in het laboratorium overleven, honderden jaren in de ISM kunnen bestaan. Daarom zijn ook veel van de moleculen die al in het ISM zijn geïdentificeerd, onstabiele/kortlevende soorten. Het onderzoek van dit soort moleculen is waar dit proefschrift over gaat.

Gebruikmakend van een combinatie van hoge-resolutie infraroodexperimenten en/of zeer nauwkeurige ab initio-berekeningen van trillingsfrequenties en spectroscopische constanten van de grondtoestand, worden hier de infraroodspectraalgegevens van  $HC_2H$ ,  $HC_4H$ ,  $HC_6H$ ,  $HC_8H$ ,  $C_3H_4$ ,  $c-C_3H_3^+$  en  $D_n$ -PAKs (polycyclische aromatische koolwaterstoffen, PAKs) gepresenteerd. Verschillende van deze moleculen waren al in het heelal geïdentificeerd, terwijl andere (zoals  $c-C_3H_3^+$ ) dat niet waren, vooral omdat spectroscopische vingerafdrukken nog niet beschikbaar waren.

## ONDERZOEKSMETHODEN

Voor de meeste projecten die hier beschreven zijn, werden de infraroodovergangen van de onderzochte koolwaterstoffen voorspeld met behulp van berekeningen op CCSD (T)-niveau. Hiervan is aangetoond dat deze nauwkeurig het experimentele spectrum van ‘stijve’ koolwaterstoffen reproduceren, zoals van  $\text{HC}_2\text{H}$ . De geoptimaliseerde geometrieën werden berekend met behulp van cc-pCVQZ, terwijl de trillingsfrequenties werden berekend met behulp van de ‘frozen-core’ basisset van ANO1. De berekeningen werden uitgevoerd met behulp van het Coupled-Cluster-techniques for Computational Chemistry (CFOUR) programma.

De experimentele spectra van de onderzochte koolwaterstoffen werden gemeten met behulp van de Supersonic Plasma InfraRed Absorption Spectrometer (SPIRAS) in het Sackler Laboratorium. Een continue infraroodlaser, werkend rond  $3\ \mu\text{m}$ , werd gebruikt als de lichtbron, zodat hiermee het golflengtedomein dat kenmerkend is voor alle C-H strekvibraties kan worden afgedekt. SPIRAS combineert continuous-wave cavity ring-down spectroscopie (cw-CRDS), een detectiemethode met een zeer hoge gevoeligheid, met een supersonische planaire plasmaontlading. Dit resulteert in spectra van reactieve en vaak onstabiele moleculen met geringe (bijna Dopplervrije) lijnbreedten en lage rotatietemperaturen. Hierdoor is het mogelijk om met SPIRAS ook zwakke ro-vibratoire overgangen te meten of van soorten die moeilijk in hogere concentraties gemaakt kunnen worden.



De SPIRAS opstelling bij het Sackler Laboratorium voor Astrofysica bij de Sterrewacht Leiden.

## DE DETECTIEGEOVOELIGHEID VAN LABORATORIUMMETHODEN EN STORINGSTHEORIE VAN PROPYN ISOTOPOLOGEN

Propyn is een ideaal molecuul om de kinetische temperatuur van astronomische omgevingen te bestuderen vanwege de geringe afstand tussen haar  $K'$ -subbanden. Daarnaast is propyn een referentiemolecuul voor het bestuderen van intramoleculaire storingen. Met behulp van SPIRAS is de sterke  $\nu_1$  acetylenische C-H strekvibratie gemeten voor het reguliere en mono-gesubstitueerde  $^{13}\text{C}$ -propyn ( $\text{H}_3\text{CC}\equiv\text{CH}$ ) zonder daarbij gebruik te moeten maken van isotoop verrijkte gasmeng-

sels. Dat betekent, dat de concentratie van de  $^{13}\text{C}$ -isotopologen ongeveer 1% van die van de normale isotopoloog is. Door dezelfde fundamentele vibratie te bestuderen voor deze vier isotopologen, kan het effect van de  $^{13}\text{C}$  positie in het molecuul op dat van intramoleculaire storingen worden onderzocht. Door de verandering in massa van een van de koolstofatomen worden immers de trillingsfrequenties verschoven, waardoor de energieniveaus op een andere manier op elkaar inwerken. Uit ab initio-berekeningen blijkt dat de langeafstands Fermi resonantie tussen de  $\nu_1$  fundamentele en de  $\nu_3+2\nu_9$  combinatieband significant sterker wordt wanneer de  $^{13}\text{C}$  zich in het midden bevindt; dit komt door de grote verschuiving in de  $\nu_3$  ( $\text{C}\equiv\text{C}$ -rek) vibratiefrequentie, die zeer gevoelig is voor de middelste koolstof. Verder vertoont het normale propyn-isotopoloog een anharmonische storing die verantwoordelijk is voor een verschuiving en herordening van de  $K'$ -subbands. Dezelfde storing wordt ook waargenomen in ons experimentele spectrum voor de isotopologen waarin het  $^{13}\text{C}$  zich op de middelste koolstof bevindt, maar niet voor de andere posities. Helaas is er niet genoeg informatie om de exacte oorzaak van deze storing te achterhalen.

#### THEORETISCHE VOORSPELLINGEN BEWIJZEN M.B.V. EXPERIMENTELE METINGEN: DE EERSTE DETECTIE VAN HET KLEINSTE AROMATISCHE MOLECUUL

*Ab initio*-berekeningen door Huang *et al.* 2011 voorspellen dat de  $\nu_4$  C-H asymmetrische strek-vibratie van het kleinste aromatische molecuul,  $\text{c-C}_3\text{H}_3^+$ , te vinden is rond  $\sim 3131.2\text{ cm}^{-1}$ . We presenteren hier het eerste infraroodspectrum van dit ion in de gasfase (de  $\nu_4$  basisband) van gemeten met SPIRAS. Op basis van onze experimentele spectra, concluderen we dat de ab initio-berekeningen buitengewoon nauwkeurig zijn, met doorgaans minder dan  $1\text{ cm}^{-1}$  verschil tussen de berekende en experimentele data. Vanwege de centrosymmetrische structuur zijn pure rotatie-overgangen niet mogelijk. Daarom kan dit molecuul op dit moment allen geïdentificeerd worden door middel van deze infraroodspectra. Ook bieden de experimenteel bepaalde spectroscopische parameters van  $\text{c-C}_3\text{H}_3^+$  dat een gelokaliseerde positieve lading bezit, goede benchmarkgegevens voor kwantumchemische berekeningen.

#### TOEPASSEN VAN EXPERIMENTELE EN THEORETISCHE INFRAROODGEGEVENS: ZOEKEN NAAR "ONTBREKENDE" MOLECULEN

Gedetailleerde infraroodspectroscopische studies staan aan de basis van de ontdekking van nieuwe moleculen in het heelal en ook is het hiermee mogelijk om andere astronomische mysteries aan te pakken. Zo is in bepaalde delen van het interstellair medium de D/H-verhouding aanzienlijk kleiner dan verwacht. Dit suggereert dat gasfase deuterium verstopt zit in stofkorrels of moleculen. Omdat polycyclische aromatische koolwaterstoffen, PAKs, alomtegenwoordige en relatief stabiele moleculen in het interstellair medium zijn en ook nog eens een groot aantal mogelijke posities hebben waar D-atomen zich kunnen bevinden, werd altijd aangenomen dat ze een reservoir vormen voor ontbrekende D-atomen. In dit proefschrift laat de vergelijking tussen ab initio DFT-berekeningen van het infraroodspectrum van gedeutererde PAKs (hetzij op een alifatische of aromatische positie) met waargenomen spectra in HII-gebieden zien dat sommige van de ontbrekende D-atomen zich inderdaad in PAKs bevinden door reacties waarin de aromaticiteit wordt verbroken. De hoeveelheid deuterium waarvoor dit van toepassing is, is zeer afhankelijk van de omgeving waarin de PAKs zich bevinden.

Een ander astronomisch probleem is dat  $\text{HC}_8\text{H}$  tot nu toe nog niet gedetecteerd kon worden. Hoewel lange koolstofketens reeds in het heelal zijn waargenomen (bijvoorbeeld  $\text{C}_n\text{H}$  en  $\text{C}_n$  tot respectievelijk  $n = 8$  en  $9$ ), zijn voor de polyynes ( $\text{HC}_n\text{H}$ ) ketens tot slechts  $n = 6$  waargenomen. In het laboratorium bestonden waren hoge resolutie infraroodgegevens alleen beschikbaar tot  $\text{HC}_6\text{H}$

- mogelijk een gevolg van de gebruikte plasmaproductiemethode - echter, in het heelal zou dit geen belemmering mogen opleveren. Uit ab initio clusterberekeningen van HC<sub>8</sub>H-vibratiemodi die in dit proefschrift worden gepresenteerd, volgt dat spectra van HC<sub>8</sub>H volledig schuilgaan achter die van HC<sub>6</sub>H en HC<sub>4</sub>H, tenminste voor de golflengten die worden gebruikt om polyynen in het heelal te identificeren (~16 μm). Waarnemingen bij andere frequenties, zoals op ~60 cm<sup>-1</sup>, waarvoor geen overgangen van andere polyynen worden gevonden, zijn nodig om definitief te bepalen of HC<sub>8</sub>H voorkomt in het heelal.

Ten slotte bieden de IR-spectra van het reeds genoemde c-C<sub>3</sub>H<sub>3</sub><sup>+</sup> voor de eerste keer een manier om te zoeken naar dit molecuul in het heelal, dat wordt beschouwd als een belangrijk tussenproduct in de vorming van moleculen met een ringstructuur. De astronomische waarneming van c-C<sub>3</sub>H<sub>3</sub><sup>+</sup> zal helpen om tekortkomingen in het koolwaterstofreactienetwerk te vullen, zodat een gasfase-route naar de vorming van PAKs gerealiseerd kan worden. De hier gepresenteerde resultaten zullen volgend jaar worden gebruikt om dit molecuul in het heelal te zoeken, met behulp van CRIFES+.

## SUMMARY

---

### INTRODUCTION

This thesis is about the study of hydrocarbons via infrared spectroscopy. All molecules investigated in the previous thesis chapters are known to exist in space or are expected to be detectable in the interstellar medium (ISM) or other astronomical environments (*e.g.*, planetary atmospheres). The underlying experiments and theoretical calculations were primarily performed at the Sackler Laboratory of Astrophysics at Leiden University, with brief stays at the University of Texas and the University of Science and Technology of China. The astronomical infrared spectra shown in the last chapter were taken using the AKARI space telescope.

Hydrocarbons are the prominent chemical component around carbon rich stars (*e.g.*, the AGB star IRC +10216 and the protoplanetary nebula CRL 618) and are abundant in hydrocarbon rich planetary atmospheres (*e.g.*, Jupiter and Saturn's moon Titan). Commonly molecules are detected/identified in space through their pure rotational transitions in the radio and submillimeter domain or through their ro-vibrational transitions in the infrared. Recent advances in spectral resolution and detection sensitivity, with instruments such as the Atacama Large Millimeter Array (ALMA) in the submillimeter/THz and CRIRES+ in the infrared, give access to more precise spectral data or spectra not detectable before. One of the goals of this thesis is to measure new molecular transitions, of molecules that are known or expected to be present in space, to aid astronomers in the assignment of observational spectra and as input for future dedicated surveys.

Given the abundant atoms in space (H, O, N, C, He and S), it is logical to assume that hydrocarbons (with the general formula  $C_nH_m$ ) and their (charged) derivatives form a large fraction of the possible molecules that could be assigned to unknown transitions. In particular, because the physical conditions in space are harsher than that on Earth - with very low particle density, typically low temperatures, and large amounts of ionizing radiation - the chemistry and stability of molecules in space is vastly different. This means that molecules like  $HC_4H$ ,  $C_3$  of  $c-C_3H_3^+$ , which can live in the laboratory for only a fractions of a second, can live for hundreds of years in the ISM. As such, many of the molecules already identified in the ISM are unstable/transient species. These species are also the focus of this thesis research.

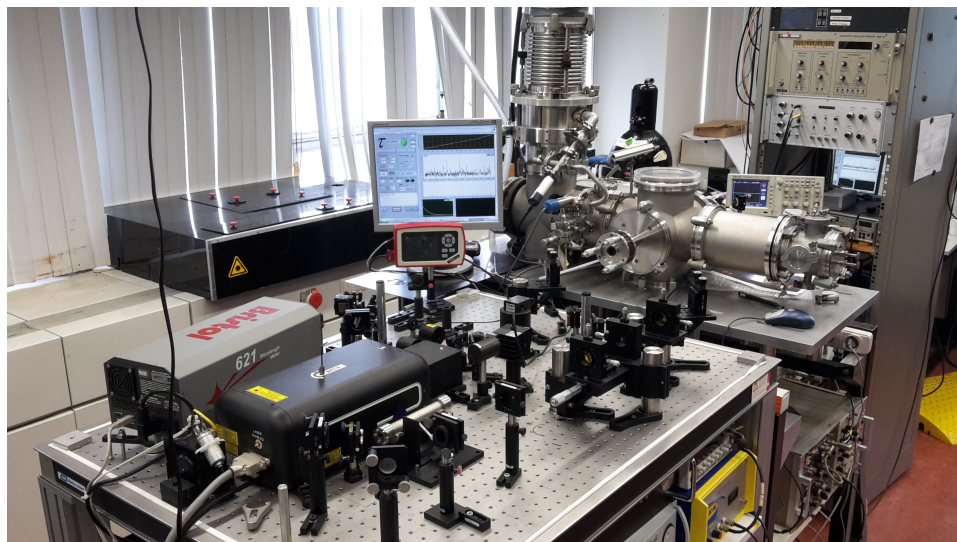
Using a combination of high-resolution infrared experiments and/or high level *ab initio* calculations of vibration frequencies and ground state spectroscopic constants, the infrared spectral data of  $HC_2H$ ,  $HC_4H$ ,  $HC_6H$ ,  $HC_8H$ ,  $C_3H_4$ ,  $c-C_3H_3^+$  and  $D_n$ -PAHs (polycyclic aromatic hydrocarbons, PAH) are presented. Several of these species were already identified in space, while others (like  $c-C_3H_3^+$ ) were not, mainly because spectroscopic fingerprint spectra were not yet available.

### RESEARCH METHODS

For the majority of the projects described here, the infrared transitions of the hydrocarbons studied were predicted using the coupled cluster with iterative single and double excitation, augmented with fixed triple excitation (CCSD(T)) level of theory, which has been demonstrated to accurately reproduce the experimental spectrum of "rigid" hydrocarbons, such as  $HC_2H$ . The optimized geometries were calculated using the large core-valence basis set of cc-pCVQZ, while the vibrational frequencies were calculated using the frozen-core basis set of ANO1. The calculations were perfor-

med using the program Coupled-Cluster techniques for Computational Chemistry (CFOUR).

The experimental spectra of the hydrocarbons studied were measured using the Supersonic Plasma InfraRed Absorption Spectrometer (SPIRAS) located at the Sackler Laboratory for Astrophysics. A continuous wave narrow band infrared laser, operating around  $3\ \mu\text{m}$ , is used as the light source, which covers the wavelength domain typical for all C-H stretch vibrations. SPIRAS combines continuous wave cavity ring-down spectroscopy (cw-CRDS), which has a very high detection sensitivity, with a supersonic planar plasma discharge, which results in spectra of molecular transients with narrow linewidths and low rotational temperatures. As a result, SPIRAS can measure the rotationally resolved ro-vibrational spectrum of weak transitions and/or low concentration species.



The SPIRAS setup at the Sackler Laboratory for Astrophysics at Leiden Observatory.

#### PROBING THE DETECTION SENSITIVITY OF LABORATORY METHODS: PERTURBATION ANALYSIS OF PROPYNE ISOTOPOLOGUES

Propyne is an ideal molecule to study kinetic temperature of astronomical objects because of the close spacing between its  $K'$ -subbands. Furthermore, propyne is a benchmark molecule for studying intramolecular perturbations. Using SPIRAS, the strong  $\nu_1$  acetylenic C-H stretch fundamental was measured for the normal and mono-substituted  $^{13}\text{C}$  propyne ( $\text{H}_3\text{CC}\equiv\text{CH}$ ) at natural abundances, where the concentration of the  $^{13}\text{C}$  isotopologues are about 1% that of the normal isotopologue. By studying the same fundamental for all four isotopologues, we are able to learn the affect of isotopic position of intramolecular perturbations. Due to the change in mass of one of the carbon atoms, the vibrational frequencies are shifted, resulting in the energy levels interacting with each other differently. From *ab initio* calculations, it was shown that the long range Fermi resonance between the  $\nu_1$  fundamental and the  $\nu_3+2\nu_9$  combination band becomes significantly stronger when the  $^{13}\text{C}$  position is the middle carbon; this is due to the large shift in the  $\nu_3$  ( $\text{C}\equiv\text{C}$  stretch) vibrational frequency, which is highly sensitive to the middle carbon. Furthermore, the normal propyne isotopologue is reported to have an anharmonic perturbation that shifts and reorders the  $K'$ -subband origins. This same perturbation is also observed in our experimental spectrum for the isotopologues that have the  $^{13}\text{C}$  on the middle or acetylenic carbon, but not on the

isotopologue where the  $^{13}\text{C}$  position is on the aliphatic carbon. Unfortunately, there is not enough information to determine the exact cause of this perturbation.

PROVE THEORETICAL PREDICTIONS WITH EXPERIMENTAL MEASUREMENT:  
FIRST DETECTION OF THE SMALLEST AROMATIC MOLECULE

*Ab initio* calculations by Huang *et al.* 2011 predict that the  $\nu_4$  C-H asymmetric stretch fundamental band of the smallest aromatic molecule,  $c\text{-C}_3\text{H}_3^+$ , would fall at  $\sim 3131.2\text{ cm}^{-1}$ . We have measured the first pure gas-phase infrared spectrum (the  $\nu_4$  fundamental band) of  $c\text{-C}_3\text{H}_3^+$  using SPIRAS. Based on our experimental spectra, the *ab initio* calculations are proven to be exceedingly accurate, with typically a less than  $1\text{ cm}^{-1}$  difference between the calculated and experimental band origins. Due to its centrosymmetric structure, pure rotational transitions are strictly forbidden by spectroscopic selection. As such, the provided infrared spectra is currently the only means to identify this molecule in space. In addition, with a delocalized positive charge, the experimentally determined spectroscopic parameters of  $c\text{-C}_3\text{H}_3^+$  offer good benchmark data for quantum chemical computations.

APPLYING EXPERIMENTAL AND THEORETICAL INFRARED DATA:  
LOOKING FOR "MISSING" MOLECULES

Dedicated infrared spectroscopic studies have been able to identify new molecules in space. In this thesis study, these also have shed light on astronomical mysteries. First, in certain parts of the interstellar medium, the D/H ratio is significantly smaller than expected from stellar processing. This suggests that some of the gas-phase D atoms are locked up in either dust grains or molecules. Since PAHs are ubiquitous and relatively stable molecules in the interstellar medium, and moreover, offer a large number of possible positions to incorporate D atoms, it was hypothesized that they provide a potentially large reservoir for the missing D atoms. In this thesis, the comparison between *ab initio* DFT calculations of the infrared spectrum of deuterated PAHs (either at an aliphatic or aromatic position) with our observed spectra from HII regions, showed that some of the missing D atoms is incorporated into PAHs through addition reactions (breaking the aromaticity), and the amount of D addition is extremely environmentally dependent.

Another astronomical problem is the non-detection of  $\text{HC}_8\text{H}$ . While long carbon chains have been observed (*e.g.*,  $\text{C}_n\text{H}$  and  $\text{C}_n$  up to  $n = 8$  and  $9$ , respectively), for the polyynes ( $\text{HC}_n\text{H}$ ) only up to  $n = 6$  has been observed. In the laboratory, high-resolution infrared data only existed up to  $\text{HC}_6\text{H}$ , which might be a result of the plasma production method, however, in space the formation mechanism should not be so hampered. From *ab initio* coupled cluster calculations of  $\text{HC}_8\text{H}$  vibrational modes presented in this thesis, it was shown that at the wavelengths used to identify polyynes in space ( $\sim 16\text{ }\mu\text{m}$ )  $\text{HC}_8\text{H}$  is completely obscured by  $\text{HC}_6\text{H}$  and  $\text{HC}_4\text{H}$ . Observations at different frequencies, such as at  $\sim 60\text{ cm}^{-1}$ , where no transitions from other polyynes are found, would determine on whether  $\text{HC}_8\text{H}$  is in space or not.

Finally, the IR spectra of the already mentioned  $c\text{-C}_3\text{H}_3^+$  offers, for the first time, a way to search for this molecule, which is considered to be an important intermediate in the formation of ring molecules. The astronomical observation of  $c\text{-C}_3\text{H}_3^+$  will help fill in gaps in the hydrocarbon reaction network, eventually providing a gas phase route to the formation of PAHs. The results presented here will be used in the next year to search for this molecule in space, using CRIRES+.



## LIST OF PUBLICATIONS

---

1. *Electronic spectra of C<sub>3</sub> from the ground state bending mode*  
Q. Zhang, **K. D. Doney**, J. Gu, D. Zhao, H. Linnartz, and Y. Chen, in preparation
2. *Stretching our understanding of C<sub>3</sub>: Experimental and theoretical spectroscopy of highly excited  $n\nu_1 + m\nu_3$  states ( $n \leq 7$  and  $m \leq 3$ )*  
B. Schröder, **K. D. Doney**, P. Sebald, D. Zhao, and H. Linnartz, submitted
3. *High-resolution infrared spectra of the  $\nu_1$  fundamental bands of monosubstituted <sup>13</sup>C propyne isotopologues*  
**K. D. Doney**, D. Zhao, and H. Linnartz, *The Journal of Physical Chemistry A*, 122 (2018) 582
4. *Theoretical investigation of the infrared spectrum of small polyynes*  
**K. D. Doney**, D. Zhao, J. F. Stanton, and H. Linnartz, *Physical Chemistry Chemical Physics*, 20 (2018) 5501
5. *The high-resolution infrared spectrum of the  $\nu_3 + \nu_5$  combination band of jet-cooled propyne*  
**K. D. Doney**, D. Zhao, J. Bouwman, and H. Linnartz, *Chemical Physics Letters*, 684 (2017) 351
6. *Deuterated polycyclic aromatic hydrocarbons: Revisited*  
**K. D. Doney**, A. Candian, T. Mori, T. Onaka, and A. G. G. M. Tielens, *Astronomy & Astrophysics*, 586 (2016) A65
7. *High-resolution infrared spectrum of triacetylene: The  $\nu_5$  state revisited and new vibrational states*  
**K. D. Doney**, D. Zhao, and H. Linnartz, *Journal of Molecular Spectroscopy*, 316 (2015) 54
8. *Laboratory gas-phase detection of the cyclopropenyl cation ( $c\text{-C}_3\text{H}_3^+$ )*  
D. Zhao, **K. D. Doney**, and H. Linnartz, *The Astrophysical Journal Letters*, 791 (2014) L28
9. *High-resolution infrared spectra of vibrationally excited HC<sub>4</sub>H in a supersonic hydrocarbon plasma jet*  
D. Zhao, **K. D. Doney**, and H. Linnartz, *Journal of Molecular Spectroscopy*, 296 (2014) 1



## CURRICULUM VITAE

---

I was born in Dallas, Texas in 1988, and spent most of my formative years in Austin, Texas. My undergraduate degree started at Texas A&M University (for one year), and was completed at The University of Texas at Austin, from which I obtained a B.Sc. in Chemistry and a B.A. in Astronomy in December 2011. For undergraduate research experience, I worked on a project to model the young stellar object IRAS 03245+3002 under the supervision of Hyo Jeong Kim and Dr. Neal J. Evans II. During my bachelor's degree, I switched from majoring in biochemistry to pure chemistry and astronomy, which required multiple labs in biology, chemistry, and physics, and cemented an interest in being an experimentalist. This interest was furthered through 1) work in the chemical stockroom during undergrad making and supplying chemicals for the teaching labs, and 2) work as a teaching assistant for general chemistry teaching labs after graduating.

In 2012, I began my graduate career at the University of Leiden. My master's study was financially supported in the first year by the Silver Leiden University Excellence Scholarship (LEXS), and in the second year by the van de Hulst fellowship. In 2014, I obtained a M.Sc. in Astronomy; with a minor project studying the high-resolution infrared spectrum of diacetylene at 3  $\mu\text{m}$  under the supervision of Dr. Dongfeng Zhao and Prof.dr. Harold Linnartz, and a major project searching for deuterated PAH infrared features in observational spectra of HII regions of the Milky Way and Magellanic Clouds under the supervision of Dr. Alessandra Candian and Prof.dr. A. G. G. M. Tielens. Immediately following the completion of my masters degree I began my doctoral degree, and on the work described in this thesis. The Ph.D. was promoted by Prof.dr. Harold Linnartz and Dr. Dongfeng Zhao as part of the Sackler Laboratory for Astrophysics. During the course of my doctoral career, I presented the work in this thesis at various conferences and workshops in the Netherlands, the United States, England, France, Finland, and China, the attendance of which were partially supported by my three Leids Kerkhoven-Bosscha Fonds (LKBF) grants, one Leids Universiteits Fonds (LUF) grant, and one University of Science and Technology of China fellowship B grant.



## ACKNOWLEDGEMENTS

---

Along the way there have been many engaging, extravagant, brilliant people without whom I would not be where I am today, and I would like to thank them for their support while I was working on and writing the parts of this thesis. Thank you, dank u wel, 谢谢

First and foremost, thank you to the Bosses: Harold and Dongfeng, and Collaborators: John, Xander, Alessandra, Qiang, Benjamin, Takashi, and Tamami for helping me to do the research I love. Strictly speaking this thesis would not be here without you; your contributions have been invaluable to the final manuscripts.

Thank you to my colleagues (past and present) in the Sackler Laboratory (SLA): Niels, Ko-Ju, Daniel, Pablo, Xavier, Gwen, Gustavo, Anton, Junfeng, Andreas, Jordy, Vincent, Danna, Michal, Gleb, Thanja, Jeroen, Martijn, and Aart, for keeping me company at work, for the scientific discussions, for all the lovely lunch discussions, and, of course, the fantastic games of Dominos. And a special thank you to my officemates Niels, Ko-Ju, and Vincent, for always being my sounding board (even when sometimes it was just gossip).

I would like to thank the ISM group: Francisco, Cameron, Pedro, Heather, Cornelia, Liz, Tao, Kim, Raymond, Sascha, and Claudia, and the Astrochem group: Arthur, Alyssa, Alex, Alan, Catherine, Sierk, Eva, Nico, Mason, Łukasz, Maria, Luke, Merel, and Mikhel, for always teaching me new things about astronomy, and for all the good times at meetings (plus all the cookies and pizza). Thank you to the UT/CFOUR group: Devin, Josh, Filippo, James, and Lam, for helping an experimentalist start doing calculations, and letting my crash in your office for a few weeks. Thank you to the USTC group: Chunting, Chao, Deping, Boxing, Jingwang, Shaowen, Hao, Zengjun, Zhengfang, and Zefeng, for letting me be a part of your group for a few months. And thank you to the Leiden support staff: Evelijn, Els, Debbie, Yvonne, Marjan, Liesbeth, and Anita, and the computer group: Erik, Eric, David and Leonardo, your continued help with day to day problems (particularly the weird logistical problems) have helped me continue my work.

Moreover, to everyone, I truly believe that the people are what make the workplace, and everyone has truly made my many workplaces fantastic. And I was lucky to have not one, but three great workplaces.

I would also like to give a special thank you to my work out buddies, because all of the sports helped balance all the academia. Thank you to the CrossFito71 community: Alice, Christian, Esther, Nelus, Jordan, Casey, Rui, Robert, Dirk, Kasper, Merlin, Francette, Marije, Marnix, Niels, Pyne, Joost, and Manuel, and to my cycling buddy: Andrej, thank you for working out with me, without y'all the suffering would be less fun.

Importantly, I would like to thank my family - I love y'all - I have been extremely lucky to have you and to have grown up with your eccentricities. So to Mom, Dad, Rachel, Jake, Grandma, Uncle Michael, Aunt Lori, Aunt Stephanie, Uncle David, Alex, Kelly, Maxie, Jack, Uncle Mark, Aunt Kim, Kaitlin, and Hanna, thank you for the years of adventures, the holidays together, and making life interesting. And many thanks for visiting/calling/texting me frequently, making the 5,000+ miles seem not too terribly far.

